# Energy Conservation Projects to Benefit the Railroad Industry

Report Type: Final Technical Report

Project start date: 8/1/08

Project end date: 12/30/09

Principle Authors:

Dr. Clifford Mirman
Dr. Promod Vohra

Date Report Issued: February 18th, 2010

DOE award number: DE-NT0004801

Address of Submitting Organization:

Northern Illinois University
Lowden Hall 301
Dekalb, Ill 60115-2860

Abstract:

The Energy Conservation Projects to benefit the railroad industry using the Norfolk Southern Company as a model for the railroad industry has five unique tasks which are in areas of importance within the rail industry, and specifically in the area of energy conservation. The NIU Engineering and Technology research team looked at five significant areas in which research and development work can provide unique solutions to the railroad industry in energy the conservation.

**Alternate Fuels** – An examination of various blends of bio-based diesel fuels for the railroad industry, using Norfolk Southern as a model for the industry. The team determined that bio-diesel fuel is a suitable alternative to using straight diesel fuel, however, the cost and availability across the country varies to a great extent.

**Utilization of fuel cells for locomotive power systems** - While the application of the fuel cell has been successfully demonstrated in the passenger car, this is a very advanced topic for the railroad industry. There are many safety and power issues that the research team examined.

**Thermal and emission reduction for current large scale diesel engines** - The current locomotive system generates large amount of heat through engine cooling and heat dissipation when the traction motors are used to decelerate the train. The research team evaluated thermal management systems to efficiently deal with large thermal loads developed by the operating engines.

**Use of Composite and Exotic Replacement Materials** – Research team redesigned various components using new materials, coatings, and processes to provide the needed protection. Through design, analysis, and testing, new parts that can withstand the hostile environments were developed.

**Tribology Applications** – Identification of tribology issues in the Railroad industry which play a significant role in the improvement of energy usage. Research team analyzed and developed solutions which resulted in friction modification to improve energy efficiency

**Table of Contents:**

Executive Summary:

This project entitled Energy Conservation Projects to benefit the Railroad industry seeks to develop energy efficient solutions to currently existing modes of operation in the railroad industry. The project develops new ideas for energy conservation and efficiency using the Norfolk Southern Company as a model for the railroad industry. The project has five unique tasks which allow the industry to explore new areas of efficiency.

**Alternate Fuels**
The Norfolk Southern Railroad Company uses 100% diesel fossil fuel as it source of locomotive energy. The project team examined the usage of various blends of bio-based diesel fuels for the railroad industry, using Norfolk Southern as a model for the industry. The team determined that bio-diesel fuel is a suitable alternative to using straight diesel fuel, however, the cost and availability across the country varies to a great extent. In addition, the team determined that some of the emission properties dropped substantially, others increased with the use of this alternate fuel. It was determined that there are issues with bio-fuel and engine part wear as this type of fuel interacts with the engine parts and surfaces. The research team examined the safety issues concerning the use and storage of bio-diesel. Existing fuel infrastructures were studied and it was determined that since the bio-diesel has a finite shelf life, and must be mixed in the various grades on site, there will be large infrastructure costs incurred as part of the switch.

**Utilization of fuel cells for locomotive power systems**
While the application of the fuel cell has been successfully demonstrated in the passenger car, this is a very advanced topic for the railroad industry. There are many safety and power issues that the research team will examine. The railroad industry would like to utilize the fuel cell as an auxiliary source of energy, thus, employing a smaller, more efficient diesel power plant to provide power. The net result will be a cost and fuel savings over various regions and terrains. The design team has determined that an SOFC cell is the best bet for this purpose. On board gasification of biodiesel will be used for the fuel. Major components include SOFC, gasifier, gas cleaning, heat exchangers for heat recovery/preheating and cooling. This cooling system has to remove heat form fuel cell stack using bi-polar plates and remove heat from electric motors and inverters. A part of the excess fuel from fuel cell stack can be burned in the combustor to supply necessary heat to steam reformers, steam generator and air-preheater. In addition, due to the large amount of heat generated through the breaking system, it has been put forward that a regenerative breaking system should be developed for the locomotive system.

**Thermal and emission reduction for current large scale diesel engines**
The current locomotive system generates large amount of heat through engine cooling and heat dissipation when the traction motors are used to decelerate the train. The research team evaluated thermal management systems to efficiently deal with large thermal loads developed by the operating engines. To do this the team researched nano-particles suspended in the cooling fluid used by the engine. Through the introduction of nano-particles, there is an increase in the rate of cooling since the fluid is able to effectively absorb more heat from the engine.

Since control plans for on-road vehicle emissions have been put into effect, locomotives could become the primary source for dangerous air pollution in the country. In addition to the requirement of reduced greenhouse gases such as carbon dioxide, the individual air pollutants to eliminate are particulate matter (PM), hydrocarbons (HC), and the oxides of nitrogen (NOx). The primary goal of this research was to understand how various changes in diesel engine operating conditions can change emissions and thermal efficiency and to be able to successful predict these changes through computational fluid dynamics and combustion modeling. The work addressed how the operating systems design for large thermal loads effects the emission factors for diesel emission components such as, greenhouse gases like carbon dioxide, carbon monoxide, oxides of nitrogen, hydrocarbons, and particulate matter. Developing related experimental and computational analysis identified several concepts that can be incorporated into innovative design and operation of diesel locomotives.

**Use of Composite and Exotic Replacement Materials**

Currently on the structure of the locomotive, there are components which are poorly designed from an energy standpoint. Many of the current components are not designed to reduce the vibration and sound loads, as well as fatigue and wear due to environmental issues. The research team examined the redesign of various components using new materials and coatings to provide needed protection. The following components were redesigned,

- Induction tubes – Exhaust ports on engine get clogged with the exhaust soot, and the design team looked at new coatings and manufacturing methods for this important part. The coatings studied offered low friction at high temperature, while providing significant cost savings.
- Air brake hosing – At various points on the train, the pressure differential in the air hosing dropped significantly, due to cable wear. It was determined that the wear can be eliminated by various mounting techniques.
- Coupling knuckle – Train couplers put heavy fatigue loads on the coupling knuckle, which in turn fails at inopportune times. The research team studied the failure of the component as well as solutions to the failure.
- Brake shoes – Current backing plate for the shoes allows for cracking as the material wears. It was found that significant longevity of the brake shoes could be realized through a novel redesign of the backing plates of the shoes.

**Tribology Applications**

The main objective was to identify tribology issues in the railroad industry which play significant roles in the improvement of energy usage and to develop solutions which result in friction modification to improve energy efficiency. New and modified lubricants, wear surfaces, and nano-lubricants were examined and analyzed for traction, and heat generation based on numerical models and actual wear tests were conducted on the materials. Bearing parameters, and load capacities, as well as seizure loads were evaluated using ASTM tests, and the lubes were tested on full scale models. It was determined that through low-cost modification in the current lubes, beneficial properties could be enhanced.

**Task2 - Alternate fuels in the railroad industry**

The objective of this task was to study the needed infrastructure and delivery costs for using biodiesel fuel in place of the current petroleum-based diesel to power locomotives. Performance, economic, and environmental issues have been evaluated.

Biodiesel – Product Definition
Biodiesel is a liquid fuel which may be derived from many natural sources and utilized in a range of diesel engines without significant efforts or required modifications. Some of the key feedstocks from which biodiesel may be derived include soybean oil, canola oil, sunflower oil, tallow/animal fat, trap grease, corn oil (e.g., sourced from ethanol plants), and reclaimed vegetable oil. The chemical name for biodiesel is fatty acid methyl ester (FAME). Pure biodiesel is referred to as B100 while one common blend is designated as B20, which is 20% biofuel. This study considers all the commercially-available blends: B5, B10, B20, B50, and B100.

To make biodiesel fuel blends, B100 is normally mixed with conventional petroleum fuel. A number of alternatives exist for this blending including splash blending, tank blending, and nozzle blending. The National Biodiesel Board (NBB) outlines procedures for proper blending that ensure the fuel product will not stratify [1].

The biodiesel industry has experienced significant growth over the past several years, resulting in expanded market reach and penetration. Many major fleets have begun adopting biodiesel blends including the U.S. Postal Service and the United States Military, as well as numerous state and local governments. In 1999, there were less than 1 million gallons of biodiesel produced, and by 2005 approximately 200 million gallons. The demand for biodiesel continues to expand, and the supply is growing in response.

The key factors for utilizing biodiesel on a large scale are its "green" nature, natural lubricity advantages, and price. All three of these factors must be considered although pricing is obviously an important criterion. There is significant price variability for biodiesel fuel blends, as there is with petroleum-based. Petrodiesel prices correlate well with crude oil as shown by Figure 2-1.

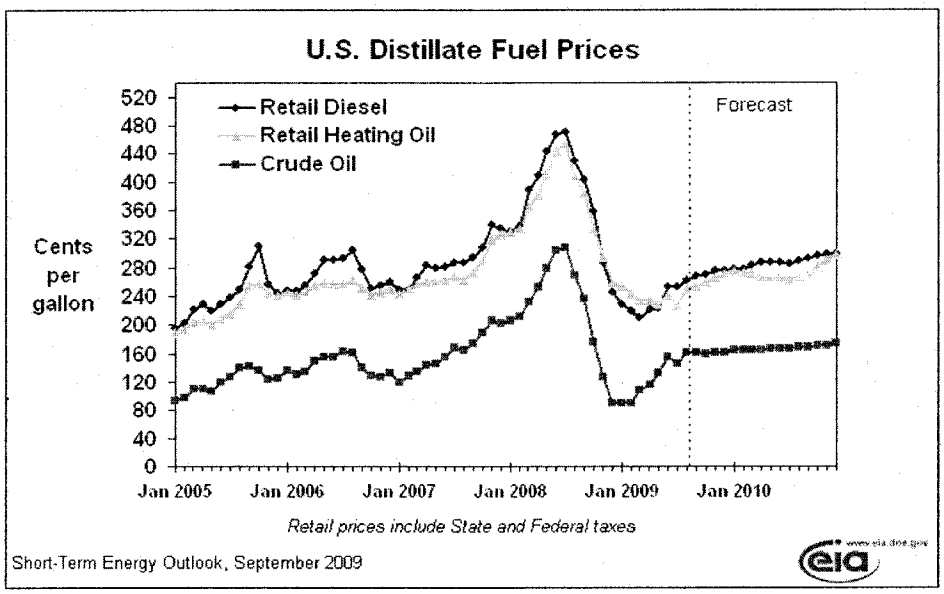


Figure 2-1- U.S. Distillate Fuel Prices

In a similar fashion, biodiesel prices follow price trends based on their input feedstocks. In biodiesel fuel production the feedstock cost is the greatest contributor to the final price [2] and currently the most common are virgin soybean oil, recycled vegetable oil, corn oil, yellow grease, and tallow. Most large-scale biodiesel production facilities use virgin soybean oil, due to its availability, although its price fluctuates widely with dynamics in the markets.

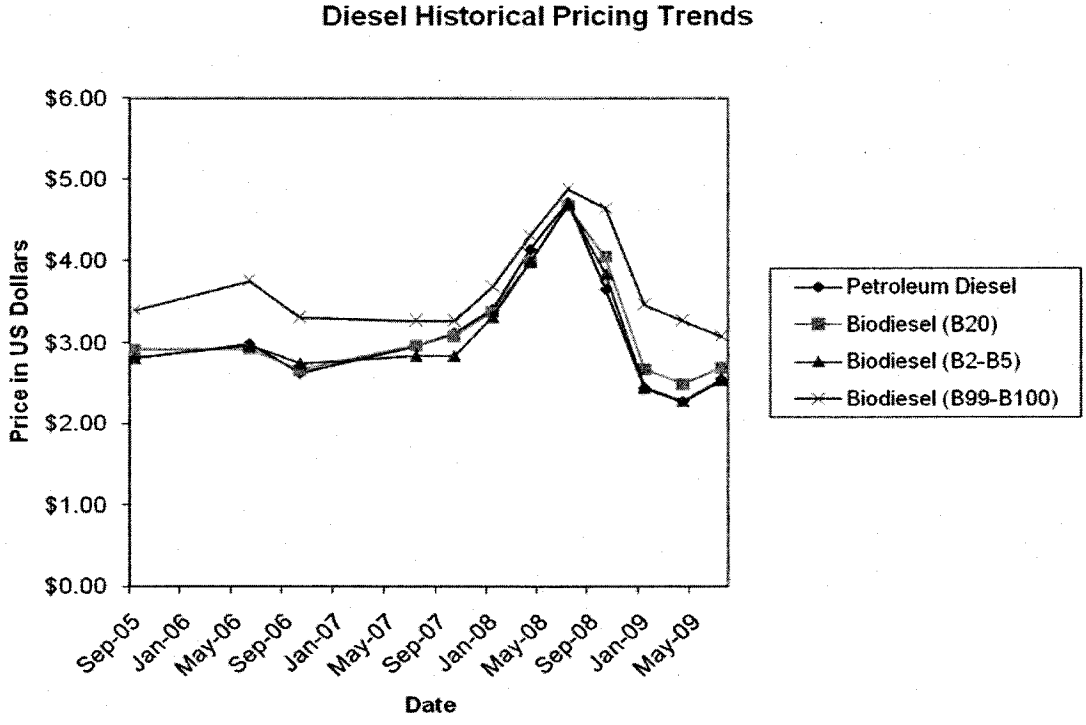


Figure 2-2 - Historical Pricing Trends, Petrodiesel and Various Biodiesel Blends

Figure 2-2 illustrates the recent price trends of petroleum diesel and blends of biodiesel, including B2-B5 blends, B20, and B99-B100 blends [3]. Note that these are national average values, and there tends to be variability in the prices of biodiesel by geographical location within the United States. The price for B2-B5, B20, and petrodiesel are nearly the same. The B99-B100 or pure, unblended biodiesel is significantly higher than petrodiesel.

Biofuels have gained significant market share over the past decade [4], with ethanol leading the transformation. Biodiesel entered the market later than ethanol and has also experienced rapid growth and market demand as seen in Figure 2-3.

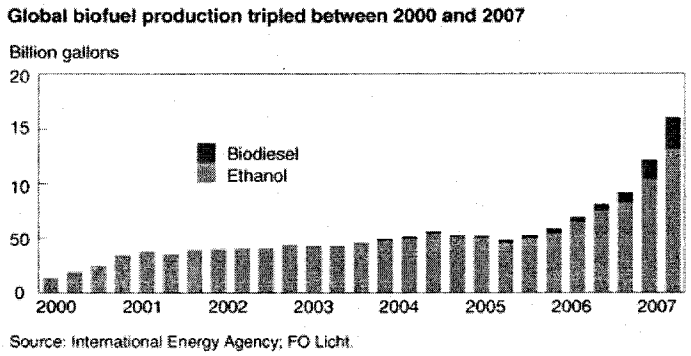

Figure 2-3 - Ethanol and Biodiesel Production

Biodiesel is currently in a high growth pattern, although the overall capacity is less than ethanol. In the United States, diesel engines are used predominantly in transportation and ample supplies are anticipated. The biodiesel industry in the United States has seen a growth rate of 50% from 2005 to 2007 and 30% additional growth is expected during the time period 2007 to 2012 [5].

Physical and Chemical Properties

Biodiesel has a slightly lower heat of combustion than its petroleum-based counterpart and typically carries a slightly higher cetane rating (analogous to the octane rating of a gasoline fuel). The higher cetane may allow better efficiencies that translate into more effective operation for higher-speed diesels. With the increased cetane rating of biodiesel and subsequently the fuel's ability to withstand higher compression prior to ignition, this might be leveraged through adaptive controls (e.g., increased turbocharger boost) for improved performance. The higher cetane number also translates into improved starting properties. Additionally, biodiesel carries a slightly higher viscosity rating than petroleum diesel [1].

The unique solvent nature of biodiesel enables it to have a cleaning effect in an engine and its fuel system. However, initial cleansing will put particulate matter into the fuel system eventually being captured by the fuel filter(s). Overall, such solvent action may beneficially reduce carbon buildup within combustion chambers, on piston heads, and in the overall fuel/engine system.

Environmental Impacts

Biodiesel offers a number of potential environmental benefits such as having a smaller carbon footprint, less particulate pollution, and less sulfur. This meshes well with the industry-wide reduction of allowable sulfur content in all diesel fuels. Biodiesel has inherently higher lubricity than petroleum diesel, compensating for the lubricity enhancement of sulfur in petrodiesel.

Especially since locomotives idling at refueling stations would produce more concentrated emissions, this study must take into account pollutants. These include carbon monoxide (CO), carbon dioxide ($CO_2$), various nitrogen oxides ($NO_x$), and hydrocarbons (HC) and would be liberated as gases. Gas emission rates and concentrations are dependent on fuel consumption rate, fuel blend, air flow rate, and other factors. Also present are particulate emissions and smoke. Biodiesel offers significant emission improvements in hydrocarbons and carbon monoxide. But nitrogen oxides are slightly elevated, although this is not consistent. According to research with an Electro-Motive Division (EMD) locomotive, B20 reduced emissions of carbon monoxide and hydrocarbons [6]. The EMD investigation revealed a 16% reduction of CO in "line-haul" tests which are representative of more steady-state operation along with a 5% reduction in HC for switch duty cycle, which may more closely simulate idling; particulate matter (PM) was somewhat higher for line-haul and slightly reduced for switch duty.

New Jersey Transit recently evaluated soy-based B20 in a 3000-hP EMD 16-645 commuter locomotive; the engine was operated statically with a load bank [7]. Overall performance was satisfactory although the solvent effect of the fuel did require maintenance of clogged fuel injectors. Their data indicated equivalent power and fuel consumption while exhaust opacity decreased 50% and $NO_x$ emissions increased only 2%. (The data confirmed that releases of hydrocarbons and carbon monoxide are favorable with mixtures up to B20 and it is the nitrogen oxides that may be problematic.) The nitrogen oxides formation increase is less than that measured with the previous EMD (16-645-E) locomotive where $NO_x$ emissions rose 6% and particulates 9% in line-haul duties [6].

A recent series of tests were conducted using a 1944 Alco S2 switch locomotive moving cargo at the Port of San Francisco [8]. The locomotive's typical run was four miles at an average speed of 10 miles/hr. This 1000-hP engine was tested with B50 and B100 and emissions were measured. Significant decreases in HC and PM were noted with large increases in nitrogen compounds while CO emissions were unchanged with B50 and 19% reduced with B100.

Another potential benefit to the adoption of biodiesel is in the event of spillage or leakage into the environment. Biodiesel is biodegradable which would reduce negative environmental effects. In general, biodiesel shows an overall improvement in some of the key emissions typically measured, while at the same time enhancing the ability to run low-sulfur fuels.

Handling and Storage

Biodiesel has handling and storage advantages. One advantage is its higher flash point, compared to petrodiesel. For example, B100 has a minimum flashpoint of 260°F while #2 diesel has a flashpoint of 125° F. This translates into lower flammability and volatility in storage and handling. But biodiesel does oxidize slightly more readily than petroleum diesel and should not be stored for periods greater than six months. Any potential for bacteria growth can be minimized by following a protocol for more rapid product turnover and proactively managed in warmer climates by the addition of a biocide. Otherwise, biodiesel handles and stores like conventional diesel and utilizes the same transport infrastructure, such as tankers and containers.

In March of 2009, Northern Illinois University sent a team of undergraduate students to visit a railroad refueling depot in Decatur, Illinois. The purpose was to learn about the current petrodiesel fuel delivery method, use of rubber and elastomers, and the ease and effort of cleaning out holding tanks and associated fuel delivery components. When refueling, a tanker truck unloads through pipes to a pump and filter station. There are two separate pumps and filter systems but only one is used at a time; the other is back-up in case a pump goes down. Additionally, between the months of November and February, a "tempo cold flow" chemical additive is injected into the fuel at a ratio of 1:2500 to prevent gumming of the fuel in extreme cold conditions. Finally the fuel ends in a 1,000,000 gallon holding tank where it is stored until needed. Fuel may be directed to one of the facility's nine fueling cranes, each with a pumping capacity of 280 gpm. A typical locomotive has a tank capacity of 4,000 to 5,000 gallons but arrives with a substantial reserve of fuel. Use of rubber is limited to about four feet of hose at each fueling crane. The hoses are aircraft grade and manufactured meeting API 1529 and NFPA 407 specifications. Paper filters and gaskets are used throughout the system. The same paper filters are also used within locomotives.

Modeling Costs to Refuel Railway Depots

To model the most cost effective way to provide a railway company with biodiesel fuel, instead of standard petrodiesel, the two main aspects of the supply chain are the depots, which need fuel, and the fuel suppliers (plants or fuel distributors). The distributors' pricing is based on transportation costs and direct fuel costs. The depots have a demand that must be fulfilled on a timely basis, perhaps monthly.

Two different approaches have been being utilized: a Heuristic approach and a Transportation model. The first consists of pragmatically applying a set of rules to consider biodiesel suppliers within a given radius of the depots and calculate the cost of providing the fuel to each. The only constraint here is plant capacity. Once a pool of potential suppliers is clustered around a depot, suppliers with the lowest cost available to each depot are selected. This selection process continues until the depot is completely satisfied. This method gives a good solution but it does not guarantee optimality.

The second approach (Transportation) generally distributes items from sources to destinations and the allocation of resources takes place by minimizing the total distribution cost. To set up the problem, each source must have a certain amount of items to supply, and the destination must have a certain demand. Here, sources are biodiesel plants/distributors, and destinations are depots. Routes between sources and destinations have a unit transportation cost. This methodology can guarantee the optimal solution. The Transportation model is well known in the operations research field and is based on linear programming. This model can be solved by using a simplex method with optimization software such as LINDO or CPLEX. Its mathematics seeks to minimize the total transportation cost given by Equation (2-1):

$$z = \min \sum_{i=1}^{m} \sum_{j=1}^{n} C_{ij} X_{ij} \qquad (2\text{-}1)$$

where $C_{ij} = cL_{ij} + F_i$.

The minimization is subject to three types of constraints:

(i) Supply given by $\sum_{j=1}^{n} X_{ij} = s_i \quad \text{for all } i = 1,2,...,m$

(This constraint states that the total amount of fuel from distributor $i$ to all depots 1 to $n$ must be equal to the amount of fuel sent from distributor $i$.);

(ii) Demand given by $\sum_{i=1}^{m} X_{ij} = d_j \quad \text{for all } j = 1,2,...,n$

(This constraint states that the total amount of fuel sent to depot $j$ from distributors 1 to $m$ must equal the total demand of depot $j$.);

(iii) Other constraints such as budgets, supply fluctuations, and non-negativity, $X_{ij} \geq 0$, for all $i,j$:

(a) Depot constraints: in some depots fuel is to be supplied direct-to-locomotive (DTL), low volume direct to locomotive (LVDTL), high volume direct to locomotive (HVDTL), and fixed tank capacity.

(b) Supplier constraints: some supplier services are limited to a particular distance.

(c) Non-negativity constraints, $X_{ij} \geq 0$, and bound constraints, $X_{ij} \geq b$, for all $i,j$. In case of non-negative constraints the supply x from the distributor j to depot n should be greater than zero, and in the case of bound constraints the supply should be greater than or equal to b.

The modeling parameters and variables are defined as:

$s_i$: This represents a single supplier $i$ ($i$=1,2,…,$n$). The suppliers in this problem are the biodiesel distributors, and the number of suppliers is equal to the total number of biodiesel distributors.

$d_j$: This represents a single destination $j$. The destinations in this problem are the refueling depots, and the number of destinations is equal to the total number of depots.

$z$: This is the total cost of supplying all depots in the system with fuel.

$X_{ij}$: This is the unit number of gallons of fuel transported from supplier (distributor) $i$ to destination (depot) $j$.

$c_{ij}$: This is the unit cost of transportation from distributor $i$ to depot $j$. It consists of the cost of the fuel and the cost of transporting the fuel.

$F_i$: This is the cost of a gallon of fuel from supplier (distributor) i.

$L_{ij}$: This is the distance between distributor i and depot j.

$c$: A cost for transporting a unit of fuel one mile.

To improve upon the utility and accuracy of the model, depot yearly demand data were obtained from a major railway and distributor pricing was surveyed for states east of the Mississippi River. The states corresponded to the area of service of that railway. Information required from the suppliers included:

- the supplier's location;
- the price per gallon;
- the additional costs for transportation, if any; and
- the blend(s) of biodiesel available.

As an example of this technique, Table 2-1 presents refueling depots in Illinois, Indiana, and Ohio. To serve this demand, approximately 30 suppliers from Illinois, 10 from Indiana, and 20 from Ohio were contacted but not all were able or willing to supply information. The ones providing data are listed in Table 2-2. Table 2-3 is an expanded version of fuel costs including data from these three states and others and is typical for supplier-provided information.

Table 2-1- Railway Refueling Depots in Illinois, Indiana, and Ohio

**Norfolk Southern Depots**

| ILLINOIS | INDIANA | OHIO |
|---|---|---|
| Chicago | Ft Wayne | ASHTABULA |
| decature | Huntingburg AAW | BELLEVUE |
| Kankakee | Lafayette | CANTON (DTL out of Cleveland) |
| | Princeton | CINCINNATI (LUDLOW, KY) |
| | Wheatfield | CLEVELAND-Canton-Lordstown |
| | | COLUMBUS (Buckeye) Consignment |
| | | FOSTORIA |
| | | FOSTORIA MIXING CENTER |
| | | LIMA |
| | | MANSFIELD |
| | | MIDDLETOWN |
| | | MINGO JCT |
| | | PORTSMOUTH |
| | | POWHATAN |
| | | SANDUSKY |
| | | TOLEDO |
| | | WALBRIDGE (Toledo area) |

Table 2-2 - Partial List of Distributors Contacted in Illinois, Indiana, and Ohio

**List of suppliers**

| ILLINOIS |
|---|
| Yoder BP Oil Company |
| Bell Fuels |
| crystal Flash Energy Fuel Services |
| AL Warren Oil Company |
| Osco Oil |
| feece Oil Company |
| Palatine Oil Co. Inc |
| Meier Oil Service |
| Andrews Oil company |
| Avalon Petroleum Company |
| Bio Energy Supply, LLC |
| G Cooper Oil Company *Inc* |
| HWRT Oil Company, LLC |
| kelly williamson Company |
| Kens's Oil Services |
| Lanman Oil Co |
| Molo Quint LLC Petroleum |
| Morgan Distributing Inc |
| Petroliance |
| Shipman Elevator Company |

| INDIANA |
|---|
| Ackerman Oil Co, Inc |
| Crystal Flash Energy Fuel Services |
| Dawson Oil Co., Inc. |
| Gulf Hydrocarbon Wolf Lake |
| Heritage Petrolium |
| Jackson Jennings Co-op |
| McClure Oil Corporation |
| Newton Oil Company |
| Paulson Oil Company |
| Petroleum Traders Corporation |

| OHIO |
|---|
| Beck Suppliers Inc. |
| Belmont-Carson Petroleum Co. |
| Britsch Inc. |
| Burke Petroleum, Inc. |
| CW Service |
| Campbell Oil Company |
| Duncan Oil Company |
| Glockner Oil Company |
| JatroDiesel |
| Hartley Oil Co. |
| Kevin Mote Petroleum Distributors |
| Lucky farmers, Inc |
| Lykins Oil Co. |
| McWherter Petroleum, LTD. |
| Santmyer Oil Co., Inc. |
| Northwest Oil |
| Western Reserve Farm Co. |

Table 2-3 - Suppliers Providing Specific Blend Pricing Information

# SUPPLIER PRICING DATA

| Company Name | State | Available Blends | Price Per Gallon | Capacity | Transportation Costs | Remarks |
|---|---|---|---|---|---|---|
| Yoder BP Oil Company | IL | B11 | $2.50 | Meets the demand | Included in Price | |
| Osco Oil | IL | B11,B20 | $1.37 | Meets the demand | Included in Price | Price of B20 Not Available |
| Feece Oil | IL | All Blends | Bio $3.24, St DL $2.10 | Meets the demand | 6-7 Cents per gallon | Prices explanined below |
| Merie Oil Co. | IL | B5,B10,B20,B100 | $1.59, $1.56, $1.65 | Meets the demand | NA | Price of B100 Not Available |
| Bio Energy Supplies | IL | B11 | $1.93, $1.88, $1.82 | Meets the demand | 3-5 Cents per gallon | price for Chicago, Decature, Kankakee |
| Heritage Petroleum | IN | All Blends | Bio $1.35, St DL $1.80 | Meets the demand | NA | Does not do DTL |
| Beck Suppliers Inc. | OH | All Blends | Bio $2.84, $1.84 | Meets the demand | Included in Price | Supplies only to Sandusky |
| CW Services | OH | All Blends | Bio $2.09, $1.89 | Meets the demand | | |
| Lucky Farmers Inc. | OH | All Blends | $2.46,$2.51,$2.61,$2.91,$3.75 | Meets the demand | Included in Price | supplies only to Walbridge |
| McWherter Petroleum, LTD. | OH | All Blends | Bio $3.00, St DL $1.75 | Meets the demand | 4-5Cents per gallon | |
| kevin mote petroirum distributors inc. | OH | All Blends | $1.85,$1.90,$195,$2.25,$2.50 | 3800 gallons | Included in Price | LVDTL & Cincinnati and Middletown |
| Enterprise Oil Co. | GA | All Blends | St D $1.57, St.Bio $1.57 | Meets the demand | | Atlanta, Eastpoint |
| S. A. White Oil Co. | GA | All Blends | St. D $1.99, St.Bio $2.50 | Meets the demand | | Atlanta, Columbus, |
| American homegrown fuel co. | FL | All Blends | St.D $2.08, St. Bio $1.99 | Meets the demand | | |
| Clean Fuels | FL | All Blends | St. Bio $1.94 | Meets the demand | | goes in production in July |
| Salathe oil | LA | All Blends | St.D $2.32, St.Bio $3.99 | Meets the demand | | |
| Talen's | LA | All Blends | St. D $1.90 | Meets the demand | | |
| Sweet water valley oil co. | TN | All Blends | St.D $2.22, St. Bio $2.22 | Meets the demand | Included in Price | |
| Tennesse bio enery | TN | B99 | $2.04 | | | |
| A & M Oil company | KY | All Blends | St. D $2.58, St. bio $2.35 | Meets the demand | danville charged | |
| Kentucky Petroleum | KY | All Blends | St. D $1.94, St. Bio $2.13 | Meets the demand | 43c | lousville |
| Clinard oil co | NC | All Blends | st.d. $1.87, St. Bio. $1.80 | Meets the demand | | |
| Monson Oil Company | NC | All Blends | St.D 2.65, St. Bio $2.69 | Meets the demand | | |
| Oakboro Oil Co. | NC | All Blends | St.D $1.80, St. Bio $1.91 | Meets the demand | | |
| Trinagle Bio Fuel | NC & SC | All Blends | St.D $1.98, St. Bio $2.05 | Meets the demand | | |
| Guttmen Oil | WV | All Blends | St.D $2.00, St.Bio $3.18 | Meets the demand | | |
| Center Oil of Virginia | VA | All Blends | St.D $2.18, St. Bio $2.00 | | 6c | brookneal, lynchburg |
| Foster fuels | VA | All Blends | St.D $2.04, St.Bio $2.04 | Meets the demand | | brookneal, lynchburg, norfolk |
| TCH | VA | All Blends | St.D $2.05, St.Bio $3.00 | | | All |
| Phillips Energy | VA | All Blends | St.D $2.38 | Meets the demand | | bristol, norfolk, richmond |

This table has the available biodiesel blends; some suppliers provide all blends while others only a few or just one. Note that pricing is extremely variable and can change several times a day, depending on the price of crude oil. Many suppliers price their blends by proportion so two prices are given: pure biodiesel (St. B. or Bio.) and #2 petrodiesel (St. DL. or St. D.). For example, B5 contains 5% biodiesel and 95% of petrodiesel, hence the pricing for this blend will be 0.05 fraction of 100% biodiesel and 0.95 fraction of #2 petrodiesel. An additional transportation cost is also stated depending on the supplier; some include the transportation within the biodiesel's price. For example Yoder BP Oil Company offers B11 at $2.50 which also includes transport to the depots irrespective of distance. Others charge separate fees depending on the distance from their facility to the depots; in the case of Feece Oil an additional 6 to 7 cents are added to the price per gallon. There are additional supplier constraints:

- Some suppliers limit their service to certain geographical locations. (In the case of Beck Suppliers Inc. and Lucky Farmers Inc., their services are limited to Sandusky and Walbridge.)
- Some have capacity-bound constraints. (Bio Energy Supplies has a minimum order of 75,000 gallons.)
- Some suppliers have limits on their service. (Heritage Petroleum does not offer DTL.)

All these constraints are taken into consideration in the Transportation model to arrive at Table 2-4 which has specific pricing for various blends shipped to sample depots in Illinois.

Table 2-4 - Supplier Pricing Direct to a Specific Illinois Depot

| B5 Suppliers | price per gallon to depot: CHICAGO | DECATUR | KANKAKEE |
|---|---|---|---|
| Feece Oil | $ 2.21 | $ 2.23 | $ 2.19 |
| Merie Oil Co. | $ 1.62 | $ 1.64 | $ 1.66 |

| B10 Suppliers | price per gallon to depot: CHICAGO | DECATUR | KANKAKEE |
|---|---|---|---|
| Yoder BP Oil Company | $ 2.50 | $ 2.50 | $ 2.50 |
| Osco Oil | $ 1.37 | $ 1.37 | $ 1.37 |
| Feece Oil | $ 2.30 | $ 2.31 | $ 2.32 |
| Merie Oil Co. | $ 1.60 | $ 1.60 | $ 1.60 |
| Bio Energy Supplies | $ 1.93 | $ 1.88 | $ 1.82 |

| B20 Suppliers | price per gallon to depot: CHICAGO | DECATUR | KANKAKEE |
|---|---|---|---|
| Feece Oil | $ 2.37 | $ 2.38 | $ 2.39 |
| Merie Oil Co. | $ 1.70 | $ 1.72 | $ 1.71 |

| B50 Suppliers | price per gallon to depot: CHICAGO | DECATUR | KANKAKEE |
|---|---|---|---|
| Feece Oil | $ 2.69 | $ 2.71 | $ 2.73 |

| B100 Suppliers | price per gallon to depot: CHICAGO | DECATUR | KANKAKEE |
|---|---|---|---|
| Feece Oil | $ 3.28 | $ 3.29 | $ 3.30 |

Results and Discussion:

There have been recent developments affecting the biodiesel fuel industry. One important change is in the ASTM D 975 fuel standard where petrodiesel may now have up to 5% biodiesel; so B5 is accepted per the Federal Trade Commission. To make biodiesel more readily available and in greater quantities, B5 was test-shipped in the Colonial Pipeline in 2006. Another (October 2008) shipment of 20,000 barrels of B5 within 500 miles of the Plantation Pipeline also proved successful; however, there remains a restriction that biodiesel cannot ship in any pipeline that also carries aviation fuel [9]. Routine and regular shipment of biodiesel fuel is expected any time.

Biodiesel's solvent-like properties may be a concern in older engines and fuel management systems. In pre-1994 models, rubber parts were used frequently, and these may need replacement when utilizing higher blends such as B100. It may not be an issue for B20 or less. Newer vehicles and equipment, designed to meet the current low-sulfur fuel requirement, have more durable rubber and elastomeric components. There is a large body of work with compatibility of materials [10, 11], including metals, with biodiesel. Usually the material was exposed to B100. Most data are quite favorable with little effects especially for B20 or less. Nevertheless for locomotive operation it is prudent to take a conservative approach to reduce the chances of

material failure or system contamination. Thus materials can be classified into three categories: "non-compatible" which cannot be used under any circumstance; "okay" but must be replaced as soon as convenient; and "compatible." A current, partial list includes:

- non-compatible = buna-N, butadiene, EPDM, natural rubber, nitrile rubber, neoprene, chloroprene, Nordel, polypropylene, styrene-butadiene, lead, tin, brass, copper, and zinc;

- okay = butyl rubber, fluorosilicone, and polyurethane; and

- compatible = nylon, polyethylene, Teflon, Viton GBL-S, Viton GF-S, steel, and aluminum.

Of course, diesel fuel storage and compression-ignition engine operation require particular attention in colder weather and the Department of Energy (DOE) publishes information for colder temperature applications [12]: "Just like common #2 diesel, certain high-freezing-point compounds in biodiesel (B100) will crystallize in very cold temperatures. Pure biodiesel crystallizes in warmer temperatures than #2 diesel fuel." B20 blends are used with similar fuel management techniques as #2 diesel and B5 and below have a small impact on cold-flow properties [12].

Fuel is stored at railroad depots in tanks and tank turnover time is measured in days. B50 and B100 have special storage requirements. The fuel would have to be heated during cold weather for flow while in hot climates the biofuel may need additives to prevent spoilage. Over the years, railroads have been eliminating below-ground storage tanks. But above-ground tanks are difficult to heat or cool. This fact along with the trend towards minimizing maintenance costs at depots dictates that only B5, B10, and B20 can be stored onsite. B50 and B100 ought to be supplied from tanker truck as direct-to-locomotive.

Depot fuel holding tanks are cleaned and inspected but not per a routine schedule. Cleaning of such tanks can be an extensive and costly effort. Fuel pumps and piping are largely steel and would not require replacement. Although gasket and fuel interactions appear to be minimal, the compatibility of any paper-based gaskets with biodiesel is unknown but it would be relatively easy to replace hoses and gaskets in the pumps and fuel line connections. Also, the amount of "tempo cold flow" chemical additive may need to be higher due to the greater viscosity of biodiesel. Overall costs would be in thousands of dollars to prepare a typical depot for biodiesel; the costs would be substantially greater if equipment must be replaced or modified.

All depot fuel handling equipment, including storage tanks, must be thoroughly cleaned. Recommended tank cleaning techniques include rinsing, triple rinsing, manhole entry, solvent flushing, or combinations of these; also a desiccant filter to keep out moisture, a 5-micron fuel filter, and periodic removal of water and bottoms sediment are recommended [11]. Likewise, suppliers must be made aware of the special handling requirements. Any truck, trailer, or rail car must also be cleaned and its last load carried must have been diesel or biodiesel and not gasoline which has a solvent effect and can put particles and contaminants into railway depots and locomotives.

The Camp Pendleton U.S. Marine Corps Base, Oceanside, California, incorporated a 20% biodiesel blend, derived from virgin soybean oil, into all its diesel-powered equipment, including a locomotive [13]. This move was in response to the April 2000 Executive Order 13149, "Greening Government Through Federal Fleet and Transportation Efficiency" and to reduce petro-based fuel use. No major maintenance issues were encountered as long as the fuel was used within the manufacturer's recommended six-month period but it was strongly recommended to clean fueling tanks prior to introducing B20. B20 was also selected by a Brazilian mining company to fuel its 216 locomotives that operate over 6000 miles of track [14].

Parvate-Patil, Vasquez, and Payne [15] tested the thermal and emissions potential of a single-cylinder, medium-speed diesel engine to obtain initial data to better understand locomotive engine performance. Four biodiesel fuels were tested: 20% and 100% canola and frying oils. Generally, the bio-based fuels require more injection pressure due to their higher densities. The higher injection pressure contributes to greater NOx release. For the 20% canola oil and frying oil blends, the NOx emission is 7% and 9%, respectively, greater than standard #2 diesel fuel. The B100 canola oil and frying oil fuels exhibit 58% and 73% more NOx, respectively. Smoke and CO emissions with the biodiesels are actually less than with petrodiesel and otherwise the biofuels have compatible engine performance. Similar trends are seen in actual locomotive studies.

With respect to manufacturer warranties, most accept blends of 5% and some up to B20. Some biodiesel end users have tended toward an adoption strategy which entails conversion of beyond-warranty vehicles and equipment, at least initially, in order to gain confidence and mitigate potential warranty coverage concerns. One application would be powering switching locomotives that tend to be older and thus engine warranty issues may not apply.

Biodiesel Fuel Testing

To check the feasibility of using a diesel engine at Northern Illinois University to generate emissions data that could be used to predict locomotive engine performance or to evaluate different biodiesel fuel feedstocks, tests were run. The engine is an 18-hP, inline, three-cylinder unit. It is instrumented for fuel consumption, power generation, thermal performance, and emissions production. Data are generated at various engine speeds at full loading. Data are recorded through DYNOmax® software which automatically compiles sensor readings into numerical tables to a personal computer.

B99 biodiesel sourced from virgin soybean oil (Lake Oil, Kirkland, Illinois), consistent with the soybean-derived fuel used in other locomotive studies, was run as the pure biodiesel case while blends were prepared using #2 petrodiesel through splash blending and mixing. Exhaust emissions measured included unburned oxygen, CO, $CO_2$, $NO_2$, and HCs. Engine speed was set to 2500, 3000, and 3500 rpm, all at full load. The results are shown in Table 2.5. The $NO_2$ content shows the same trending to significant increases, as the case with locomotive data, when biodiesel blends are used. However compared to locomotive studies the hydrocarbons are generally greater with the 18-hP test engine, although the 3500 rpm runs do show significant reduction. The CO data are inconsistent primarily due to instrument inaccuracy. When all the rpm data points are averaged for each blend, the general trends includes a 50% increase in $NO_2$.

Table 2-5 - Percent Change in Measured Emissions using a Biodiesel Blend Compared to Petrodiesel for Northern Illinois University Test Engine

| **Fuel/Application** | **$NO_2$** | | | | **HC** | | | | **CO** | | |
|---|---|---|---|---|---|---|---|---|---|---|---|
| engine speed (rpm) | 2500 | 3000 | 3500 | | 2500 | 3000 | 3500 | | 2500 | 3000 | 3500 |
| B20/Hydro Loading | +20 | +35 | +3 | | -15 | -44 | -39 | | 0 | 0 | -100 |
| B50/Hydro Loading | +103 | +101 | +57 | | +67 | +16 | -28 | | +100 | +100 | -86 |
| B99/Hydro Loading | 0 | +15 | +78 | | +50 | -21 | -20 | | +100 | 0 | -100 |

Heuristic Sample Analysis for Cost of Refueling Depots

There are several parameters for the Heuristic approach. These are the location of the depots and the surrounding suppliers, the capacity of the suppliers, the demand of depots, and the distances between the given suppliers and depots. For a sample run, the depots are Decatur, IL, and Elkhart, IN, while distributors were located by information from the NBB. Distances were obtained with MapQuest®. The capacity of an individual distributor is estimated as 30,000 gallons/month. Demand is assumed for an individual depot of approximately 877,000 gallons.

Figure 2-4 is a pictorial representation of the method. There are two depots within a given number of plants/distributors, 50 in this example. This approach can be generalized for any number of depots and *i* distributors within radius *r*. The radius will vary with depot depending on the number and capacity of each distributor.

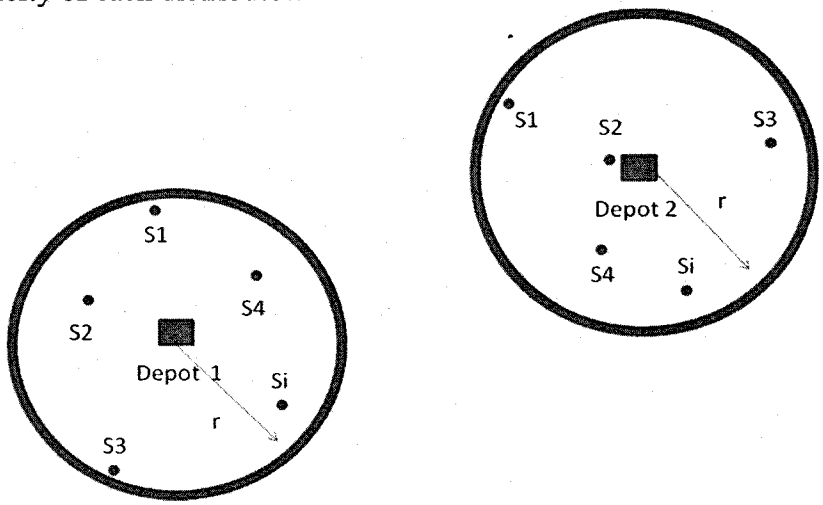


Figure 2-4 - Example of Spatial Relationship between Fuel Depots and Suppliers

Using Decatur and Elkhart depots along with the 50 closest distributors, capacities were assumed ranging from 25,000 and 35,000 gallons at $3.00 and $4.50 per gallon. Trucking volumes are taken as 7500 to 9900 gallons. Table 2-6 shows the distance, capacity, and cost of a single delivery from different distributors to Decatur. All plants were then sorted from least to greatest pricing, and demand is fulfilled from the lowest-cost providers until the full demand of 877,000 gallons is met. Table 2-7 summarizes the final results with the total cost calculated as $3,071,030. Using the same Heuristic approach for Elkhart, total cost is $2,955,120 and summarized in Table 2-8.

Table 2-6 - Heuristic Parameters for Decatur, IL, Depot

| PLANT | DISTANCE (1) | Price/Gallon (2) | THEORETICAL CAPACITY (3) | Truck Size (4) | COST OF SINGLE DELIVERY (5) =7.35*(1)+(2)*(4) | COST/GALLON (6)= (5)/(4) |
|---|---|---|---|---|---|---|
| Morgan Distributing, Inc. (Decatur) | 1 | $3.50 | 36000 | 7500 | $26,257.35 | $3.50 |
| Evergreen FS (Maroa) | 14 | $4.00 | 28000 | 7800 | $31,302.90 | $4.01 |
| Effingham Equity (Lovington) | 22 | $3.00 | 31000 | 8100 | $24,461.70 | $3.02 |
| Piatt County Service Company (Bement) | 26 | $4.50 | 27000 | 7700 | $34,841.10 | $4.52 |
| Corn Belt FS (Wapella) | 28 | $4.15 | 30000 | 9900 | $41,290.80 | $4.17 |
| E-K Petroleum (Sullivan) | 29 | $4.25 | 32000 | 9300 | $39,738.15 | $4.27 |
| Gesell Oil, Inc (Christiaon County FS) | 29 | $3.75 | 29000 | 8800 | $33,213.15 | $3.77 |
| Agland FS, Inc | 36 | $3.40 | 31000 | 8100 | $27,804.60 | $3.43 |
| Pangburn Oil Company (Tuscola) | 38 | $3.35 | 28000 | 7900 | $26,744.30 | $3.39 |
| Nelson Oil Company (Springfield) | 39 | $4.15 | 33000 | 9700 | $40,541.65 | $4.18 |
| Piatt County Service Company (Mansfield) | 43 | $4.05 | 34000 | 9200 | $37,576.05 | $4.08 |
| Evergreen FS (Bloomington) | 46 | $3.95 | 29000 | 8400 | $33,518.10 | $3.99 |
| Molo Quint LLC (Moline) | 46 | $3.20 | 34000 | 7600 | $24,658.10 | $3.24 |
| Illini FS (Tolono) | 48 | $3.35 | 26000 | 7500 | $25,477.80 | $3.40 |
| Home Oil Co., Inc (Raymond) | 50 | $4.15 | 29000 | 7800 | $32,737.50 | $4.20 |
| Lanman Oil Co (Mattoon) | 52 | $3.40 | 32000 | 8100 | $27,922.20 | $3.45 |
| Illini FS (Rantoul) | 61 | $4.00 | 36000 | 7700 | $31,248.35 | $4.06 |
| Heritage FS (Gibson City) | 64 | $3.15 | 28000 | 9900 | $31,655.40 | $3.20 |
| Wax Oil Company (Allerton) | 64 | $3.85 | 31000 | 9300 | $36,275.40 | $3.90 |

The cost of moving a truck per one mile is assumed to have a value of 7.35.

Table 2-7 - Heuristic Results for Decatur, IL, Depot

| PLANT | THEORETICAL CAPACITY (1) | COST/GALLON (2) | TOTALED CAPACITY MET (3)=SUM(1) | TOTAL COST (4)=(2)*(3) |
|---|---|---|---|---|
| Effingham Equity (Lovington) | 31000 | $3.02 | 31000 | $93,618.85 |
| Agland FS, Inc (Tremont) | 29000 | $3.05 | 60000 | $88,472.27 |
| Fulton FS (Lewistown) | 34000 | $3.09 | 94000 | $105,083.18 |
| Heritage FS (Gibson City) | 28000 | $3.20 | 122000 | $89,530.42 |
| Evergreen FS (Flanagan) | 32000 | $3.23 | 154000 | $103,292.00 |
| Molo Quint LLC (Moline) | 34000 | $3.24 | 188000 | $110,312.55 |
| Illini FS (Paris) | 36000 | $3.27 | 224000 | $117,605.45 |
| Pangburn Oil Company (Tuscola) | 28000 | $3.39 | 252000 | $94,789.92 |
| Illini FS (Tolono) | 26000 | $3.40 | 278000 | $88,323.04 |
| Lincoln Land FS, Inc. (Jacksonville) | 34000 | $3.42 | 312000 | $116,213.89 |
| Evergreen FS (Roanoke) | 28000 | $3.42 | 340000 | $95,858.00 |
| Meier Oil Service, Inc (Ashkum) | 36000 | $3.43 | 376000 | $123,436.95 |
| Agland FS, Inc | 31000 | $3.43 | 407000 | $106,412.67 |
| Lanman Oil Co (Mattoon) | 32000 | $3.45 | 439000 | $110,309.93 |
| Meier Oil Service, Inc (Pontiac) | 27000 | $3.47 | 466000 | $93,600.37 |
| Yoder BP Oil Company (Eureka) | 29000 | $3.47 | 495000 | $100,622.19 |
| Tri-County Petroleum Inc. (Pierron) | 32000 | $3.49 | 527000 | $111,777.22 |
| Morgan Distributing, Inc. (Decatur) | 36000 | $3.50 | 563000 | $126,035.28 |
| Southern Central FS Inc. (Vandalia) | 30000 | $3.56 | 593000 | $106,796.67 |
| Heritage FS (Onarga) | 28000 | $3.59 | 621000 | $100,401.00 |
| Effingham Equity (Effingham) | 27000 | $3.76 | 648000 | $101,388.38 |
| Gesell Oil, Inc (Christiaon County FS) | 29000 | $3.77 | 677000 | $109,452.43 |
| Effingham Clay Service Co. (Sandoval) | 31000 | $3.79 | 708000 | $117,464.58 |
| Sunrise Ag Service Company (Virginia) | 34000 | $3.82 | 742000 | $129,899.04 |
| Agland FS | 29000 | $3.84 | 771000 | $111,381.48 |
| Wax Oil Company (Allerton) | 31000 | $3.90 | 802000 | $120,918.00 |
| Wabash Valley Service Co. (Newton) | 29000 | $3.94 | 831000 | $114,146.10 |
| Evergreen FS (Bloomington) | 29000 | $3.99 | 860000 | $115,717.25 |
| Manito Oil and Propane Company (Manito) | 32000 | $4.01 | 892000 | $68,171.10 |
| | | | | **$3,071,030.21** |

Table 2-8 - Heuristic Results for Elkhart, IN, Depot

| PLANT | THEORETICAL CAPACITY (1) | COST/GALLON (2) | TOTALED CAPACITY MET (3)=SUM(1) | TOTAL COST (4)=(2)*(3) |
|---|---|---|---|---|
| Dubois County FBCA | 29000 | $3.07 | 29000 | $89,103.45 |
| GSC City Ltd | 31000 | $3.08 | 60000 | $95,462.62 |
| Conserv FS (Caledonia) | 34000 | $3.15 | 94000 | $107,132.35 |
| Ag Plus, Inc | 32000 | $3.21 | 126000 | $102,745.48 |
| LaSalle County Farm Supply (Ottawa) | 33000 | $3.28 | 159000 | $108,331.55 |
| Heritage FS (Gibson City) | 28000 | $3.30 | 187000 | $92,316.00 |
| Evergreen FS (Flanagan) | 32000 | $3.32 | 219000 | $106,232.00 |
| Bocosky Oil Company | 36000 | $3.34 | 255000 | $120,324.53 |
| Meier Oil Service, Inc (Kempton) | 30000 | $3.37 | 285000 | $100,998.00 |
| Paulson Oil Company | 32000 | $3.41 | 317000 | $108,989.57 |
| Steffan Oil Company | 30000 | $3.43 | 347000 | $102,823.55 |
| Conserv FS (Tinley Park) | 28000 | $3.44 | 375000 | $96,238.28 |
| Bell Fuels | 34000 | $3.44 | 409000 | $116,878.61 |
| Triple J Mar Petroleum Inc. | 36000 | $3.46 | 445000 | $124,605.00 |
| Heritage FS (Peotone) | 33000 | $3.47 | 478000 | $114,357.11 |
| Meier Oil Service, Inc (Ashkum) | 36000 | $3.47 | 514000 | $124,882.70 |
| Avalon Petroleum Company | 31000 | $3.48 | 545000 | $107,960.38 |
| Newton Oil Company | 29000 | $3.50 | 574000 | $101,380.22 |
| Feece Oil Company (Batavia) | 32000 | $3.51 | 606000 | $112,387.39 |
| Conserv FS (Woodstock) | 31000 | $3.54 | 637000 | $109,638.50 |
| Meier Oil Service, Inc (Pontiac) | 27000 | $3.54 | 664000 | $95,543.95 |
| Dawson Enterprises | 34000 | $3.57 | 698000 | $121,444.67 |
| Blake Oil Company | 29000 | $3.58 | 727000 | $103,859.55 |
| DeGorate Petroleum Service Inc (New Lenox) | 36000 | $3.61 | 763000 | $129,920.00 |
| Meier Oil Service, Inc (Kankakee) | 34000 | $3.63 | 797000 | $123,396.97 |
| Conserv FS (DeKalb) | 30000 | $3.63 | 827000 | $108,955.36 |
| Heritage FS (Onarga) | 28000 | $3.66 | 855000 | $102,459.00 |
| King Oil Inc. | 29000 | $3.82 | 884000 | $26,753.89 |
| | | | | **$2,955,120.70** |

Transportation Model Analysis

The Heuristic model demonstrated that this costing approach is feasible and reasonable but does not provide the best solution. Thus the better methodology is the Transportation model which now takes the Heuristic input data but replaces the Heuristic approach completely. Graphically, Figure 2-5 locates suppliers and depots in the states of Illinois and Indiana; the pushpins represent suppliers and squares represent depots. But in order to minimize the number of geographical areas, states were grouped into regions. Two examples are the Eastern region of Figure 2-6 and the Southern U.S. region of Figure 2-7. Of course the groupings may be changed in size and scope at any time and only serve for convenience in analyzing the results. In the north, states include Illinois and Indiana while the southern region has Georgia, Florida, Louisiana, Tennessee, and Kentucky. In the east are North Carolina, South Carolina, West Virginia, and Virginia.

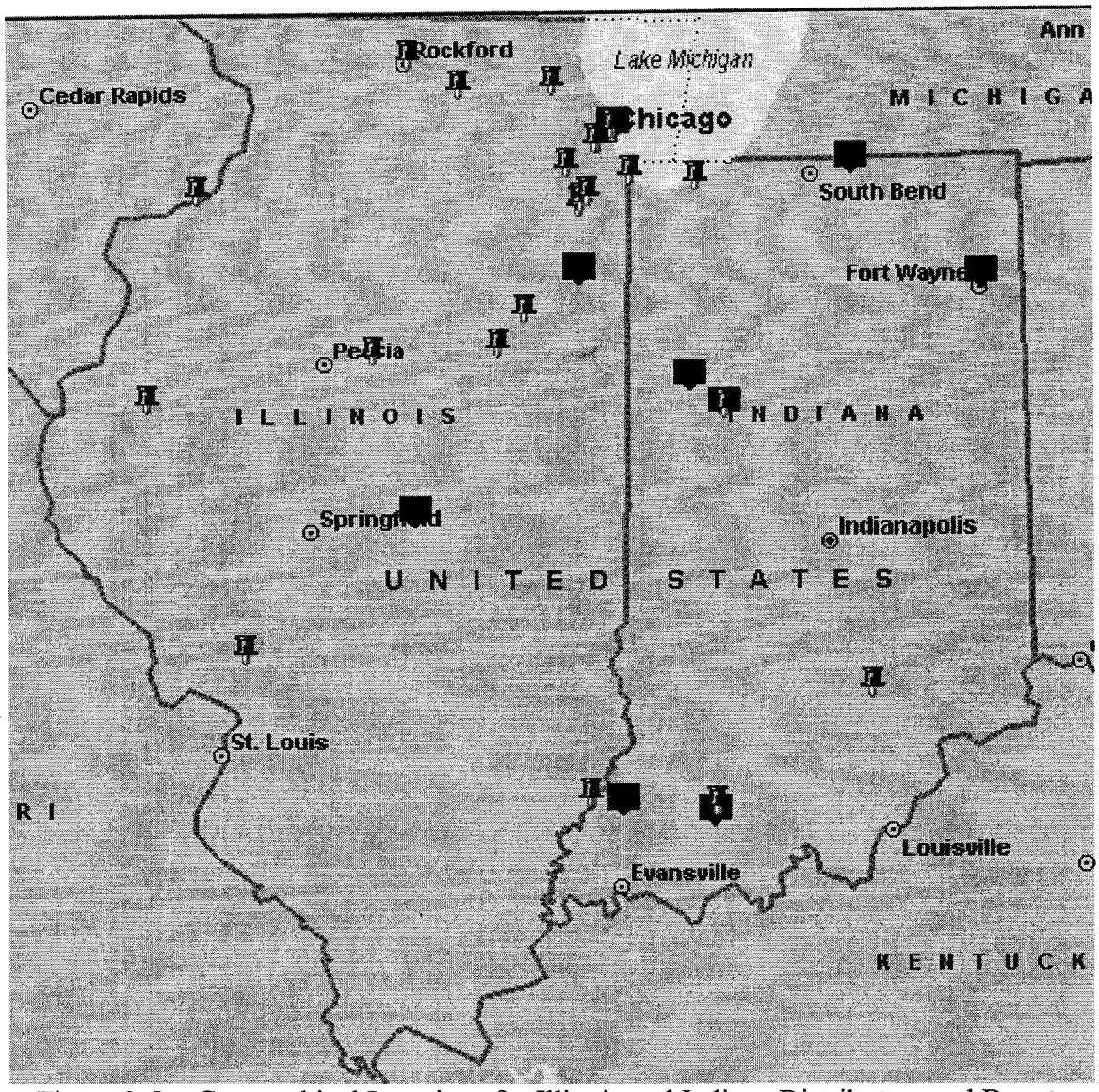

Figure 2-5 - Geographical Locations for Illinois and Indiana Distributors and Depots

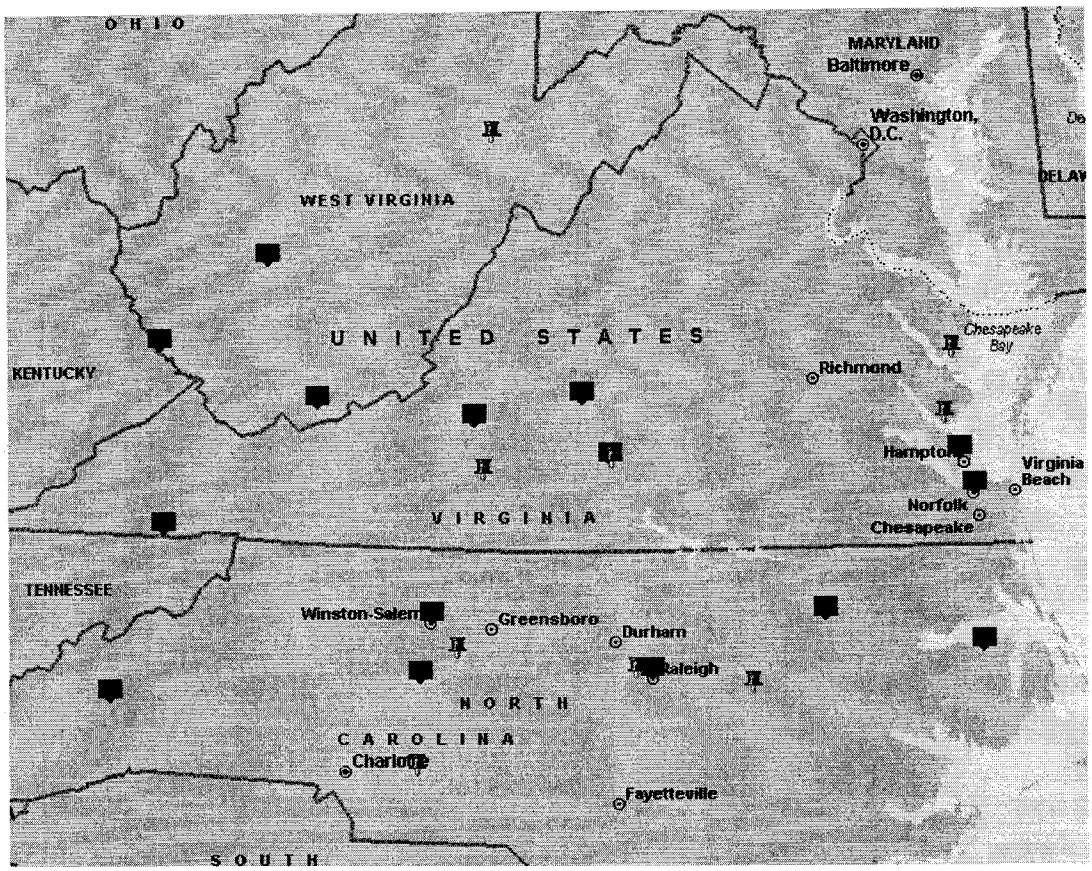

Figure 2-6 - Locations of Suppliers and Depots in Eastern United States

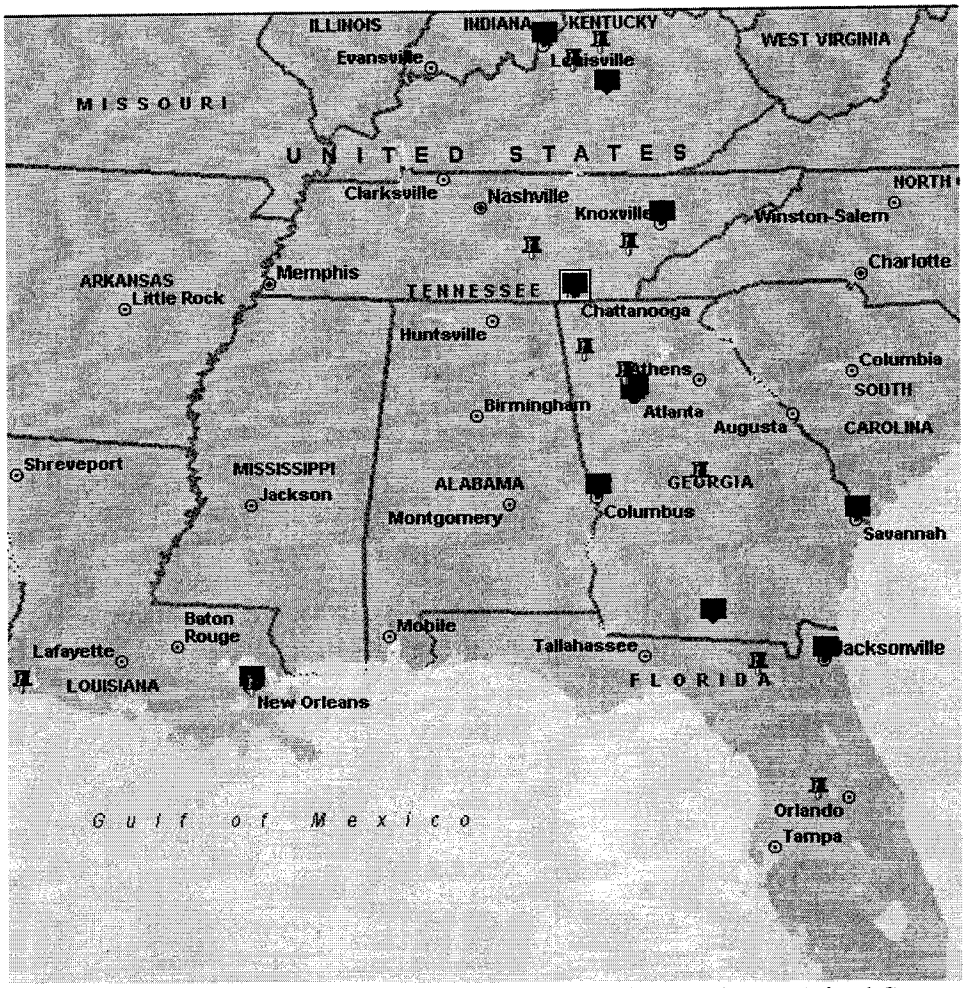

Figure 2-7 - Locations of Suppliers and Depots in Southern United States

Once the states were organized by region, the Transportation model was executed and the optimal costing solution to supply the railway's depots was found. The results are presented by B5, B10, B20, B50, and B100 blends. (Note that other blends such as B6, B11, and B99 exist to take advantage of federal and local tax treatments; thus for the purposes of this study there is no distinction between B5 and B6, B10 and B11, or B99 and B100.) For comparison purposes the biodiesel costing has been normalized by dividing by the cost of petrodiesel from the same geographical area. Thus a normalized value of unity indicates no difference between the two fuel types. But values above unity indicate that the biodiesel blend is more costly. Additionally to account for any engine inefficiency when utilizing blends, a fuel efficiency factor is programmed into the model as a constraint. This especially affects B50 and B100 as more gallons of these blends are necessary since locomotive mileage decreases measurably.

Analysis Conclusion

Overall, there is a significant amount of technology development in the area of biodiesel feedstock innovation. Some of the technological advances are nearing the commercialization stage, while others are more long range, strategic opportunities. These developments and research activities suggest that innovations will make the biodiesel proposition even more

attractive from an economic standpoint. The Transportation analysis indicates that use of biodiesel to power railroad locomotives is feasible.

Grades

Overall, the industry consensus is that B5 and B10 require no retrofit of equipment while B20 requires minor changes. B50 and B100 require expertise and major changes. It is anticipated that no operational problems, other than engine manufacturer warranty issues, would be encountered in locomotives powered by biodiesel fuels. This summary draws on key knowledge of biodiesel in the current state of commercial development. It must be noted that the biodiesel industry today is in relatively early stages of technological and market development, and it is anticipated that biodiesel will experience new technology development, such as feedstock innovation and specific blending breakthroughs.

Fuel Availability

The Transportation model has shown that adequate supply is available from existing suppliers throughout the United States. In some cases this supply is projected, as current demands do not justify greater fuel production rates. But fuel suppliers have indicated that production rates would be increased to meet the large demands of the railroad industry.

Emissions

Hydrocarbon, carbon monoxide, and particulate emissions are unchanged or less with biodiesel fuel usage. Nitrogen oxides are elevated but it is believed that engine operation and/or modifications can minimize these emissions. Table 2-9 summarizes emissions using biodiesel compared to the petrodiesel baselines from experimental studies with actual locomotives.

Table 2-9 - Percent Change in Measured Emissions using a Biodiesel Blend Compared to Petrodiesel

| Fuel/Application | $NO_x$ | HC | CO | PM |
|---|---|---|---|---|
| | | | | |
| B20/Line-Haul [2-6] | +6 | 0 | -17 | +9 |
| B20/Switch Duty [2-6] | +5 | -5 | -9 | -3 |
| B20/Static Loading [2-7] | +2 | 0 | ± (varied with load) | -50 |
| B50/Switch Duty [2-8] | +21 | -49 | 0 | -50 |
| B100 Switch Duty [2-8] | +48 | -48 | -19 | -73 |

In drawing conclusions regarding locomotives, the 18-hP NIU test engine has limited value in emissions data but does display some useful trending. It may become more helpful when running biodiesel fuels produced from different feedstocks.

Delivery Economics and Distribution Model

The Transportation model is a reasonable tool in demonstrating that enough biodiesel production is available, or would be available, to supply refueling depots. Supplier pricing has been obtained

for B5, B10, B20, B50, and B100. Tables 2-10 through 2-12 present the comparative results for three major geographical regions.

Table 2-10 - Minimized Relative Total Cost to Supply All Depots in Northern U.S. Based on Ratio of Blend Cost to Petrodiesel Cost

| BLEND | RELATIVE COST TO SUPPLY NORTHERN DEPOTS |
|---|---|
| B5 | 1.05 |
| B10 | 1.01 |
| B20 | 1.12 |
| B50 | 1.07 |
| B100 | 1.08 |

Table 2-11 - Minimized Relative Total Cost to Supply All Depots in Southern U.S. Based on Ratio of Blend Cost to Petrodiesel Cost

| BLEND | RELATIVE COST TO SUPPLY SOUTHERN DEPOTS |
|---|---|
| B5 | 1.03 |
| B10 | 1.03 |
| B20 | 1.04 |
| B50 | 1.07 |
| B100 | 1.09 |

Table 2-12 - Minimized Relative Total Cost to Supply All Depots in Eastern U.S. Based on Ratio of Blend Cost to Petrodiesel Cost

| BLEND | RELATIVE COST TO SUPPLY EASTERN DEPOTS |
|---|---|
| B5 | 1.04 |
| B10 | 1.05 |
| B20 | 1.08 |
| B50 | 1.16 |
| B100 | 1.26 |

It is observed for the northern U.S. that supplying B10 fuel is significantly less expensive than the other blends. For the South and East, B5 and B10 are priced the same and significantly less compared to other blends. In the southern U.S. biodiesel has the lowest cost and represents a minimal premium to petrodiesel. At the time of this report, petrodiesel prices have decreased from their historical highs, and thus all biodiesel blends are priced more, up to 26%. Nevertheless the results demonstrate that blends up to B20 do not have a large price differential compared to petrodiesel. Thus this range of blends will have a significant economic advantage if crude oil prices rebound towards their historical peaks. B50 and B100 may also become viable in a longer time frame. Note that the analysis represents the optimal selection of supplier(s) for each depot. Often this meant that several suppliers served a single depot but, at times, only one was needed to minimize refueling cost.

Engine Thermal Management, Power Production, and Component Wear

B20, without any engine modifications, may exhibit a 1%-2% reduction in energy output and fuel economy [16]; B100 would exhibit even greater inefficiency possibly affecting fuel depot spacing. But it ought to be remembered that even #2 diesel fuel, due to blending process variability, may vary up to 15% [17]. Table 2-13 presents an adjustment factor that was used within the Transportation model to account for the reduced fuel efficiency. The factor calls for additional gallons of demand at each depot when using biodiesel. The factor is the ratio of required gallons of petrodiesel to biodiesel for each biofuel blend. As anticipated, as biodiesel content increases more fuel volume is needed to compensate for the engine power inefficiency.

Table 2-13 - Fuel Efficiency Adjustment Factor

| BLEND | FUEL EFFICIENCY FACTOR |
|---|---|
| B5 | 1.00 |
| B10 | 0.99 |
| B20 | 0.98 |
| B50 | 0.96 |
| B100 | 0.92 |

A relatively new issue is the dilution of engine oil (API CJ-4) with B20 or higher bio-blended fuel which are less volatile, denser, and more viscous than petrodiesel. Thus fuel accumulates at a greater rate and concentration. Up to 15%-20% dilution has been seen in vehicle studies and inspection of engines has noted some oxidation, corrosion, and piston deposits [18]. Other problems from oil dilution are acidity, from organic acids, and potential extra wear of engine parts. Research is in progress world-wide on this issue. No data for locomotive engines are available but it is prudent to shorten the time between oil changes when using any biodiesel blend.

**Task 3 - Utilization of fuel cells for locomotive power systems**

This project is concerned with determining the feasibility of using fuel cell in a locomotive system. The locomotive does not suffer from some of the problems that face the use of fuel cells in other applications. As locomotives are relatively large they are not as constrained by size when compared to other transportation applications. Also they do not need accelerate quickly.

Locomotives can be used in different types of applications. These include switcher, pusher, and long haul. Depending on the application the fuel cell may not be able to accommodate the dynamic power requirements of the load. Therefore auxiliary storage units (ASU) may be needed to supplement the power need.

When investigating the use of a fuel cell in this new application, several fundamental items must be considered. Unexpected ergonomic issues may develop. Safety issues also need to be explored in this application. As the fuel used in the fuel cell may be different from the standard diesel, it is important to investigate refueling issues and develop a map of refueling stations.

Feasibility analysis for solid oxide fuel cells as a locomotive power source

For purposes of this analysis the assumption will be made that the Department of Energy (DOE) /Solid State Energy Conversion Alliance (SECA) goals for solid oxide fuel cell (SOFC) cost, performance, size, etc. are all met. On board gasification of biodiesel will be used for the fuel. Figure 3-1a shows SOFC power system that includes on-board gasification of biodiesel and necessary subsystems such as thermal and water management. Major components include SOFC, gasifier, gas cleaning, heat exchangers for heat recovery/preheating and cooling. This cooling system has to remove heat form fuel cell stack using bi-polar plates and remove heat from electric motors and inverters. A part of the excess fuel from fuel cell stack can be burned in the combustor to supply necessary heat to steam reformers, steam generator and air-preheater. Table 3-1 shows a summary of DOE-SOFC goals for coal-based power system SOFC for distributed generation (DG). This includes operating cell conditions, cell size, and cost. While most of these are directly applicable to locomotive use some are not. There is no practical way to store $CO_2$ for transportation applications and if biodiesel is used as a fuel $SO_2$ removal is probably unnecessary.

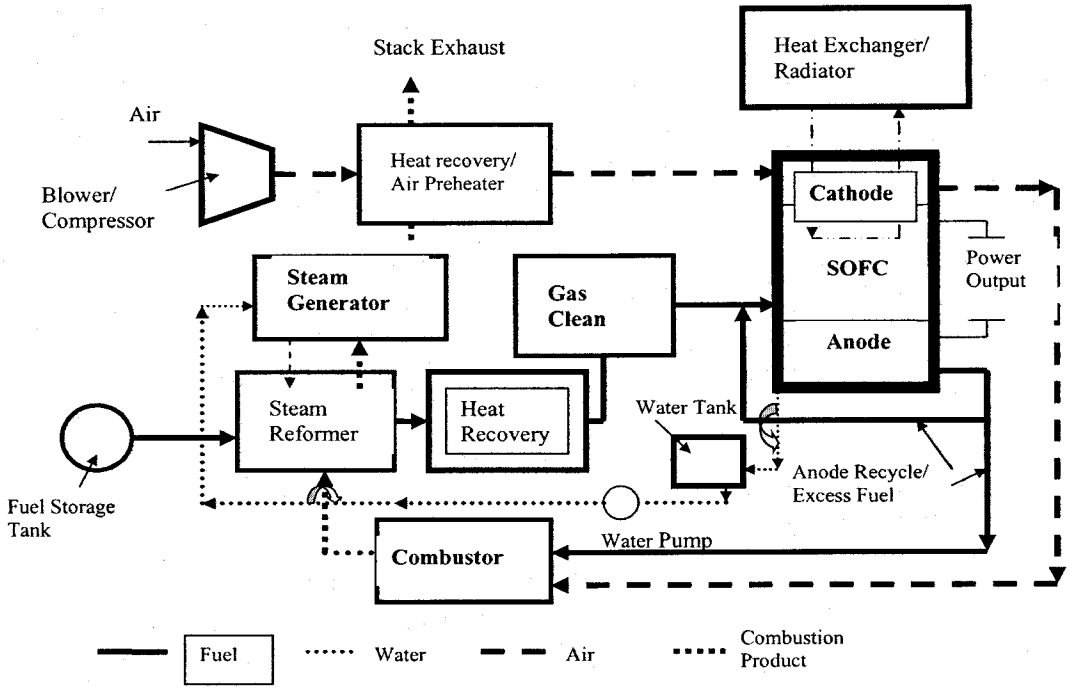


Figure 3-1a - Integrated gasifier fuel cell (IGFC) power system with fuel gasification, heat and water management subsystems for locomotive.

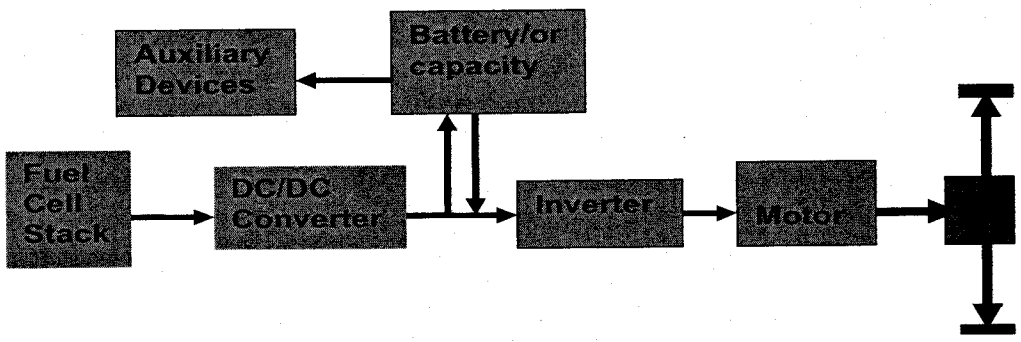


Figure 3-1b- Fuel cell power train

In a fuel cell power locomotive, the energy from the fuel cell is transmitted to the wheels through a electrical power train system show in Figure 1b. In this system, the fuel cell supplies the power to the motors and keeps the battery fully charged which may provide extra power as needed as well supply power needed for all auxiliary components such compressor, cooling pumps and fans.

The DC/DC converter increases the fuel cell output voltage and maintains at operating level of 650V. The inverter is used to convert DC to AC for power input to AC electric motors. It is possible use either a single electric motor to drive two wheels using drive shaft, gears and an axle. An alternative, power could be supplied to two motors connected to each wheel.

Table 3-1- DOE-SECA goal for coal-based SOFC power system for distributed based on IGFC

| | |
|---|---|
| Demonstration of 1 MW SOFC Module | By year 2012 |
| Demonstration of 5 MW SOFC Module | By year 2014 |
| Stack Cost | Less than $100/kW |
| Capital cost | Less than $400/kW |
| Operating cell current density | 400-500 $mA/cm^2$ |
| Operating cell voltage | 0.7-0.85 V |
| Power density | 300-400 $mW/cm^2$ |
| Efficiency | 45-50% (based on HHV) |
| $CO_2$ capture | 90% Capture by 2012 |
| $SO_2$ Capture | 99% capture by 2010 |

System power and duty cycle requirements

Current railroad road locomotives use turbo diesel engines with peak power of over 5000 hp (3.7 MW). In the case of road locomotives, peak power can be required for many consecutive hours. Also, while the locomotive itself is powered by electric traction motors and thus could be capable of some regenerative braking, the freight cars have no such capability. Without major redesign of the existing freight car stock it is not possible to recover a significant amount of the total potential of regenerative braking. Note that is most likely not the case for switcher locomotives. For these reasons it is not feasible to use short term energy storage to make up for deficiencies in peak power. It will be necessary for the SOFC system to provide approximately 4 MW of maximum power.

Duty cycle, defined here as the variation of power requirements over a trip for a road locomotive, varies widely. In cases where the locomotive is required to pull heavy loads up a slight grade for many miles near maximum power may be required for the entire trip. On the other hand on the same reverse trip power requirements will be significantly lower than the maximum power. Because SOFC's will only operate with high efficiency when producing a relatively large fraction of maximum power the system will need to be designed with multiple fuel cell stacks such that some can be idled while others are near maximum loading when demand is well below the overall system maximum. Figure 3-2 shows a 4MW SOFC power system with array of 4-1MW stacks that can meet the power needs of the locomotive during part-load as well as peak load operation.

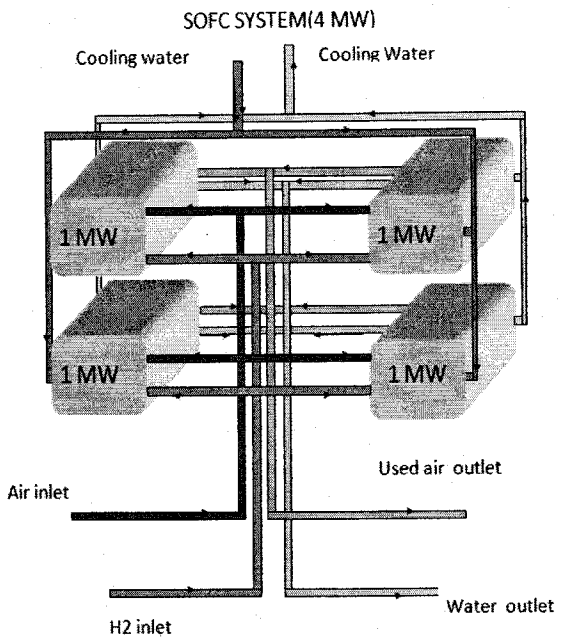


Figure 3-2 - 4MW SOFC system comprised of 4-1MW stacks.

Gasification requirements

Steam gasification has been selected for an input into the fuel cell simulation primarily because it is expected that sufficient waste heat will be available to produce high temperature steam and because it will minimize energy lost to the gasification process. It will be assumed that the gasification reaction will proceed to completion. Starting from the combustion of soy biodiesel, soy methyl ester,

$$C_{10}H_{19}0+14.25O_2 \rightarrow 9.5H_2O+10CO_2 \qquad \Delta G^o = -5.76\frac{MJ}{mol} - T\cdot 6.75\frac{kJ}{mol\cdot K} \qquad (1)$$

combining with steam and $CO_2$ reduction, and assuming that any oxygen produced through steam gasification will cause combustion of the biodiesel gives an overall steam gasification reaction of

$$C_{10}H_{19}0+11.6H_2O \rightarrow 7.40CO+21.1H_2+2.60CO_2 \qquad \Delta G^o = 1.52\frac{MJ}{mol} - T\cdot 8.55\frac{kJ}{mol\cdot K} \qquad (2)$$

Steam gasification then will be thermodynamically favorable at temperatures over 178K and will require 1.52 MJ/mol, or 9.81MJ/kg, of heat to proceed. Obviously, the reactions required for

steam gasification will not proceed with reasonable rates at temperatures near room temperature. For the remaining calculations 800°C (1073K) will be assumed for the gasification temperature. Each mole of biodiesel will then produce 7.40 moles of CO, 21.1 moles of $H_2$, and 2.6 moles of $CO_2$.

While a large number of subsequent reactions may take place, only the water gas shift (WGS) reaction will be considered. Coke formation is almost certain to also occur to some extent. In general, the amount that forms will be related to gasifier design as well as the concentration of excess steam. For purposes of the present analysis coke formation will be ignored and the input to the fuel cell will be assumed to be $H_2$, $CO_2$, $H_2O$, and CO. The amount of each will depend on the extent to which excess steam is added to the gasifier according to the water gas shift reaction

$$CO + H_2O \rightarrow CO_2 + H_2 \qquad \Delta G^o = -41.1\frac{kJ}{mol} - T \cdot 42\frac{J}{mol \cdot K} \qquad (3\text{-}3)$$

and using, $\Delta G^o = -RT \ln \frac{[pCO_2][pH_2]}{[pCO][pH_2O]}$ (3-4)

to determine the final gas concentrations.

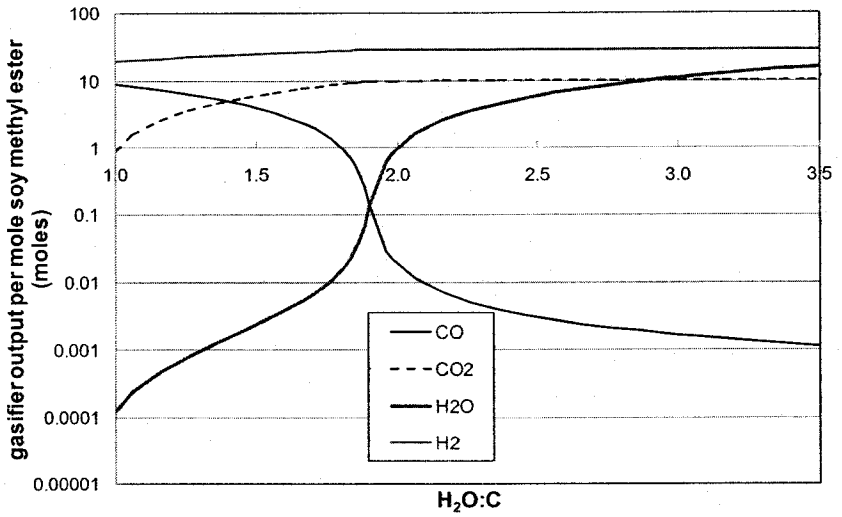


Figure 3-3 - Equilibrium gasifier output vs. molar steam to carbon ratio.

The number of moles of each output produced from one mole of biodiesel as a function of steam to carbon molar ratio is shown in Figure 3 under the assumption that equilibrium concentrations can be reached. Whether or not this assumption is valid depends upon the size of the gasifier. Because coke formation is more likely in cases of low steam, high CO, a steam to carbon ratio of 3.0 will be used for estimating the gasifier requirements.

As the SECA targets primarily relate to large scale stationary power generation, it may be more accurate to follow the work of Thijssen who analyzed achievable efficiency for smaller scale distributed generation systems and found 58% efficiency (HHV) and 86% overall fuel utilization to be achievable. This probably still overestimates the achievable efficiency for a transportation application because the power output will be more variable than the stationary application and

there are more limits on the size of heat exchangers. Based on this system efficiency and excess steam level, the gasifier must be capable of gasifying 711 kg/hour (1.27 moles per second) of biodiesel using 2480 kg/hr of steam. Under these conditions the gasifier would be producing 0.002, 10.0, 11.0, and 28.5 mole/second of CO, $CO_2$, $H_2O$, and $H_2$ respectively. Heat available at the combustor would be 4500 MJ/hr and 990 kg/hour of water would be consumed at full, 4 MW, output.

Another very likely output from the gasification of soy methyl ester is $PH_3$ gas. ASTM D6751-07b specifies 10 ppm for the upper limit on phosphorous content for biodiesel (B100). Several studies have indicated that actual phosphorous content is essentially at this level. As this level, phosphorous is detrimental to SOFC Ni based catalysts and it would need to be removed before entering the fuel cell. No other impurity elements are expected to be problematic if soy methyl ester is used as a fuel. However, sufficient analysis of biodiesel from multiple sources and multiple lots has not been performed so this cannot be stated with certainty. If compatibility is desired with petroleum based diesel, sulfur will also need to be removed.

In addition to chemical requirements, physical size of the power source will be of major issue for this application.

Table 3-2 - Dimensions of fuel cell stack vs. membrane electrode assembly size.

| Dimensions(**cm**) Of MEA(W*H) | 25×25 | 33×33 | 50×50 | 75×75 | 100×100 |
|---|---|---|---|---|---|
| Dimensions of unit cell(**cm**) W*H*L | 25×25×0 | 33×33×0.78 | 50×50×0.78 | 75×75×0.78 | 100×100×0.78 |
| No. of cells | 4571 | 2624 | 1143 | 508 | 286 |
| Total length of cell(No. of cells *L)(**m**) | 35.65 m | 20.46 m | 8.91 m | 3.96 m | 2.23 m |
| H2 gas flow rate (CFM) | 27 | 27 | 27 | 27 | 27 |
| Air flow rate (CFM) | 1376 | 1376 | 1376 | 1376 | 1376 |
| Heat generation rate (**kJ/sec**) | 840 | 840 | 840 | 840 | 840 |
| Water Production rate l/hr | 480 | 480 | 480 | 480 | 480 |

The gross volume of a typical locomotive is 300 m3 if everything is pushed to the rails. Approximately half of this space should be available for SOFC, fuel, water, and gasifier. To be a reasonable replacement for IC diesels the fuel cell system should fit within this range of volume. Table 2 shows the typical dimension of a 1MW SOFC stack, estimated based on the assumption of a cell operating voltage and current density of 0.7 V and 0.5 A/cm2 respectively and an operating temperature of 800 °C (1073K). Results show that for a cell size of 50cm x 50cm the size of a 1MW SOFC is estimated as 0.5m x 0.5m x 8.91m.

Gasifier

Estimates of required gasifier size have been produced by assuming that the gasifier can essentially follow the design of a methane reformer without the requirement for reducing CO and CH4 concentrations to near zero. Detailed gasifier design is outside of the scope of this report but estimates can be made using previously published work. The gasifier volume is estimated to be 40 m3 to convert approximately 90% of the methane to H2 and CO, and the estimated required volume is larger, 60 m3, at similar methane conversion. Some additional volume may be required to hydrocrack the biodiesel to smaller hydrocarbon molecules but the kinetics of those reactions should be very fast compared to the decomposition of methane and are therefore neglected. These estimates also do not include the size of the boiler required for steam supply.

Complete System

Table 3-3 shows estimated volumes of other components of the power plant for the locomotive. The increased volume of the SOFC compared to that in Table 3-2 is due to the addition of insulation and piping. Based on these estimates it should be possible to build a locomotive that contains all of the necessary components without resorting to tender cars.

Table 3-3: Estimated volume of system components.

| **Component** | **Volume** |
|---|---|
| Gasifier | 40-60 $m^3$ |
| SOFC stacks* | 20 $m^3$ |
| Fuel | 18 $m^3$ |
| Water | 21 $m^3$ |
| Heat Exchangers/boiler | 30-50 $m^3$ |
| **Total** | **129-169 $m^3$** |

Cost Analysis

The railroad industry is generally a low margin, high volume, business. As such, it is extremely cost sensitive. Any move toward embracing SOFC's as a power source over traditional internal combustion (IC) diesel engines needs to be cost justified. The analysis presented here assumes that regulatory action does not occur that tightens emissions restrictions to the point that fuel cell based systems become the only way to meet the requirements. Clearly, action of this type is a

possibility but because of uncertainty in how or when this may occur it is not considered in this analysis.

Cost considerations provided in this section are for the power generation equipment only, it is assumed that the locomotive frame, trucks, traction motors, controls, etc. will not vary significantly between diesel IC and SOFC based power generation systems. Maintenance costs, other than those associated with power generation, are assumed to be the same for both platforms as well. The cost estimates provided here are based on the assumptions in Table 4. Other items held constant for both power plant types include: internal rate of return, 40 year time period of the analysis, fuel costs for petroleum diesel and biodiesel are equal, 900 MWh per year is generated, and maximum power output is 4MW. SOFC costs are based on NETL and SECA program goals while efficiency is based on estimates for small distributed generation.

Table 3-4 - Assumptions Used in Cost Comparisons

| | Diesel IC | SOFC |
|---|---|---|
| Efficiency | 35% | 58% |
| Initial Capital Cost | $250/kW | $675/kW |
| Power Production Between Major Maintenance | 36,000 MWh | 32,000 MWh |
| Rebuild Cost | $75/kW | $175/kW |

For this analysis biodiesel will be assumed to be the fuel for both IC and SOFC platforms, though the results of the analysis would not be expected to change regardless of the choice of petroleum or biodiesel. At current biodiesel cost ($2.50/gallon), assuming fuel costs do not change over the 40 year time frame, capital costs dominate the cost analysis and the life cycle cost (present value) of the diesel IC power plant is $3.2 million compared to $4.9 million for the SOFC power plant. However, fuel costs will almost certainly not remain flat over that time period. Figure 3-4 shows the cost of the two power plants as a function of annualized fuel cost increases. This analysis indicates that at a 9% or higher annualized fuel cost increase the SOFC power plant is expected to be less expensive. This estimate of cost increase may seem high but it actually projects returning only to the prices of two years ago over the next seven years which seems entirely possible especially in the case of the adoption of carbon taxation. Table 3-5 shows the cost breakdown of each type of power plant over a 40 year time period at an IRR of 8% assuming no fuel cost increases, and assuming an annualized fuel cost increase of 9%.

Because fuel costs represent such a large fraction of total costs and they are recurring costs over the long life of a locomotive, assumptions regarding the time value of money also play an important role in determining the relative cost of the two platforms. Figure 3-5 shows costs under the same set of assumptions as Figure 3-4 except that the IRR is assumed to be 3% instead of 8%. In this case the SOFC system becomes the more cost effective option if only 3% annual increase in fuel costs is realized.

Table 3-5 - Diesel IC and SOFC Cost Breakdown (costs in millions)

| | Diesel IC (no fuel cost increases) | SOFC (no fuel cost increases) | Diesel IC (9% annual fuel cost increase) | SOFC (9% annual fuel cost increase) |
|---|---|---|---|---|
| Capital Cost | $1.0 | $2.7 | $1.0 | $2.7 |
| Maintenance Cost | $0.014 | $0.046 | $0.014 | $0.046 |
| Fuel Cost | $2.0 | $1.4 | $7.3 | $5.3 |
| **Total** | **$3.0** | **$4.2** | **$8.3** | **$8.1** |

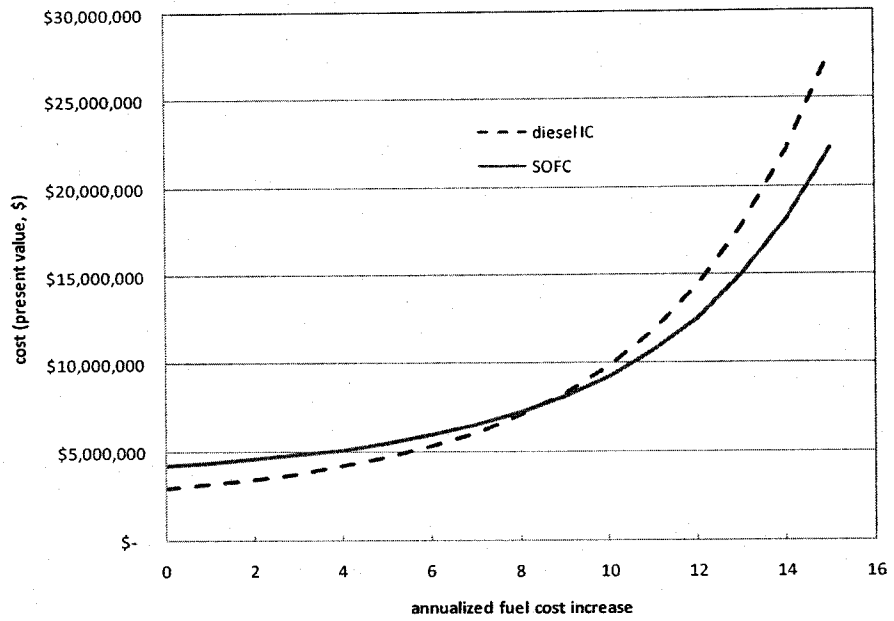


Figure 3-4: Cost vs. annualized fuel cost increases for SOFC and diesel IC locomotive power plants over a 40 year time period assuming 900 MWh/year, and 8% IRR.

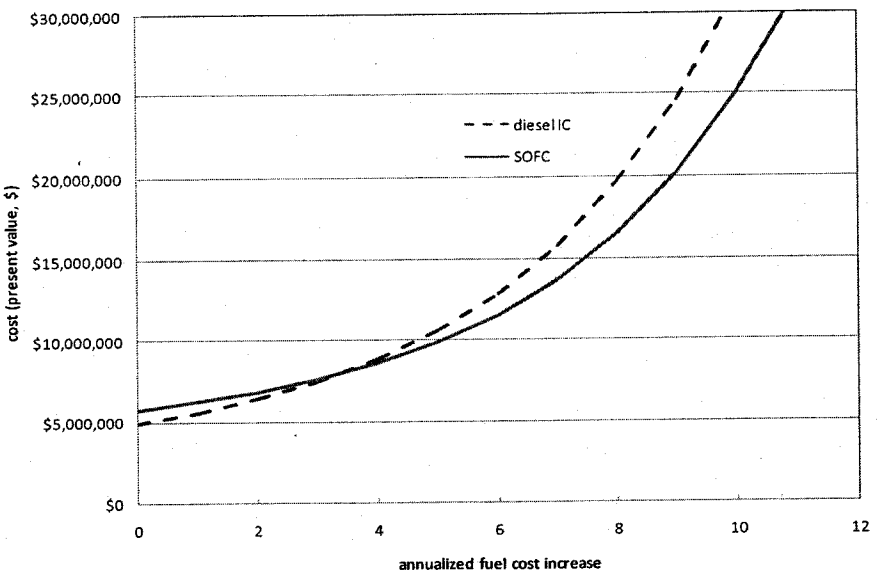


Figure 3-5: Cost vs. annualized fuel cost increases for SOFC and diesel IC locomotive power plants over a 40 year time period assuming 900 MWh/year, and 3% IRR.

In addition to fuel cost uncertainty over time, uncertainty in the actual system efficiency when used in a locomotive duty cycle and uncertainty in required maintenance interval may significantly influence the cost comparison.

Locomotive diesel IC engines are known to be capable of running for one million miles (approx 36,000 MWh) between major rebuilds. For the SOFC system lifetime of the stack is much less clear. Most stack life testing has been done under assumptions consistent with large scale stationary power generation not under assumptions consistent with locomotive duty cycles. The stack lifetime of 32,000 MWh used in the above calculations assumes that over the target stack lifetime of 40,000 hours the stack on average produces 20% of its rated power. In this case the stack needs to be replaced after 35.5 years in service. However, repeated shutdown and startup of the locomotive may significantly shorten this lifetime. To evaluate sensitivity to this parameter costs were estimated as a function of stack lifetime assuming IRR of 3% and 8% and using an annualized fuel cost increase of 5%. Results of this analysis are displayed in Figure 6. If stack lifetime drops below 8000 MWh (8.9 years) it becomes rapidly more difficult to cost justify the SOFC platform.

Again because of the large impact of fuel cost on the overall cost of a locomotive, system efficiency will be a significant factor in overall cost. Adjusting system efficiency according to a likely duty cycle according to Table 3-6 (1992) gives a power weighted average efficiency of 34.6% for diesel IC and 47.6% for SOFC. Under these efficiency assumptions even at 3% IRR fuel costs have to increase at an annualized rate of 8% or more for the SOFC system to be cost justified, see Figure 3-7. With IRR of 8% the crossover point becomes 13% annualized fuel cost increase. These results also assume that whatever cost of unavoidable idle or braking time is the same for both IC and SOFC power plants.

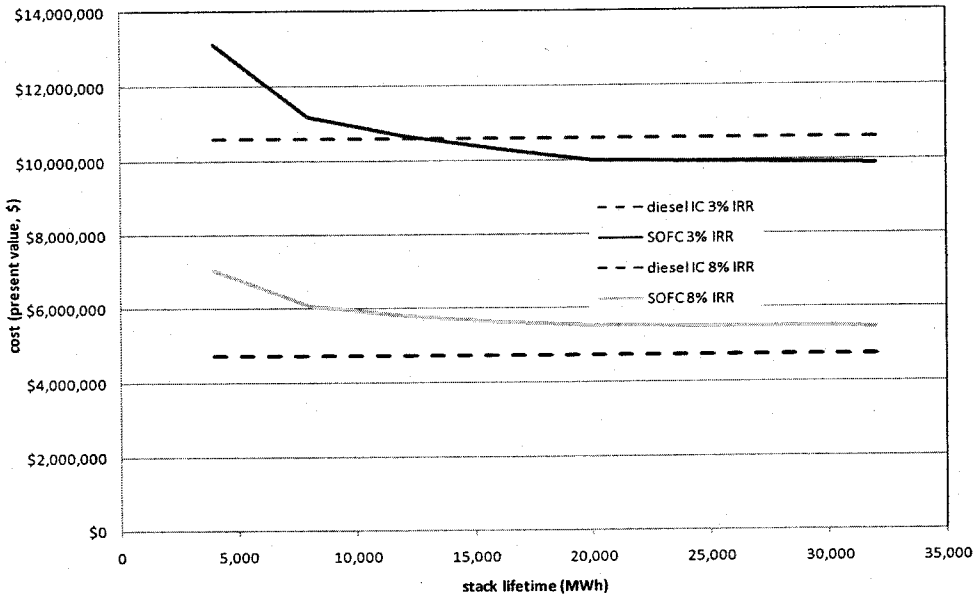


Figure 3-6: Cost vs. SOFC stack lifetime. Four thousand MWh corresponds to stack replacement every 4.4 years.

Table 3-6: Duty cycle and efficiency comparison for diesel IC and SOFC

| % Power | Diesel IC Efficiency, % | SOFC Efficiency, % | % time at power | % total power generated |
|---|---|---|---|---|
| 4-5 | 12-15 | 18-22 | 4 | 0.9 |
| 10-11 | 17-19 | 24-30 | 4 | 2.0 |
| 22-26 | 23-27 | 48-54 | 4 | 4.6 |
| 24-28 | 25-30 | 53-57 | 5 | 6.2 |
| 48-53 | 30-35 | 51-55 | 4 | 9.6 |
| 67-68 | 32-37 | 48-52 | 4 | 12.8 |
| 82-83 | 33-38 | 46-50 | 3 | 11.8 |
| 100 | 35-40 | 44-48 | 11 | 52.2 |
| idle | | | 49 | |
| Braking | | | 12 | |

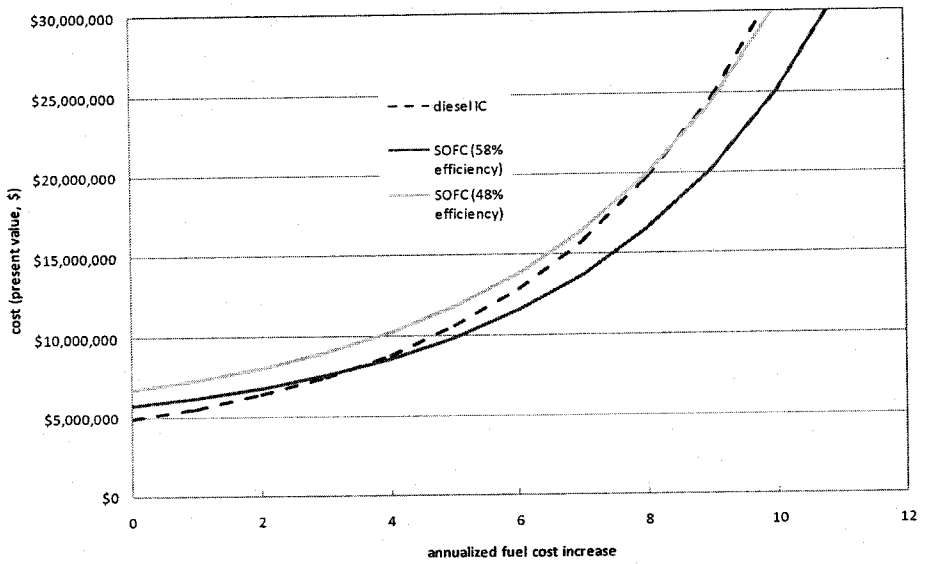


Figure 3-7: Effect of efficiency on cost vs. annualized fuel cost increase.

Conclusion

From a technical perspective, the analysis here concludes that SOFC based locomotives could be developed to replace current diesel internal combustion based locomotives. Sufficient power, range, and space in the locomotive is available to gasify a liquid hydrocarbon fuel for use in SOFCs. Economic justification is more difficult. While cost of fuel is the dominant overall cost of the locomotive power plant over its life cycle under any reasonable assumption of future fuel costs, the efficiency of the SOFC is not high enough to offset its higher capital cost under most scenarios. However, this could significantly change. Regulatory standards that make diesel internal combustion engines more expensive, such as by requiring catalytic converters, or that make it impossible for diesel internal combustion engines to meet the standards may either alter the economic analysis or make it irrelevant with respect to adoption of fuel cell based systems.

Fuel Cell Power Analysis Models – Theoretical Assessment

As part of the process of meeting the specific goals of this project, some fundamental groundwork needed to be accomplished first. Particularly models of the fuel cell, batteries and other components were required in order to analyze the proposed systems.

To look at the behavior of the fuel cell when operating in a locomotive power system, a dynamic model suitable for system simulation needed to be developed. The simple fuel cell model used was based on a model previously developed in the literature [19, 20]. Modifications to the model were made to match the power requirements for the particular locomotive application.The fuel cell model is based on lumped model. The input for the model is current demand and output is fuel cell voltage. Partial pressures of hydrogen gas, carbon monoxide gas and water also taken as inputs. These pressures are varied with output voltage. The fuel cell output voltage, $V_{fc}$, is,

$$V_{fc} = E - V_{act} - V_{con} - V_{ohmic} \tag{3-5}$$

where E is Nerst reversible voltage, $V_{act}$ is activation voltage, $V_{con}$ is concentration loss voltage and $V_{ohmic}$ is ohmic loss voltage. The Nerst voltage, E, is the open circuit voltage of the solid oxide fuel cell. The expression for the Nerst voltage is

$$E=E_0+\frac{RT}{2F}\ln\left(\frac{P_{H_2}*P_{o_2}^{0.5}}{P_{H_2o}}\right) \tag{3-6}$$

where $E_0$=1.1V is the standard potential, R=8.314 kJ/kmol-K is the universal gas constant and F=96486 C/mol is the Faraday's constant. $P_{H_2}$, $P_{o_2}$ and $P_{H_2o}$ are the partial pressures of hydrogen, oxygen and water respectively.

The activation voltage $V_{act}$ is given as

$$V_{act}=\frac{RT}{2F}\left(z+\sqrt{\left(1+z^2\right)}\right) \tag{3-7}$$

where $z=\frac{I_{fc}}{2I_o}$. $I_{fc}$ is fuel cell current and $I_o$ is exchange current density. This current density can be found using

$$I_o=Ae^{-E_{act}/RT} \tag{3-8}$$

Where A = 101.2 kA/cm$^2$ is pre exponential factor obtained by curve fitting the distributed model. $E_{act}$ = 120 kJ/mol is the activation energy for the electrochemical reaction. The concentration loss, $V_{con}$, is given as,

$$V_{con}=\frac{RT}{nF}\ln\left(1-\frac{I_{fc}}{I_L}\right) \tag{3-9}$$

where $I_L$ is limiting current density assumed to be 2.65A. The ohmic loss, $V_{ohmic}$, is given as,

$$V_{ohmic}=\left(\gamma\exp\left[\beta\left(\frac{1}{T_o}-\frac{1}{T}\right)\right]\right)I_{fc}=r\cdot I_{fc}=0.0257\cdot I_{fc} \tag{3-10}$$

The fuel cell dynamics were modeled using the lumped parameter mode described by [19, 20]. This dynamics uses a first order model for the partial pressures of the gases involved in the Nerst equation, hydrogen, oxygen and water. This response is modeled using a simple RC network for each of the gases.

A solid oxide fuel cell is modeled using the above equations. Gains in the model were adjusted to obtain the desired dynamic response. A step change is introduced in the current demand for the fuel cell which reflects a change in the fuel cell voltage. The waveform of the output voltage for a step change in current demand is given in the results.

A two-dimensional simulation model is was under development for analyzing a tri-layer SOFC fuel cell. This mode could incorporate hydrogen or a reformed fuel gas stream with enriched hydrogen as the fuel. This model's objective is to determine the performance characteristics of a tri-layer cell in the form of polarization curves based on the state-of the art cell components types and materials. Based on these performance characteristics, the analysis, design and selection a fuel cell energy system in terms of its operating performance and integration with other sub-system can be carried out.

The simulation model includes combined heat and mass transfer processes in the electrodes, membrane and gas channels. The associated electro-chemical reaction in a planar tri-layer fuel cell design is also included. A schematic of the computational domain is shown in figure 3-8. The two-dimensional simulation model for a tri-layer SOFC membrane-electrode assembly (MEA) and bipolar plates with straight through channels is developed for the voltage and power polarization curves using state-of-the-art materials for electrode and membrane materials.

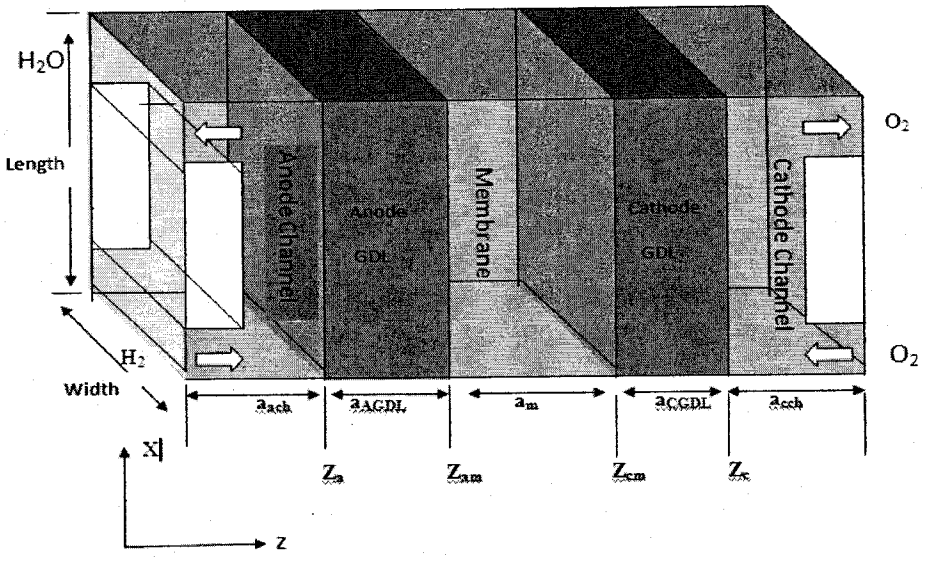


Figure 3-8 - Computational domain for a tri-layer solid oxide fuel cell

Since a battery is to be used as an ASU, a dynamic model for it was also needed. The model used is based on an equivalent circuit model found in literature [21]. The basic equivalent circuit for this model is shown if figure 3-9.

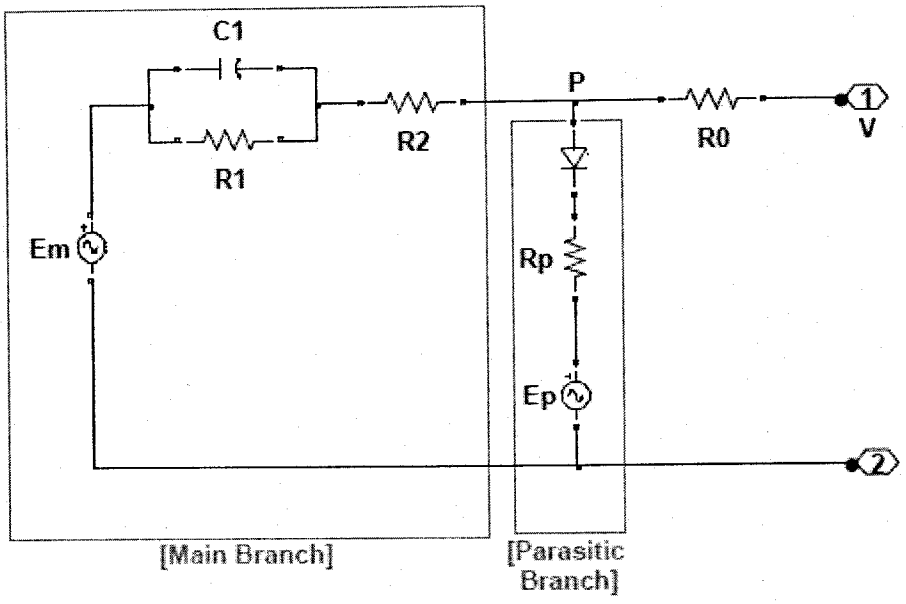


Figure 3-9 - Schematic of dynamic battery model.

The value of each component in the equivalent circuit depends on the battery parameters. The terminal voltage profile for a battery depends on the current profile that the battery has to supply. To account for this effect along with the state of charge (SOC) parameter another parameter called the depth of charge (DOC) is also employed.

The SOC gives the amount of charge that is left in the battery with reference to the maximum capacity of the battery is able to deliver at a given temperature. The expression for the SOC is

$$SOC = 1 - \frac{Q_e}{(K_C C(I^*))} \tag{3-4}$$

where $Q_e$ is the charge dissipated from the battery given by

$$Q_e = \int_0^t -I_m(\tau)d\tau\,, \tag{3-12}$$

$K_C$ is an empirical constant, and $C(I^*)$ is the capacity of the battery in AH at rated current.

The DOC is the indicator of how full the battery is with reference to the actual discharge regime. It is the amount of charge that is left in the battery with reference to the capacity of battery at the average discharge current at that point of time. The expression for the DOC is

$$DOC = 1 - \frac{Q_e}{(K_C C(I_{avg}, \theta))} \tag{3-13}$$

where $Q_e$ is the charge dissipated from the battery, $C(I_{avg}, \theta)$ is the capacity of the battery at a current of $I_{avg}$, and $\theta$ is the temperature.

Using these definitions for SOC and DOC the individual circuit elements are defined. The main branch voltage, Em, is given by

$$E_m = E_{m0} - K_E(273+\theta)(1-SOC) \tag{3-14}$$

where:

$E_{m0}$ is the open-circuit voltage at full charge.
$K_E$ is a constant in volts/°C.
$\theta$ is the electrolyte temperature in °C.
SOC is the state of charge.

The terminal resistance, $R_0$, is given by:

$$R_0 = R_{00}[1 + A_0(1-SOC)] \tag{3-15}$$

where:

$R_{00}$ is the terminal resistance at SOC= 1 in Ohms.
$A_0$ is a constant.
SOC is the state of charge.
The main branch resistance, $R_1$, is given by

$$R_1 = -R_{10}\ln(DOC) \tag{3-16}$$

where:

$R_{10}$ is a constant in Ohms.
DOC is the depth of charge.

The main branch capacitance, $C_1$, is given by

$$C_1 = \tau_1 / R_1 \tag{3-17}$$

where:

$\tau_1$ is main branch time constant in seconds
$R_1$ is main branch resistance in Ohms

The average battery current, $I_{avg}$, is given as

$$I_{avg} = \frac{I_m}{(\tau_1 s + 1)} \tag{3-18}$$

where:

$I_m$ is main branch current in Amps
$\tau_1$ is main branch time constant in seconds

The expression for the electrolyte temperature, $\theta$, is given by

$$\theta(t) = \theta_{init} + \int_0^t \frac{\left(P_s - \frac{(\theta - \theta_a)}{R_\theta}\right)}{C_\theta} d\tau \qquad (3\text{-}19)$$

where:

$\theta_{init}$ is the battery's initial temperature in °C.
$\theta_a$ is the ambient temperature in °C.
$P_s$ is the $I^2R$ power loss of $R_0$ and $R_2$ in Watts.
$R_\theta$ is the thermal resistance in °C/Watts.
$C_\theta$ is the thermal capacitance in Joules/ °C
$\tau$ is the integration time
t is the simulation time in seconds

The parasitic branch contains non-linear components. So, instead of modeling the components the parasitic current '$I_P$' through the branch is modeled as below:

$$I_P = V_{PN} G_{p0} \exp\left(\frac{V_{PN}}{V_{p0}} + A_P\left(1 - \frac{\theta}{\theta_f}\right)\right) \qquad (3\text{-}20)$$

where:

$V_{PN}$ is voltage in parasitic branch
$V_{p0}$ is constant in volts
$G_{P0}$ is constant in Siemens
$A_P$ is a constant
$\theta$ is electrolyte temperature in °C
$\theta_f$ is the electrolyte freezing temperature in °C

The capacity of the battery at a discharge current, I, and electrolyte temperature, $\theta$, are given by

$$C(I,\theta) = \frac{K_C C_{0^*}\left(1 + \frac{\theta}{-\theta_f}\right)^{\epsilon}}{1 + (K_C - 1)(I/I^*)^{\delta}} \qquad (3\text{-}21)$$

where:

$\epsilon$, $\delta$ and $K_C$ are empirical constants.
$C_{0^*}$ is the capacity at nominal current $I^*$ and at a temperature of 0°C.
$I^*$ is the nominal current in Amps.

To verify the model the parameters were calculated for a 500 Ah valve regulated lead acid (VRLA) battery. Simulation values using these parameters were compared to these values and are discussed in the results section.

After verifying the model the parameters were adjusted to match the battery requirement for the switcher application. The outcome of this simulation is given in the results section.

Several tasks have been accomplished in developing the groundwork for performing the required analysis. This include the development a fuel cell models and battery models to be used in analysis of the proposed systems.

A fuel cell model was developed in Matlab/Simulink that is useful in representing the fuel cell in the locomotive power system. The model is based on the equations (3-1 – 3-6) developed above with parameters associated with a SOFC. To verify the model, the output voltage of the SOFC is simulated. A voltage vs. current polarization curve of the SOFC is obtained, which is shown in Figure 3-10. For small currents, the cell voltage drops rapidly as current increases due to activation energy losses of the electrochemical reaction. Next, a linear decrease of voltage is observed due to ohmic loss as the cell current increases. Last, the fuel cell voltage drops sharply to zero as the current approaches the limiting current. This voltage drop is due to concentration loss.

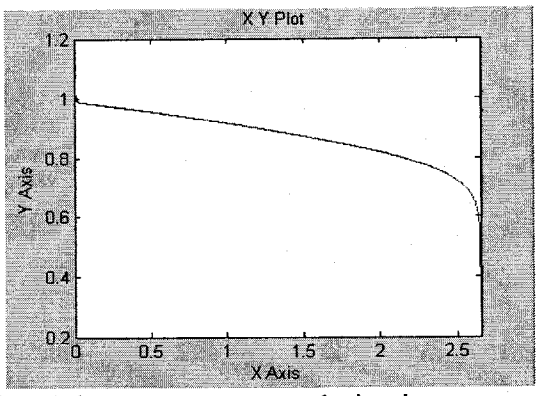


Figure 3-10 - Voltage vs. current polarization curve of an SOFC

To model the transient behavior of the fuel cell, the Nernst reversible voltage of the fuel cell is implemented using the equivalent electrical circuit of the flow mass conversion equations of hydrogen, water and oxygen [19, 20]. Dynamics of the SOFC is embedded in the equivalent RC circuit. The transfer function of the RC circuit is R/(1+RCs). Resistance and capacitance of the equivalent RC circuit for hydrogen, oxygen and water respectively are shown in Table 3-7. Transient response of the SOFC is studied. When the fuel cell current decreases from 1.563 A to 1.436 A at 85 seconds, the response of the cell voltage is shown in figure 3-11. When the fuel cell current increases from 1.563A to 1.695A at 85 seconds, the response of the cell voltage is shown in figure 3-12.

Table 3-7 - Model Parameters for RC Equivalent Circuit

| Parameter | Value | Unit |
|---|---|---|
| Resistance of Hydrogen ($R_1$) | 1.1826 | kΩ |
| Resistance of Oxygen ($R_2$) | 0.396 | kΩ |
| Resistance of Water ($R_3$) | 35.587 | kΩ |
| Capacitance of Hydrogen($C_1$) | 233.23 | $\mu F$ |
| Capacitance of Oxygen($C_2$) | 734.84 | $\mu F$ |

| | | |
|---|---|---|
| Capacitance of Water($C_3$) | 233.23 | $\mu F$ |

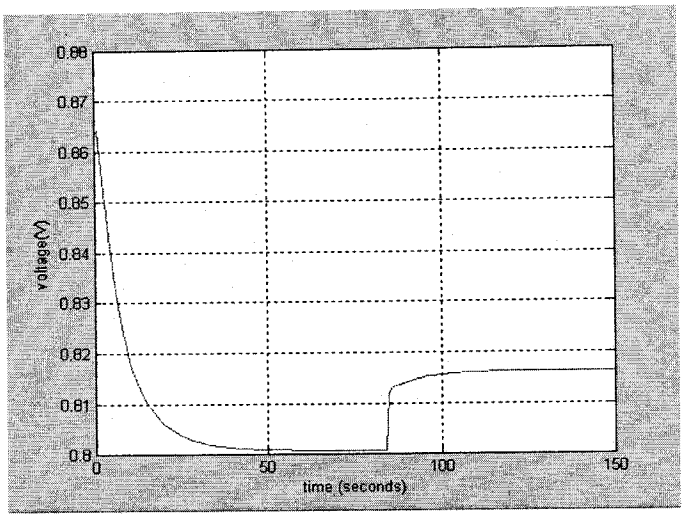


Figure 3-11 - Transient response of fuel cell voltage with current decreasing from 1.563 A to 1.436 A

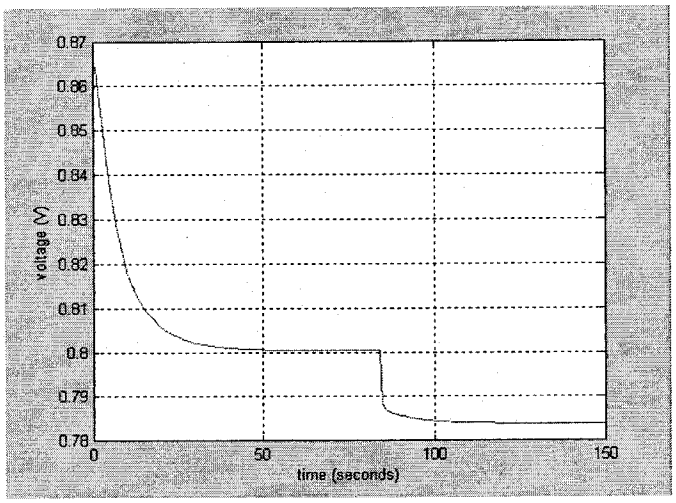


Figure 3-12 - Transient response of fuel cell voltage with current increasing from 1.563A to 1.695A

Along with these results, work continues on a multidimensional simulation for a tri-layer SOFC membrane-electrode assembly (MEA) and bipolar plates. This model uses state-of-the-art materials for the electrode and membrane to determine the voltage and power polarization curves.

The reactant material and energy transport equations in porous electrodes, electrolyte membrane, and reactant gas flows in gas channels are derived based on conservation of the reactant material and energy over a differential element. Basic assumptions include: The transport model is solved

for two-dimensional model; the system is in steady state; both water and gas phases are considered to be distinct in diffusion layer; the catalyst layer is considered as a monolayer to incorporate the source and sink terms and constant inlet gas velocities. All dimensions and material properties are given in Tables 3-8 through 3-10.

Table 3-8 - Anode gas diffusion layer properties

| **Anode GDL Properties** | |
|---|---|
| Material Used | Ni/YSZ cermet |
| Density | 8910 $Kg/m^3$ |
| Specific Heat | 0.444 J/g.K |
| Thermal Conductivity | 90.5 W/m.K |
| Permeability | $1.76*10^{-11}m^2$ |
| Porosity | 0.5 |
| Thickness | 0.5mm |
| Length | 100cm |
| Width | 100cm |

Table 3-9 - Membrane properties

| **Membrane Properties** | |
|---|---|
| Material Used | 8% $Y_2O_3$ doped $ZrO_2$ (YSZ) |
| Density | 5940 $Kg/m^3$ |
| Specific Heat | 0.471 J/g.K |
| Thermal Conductivity | 1.62W/m.K(T=1144K) |
| Thickness | 1.8mm |
| Length | 100cm |
| Width | 100cm |

Table 3-10 - Cathode gas diffusion layer properties

| **Cathode GDL Properties** | |
|---|---|
| Material Used | LSM |
| Density | 6600 $Kg/m^3$ |
| Specific Heat | 0.432 J/g.K |
| Thermal Conductivity | 1.95W/m.K(T=298K) |

| | |
|---|---|
| Permeability | $1.76*10^{-11}$ $m^2$ |
| Porosity | 0.5 |
| Thickness | 0.5mm |
| Length | 100cm |
| Width | 100cm |

Figure 3-13 shows some preliminary results of a tri-layer solid oxide fuel cell. Figure 3-13a shows the variation of the open-circuit theoretical voltage of a SOFC using hydrogen-oxygen fuel cell as a function of operating temperature. Similar results are also obtained for the operation a fuel cell with a reformed gas mixture consisting of 90% hydrogen and 10% carbon monoxide and presented in figure 3-13bb.

Figure 3-14 shows the distribution of hydrogen and oxygen gas concentration across the anode and cathode gas diffusion layers. Results show considerable variation in gas concentrations along the channel and across the gas diffusion layers with significant drop at the electrode-membrane interfaces.

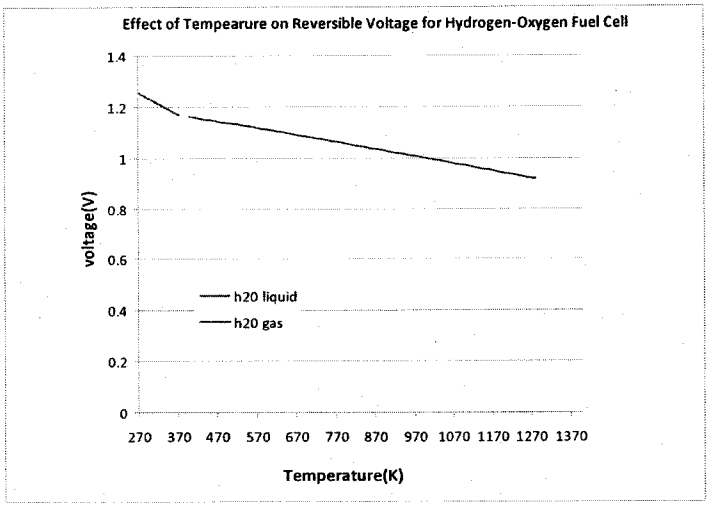


Figure 3-13a - Open circuit theoretical voltage as a function of operating temperature ( $H_2$ )

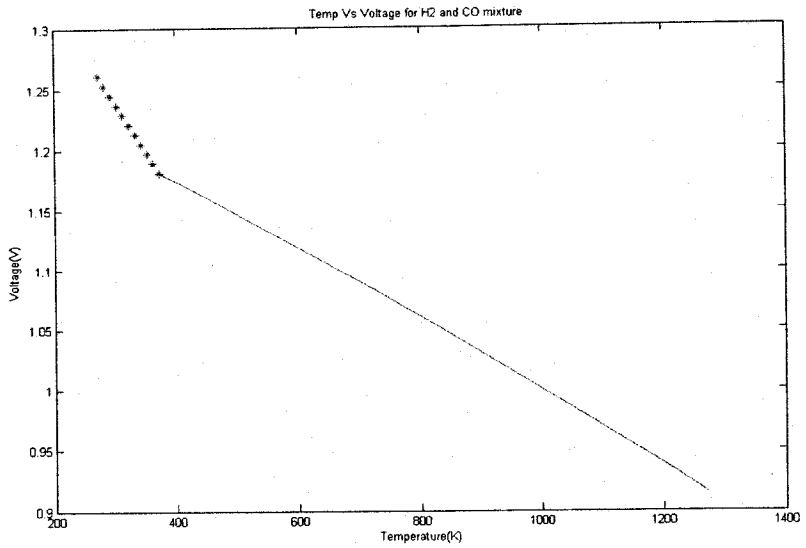


Figure 3-13b - Open circuit theoretical voltage as a function of operating temperature $(90\%H_2 - 10\%CO)$

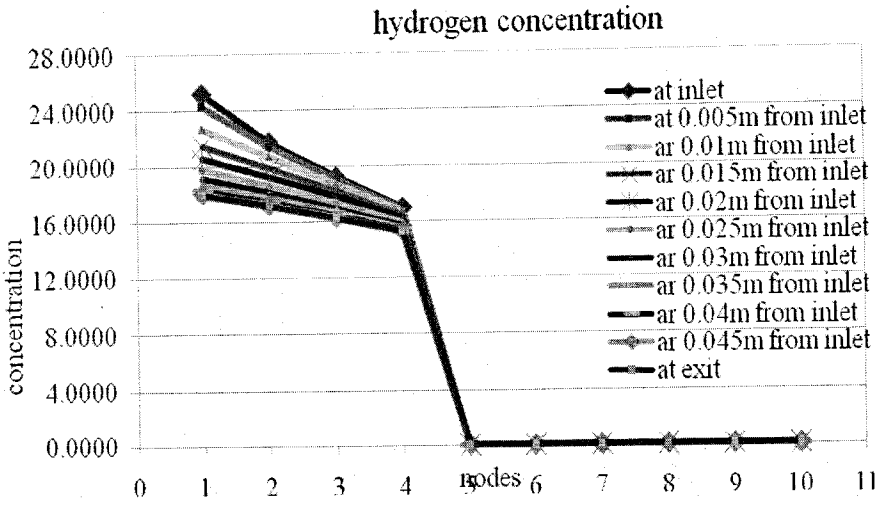


**(a)** Hydrogen concentration in anode gas diffusion layer

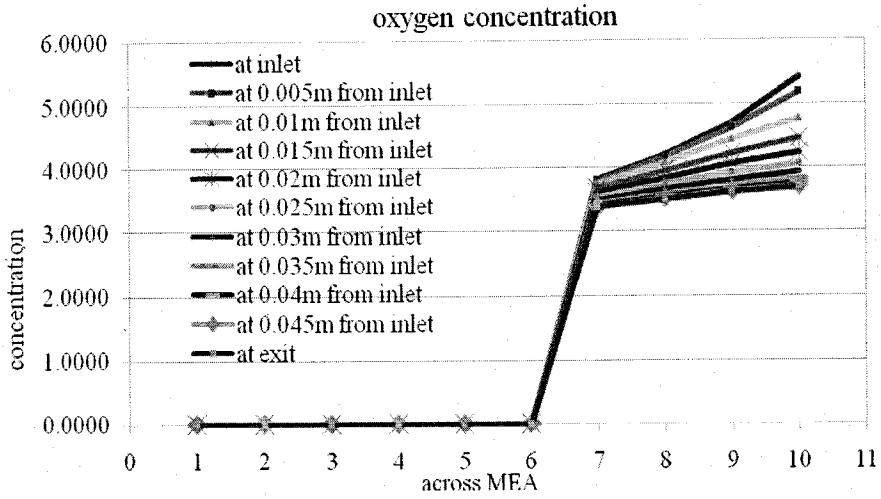


**(b)** Oxygen concentration in cathode gas diffusion layer

Figure 3-14 - Gas concentration distributions across gas diffusion layers

Figure 3-15 shows the polarization curve for three different operating temperatures for an exchange current density of $i_0 = 0.1 A/cm^2$. These computations include activation, ohmic and mass transfer losses. Results show the effect of operating temperature on the operating voltage and power of a tri-layer solid oxide fuel cell.

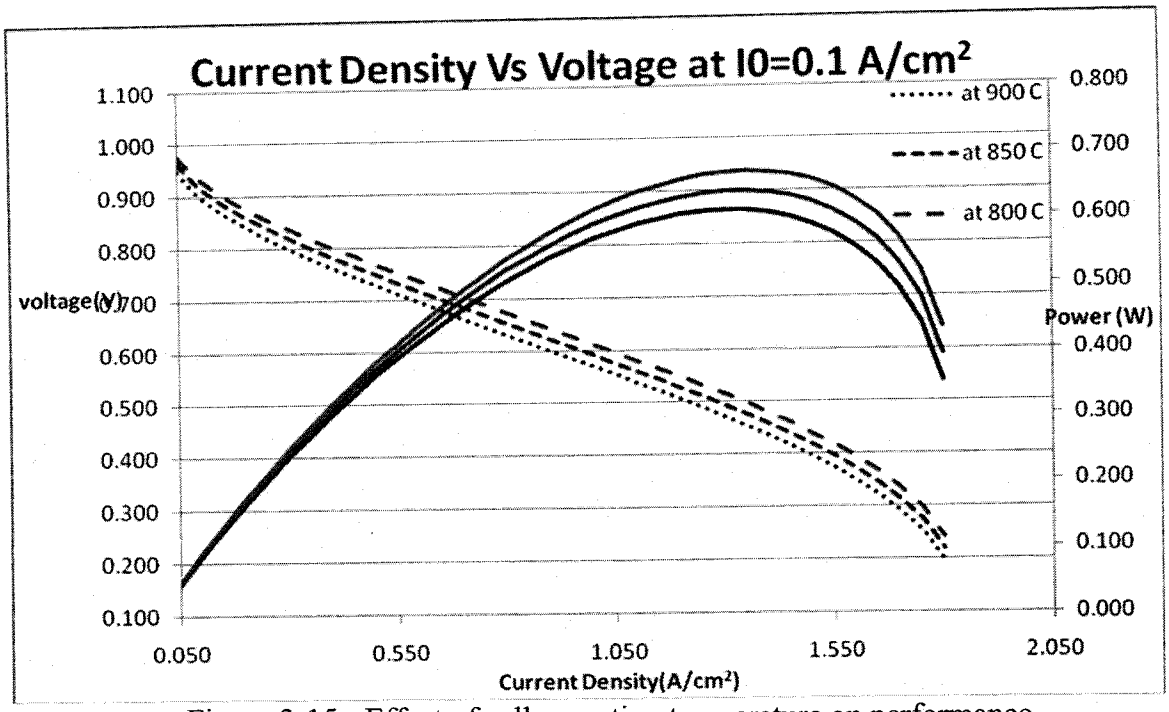


Figure 3-15 - Effect of cell operating temperature on performance.

In order to see the effect of activation overpotential on the polarization, computations are carried out with different values of exchange current density and results are presented in figure 3-16, and results show improved performance in terms of operating voltage and power in a operating current density range of 1.1 -1.25 $A/cm^2$ here a high exchange density represents an improved electrochemical kinetics.

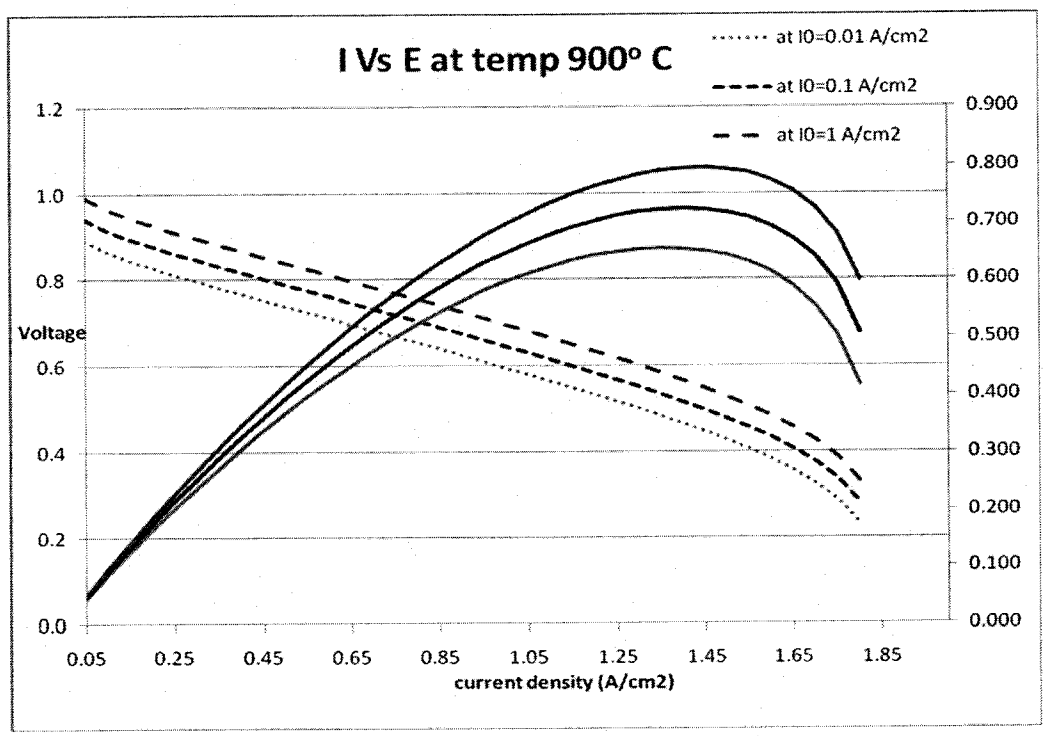

Figure 3-16 - Effect of exchange current density on cell performance

Design and analysis work for a fuel cell stack system with a rated power of the locomotive is being performed to determine number and size of cell; fuel and air flow rates and fuel storage requirements; heating and cooling requirements and reforming needs.

A battery model was also developed in Matlab/Simulink so that it could be incorporated in the fuel cell power system. The model is based on the equations (3-11 – 3-21) above. The parameters were adjusted to meet the power demand for the required system. To test the model, however, parameters based on a 500Ah valve regulated lead acid (VRLA) battery discussed in [21] were used. Table 3-10 summarizes these parameters.

Table 3-10 - Parameters for a VRLA battery [Ceraolo].

| | | |
|---|---|---|
| Parameters referring to the battery capacity | $I^*$=51.5A | $C_{\theta^*}$=317.9AH |
| | $K_c$=1.11 | $\theta_f$ = -40°C |
| | $\epsilon$ = 1.19 | $\delta$ = 1.75 |
| Parameters referring to the main branch of the electrical equivalent | $\tau_1$ = 1500 s | $E_{m0}$=2.18V |
| | $K_E$=0.839e-3 V/ °C | |
| | $R_{00}$=2.0mΩ | $R_{10}$=0.4mΩ |
| | $A_0$ = -0.20 | $R_{20}$= 15mΩ |
| | $A_{21}$=-8.0 | $A_{22}$=-8.45 |
| Parameters referring to the parasitic reaction branch of the electrical equivalent | $E_P$=1.95V | $V_{p0}$=0.1V |
| | $G_{p0}$=20mS | $A_p$=2.0 |
| Parameters referring to the battery thermal model | $C_\theta$ = 15 Wh/°C | $R_\theta$ = 0.2°C/W |

The battery model is built using the above parameters. To verify the discharge rate the battery is tested for a discharge of 58A for duration of 8.6 hours then the discharge current is made zero. The simulation was continued for several additional hours to observe the voltage recovery. The cell voltage, shown in figure 3-17, appears very similar to examples found in literature [21] thus verifying the model.

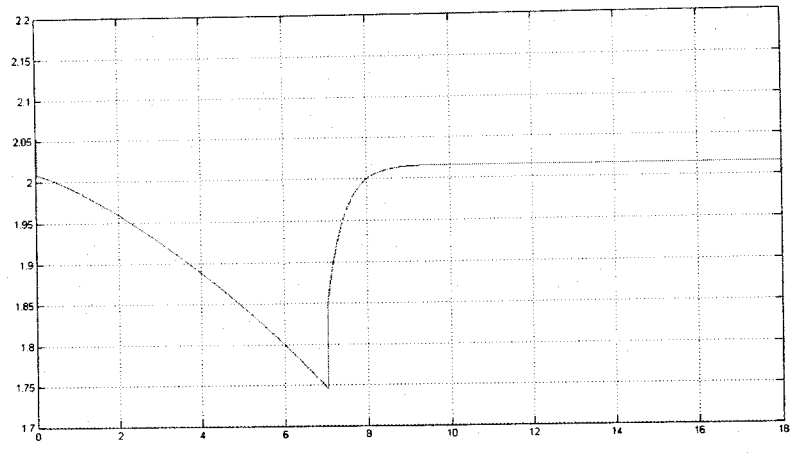


Figure 3-17 - Simulated discharge characteristic of a lead acid cell.

Milestone Results Power needs of current locomotive systems
It was determined that the power needs for a locomotive depended highly on the specific application. The applications investigated included the switcher, pusher and road locomotive.

*Switcher* The switcher is used assemble trains in a rail yard. This application requires lots of starts and stops with a peak power several orders of magnitude above the average power. Several load duty cycles were obtained for the switcher, a typical example of which is shown in figure 3-18 [22]. In this figure power generated is negative. The maximum instantaneous power from the generator is observed to be -1136 HP (-848 kW). The instantaneous generator power is averaged over the 10 hour interval and the average was found to be -48.13 HP (-35.9 kW).

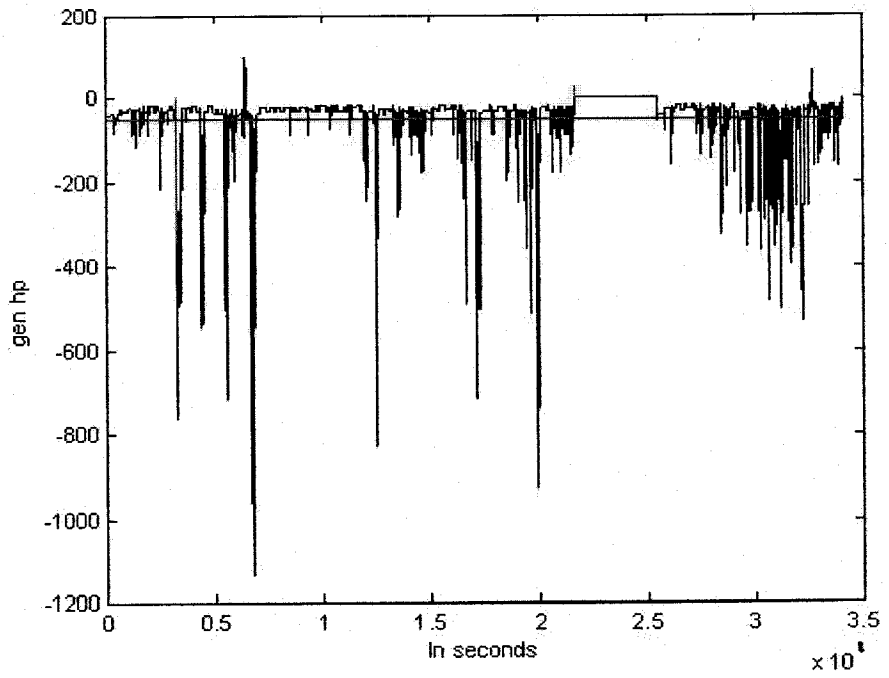


Figure 3-18 - Duty cycle in a switcher locomotive

A histogram of the generator power is shown in figure 3-19. The x axis is the generator power, the y axis is the percentage of a specific value of power. The highest percentage of around 28% is at the power of approximately -50 HP (-37.3 kW) which corresponds to the average power.

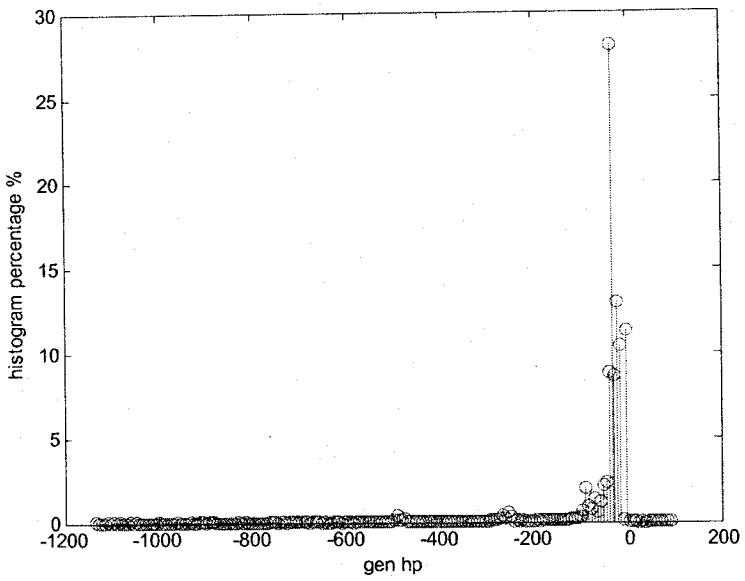


Figure 3-19 - Histogram of generator power

To determine the power needs a statistical analysis was done by fitting the data to a normal and Rayleigh distribution. The normal distribution was not a very good fit in that a good part of the distribution would be in the region where power is absorbed by the fuel cell. As this was not possible a Rayleigh distribution was tried. In this case, the shape of the distribution compared well with the histogram (figure 3-20).

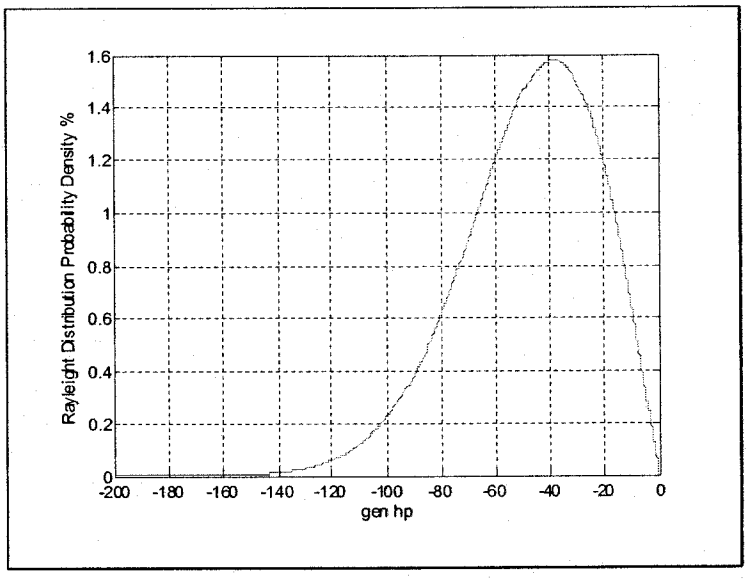


Figure 3-20 - Rayleigh distribution of the power request

To look at the other energy storage requirements of the ASUs, the difference between the average power and the power required at any instant is analyzed using the duty cycle data in figure 3-18. When the generator power magnitude is lower than the average power, the ASU is discharged and energy flows out of the unit. When the generator power magnitude is higher than the average power, ASU is charged and energy flows into the unit. By integrating the difference of the average power and the instantaneous power, the energy usage of the battery is obtain and shown in figure 3-21. A negative energy means energy flows into the ASU. The negative energy peaks at $2.8\times10^4$ second with the value of $-1.25\times10^5$ HP·second ( -93 MJ). It happens after a relative long period of idling of the train as shown in figure 3-11. A positive energy means energy flows out of the ASU. The positive energy peaks at $0.7\times10^4$ second with the value of $1.75\times10^5$ HP·second (130 MJ). It happens after several frequent power request peaks.

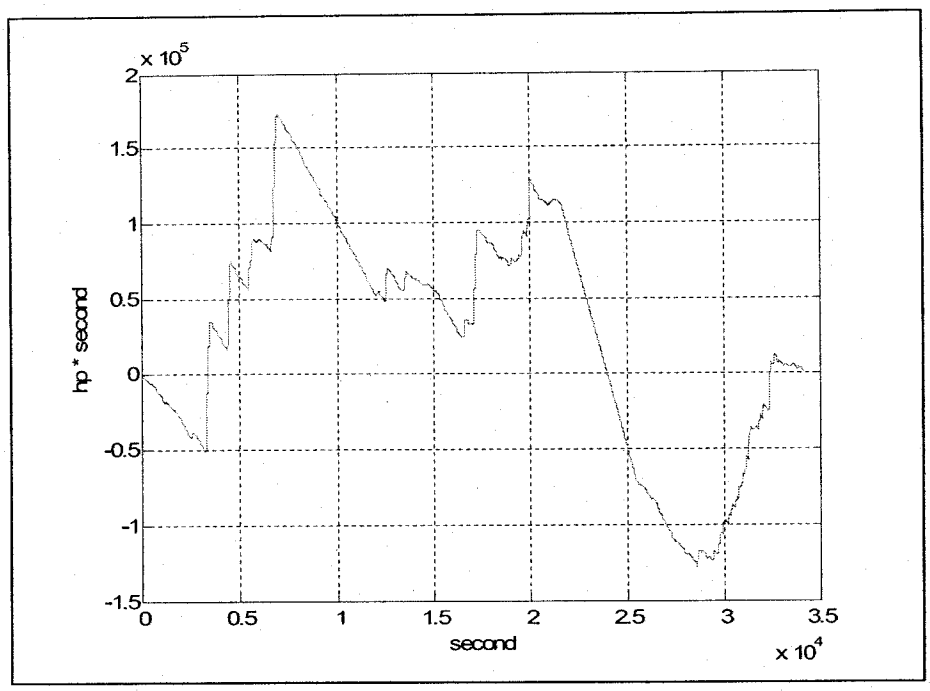


Figure 3-21 Energy flow into and out of ASUs

For this locomotive application the bus voltage is 648V. So as to have the battery voltage near the nominal bus voltage a battery consisting of 300 cells in series is needed. To meet the energy requirements 6 sets of these series batteries would need to be connected in parallel.

When investigating ASUs for the use with fuel cell it became apparent batteries would not be able to handle the dynamic response required by the power demands. Since ultra-capacitors have very high discharge rates, these were also included as energy storage units in the switcher application. The rating of the ultra-capacitor is adjusted to limit the voltage fluctuation of the battery to about 60V. The ultra-capacitor is modeled as a capacitor in series with a resistance. Upper voltage of the capacitor is limited to 650V.

Battery life is affected by SOC variation. For longevity of battery life SOC has to maintain between 40% and 80%. In order to achieve this current demand for the battery has to be limited. For this application the current demand from the battery is limited to about 400A and the charging current to 20A. Assuming the power demand shown in figure 3-18, the variation of the SOC when the current demand is supplied by battery is in figure 3-22. In this simulation power demands outside of the range of operation is assumed to be supplied by the ultra-capacitor.

For this system the rating of the ultra-capacitor is adjusted to limit the voltage fluctuation of the battery to about 60V. The ultra-capacitor is modeled as a capacitor in series with a resistance. The upper voltage of the capacitor is limited to 650V.

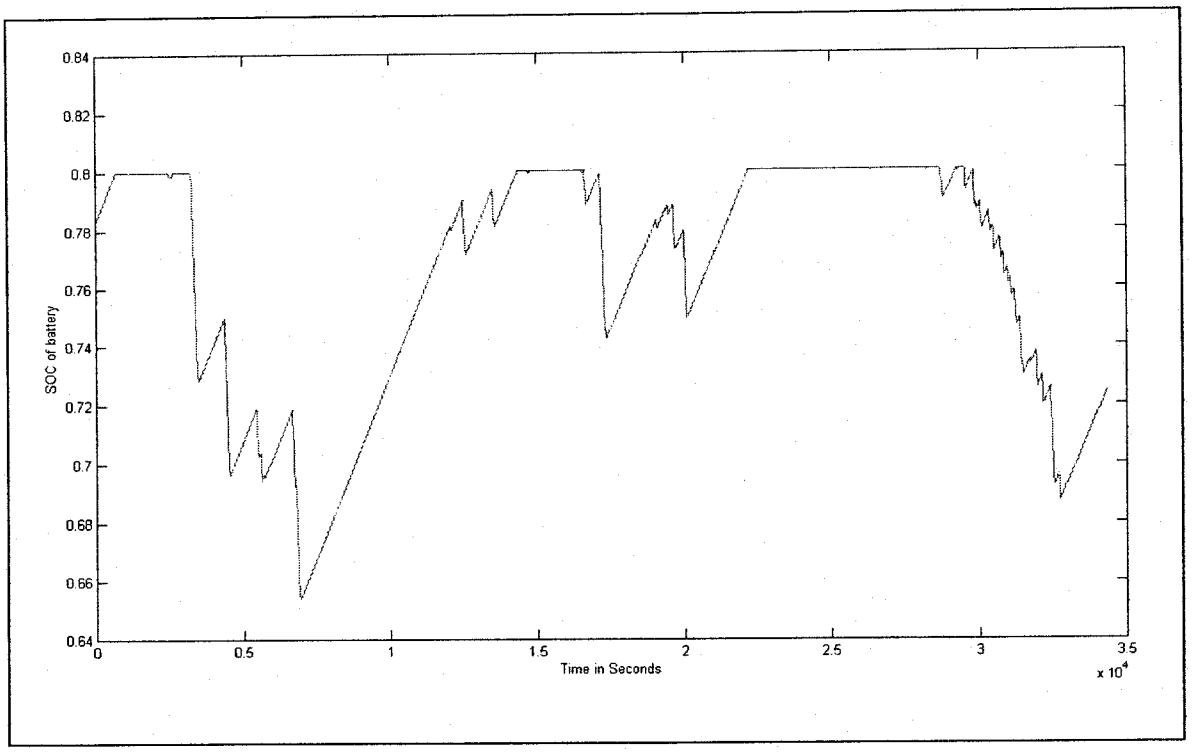


Figure 3-22. SOC of the battery with a SOC control.

*Pusher* The pusher is a locomotive used to aid a train going up a steep grade. In this application the locomotive needs to supply relatively long periods in the range of an hour. Between these periods of high intensity there are long periods of low power and there are possible periods where energy can be recovered during the downhill returns. A typical load duty cycle for this type of application is shown in figure 3-23.

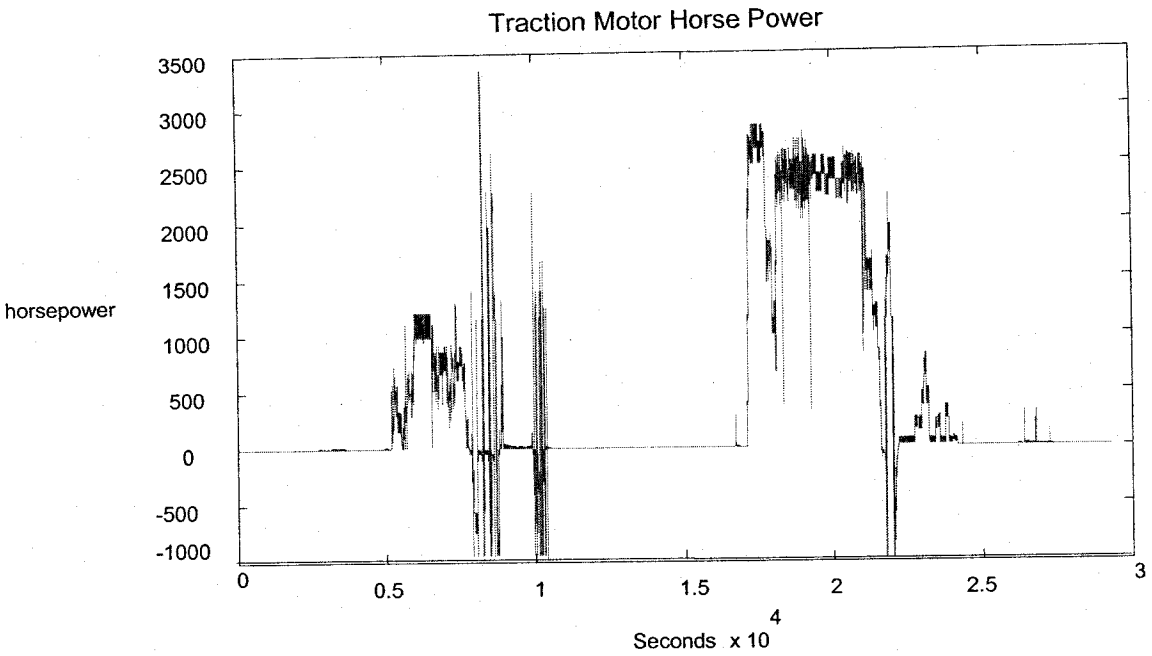


Figure 3-23. Duty cycle of pusher locomotive

The battery size for the pusher application was chosen based on the amount of energy recovery available during a typical operation of the pusher. From data supplied by Norfolk Southern [23] a battery capable of absorbing 750 kWh of energy would be able acceptable for 95% of the possible regenerative cycles. If this energy is dissipated over the typical pushing time of one hour would give an average dissipation of 750 kW. Using the typical pushing run is operated at 3000 Hp (2.25 MW), the fuel cell would need to supply 1.5 MW of power.

To implement the 1.5 MW fuel cell, it was decided to use 6 – 250 kW cells switching them in and out depending on the specific command setting. This would allow for each fuel cell to operate at closer to its highest efficiency point. It would also allow for more redundancy in the system.

Investigation of the pusher is still ongoing. Analysis and computer simulation of the system is needed to verify the proposed operation.

*Long-haul* The long-haul locomotive is used to run long trains over large distances. Often several of these locomotives operate in tandem on a single train. They generally need to supply high power for long periods of time. Because stops are rare and recovery of the stored energy would be difficult, the ASUs are limited to storing only the energy required for initial startup. Thus the majority of power is developed is supplied from the fuel cell.

Current long-haul locomotives have power capabilities in the range of a few megawatts. Thus the system was proposed to have a power level capability of 2 MW. The system would consist of 8 - 250 kW fuel cells. The fuel cells would be switched in and out the system depending on power demand, and allowing them to operate at close to their optimal efficiency, where a typical arrangement for a system is shown in figure 3-24.

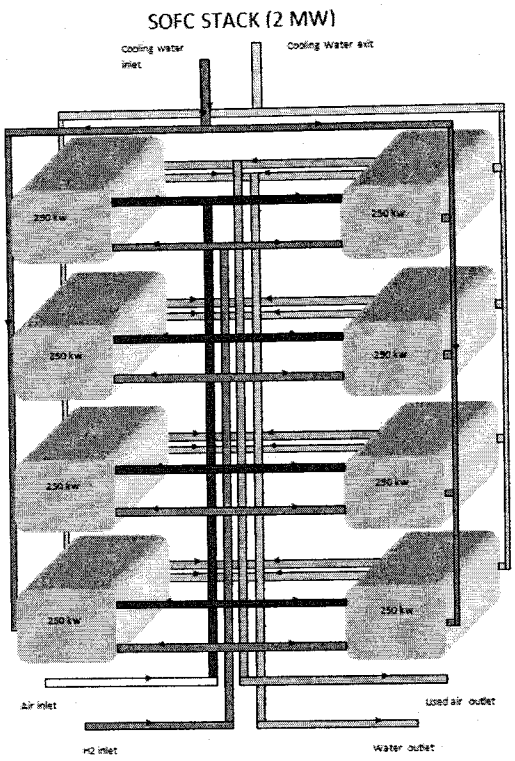


Figure 3-24. Possible for fuel cell arrangement in long haul locomotive.

Investigation of the use of fuel cells in the long haul locomotive is still continuing. Investigation of the power density of available fuel cells is being investigated for appropriateness in this application. Also a control strategy to optimize to power delivered between the various fuel cells is being considered.

Market analysis of fuel cell availability

The most attractive fuel cell for locomotive applications is the SOFC. This is based on its high performance, compactness, ability to use different fuel types, and potential integration with existing locomotive components. Some of the major factors that make the high temperature SOFC more attractive compared to other high temperature fuel cell such as molten-carbonate fuel cells (MCFC) and low temperature fuel cell such as proton exchange membrane (PEM) can be summarized below:

Attractive features of SOFC over PEM:

- Flexible in fuel types: hydrogen, hydrocarbons such as diesel, biodiesel, clean coal gas
- More tolerant to the presence of impurities in the reactant gases
- No use of expensive metal catalyst
- High temperature operation
  - Better system match with other components and systems
  - Provides high quality waste heat for cogeneration

- Lower activation losses and better system match results in higher overall conversion efficiencies
- Simpler fuel processing process
- Allows internal reforming of hydrocarbon fuels to produce hydrogen and carbon monoxide, which acts as a fuel.

Attractive features of SOFC over MCFC:

- All solid components makes it compact
- No electrolyte depletion and corrosion of FC components by liquid
- Higher operating current and power density.

For the system to be reasonable fuel cells in the power range required for this application need to be currently available or obtainable in the near future. A list of major manufacturers of high temperature fuel cell is given below:

- Fuel Cell Energy: SOFC 30 KW under development
- Acumentrics Corp: SOFC, 10 KW (2003)
- Ceramic Fuel cells: SOFC, 200 KW (2003)
- Delphi Tech.: SOFC, 25 KW demonstrated (2003), 12.5 MW (5 * 500KW) under development, Reforming technology, APU
- Fuel Cell Technology: SPFC, 50 kW (2003)
- General Electric (with Plug Power): SOFC, 10 KW (2003)
- Global Thermoelectric: SOFC, 10 MW power plants
- Rolls-Royce Group: SOFC, 1 MW (expected by 2007), $1000/kW (expected by 2009)
- Siemens Westinghouse: SOFC, 100 kW (tested in 2003), 20 kW SOFC/gas turbine system tested (2003), 500-750 kW planned, 2-3 MW SOFC/gas turbine system planned.
- ZTEK Corp: SPFC, 200 kW.

Most of the manufacturers are in the process of developing and /or demonstrating their unit at the high power range. A higher power range unit such 1MW is developed based on assembling four smaller units such 250 KW and with a common supply line for air and fuel delivery system. SOFC fuel cell systems with a power level of 1-2 MW are expected to be in the market in near future. Therefore, fuels cells with the required power capacity would be available for use in a locomotive in the near future.

When analyzing the fuel cell availability, consideration of the fuel used needs to be made. One important factor in determining a fuel is the energy storage requirements of a typical locomotive. As a quick assessment of energy storage requirements, compressed hydrogen can be compared to current diesel engines. The energy content of hydrogen under high pressure (700 bar) is about 5.6 MJ/l compared to 38.6 MJ/l for diesel. Assuming a 35% efficient diesel engine and a 50% efficient fuel cell system, the volume of hydrogen would need to be 4.83 times that of diesel. As a typical long haul locomotive has a 5000 gallon fuel tank, this would expand to 24,000 gallons

of compressed hydrogen. This increase in storage volume is a significant argument for not using hydrogen to power the locomotive.

From the above analysis SOFC using diesel as the fuel was favored by this project. As one of the goals of the project was to reduce the needs for fossil fuel sources, biodiesel was investigated as a fuel for the locomotive.

Although biodiesel can be used as a fuel in a SOFC, it needs to be gasified before being supplied to the fuel cell. The gasification process separated the hydrogen from the fuel and in the process several other compounds are formed. To determine the feasibility of this gasification, calculations were done to approximate:

1) the relative concentrations of CO and $H_2$ that will be produced when gasifying soy-based biodiesel
2) the energy consumed by the gasification process
3) the amount of energy that must be provided to drive the endothermic steam gasification reaction

Steam gasification has been selected for an input into the fuel cell simulation primarily because it is expected that sufficient waste heat will be available to produce high temperature steam and because it will minimize energy lost to the gasification process. It will be assumed that the gasification reaction will proceed to completion. The steam gasification process is assumed to start with soy biodiesel (soy methyl ester) and goes through several chemical reactions [24]. The net reaction and energy requirement is found to be

$$C_{10}H_{19}0+11.6H_2O \rightarrow 7.40CO+21.1H_2+2.60CO_2 \quad \Delta G^o = 1.52\frac{MJ}{mol} - T\cdot 8.55\frac{kJ}{mol\cdot K} \quad (3\text{-}23)$$

Steam gasification then will be thermodynamically favorable at temperatures over 178K and will require 1.52 MJ/mol, or 9.81MJ/kg, of heat to proceed. Obviously, the reactions required for steam gasification will not proceed with reasonable rates at temperatures near room temperature. For the remaining calculations 800°C (1073K) will be assumed for the gasification temperature. Each mole of biodiesel will then produce 7.40 moles of CO, 21.1 moles of $H_2$, and 2.6 moles of $CO_2$.

While a large number of subsequent reactions may take place, only the water gas shift (WGS) reaction will be considered:

$$CO+H_2O \rightarrow CO_2+H_2 \qquad \Delta G^o = -41.1\frac{kJ}{mol} - T\cdot 42\frac{J}{mol\cdot K} \quad (3\text{-}24)$$

and using, $\Delta G^o = -RT\ln\frac{[pCO_2][pH_2]}{[pCO][pH_2O]}$ (3-25)

where the concentrations of the reactants and products are constrained by the output of the steam reforming reaction (3-24) and the amount of additional steam added beyond that required to drive reaction (3-24).

Coke formation is almost certain to also occur to some extent. In general the amount that forms will be related to gasifier design as well as the use of partial combustion and concentration of excess steam. For purposes of the present project coke formation will be ignored and the input to the fuel cell will be assumed to be $H_2$, $CO_2$, $H_2O$, and CO. The amount of each will depend on the extent to which excess steam is added to the gasifier. The number of moles of each component produced from one mole of biodiesel as a function of excess steam beyond the 11.6 moles required for the steam gasification reaction is shown in figure 3-25. Since the WGS is exothermic, this will reduce somewhat the required heat input to drive the steam gasification reaction.

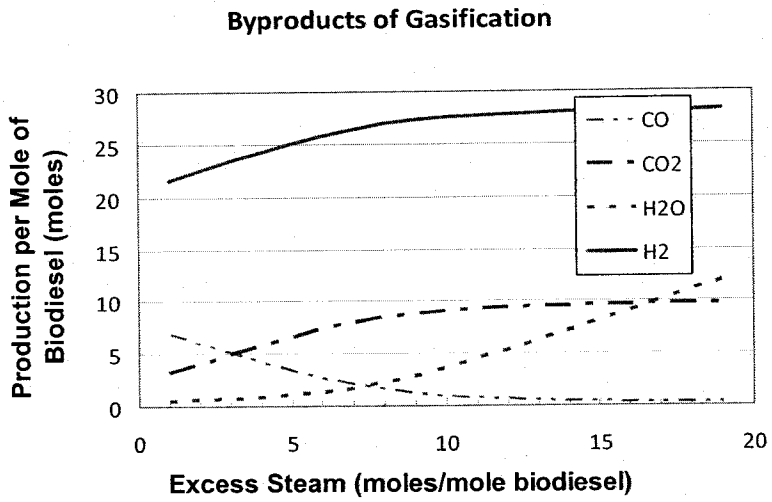


Figure 3-25. Relation of gasifier products to excess steam

In considering biodiesel as the fuel, impurities in the available supply must further be investigated. Most of the biodiesel available in the United States is soy based and contains a significant quantity of phosphorous. During the gasification process, the phosphorous will produce a small amount of phosphorus trihydride ($PH_3$) is produced. The effects of this chemical on the fuel cell needs further investigation.

Ergonomic concerns and safety issues

There are very few ergonomic concerns related to the use of fuel cells in a locomotive. Thoughtful design would make the operation and maintenance of the fuel cell straightforward. The locomotive controls could be made similar to systems currently available. The major ergonomic concern would be the safety of personnel around the fuel cell. The important safety issues that were considered were the storage and use of the biodiesel, the fuel gasification, and the use of hydrogen.

*Biodiesel Safety:* Biodiesel has a flash point of over 266 $^0$F [25], meaning it cannot form a combustible mixture until it is heated well above the boiling point of water. It is rare that fuel is subjected to these types of conditions, making biodiesel significantly safer to store, handle, and transport than petroleum diesel. The National Fire Protection Association classifies biodiesel as a non-flammable liquid.

Being derived from vegetable oils, biodiesel is naturally non-toxic. The acute oral LD50 (lethal dose) of biodiesel is more than 17.4 g/Kg. In both soil and water, biodiesel degraded at a rate 4 times faster than regular diesel fuel, with nearly 80% of the carbon in the fuel being readily converted by soil and water borne organisms in as little as 28 day [26]. To safely use biodiesel a safety program needs to be implemented. a biodiesel safety program consists of the following components:

1. Management Commitment
2. Receiving and storage
3. Material handling
4. Employee training
5. Maintenance procedures
6. Spill response
7. Incident response
8. Combustion Procedures

*Management commitment*: The management needs to develop a commitment to developing a safety culture within the organization. An organization's safety culture can be observed in the beliefs and behaviors of its staff members regarding the importance of eliminating or minimizing workplace hazards. An organization's safety goals should be clearly communicated and understood by all staff. Everyone should be focused on doing their jobs safely and avoiding accidents and injuries. If a safety issue is raised by a staff member, it should be addressed in a timely manner. A "management and labor" safety committee will be established to facilitate the communication. Safety improvements should be implemented as needed and communicated to the entire organization. All safety related information should be maintained and should be made available to employees. Additionally, a mechanism should be in place for ownership and responsibility of safety related reports that are generated (for example, a "keeper of documents").

*Receiving, storage, and handling*: Safe operating procedures need to be developed for receiving, storage, and handling of biodiesel. Such procedures are detailed in the section on refueling issues below.

*Employee training*: The employees must understand their role and responsibilities in handling biodiesel compounds. They must be aware of all safety and health hazards. At a minimum, all employees will be trained in:

- SOPs, including proper PPE
- Proper inspection, use, storage, repair, and disposal of PPE
- Hazard Communication
- Bloodborne pathogens

- Lockout/Tagout awareness
- Confined Space awareness
- Fire extinguishers
- Spill response awareness

*Maintenance procedures:* The integrity of the system will be maintained by a preventative maintenance system. The key components of the system will be maintained in accordance with manufactures recommendations. Records will be maintained and the periodicity of the maintenance procedures will be adjusted relative to operational history. Before working on or in tanks that contain or have contained biodiesel fuel, all work procedures should be verified relative to the OSHA regulations, ANSI Z49.1 and other references pertaining to cleaning, repairing, welding, or other operations. Empty containers retain residue and may be dangerous. Do not pressurize, cut, weld, braze, solder, drill, grind, or expose such containers to heat, flame, sparks, or other sources of ignition. They may explode and cause injury or death. Empty drums should be completely drained, properly bunged, and promptly shipped to the supplier or a drum reconditioner. All containers should be disposed of in an environmentally safe manner and in accordance with governmental regulations. In addition to the general employee training, the maintenance personal will receive additional training in:

- Lockout/Tagout Authorized Workers, including machine or instrument specific procedures
- Confined space entry
- Hot work and the permitting system
- Line breaking and the permitting system
- Maintenance documentation
- Spill response
- Safe electrical work practices
- Arc flash protection.

*Spill Response*: Spill procedures include:

- Take proper precautions to ensure your own health and safety before attempting spill control or clean-up.
- Take precautions for a combustible Liquid. Release can result in a fire hazard.
- Evacuate all non-essential personnel from release area.
- Establish a regulated zone with site control and security.
- Eliminate all ignition sources.
- Stop the leak if it can done without risk.
- A vapor-suppressing foam may be used to reduce vapors.
- Properly bond or ground all equipment used when handling this material. Avoid skin contact. Do not walk through spilled material.
- Verify that responders are properly trained and wearing appropriate personnel protective equipment.
- Dike far ahead of a liquid spills. Do not allow released material to entry waterways, sewers, basements, or confined areas. This material will float on water.

- Absorb or cover with dry earth, sand or other non-combustible material. Use clean, non-sparking tools to collect absorbed material.
- Place spent sorbent materials, free liquids and other clean-up debris into proper waste containers for appropriate disposal. Certain releases must be reported to the National Response Center (800/424-8802) and state or regulatory authorities.
- Comply with all laws and regulations.

*Incident Response*: All incidents (injury, illness, spill, leak, property damage, near misses) will be investigated. The investigation team will consist of an "operator", supervisor, and a subject matter expert, as a minimum. The investigation will be formalized in a written report. The report will be submitted to the plant safety committee and management for review. SOPs and training requirements will be reviewed and modified as necessary.

*Combustion Procedures*: The combustion of diesel fuels generates thermal decomposition products that exhibited toxicity greater than the parent compound. Therefore, the following procedures will be followed:

- Ensure proper ventilation in garages, fueling, idling, maintenance, or other enclosed areas to reduce exposures to diesel exhaust. For example, use exhaust extractor hose attachments on the exhaust pipes of vehicles that must idle for long periods of time in indoor work areas such as vehicle maintenance shops.
- Provide regular maintenance and frequent tune-ups to all diesel equipment.
- Assign workers to check exhaust systems for leaks.
- Retrofit vehicles with the best available technologies for emissions control.
- Keep workers as far away as possible from areas containing diesel exhaust to limit exposure of workers not directly involved in operating or maintaining diesel-powered vehicles.
- Do not allow workers to run diesel engines near the air intake of building ventilation systems.

Overall, biodiesel, when compared to petrodiesel, will be safer to handle based on reduced toxicity and flammability, as well as increased biodegradability. There are several safety issues associated with the gasification process. The temperatures and pressures associated with the reactor process poses physical hazards. The high temperature method, operates at temperatures that range from 700 to 1100 $^{O}$C.[27]

From the above analysis the resulting exhaust from a biodiesel system would mostly consist of water and carbon dioxide. Short-term exposure to $CO_2$ at levels below 2% (20,000 parts per million or ppm) has not been reported to cause harmful effects. Higher concentrations can affect respiratory function and cause excitation followed by depression of the central nervous system. High concentrations of $CO_2$ can displace oxygen in the air, resulting in lower oxygen concentrations for breathing. Carbon dioxide is also considered a "green-house" gas [28].

Although the resultant exhaust would consist of carbon dioxide and water, the intermediate chemical reaction produces a toxic and flammable gas, carbon monoxide, as well as a flammable gas, hydrogen. Carbon monoxide has a density comparable to air and does not readily diffuse

and reduce the concentration. It has a wide flammable range 12.5 to 74 percent by volume with an autoignition temperature of 630 $^{O}$C [29].

Carbon monoxide is a chemical asphyxiant that exerts its toxic effects by combining with the hemoglobin of the blood, which decreases the amount of oxygen delivered to the tissues [30]. The affinity of hemoglobin for carbon monoxide is 200-300 times greater than its affinity for oxygen. All the disorders are due to the markedly reduced cellular respiration and may include central nervous system impairment, cardiovascular collapse, renal insufficiency, and coma [31]. Exposures to carbon monoxide become immediately dangerous to life and health at 1,200 parts per million (ppm) [32]. As the analysis above has shown the relative amount of carbon monoxide is small, the danger associated with these risks is small.

*Hydrogen Safety:* Hydrogen gas mixes well with air. Therefore, explosive mixtures are easily formed. Hydrogen has a wide flammable range 4.0 to 74.5 percent by volume with an autoignition temperature of 570 $^{O}$C [15]. Metal catalysts, such as platinum and nickel, greatly enhance the potential for fire or explosion. Hydrogen has a vapor density significantly lighter than air (0.07 relative to air at 1.0) and diffuses quickly thereby readily reducing the concentration [33].

Hydrogen can be absorbed into the body by inhalation. High concentrations of this gas can cause an oxygen-deficient environment. Individuals breathing such an atmosphere may experience symptoms which include headaches, ringing in ears, dizziness, drowsiness, unconsciousness, nausea, vomiting and depression of all the senses. The skin of a victim may have a blue color. Under some circumstances, death may occur. Hydrogen is not expected to cause mutagenicity, embryo- toxicity, teratogenicity or reproductive toxicity. Pre-existing respiratory conditions may be aggravated by overexposure to hydrogen [34].

Exposure to hydrogen also results in the embrittlement of metals. Embrittlement is enabled by the ability of hydrogen molecules to dissociate into hydrogen atoms on metal surfaces, which then diffuse into the metal making it more susceptible to cracking [35].

A process safety program for handling of hydrogen would start with a management commitment similar to the biodiesel safety program. Management needs commitment to safety including proper education of workers, development of safe procedure that follows safety regulations and guidelines. Proper records should be kept that include standard operating procedure, maintenance plans and maintenance logs. Some specific concerns related to hydrogen are given below.

*Fire Protection and Suppression:* Normally hydrogen fires are not extinguished until the supply of hydrogen has been shut off due to the danger of re-ignition and explosion. Personnel who work around hydrogen should be trained in the characteristics of hydrogen fires and proper procedures for dealing with them.

- A hydrogen fire is often difficult to detect without a thermal imaging camera or flame detector.

- Let a gaseous hydrogen fire burn. Cool adjacent equipment with a water spray. Be careful not to spray pressure-relief devices, since ice formation could make them inoperable.

*Protection from Exposure to Fire:* Hydrogen fires can damage objects in the vicinity through heat radiation and convection. Water spray or mist should be used to attenuate radiant heat from a hydrogen flame. Since hydrogen is colorless, odorless, burns with a nearly invisible flame (especially during daylight hours), and gives off relatively little radiant heat, a hydrogen fire is often difficult to detect. Thermal imaging cameras and flame detectors should be used to verify that a hydrogen flame is present. If these tools are not available, personnel should cautiously approach a suspected leak and watch for thermal waves that signal the presence of a flame, and put flammable objects or dust particles into the flame to emit in the visible spectrum. Although hydrogen fires do not produce smoke themselves, burning of nearby combustible materials can result in smoke. Thus, personnel should be aware that smoke inhalation can be a danger in a hydrogen fire.

*Gaseous Hydrogen Fires* Best practices for dealing with a gaseous hydrogen fire include:

- Do not extinguish the fire until the hydrogen supply has been shut off, as unburned gaseous hydrogen can result in an explosion. Spray water on adjacent equipment to cool it.
- Do not try to put out a hydrogen cylinder fire unless the cylinder is out in the open or in a well-ventilated area free of combustibles and ignition sources.
- Do not attempt to remove a burning cylinder. Keep it and surrounding cylinders cool by spraying with water.
- If multiple cylinders are burning, fight the fire from as great a distance as possible to protect against the possibility of flying debris.

*Warning Placards* All areas where hydrogen is stored or used should contain a permanent placard stating:

**WARNING: HYDROGEN - FLAMMABLE GAS - NO SMOKING - NO OPEN FLAMES**

*Impact of Hydrogen Properties on Facility Design* An understanding of the properties of hydrogen is critical for the proper design of a facility or workspace. A workspace can be configured to mitigate hazards by understanding and taking advantage of some of the characteristics of hydrogen. Designers and operators of hydrogen storage facilities must be aware that hydrogen's flammability range is very wide compared to other fuels. Additionally, under optimal combustion conditions (at a 29% hydrogen-to-air volume ratio), the energy required to initiate hydrogen combustion is much lower than that required for other common fuels (e.g., a small spark).

For any incident involving hydrogen, it is important to consider the properties of hydrogen and watch for potential ignition sources that can ignite a hydrogen leak, for example,

- Electrical (e.g., static electricity, electric spark from operating equipment)
- Mechanical (e.g., impact, friction)
- Thermal (e.g., open flame, hot surfaces, vehicle exhaust)

*Passive Ventilation:* Proper ventilation will reduce the likelihood of a flammable mixture of hydrogen forming in an enclosure, following a release or leak. Hydrogen is unlike other fuels such as gasoline vapors or propane, which are heavier than air and tend to accumulate at ground level. Hydrogen is lighter (less dense) than air and will accumulate near the ceiling, roof area, or in pockets at these locations.

When the buoyancy of hydrogen is not properly taken into account in the design of facilities, hydrogen leaks can become more dangerous than leaks or spills of conventional fuels such as gasoline, LPG and propane. The building codes require storage and maintenance facilities to have ventilation openings near the ground to remove gasoline vapor, but ventilation high in the workspace is not always addressed. As a result, even slow releases of hydrogen in such buildings could lead to the formation of a flammable concentration at the ceiling.

Passive ventilation features such as roof or eave vents can prevent the buildup of hydrogen in the event of a leak or discharge. Outdoor installations offer the best passive ventilation. In designing passive ventilation, ceiling and roof configurations should be thoroughly evaluated to ensure that a hydrogen leak will be able to dissipate safely. For example, NFPA 55 (paragraph 10.4.2.22) requires 2 $ft^2$ of wall/roof opening per 1000 $ft^3$ of room volume.

*Active Ventilation:* Active (mechanical) ventilation can be used to prevent the accumulation of flammable mixtures, if passive ventilation is insufficient. Active ventilation can ensure sufficient vent flow to maintain the concentration of hydrogen below the lower flammable limit (establishing a vent flow to ensure concentration is less than 25% LFL = 1% hydrogen gas by volume). For example, NFPA 52 (paragraph 9.3.3.5.5) requires a minimum of 1 $ft^3$ per minute per $ft^2$ of room area and at least 1 $ft^3$ per minute per 12 $ft^3$ of room volume for proper hydrogen ventilation. However, no practical ventilation rate can effectively disperse hydrogen from a massive release from a pressurized vessel, pipe rupture, or blowdown. Active ventilation may be required when the configuration of the room may cause hydrogen to accumulate in the ceiling or roof area. Hydrogen accumulation may be a problem, for example, in rooms with a peaked roof or in rooms with dropped or false ceilings. Equipment used in forced ventilation systems (fan motors, actuators for vents and valves, etc.) should have the applicable electrical classification (class, division, group, and operating temperature) and should be approved for hydrogen use. Systems that recirculate air will be avoided. If active ventilation systems are relied upon to mitigate gas accumulation hazards, procedures and operational practices should ensure that the system is operational at all times when hydrogen is present or could be accidentally released. Hydrogen equipment and systems should be shut down if there is an outage or loss of the ventilation system. If the hazard is substantial, an automatic shutdown feature may be appropriate.

*Selection of Materials:* Materials of construction, including materials used in valves and seals, must be carefully selected to account for their deterioration when exposed to hydrogen at the intended operating conditions. The mechanical properties of metals, including steels, titanium

and titanium alloys, and nickel and nickel alloys are detrimentally affected by hydrogen. Exposure of metals to hydrogen can lead to embrittlement, cracking and/or significant losses in tensile strength, ductility, and fracture toughness. This can result in premature failure of load-carrying components. Additionally, hydrogen diffuses through many materials, particularly nonmetals, due to its small molecular size.

*System purging:* Inert gas subsystems are used to provide purge and pressurization gases, to ensure that all hydrogen-containing volumes are capable of being purged, and to ensure that purge gas is vented. The inert gas subsystem is protected from hydrogen contamination by maintaining the subsystem at higher pressure and using check valves and/or a double block and bleed arrangement.

There are three general approaches to purging a system:

- Flowing gas purge: An inert gas, typically nitrogen or helium, flows into one part of the system and out of another part of the system. Considerations include the volume to be purged, gas flow rate, regions of poor flow (voids or dead ends), and the duration of the purge. Rapid or turbulent flow such that all parts of the system are thoroughly purged is desired. Depending on the flow path geometry of the volume to be purged, this technique may be least likely to ensure a positively purged system.
- Pressurizing-venting cycle purge: Alternate pressurizing and venting is used to successively dilute the contents of a volume until the desired mixture concentration is obtained. A greater internal pressure is maintained during venting to prevent the backflow of air. Analysis of residual gas, by measurement or calculation, is necessary to determine the completeness of the purge. This approach may require greater use of purge gas resources that other approaches.
- Vacuum purging: The system is vented to atmospheric pressure, then pumped to a relatively low pressure (pump limits are typically 1.3 kPa (10 torr) for a mechanical pump), re-pressurized with the desired gas to a positive pressure, and then vented to atmospheric pressure. The system being pumped must be capable of maintaining structural integrity (not collapsing) and preventing in leakage during pumping.

One of the advantages of using fuel cell over hydrogen is that refueling issues become less of a problem. The handling of diesel fuels has been conducted safely for years. As bio-diesel has a lower volatility than diesel, refueling would have less stringent requirements.

The storage tanks should be enclosed by a secondary containment constructed in accordance to local building codes. The containment should have an automated leak detection system. The containment should also be equipped with a fire suppression system approved by the State Fire Marshall. The tanks and/or the containment should be placarded in accordance with the National Fire Protection Association. The proper placard for biodiesel (B-100) includes a zero health hazard, a minimal, or 1, fire hazard, and a zero reactivity hazard. A biodiesel/diesel blend would have a similar placard with the exception of a 2 for a flammability rating. All unloading couplings should be proper labeled. The coupling should have secondary containment in the event of a spill, release, overflow, etc. All connections should be verified before unloading any

vehicle to ensure that the material is received into the proper tank(s). Prior to unloading, the vehicle drivers should complete a site specific training course, including emergency procedures. At a minimum, the training should include:

- Emergency notifications
- Site Alarms
- Site fire suppression systems
- Spill procedures
- Contamination (personnel and site) procedures
- Evacuation routes
- Roles and responsibilities

The vehicle driver should be required to stay in the area to observe the unloading process so that immediate action can be taken in the event of a spill or leak. The unloading process should be audited to ensure that the proper procedures are being followed.

Standard operating procedures (SOP) will be developed, in writing, for all operations. The employees will participate in the development of the procedures. The SOPs will be reviewed annually, and revised as necessary. Safety information will be conducted as follows,

- The biodiesel fuel should be maintained in a closed system.
- All piping should be conspicuously labeled.
- All secondary or day tanks should be placarded identically to the storage tanks.
- The fuel system should be grounded to prevent the buildup of a static electrical charge, and the grounding system should undergo a periodic integrity program. NFPA-704 and/or American Petroleum Institute (API) RP 2003 should be consulted for the specific bonding/grounding requirements.
- Use good personal hygiene practices before eating, drinking, smoking, or applying cosmetics.
- High pressure injection of hydrocarbon fuels, hydraulic oils or greases under the skin may have serious consequences even though no symptoms or injury may be apparent. This can happen accidentally when using high pressure equipment such as high pressure grease guns, fuel injection apparatus or from pinhole leaks in tubing or high pressure hydraulic oil equipment.
- When making connections, dispensing, or handing open containers, the proper personnel protective equipment (PPE) should be worn. A NIOSH certified air purifying respirator with an organic vapor cartridge maybe used under conditions where airborne concentrations are expected to exceed exposure limits. Protection provided by air purifying respirators is limited (see manufacturer's respirator selection guide). A positive pressure air supplied respirator should be used if there is a potential for an uncontrolled release, exposure levels are not known, or any other circumstances where air purifying respirators may not provide adequate protection. A respiratory protection program that meets OSHA's 29 CFR 1910.134 and ANSI Z88.2 requirements must be followed whenever workplace conditions warrant a respirator's use.

- The use of impervious gloves impervious will be worn to prevent skin contact; possible irritation and skin damage (see glove manufacturer literature for information on permeability). Typical impervious materials include nitrile rubber or viton.
- Depending on conditions of use, apron and/or arm covers may be necessary. Impervious clothing must be worn when skin contact is possible.
- Approved eye protection to safeguard against potential eye contact, irritation, or injury is required. Depending on conditions of use, a face shield may be necessary.
- Eye wash and quick-drench shower facilities should be available in the work area.
- Personnel should not wear contaminated clothing or shoes. Contaminated clothing needs to be kept away from sources of ignition such as sparks or open flames.

A Norfolk Southern map of the refueling station would not need to vary from the of petrol diesel fueling stations. For switcher and pusher applications, the locomotive would return to the originating yard so the location of refueling is fixed. Long haul locomotive could be designed to have a range compatible to current locomotives. Thus there would be little need for modification to the refueling map.

Development of an off-line power management system
A general form of the power system to operate the locomotive is shown in figure. DEVa. This diagram includes the fuel cell as the overall energy source and various auxiliary storage units (ASU) that can be employed for transient conditions in the various types of locomotives. It is proposed that these devices be connected to a common bus through electronic converters. The specific implementation of this power system would depend on the type of locomotive being considered.

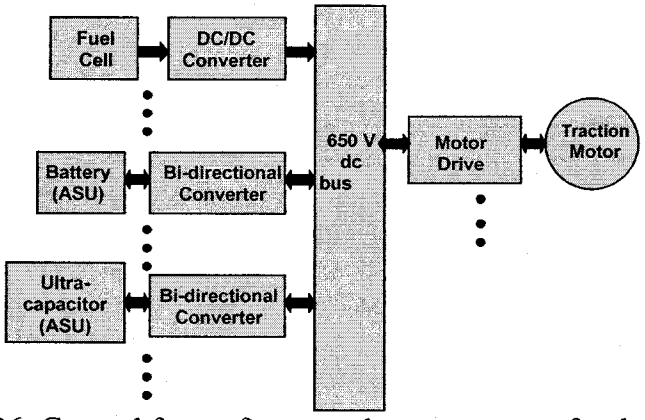

Figure 3-26. General form of proposed power system for the fuel cell.

*Switcher*
Based on the severity of the power requirements of the switcher locomotive, it was determined that the power system would require batteries as well as ultra-capacitors to be used as ASUs. The DC bus is assumed to be at 648V. The voltages at the sources fluctuate depending on the current demand they have to supply. Each source is connected to the bus via a converter in order to filter the voltage fluctuations to some extent. Power flow for the battery and ultra-capacitors is bidirectional. So bidirectional converters are appropriate for these sources. The converters are assumed to be operating at 90% efficiency. They are modeled just to estimate the power demand

for the sources at their terminals. The model for these converters, done in Simulink, distinguished between discharging and charging modes. The expressions used during discharging is

$$\eta = \frac{P_{out}}{P_{in}} = \frac{V_{bus} * I_{bus}}{V_{bat} * I_{bat}} \tag{3-26}$$

Where $V_{bus}$ = 648V and $I_{bus}$ is the current demand at that instant. The current demand at the terminals of the battery is estimated by using above expression assuming the converter efficiency to be 90%. Therefore, the expression for battery current is

$$I_{bat} = \frac{648 * I_{bus}}{0.9 * V_{bat}} \tag{3-27}$$

The expressions used during discharging is

$$\eta = \frac{P_{out}}{P_{in}} = \frac{V_{bat} * I_{bat}}{V_{bus} * I_{bus}} \tag{3-28}$$

Where $V_{bus}$ = 648V and $I_{bus}$ is the current supplied to battery for charging. Current that used to charge battery can be calculated from the above expression as.

$$I_{bat} = \frac{0.9 * 648 * I_{bus}}{V_{bat}} \tag{3-29}$$

Converters used for fuel cell is a single directional converter. As power flows only out of the fuel cell it has only discharging cycle. The expression for estimating the current demand at terminals of fuel cell is.

$$\eta = \frac{P_{out}}{P_{in}} = \frac{V_{bus} * I_{bus}}{V_{fc} * I_{fc}} \tag{3-30}$$

Where $V_{bus}$ = 648V and $I_{bus}$ is the current demand at the bus. Efficiency of fuel cell is assumed to be 90%. Current demand at terminals of fuel cell is.

$$I_{fc} = \frac{648 * I_{bus}}{0.9 * V_{fc}} \tag{3-31}$$

Losses in system increase when converters are employed. To compensate for these losses the average power supplied by the fuel cell has to be increased. So the average current that the fuel cell has to supply is increased by 50A. Voltage waveforms at input terminals of the converters at power sources (i.e. battery, ultra capacitor and fuel cell) are shown in figure 3-27. This simulation calculated these voltages assuming the system met the power demand given in figure

3-18. From the simulation it is observed that the voltages are able to be maintained at a reasonable level indicating the system would function properly under the given power demand.

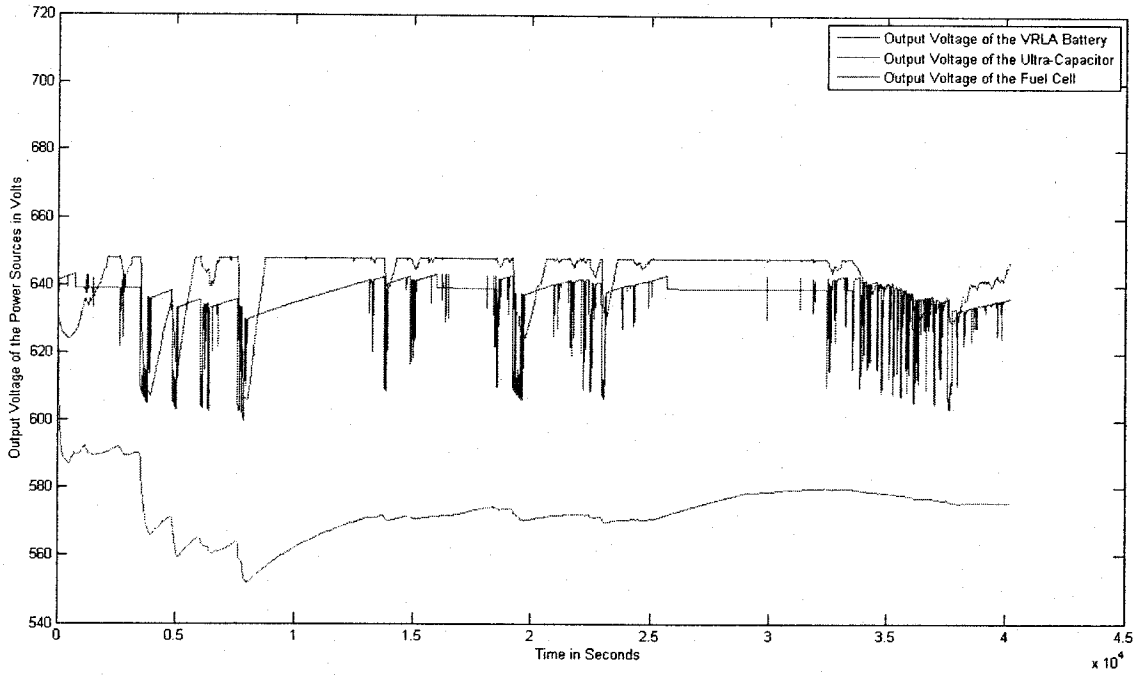


Figure 3-27. Output Voltage of Power sources at the input terminal of converters.

*Pusher*

The power system for the pusher would be of a similar form as the switcher. As the power transients are not as large, however, it would not need ultra-capacitors. The fuel cell would supply the power needed throughout the normal operation, and would be supplemented with batteries during an uphill push.

*Long Haul*

The long haul power system would basically consist of several fuel cascaded together to obtain the desired power ratings. Battery power would be limited to what is needed to restart the fuel cells. Control would consist of turning the various fuel cells on as the power demand is increased. When running each fuel cell would be operated as near to its peak efficiency point as possible.

Section Conclusion

Fuel cell systems can be designed that are capable of supplying power to a locomotive. Auxiliary power units are required to handle the dynamic power changes in some applications such as the switcher. By using a solid oxide fuel cell with biodiesel fuel, safety and refueling issues are minimizes and can be accommodated by standard safety procedures. Maps of refueling station would be the same as what is currently available. Power systems can be implemented to use fuel cells in switcher, pusher, and long haul applications. Simulations of the switcher application indicate the power system is capable of supplying a typical switcher duty cycle.

**Task 4 - Thermal and emission reduction for current large scale diesel engines**

According to a recent study conducted by the U.S. Environmental Protection Agency (EPA), locomotive diesel engines contribute significantly to air pollution in many of our nation's cities and towns. Since control plans for on-road vehicle emissions have been put into effect, locomotives could become the primary source for dangerous air pollution in the country. In addition to the requirement of reduced greenhouse gases such as carbon dioxide, the individual air pollutants to eliminate are particulate matter (PM), hydrocarbons (HC), and the oxides of nitrogen (NOx). Many studies are focused on achieving cleaner emissions and improved performance of diesel engines through use of alternative fuels, specifically biodiesel and improved thermal management of exhaust heat and cooling of the engine. The study of biodiesel is relatively new, particularly the study of how biodiesel can have an effect on the emissions of large scale diesel engines. Understanding all the above through experimental and computational analysis may help to identify concepts to be incorporated into the operation of every day diesel engines.

The primary goal of this research is to understand how various changes in diesel engine operating conditions can change emissions and thermal efficiency and to be able to successful predict these changes through computational fluid dynamics modeling including combustion modeling. The work will specifically address how the operating systems design for large thermal loads effects the emission factors for diesel emission components such as, greenhouse gases like carbon dioxide, carbon monoxide, oxides of nitrogen, hydrocarbons, and particulate matter. Developing related experimental and computational analysis will identify several concepts that may be incorporated into innovative design and operation of diesel locomotives. In order to meet the targeted objectives and goal, experimental and computational simulation analysis of the diesel engine and diesel engine system will be performed. A simulation model for the combustion process and heat transfer performance of the diesel engine was developed. The results for emission compositions and thermal load will be analyzed and compared with the experimental data.

Experimental evaluation of diesel engine emission, thermal load, and cooling
Engine testing will allow monitoring of the engine's performance and complete emissions composition analysis under different types of fuels and operating parameters. During the test phase, all major variables will be analyzed for a range of operating conditions using different fuel compositions. The pressure ratio, stoichiometric air flow rates, variable temperatures, cooling media, fuel consumption, and more will be incorporated into the emission analysis study.

Experimental Test Facility for diesel engine emission test
A small scale test facility is fabricated to evaluate the diesel engine thermal load, emissions, and performance of the engine. This experimental test facility will be used to evaluate the engine emission and thermal load of the engine with varying operating conditions, evaluate number of fuels including regular diesel and bio-diesel. A schematic of the test setup is shown in Figure 4-1.

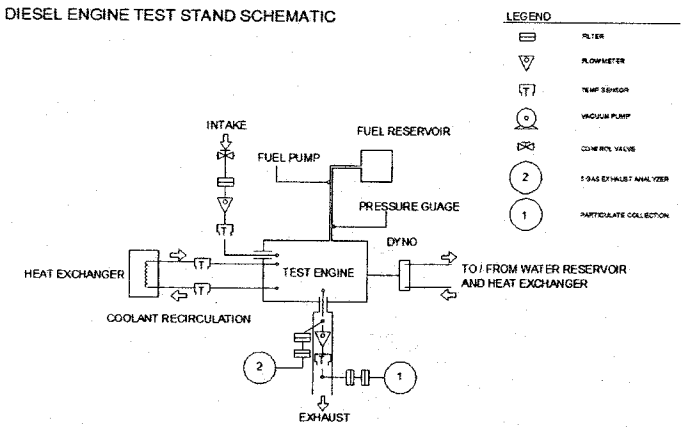


Figure 4-1 - Diesel engine test stand

The test facility is equipped with Briggs and Stratton 18HP 3-Cylinder liquid cooled engine, a dynamometer and a number of temperature and pressure sensors, gas flow meters, gas flow analyzer and a computer data acquisition system. To begin to understand the effects of different fuels on a large scale diesel engine, a smaller scale diesel engine is acquired, tested, and understood. The research methodology should be proven at the small scale level before attempting on a large diesel locomotive. To conduct engine experiments with accurate results, a load must be placed on the engine. A dynamometer will be used to create the load on the engine. The dynamometer is a water-brake style loading mechanism that reacts against the rotation of the flywheel (Land and Sea). An impeller is rotated by water flowing against the natural rotation of the flywheel, thus creating the load on the engine. Furthermore, it also monitors the torque and horsepower, and allows the load to vary as needed. The load can be adjusted for different engine speeds, because the engine will need to be tested for all similar situations to the diesel locomotive. To adapt the dynamometer to the engine, an input shaft is machined to a 3 and 4 degree taper. The taper is needed so the dynamometer can be securely attached to the shaft. The shaft is pressed into a circular flange with the correct hole locations, and then attached to the engine. Figure 4-2 shows the installed engine-dynamometer setup in the experimental facility.

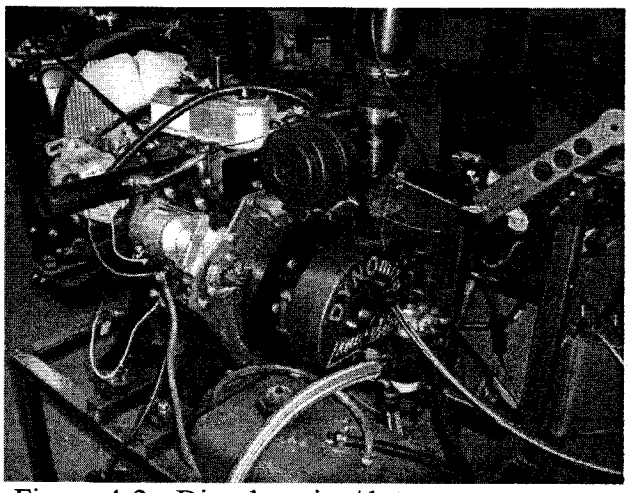

Figure 4-2 - Diesel engine/dynamometer setup

During engine loading, the emission content can be monitored. There are two methods for testing the emissions. One test is a five-gas analysis that monitors different types of pollutants in the raw exhaust. The individual gases most important to the research are CO, $CO_2$, HC's, $O_2$, $NO_x$. A Nova five gas diesel emission analyzer provides real time monitoring of each gas, and enables data collection on a PC. The information can be related to the engine speed and load placed on the engine by the dynamometer. An additional data acquisition system is used to monitor the engine operation using number of sensors. This includes temperature sensors for intake air, exhaust air, individual cylinder head, and coolant, as well as flow sensors for the intake air flow and exhaust gas flow. The test engine will be equipped a brake specific fuel consumption transducer that transmits real time data of the fuel being delivered to the cylinders. To correctly understand the efficiency of the engine, the coolant flow and heat transfer to the coolant from the engine will be monitored. The major pieces of equipment in the test stand include,

- Briggs and Stratton 4-cycle diesel engine: 18 horsepower, inline 3-cylinder liquid Cooled engine.

Table 4-1 - Engine dimensions and operating parameters

| **Briggs and Stratton 4-Stroke Diesel Engine** | |
|---|---|
| Engine | In-Line 3 Cylinder |
| Valve Mechanism | Gear-Driven Overhead Valve |
| Displacement (cc) | 700 |
| Bore x Stroke (mm) | 68 x 64 |
| Timing | 1-2-3 ( Front, Center, Back ) |
| Compression Ratio | 24.0 : 1 |
| Gross HP @ 3600 RPM | 18 |
| Gross Torque @ 2400 RPM (ft. lbs.) | 32.5 |

- Land and Sea Dynamometer: 9" Water break absorber with data acquisition (DYNO-Max 2000 Pro +), Automatic throttle controller, Exhaust gas temperature probes kit, Head thermocouple, Air intake flow meter, and RTD probes.

- Nova Analytical ***Exhaust Analysis*** System: Diesel Exhaust 6 Gas Analyzer and "NovaLogger" Data Acquisition Software

Additional items include temperature, pressure and flow sensors; computer data acquisition system; fuel and water coolant reservoirs; heat exchangers and particulate collection set up. A small scale diesel engine test stand is being assembled with the intent of measuring energy flows to determine overall thermal efficiency under a variety of test conditions as well as to verify results of the modeling work that is being done as a part of this task. Specifically the following measurement capabilities will be available: Engine Speed, Torque and Horsepower, Exhaust Gas

Temperature, Exhaust Gas Flow Rate, Coolant Temperature, Coolant Flow Rate, Air Intake Flow Rate, Air Intake Temperature and Fuel Flow Rate. Because emissions are also a critical portion of this task, important emissions concentrations will also be measured and monitored. In addition to providing feedback for experimental test conditions, concentration of exhaust emissions will also be an output of the modeling work.

Diesel Engine Test Procedure and Results

Before collection of any data, the engine was warmed up by running it until the engine reached a stable operating temperature. This is followed by ramping up RPM to designated RPM and load setting until a steady operating conditions are reached. Engine diagnostics recording and emission sample recording are performed while making sure that exhaust reading is stable. Tests were performed for full load condition and for different operating RPMs typical length of a run was 20 minutes. Tables 4-2 - 4.4 show typical operating parameters and the recorded input and outputs dada for the engine during testing.

Table 4-2 - Engine Test Modes

| Mode | 1 | 2 | 3 |
|---|---|---|---|
| RPM | 3500 | 3000 | 2500 |
| Torque % | 100 | 100 | 100 |
| Number of Runs | 7 | 7 | 7 |

Table 4-3 - Recorded Inputs

| Engine Speed (RPM) | Fuel Consumption (GAL/HR) | Air Intake Flow (CFM) | Air Intake Temp (F) | Coolant Flow (GPM) | Coolant Temp (F) | Coolant Pressure (PSI) |
|---|---|---|---|---|---|---|
| 3500 | 0.99 | 34.19 | 71 | 4.3 | 131.24 | 7.29 |
| 3000 | 0.861 | 30.54 | 71 | 2.82 | 123.86 | 6.71 |
| 2500 | 0.694 | 25.54 | 71 | 1.67 | 110.67 | 7.16 |

Table 4-4 - Recorded Outputs

| Engine Speed (RPM) | Horsepower | Torque (FT-LBS) | Exhaust Flow (CFM) | Exhaust Temp (F) | Coolant Flow (GPM) | Coolant Temp (F) | Coolant Pressure (PSI) |
|---|---|---|---|---|---|---|---|
| 3500 | 14.29 | 21.43 | 92.33 | 998 | 4.3 | 169.31 | 6.89 |
| 3000 | 12.82 | 22.44 | 81.4 | 978 | 2.82 | 160.68 | 6.35 |
| 2500 | 11.05 | 23.21 | 67.37 | 965 | 1.67 | 152.8 | 6.73 |

Figure 4-3 shows power output from the engine with time for different operating engine speed. While power outputs are quite steady for operation in the engine speed range of 2000-3000, the operation, however showed some fluctuation around the mean power output of 14 HP for the engine speed of 3500. Figure 4-4 shows exhaust temperature measurements during engine startup under full load conditions for various engine speeds. Exhaust temperature tends to reach a steady state value for all engine speeds within 3 minutes of operation.

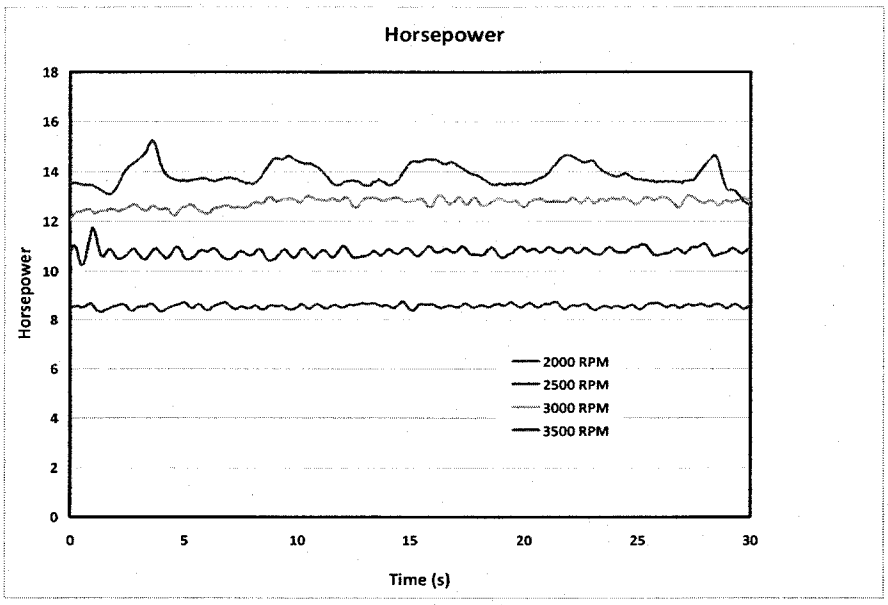


Figure 4-3 - Operating horsepower for varying RPM

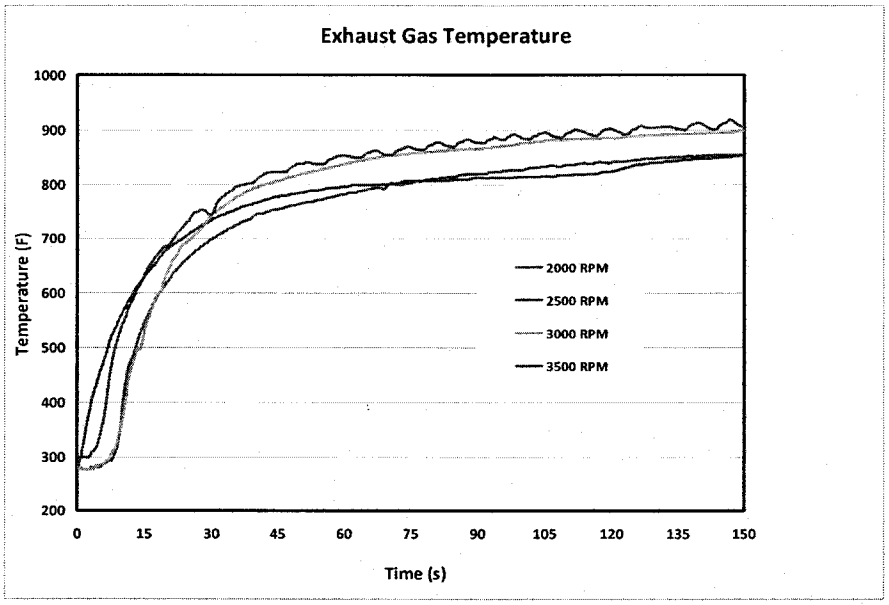


Figure 4-4 - Exhaust gas temperature at varying RPM

Average overall engine efficiency for each RPM range and load was calculated by integrating power output to the dynamometer over time and comparing with the HHV of the fuel consumed determined by mass loss. Fuel consumption was determined by mass loss. Tabulated average efficiency results are given in Table 4-5 and the results are depicted graphically in Figure 4-5. In this figure the diamond symbol represents the mean efficiency with 95% confidence intervals for the mean. Efficiency was near 27% based on the higher heating value (HHV) of the fuel for all rpm measured under full load conditions.

Table 4-5 - Calculated Engine Efficiencies for Each Run

| run | 2500 rpm | 3000 rpm | 3500 rpm |
|---|---|---|---|
| 1 | 0.2638 | 0.2579 | 0.2636 |
| 2 | 0.2658 | 0.2702 | 0.2608 |
| 3 | 0.2697 | 0.2887 | 0.2722 |
| 4 | 0.2684 | 0.2475 | 0.2766 |
| 5 | 0.2702 | 0.2651 | 0.2781 |
| 6 | 0.2728 | 0.2722 | 0.2684 |
| 7 | 0.2691 | 0.2709 | 0.2636 |

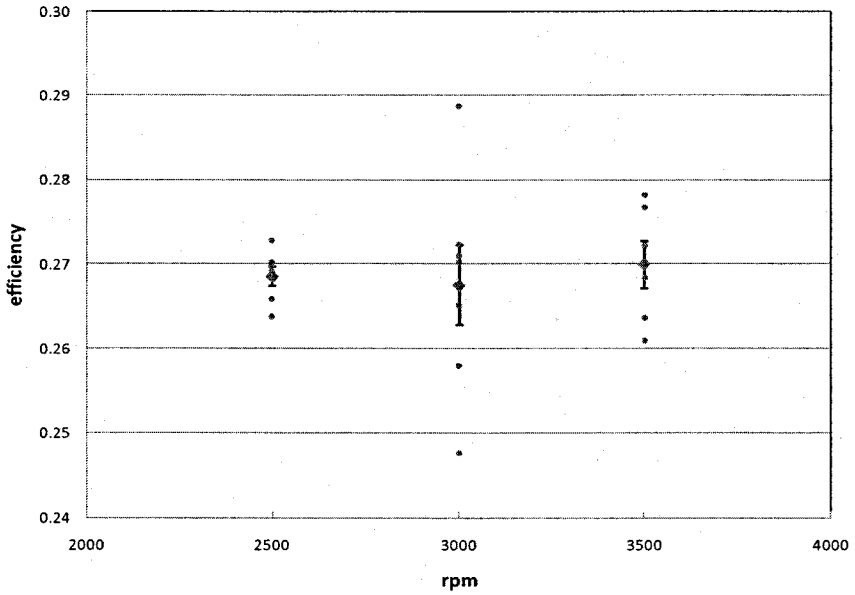


Figure 4-5 - Engine efficiency vs. rpm at full load

Emissions results for $CO_2$, hydrocarbons (HC), $O_2$, $NO_2$, and NO are shown in Figure 4-6a-e. Carbon monoxide was also measured but was at or near the detection limit (0.1%) for all conditions. Oxygen content increased somewhat between 3000 and 3500 rpm (Figure 4-6a) while $CO_2$ content dropped (Figure 4-6b) over the same rpm range. This may indicate some resistance to air flow in the intake manifold. NO and NO2 concentrations show a statistically significant rise (Figures 4-6c and 4-6d) as rpm increases but the increase is probably not practically significant. Hydrocarbon content decreases substantially as engine rpm increases (Figure 4-6e) from almost 15 ppm at 2500 rpm to less than 4 ppm at 3500 rpm.

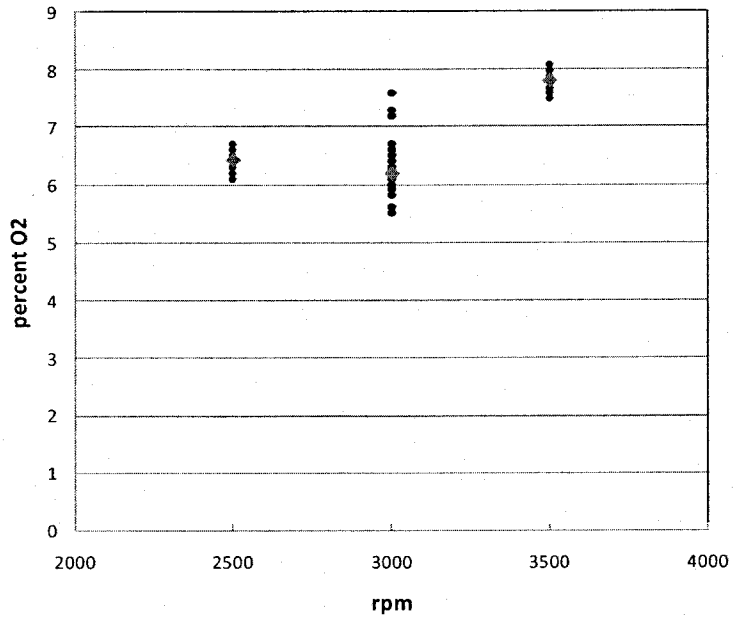


Figure 4-9 - Variation of exhaust gas composition with rpm under full load
(a) Exhaust oxygen concentration.

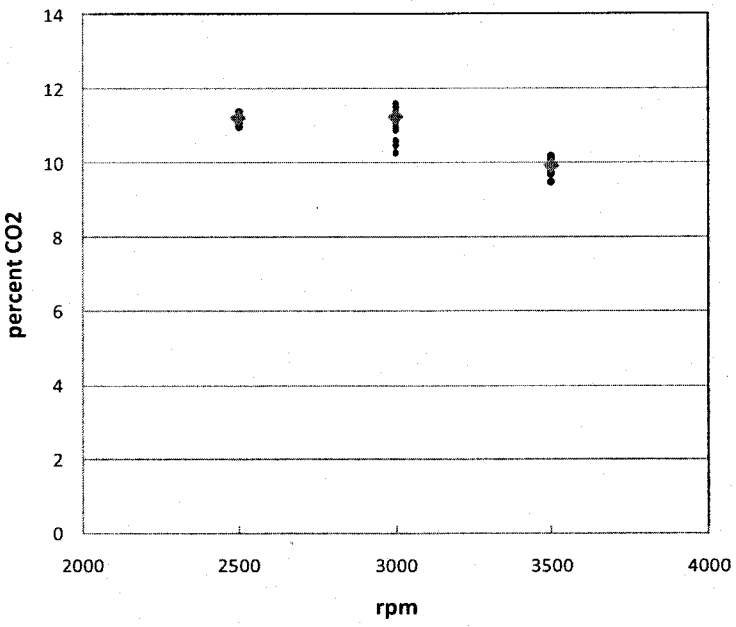


Figure 4-6 - Variation of exhaust gas composition with rpm under full load
(b) Exhaust carbon dioxide concentration

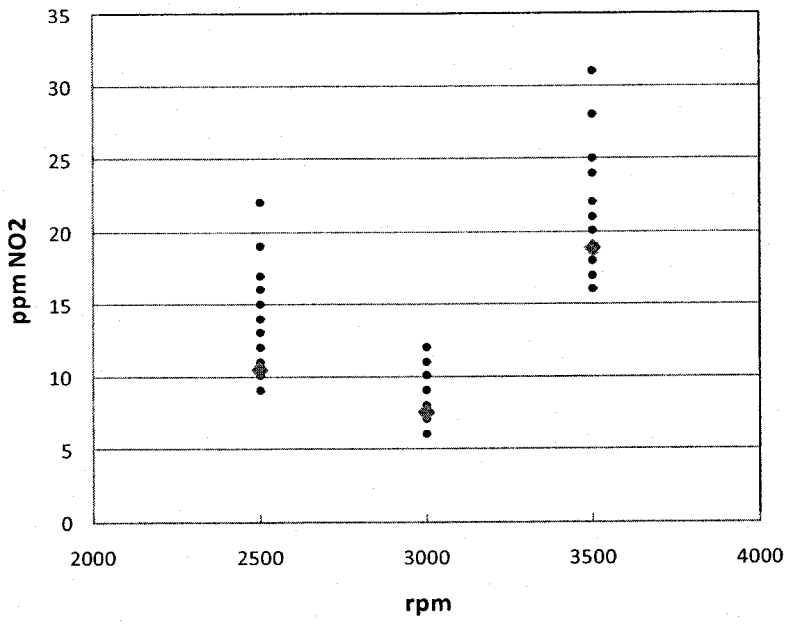


Figure 4-6 - Variation of exhaust gas composition with rpm under full load
(c) Exhaust $NO_2$ concentration

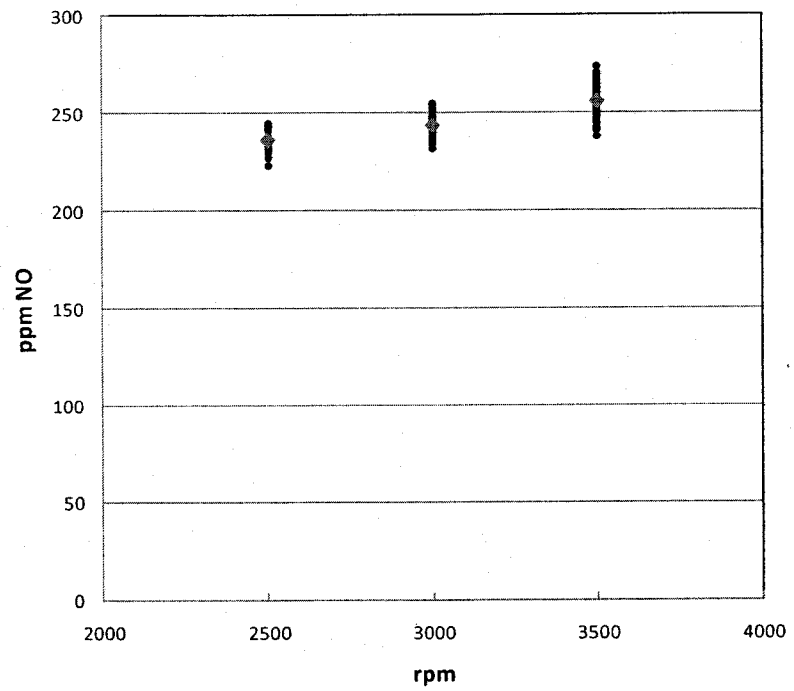


Figure 4- - Variation of exhaust gas composition with rpm under full load
(d) Exhaust NO concentration

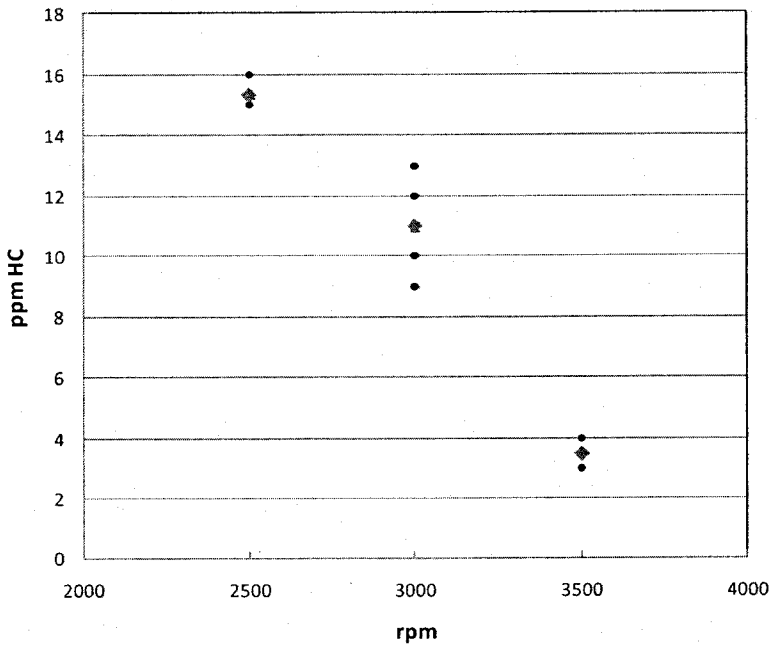


Figure 4-6 - Variation of exhaust gas composition with rpm under full load
(e) Exhaust hydrocarbon concentration

Exhaust Particulate Measurement

In addition to exhaust gasses, the concentration of exhaust particulates is also important as an indicator of cleaner emissions. In order to compare the emissions of regular diesel and bio-diesel a product must be designed in order to measure the relative amount of exhaust particulates. Due to the cost of commercial analysis equipment, a measurement apparatus is being constructed using a dilution chamber, to provide mixing with air as would normally occur as exhaust is discharged, including a filtration apparatus to measure particulates by mass. Tests are performed following EPA Part 1065. The main objective is to design a system to generate and collect particulate matter (PM) from a diesel engine for different engine settings (speed and torque). The PM is analyzed to determine size distribution, composition and amount for a given type of fuel. Furthermore, data from the flow meters and thermocouples are recorded using computer data acquisition (DAQ).The intended functions for this system are:

1. Generating particulate matters.
2. Collecting particulate matters.
3. Complying with EPA specifications (2).
4. Determining the amount of the particulate matters.
5. Determining sizes of the particulate matters.

The function of this product is to measure the relative amount and size of particulate generation given different diesel engine settings. Overall Diesel Particulate retrieval system is shown in Figure 4-7. The system includes three sub-functions: ambient air mixing for particulate generation, particulate collection, and maintenance of sufficient airflow pressure. The basic concept for diluting the sample gas involves mixing ambient air and the exhaust gas in a dilution chamber before it passes through the first filter.

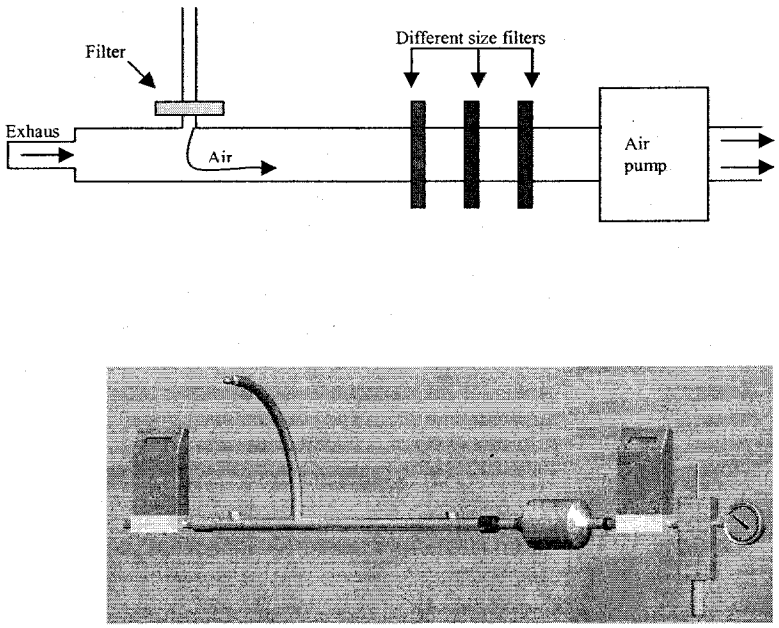


Figure 4-7 - Diesel Particulate Retrieval System

The setup include two flow meters, a venturi pump, filter holder, temperature sensors and PTFE membranes for filtration purposes, and thermocouple sensors and a computer data acquisition system. PTFE membranes are used because they can withstand high temperatures and corrosive elements. The filters available came in 5 different pore sizes: 5, 1, .45, .22, and .10 μm. Filters with pore sizes 5, 1, and .22 μm were chosen for initial testing. Figure 4-8 shows a typical SEM image of the particulate collection in a 20um filter.

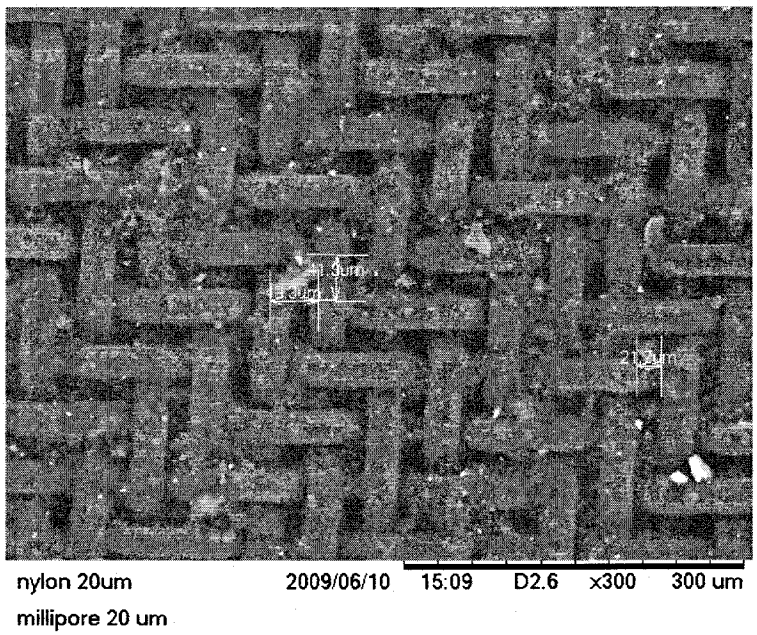


Figure 4-8 - SEM image of particulate collection in.

The results from the first test show an increase in weight of 0.0018 grams for the 30um filter and 0.0011 for the 20um filter. The increase in weight is a representation of the weight of particulate collected over the duration of the test. In order to show the size distribution smaller pore size filters are installed under the same engine settings. However, more testing and analysis of the tests data has to be performed to quantify the amount average particulate concentration as well the distribution of particulate sizes in the exhaust over a range of operating conditions.

Computational Fluid Dynamic Modeling

The objective for this part of the project is to perform analysis of the diesel cycle combustion events using both regular petro-diesel and various biodiesels. The engine performance and emissions can be predicted and compared for different operating conditions and fuel types using a computational fluid dynamics (CFD) simulation model. In addition, by studying the factors involved, these parameters can be used to control the pollutant composition of the engine exhaust. A computational fluid dynamic simulation model is developed using Fluent to simulate air-fuel mixing, combustion and emission in the Daihatsu/ Briggs and Stratton test engine that is being used in the experimental test facility. This model will be useful to evaluate number of key factors that affect diesel engine emission and thermal load. Initially, a single cylinder model is being used for a starter model to develop different processes such as air-intake and suction, air compression, combustion and power expansion, and air exhaust processes using moving piston and a deforming mesh system. Processes corresponding to four stroke diesel engine with corresponding piston position and crank angles considered are : is shown in All engine parameters such crank shaft speed, compression ratio and piston stroke length corresponds to the Briggs and Stratton test engine for initial simulation study and presented in Table 4-6

Table 4-6 - Engine parameters and operating conditions for simulation

| | | |
|---|---|---|
| 1. | Bore diameter(mm) | 68 |
| 2. | Stroke length(mm) | 64 |
| 3. | Connecting rod length(mm) | 110 |
| 4. | Compression ratio(Vc/Vt) | 24 |
| 5. | Crank shaft speed(rpm) | 2000 |
| 6. | Type of fuel | C10H22 |
| 7. | Air-Fuel ratio(Ma/Mf) | ~17 |
| 8. | Fuel mass-flow rate(kg/s) | 0.004 |

The piston is initially at the Top Dead-end Center (TDC) moving down inhaling the atmospheric air. At 0° intake valve opens while the exhaust valve is closed it remains open and closes at 200° crank angle position. Both the valves are closed now and the air which is sucked in gets compressed to the desired compression ratio raising the temperature and pressure. Fuel is injected into the cylinder at 300° crank angle position before piston reaches the TDC position till 360° crank angle position. During this time the combustion of fuel takes place and then the piston starts to move to the BOTOM Dead-end Center (BDC). Exhaust valve opens at 540° and remains open till 720° crank angle position. Figure 4-9 shows the dynamic mesh system that deforms based on the piston positions during the engine cycle. with the process of air intake and expansion of piston in the cylinder.

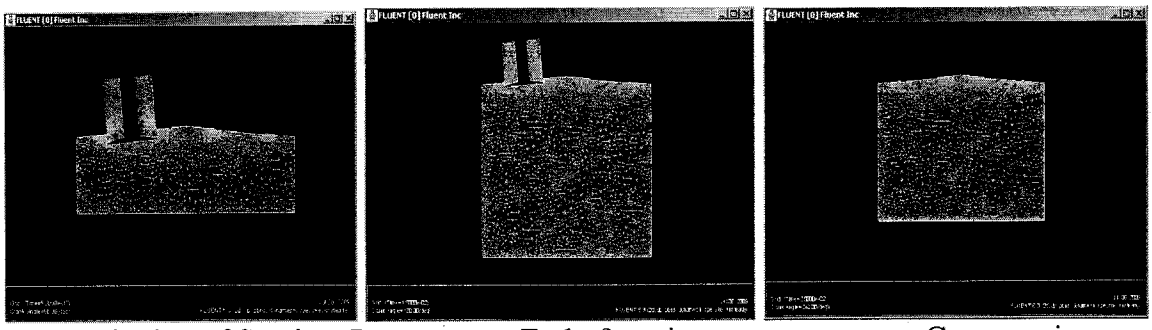

Beginning of Suction Process End of suction Compression

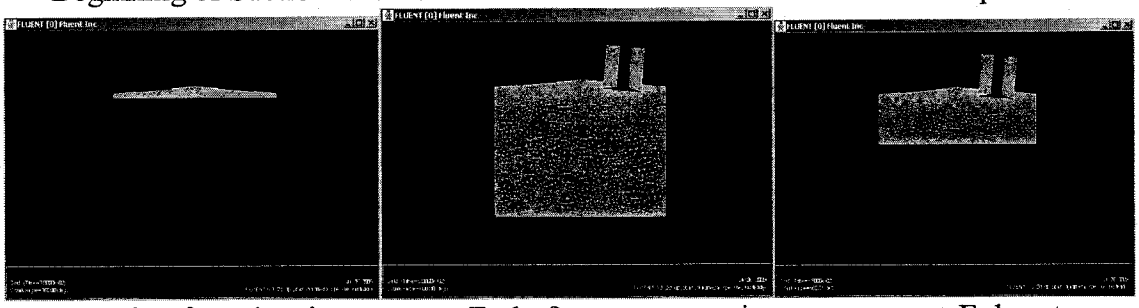

Begin of combustion End of power expansion and expansion Exhaust

Figure 4-9 - Dynamic mesh system for the four-stroke diesel engine cycle

Computational model is based on two-dimensional- unsteady implicit formulation along with k-epsilon turbulence model with standard wall function. The combustion model includes species transport and turbulence-chemistry interaction based on Finite-Rate/Eddy-Dissipation combustion model. While modeling the ignition delay in diesel engines, chemical reactions are allowed to occur when the ignition species reaches a critical value in the domain. For the ignition delay model, the source term estimated is based on Hardenburg and Hase correlation.

Figures 4-10 through 4-15 shows variation of various contour plots of pressure, temperature, and fuel and gas composition at different crank angle position during combustion, expansion and exhaust processes of the engine cycle. Combustion started before the piston reaches the TDC. Results show that the fuel spray is propagating from top to bottom of the engine cylinder. The fuel mass fraction contour shows a relatively low fraction in front of the spray and high behind the spray. Results shows composition of carbon dioxide, water as well as presence of NO and $N_2O$. As combustion progresses, the product gas composition increases and engine undergoes power expansion.

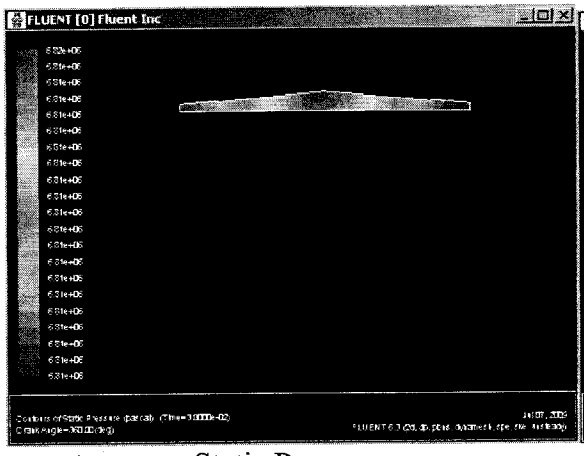


Static Pressure

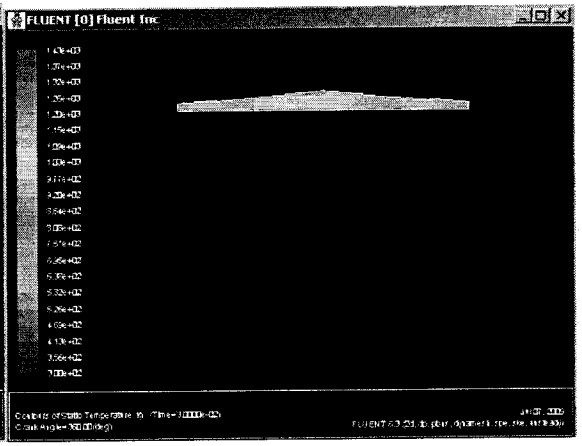


Temperature

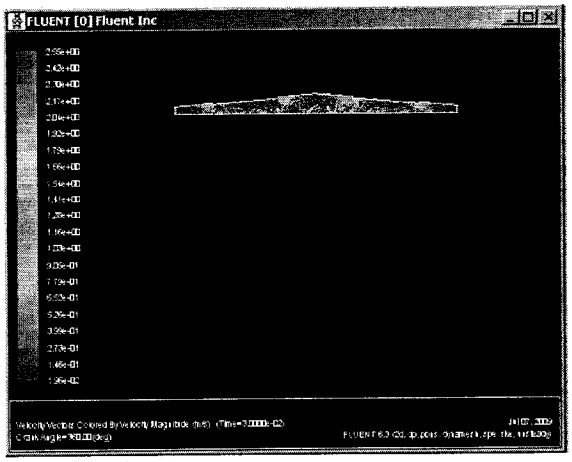


Velocity vector

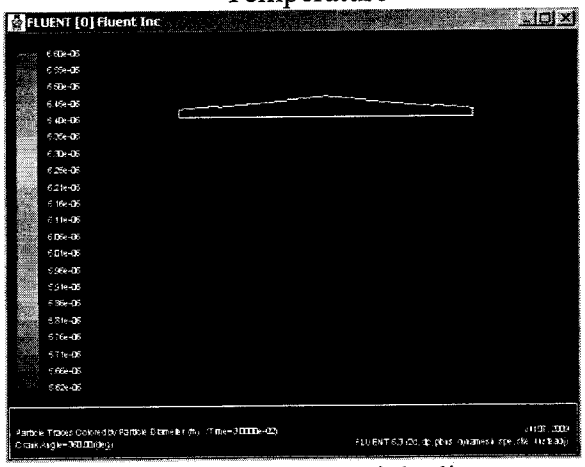


Particle track colored by particle diameter

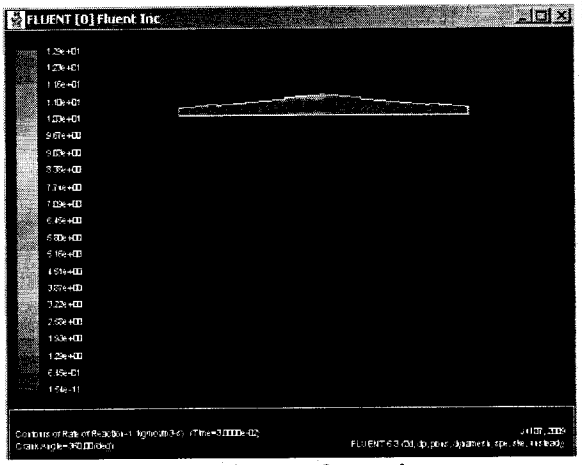


Contours of rate of reaction

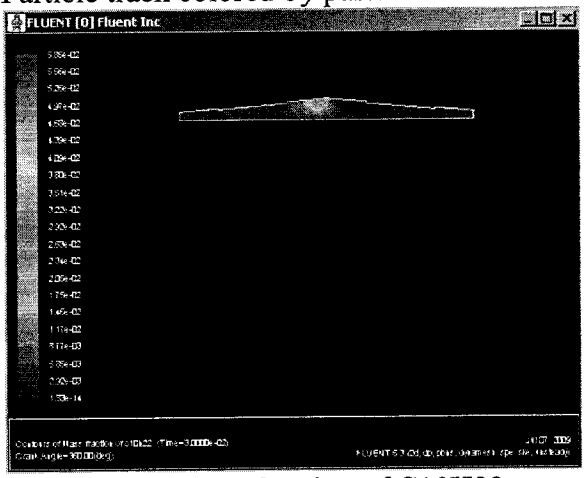


Contours of mass fraction of C10H22

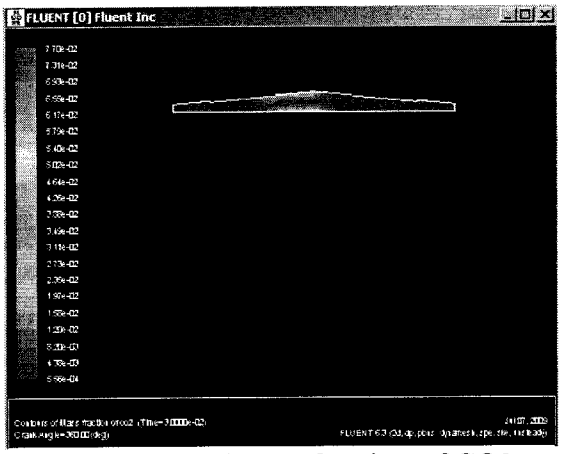


Contours of mass fraction of CO2

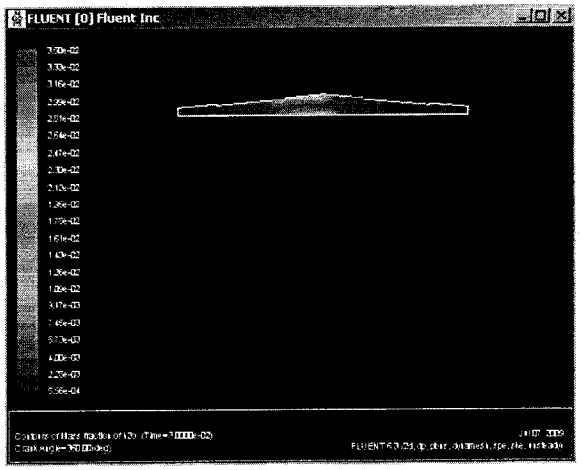


Contours of mass fraction of H2O

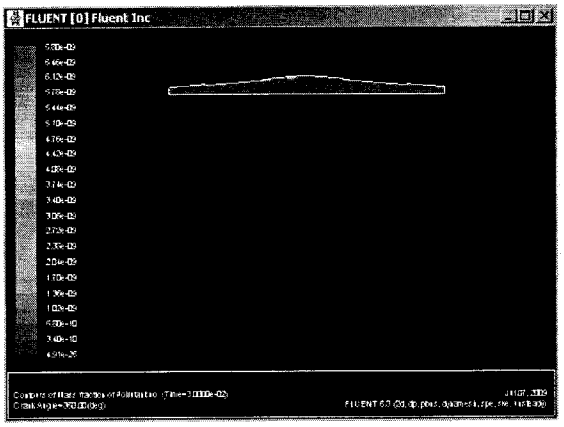


Mass fraction of Pollutant NO

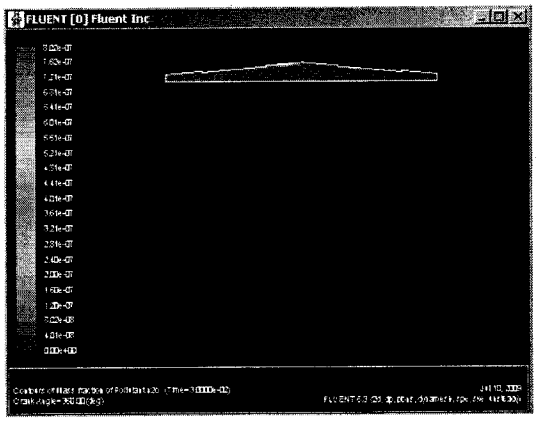


Mass fraction of $N_2O$

Figure 4-10 - Piston at TDC

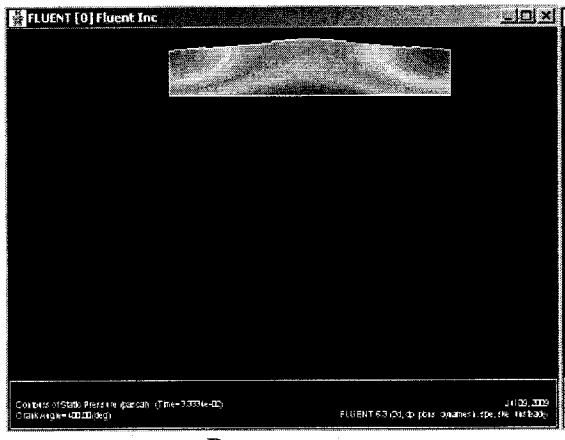


Pressure

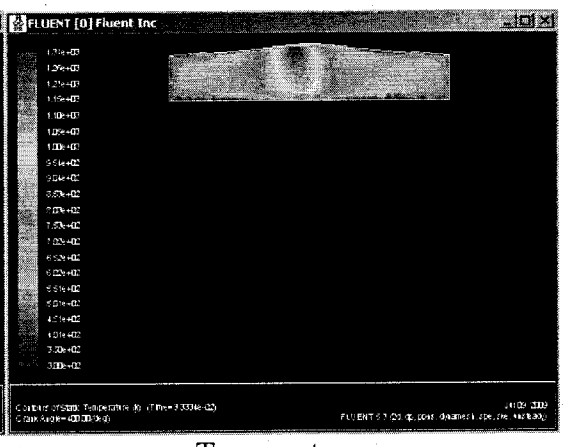


Temperature

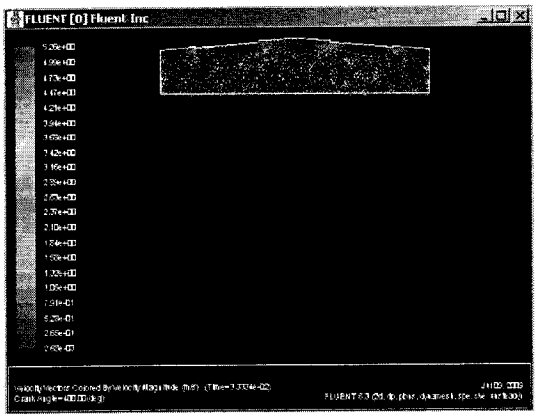


Velocity vectors

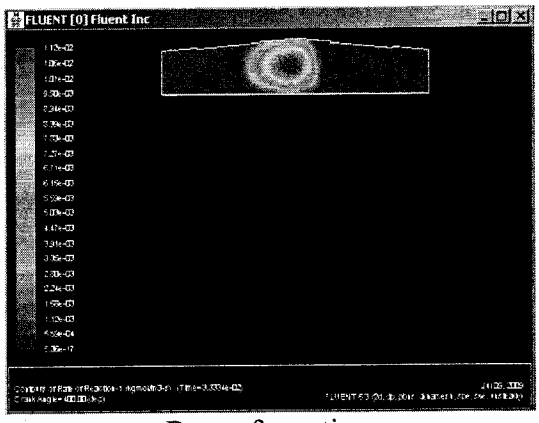


Rate of reaction

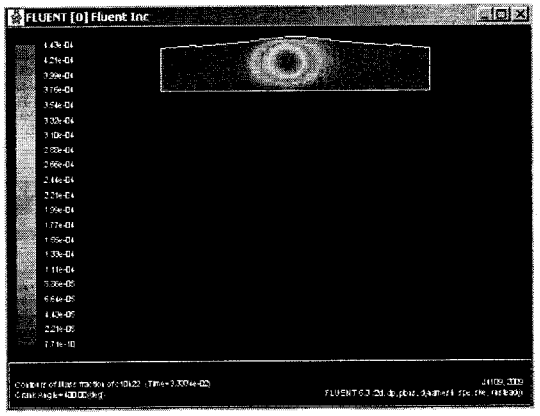


Mass fraction of C10H22

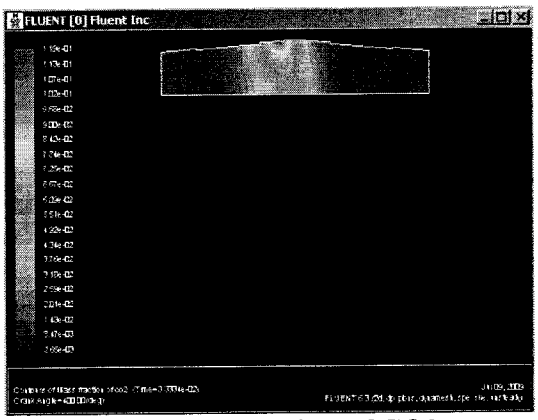


Mass fraction of CO2

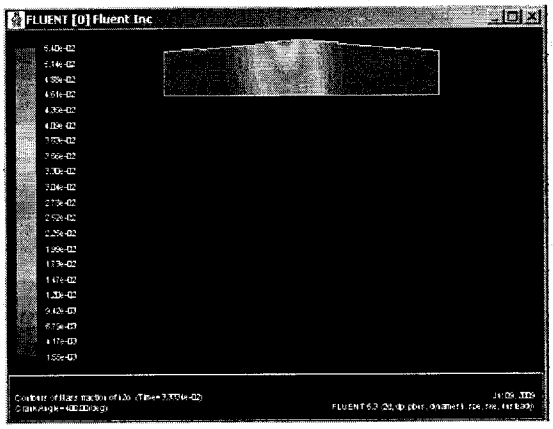


Mass fraction of H2O

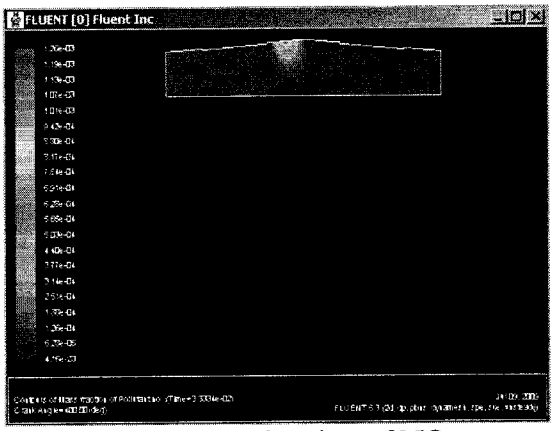


Mass fraction of NO

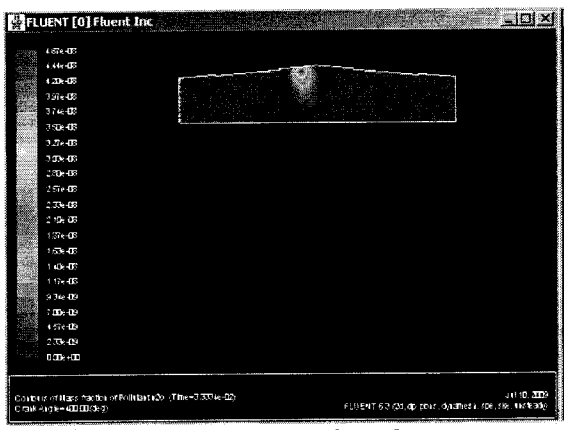


Mass fraction of N2O

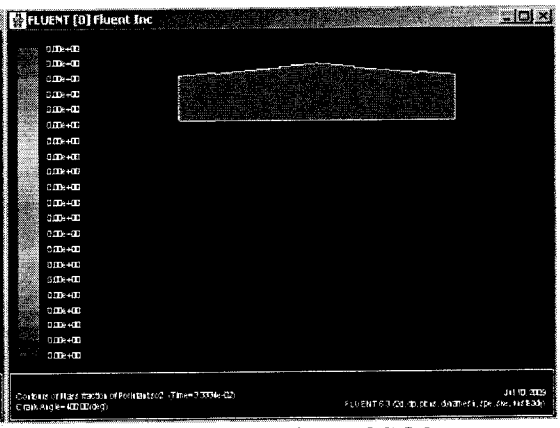


Mass fraction of SO2

Figure 4-11 Piston is at 40° after TDC

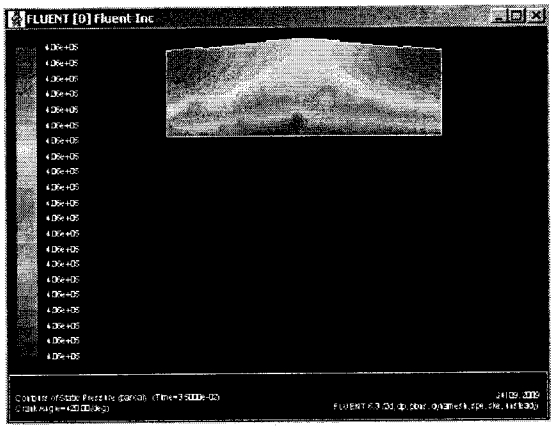


Static pressure

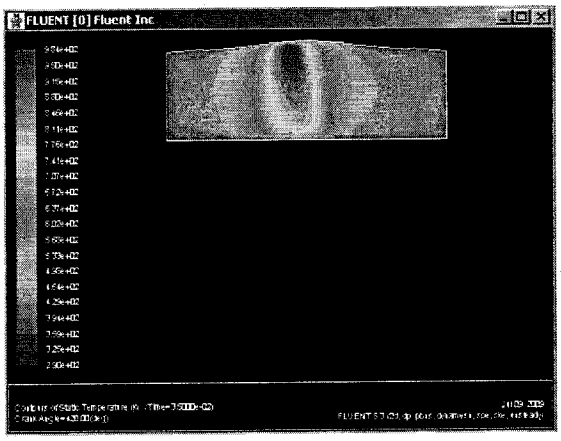


Temperature

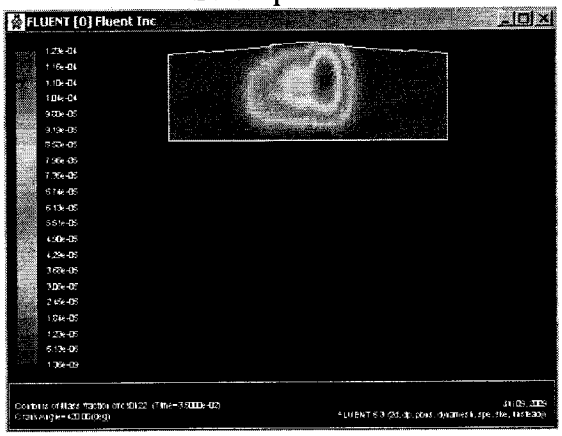


Mass fraction of C10H22

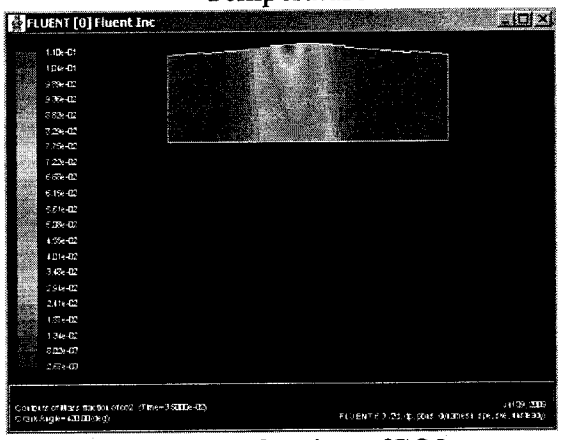


Mass fraction ofCO2

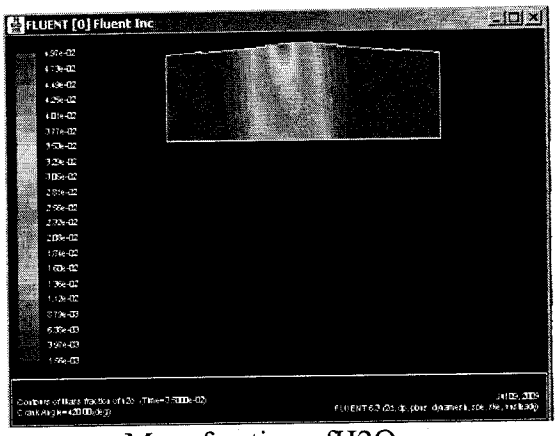


Mass fraction ofH2O

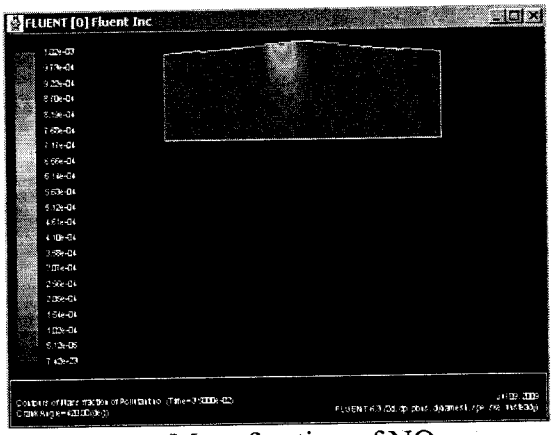


Mass fraction of NO

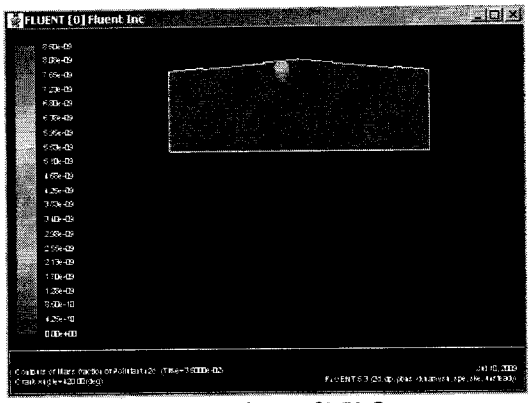


Mass fraction of N2O

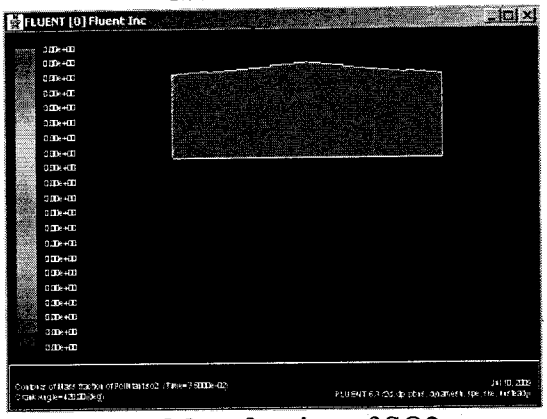


Mass fraction of SO2

Figure 4-12 - Piston at 60 after TDC

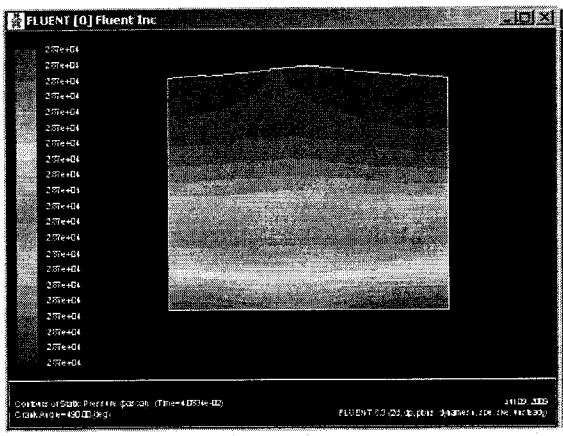


Static pressure

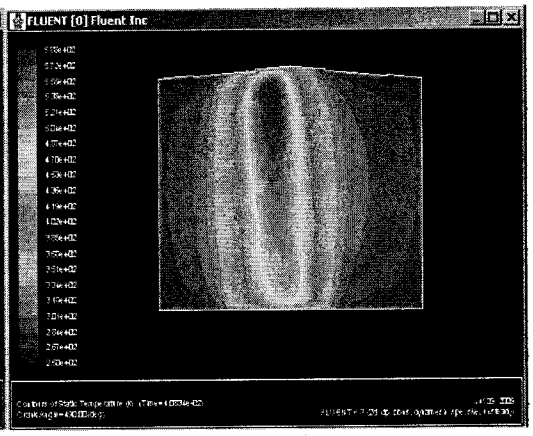


Temperature

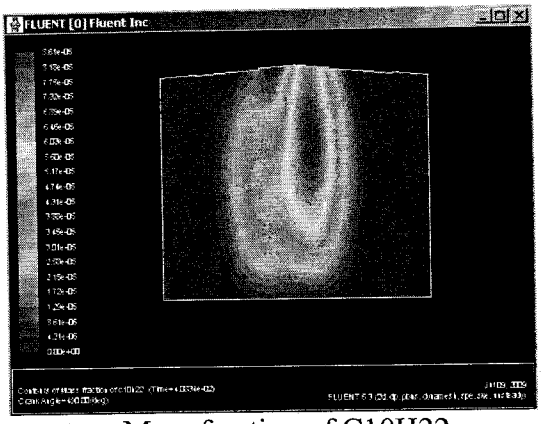


Mass fraction of C10H22

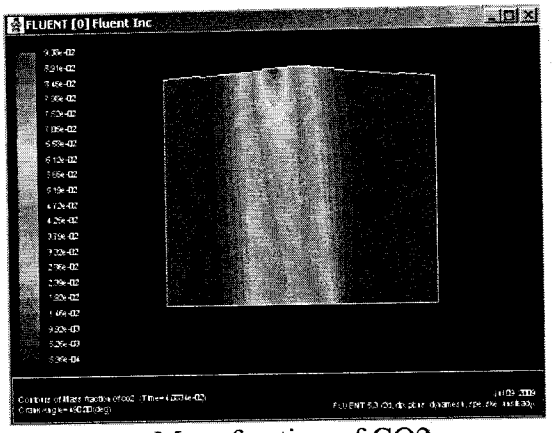


Mass fraction of CO2

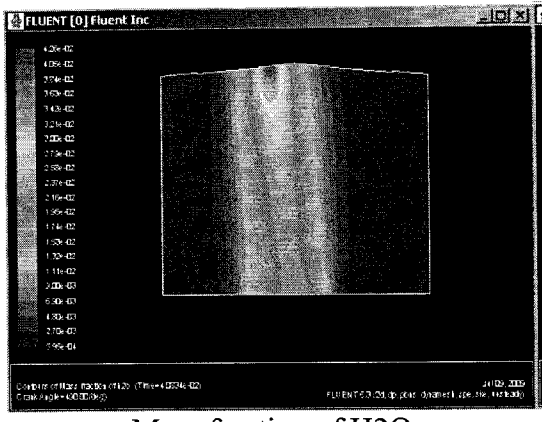


Mass fraction of H2O

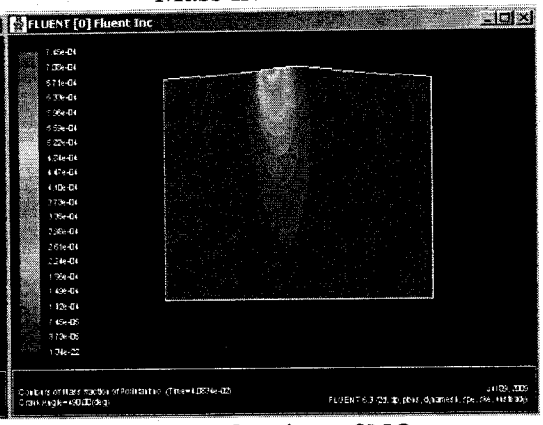


Mass fraction of NO

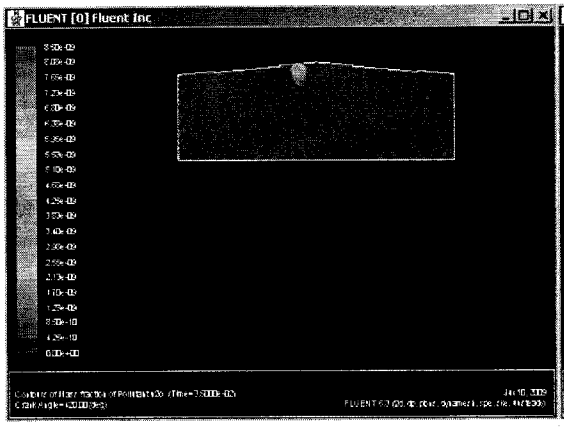


Mass fraction of N2O

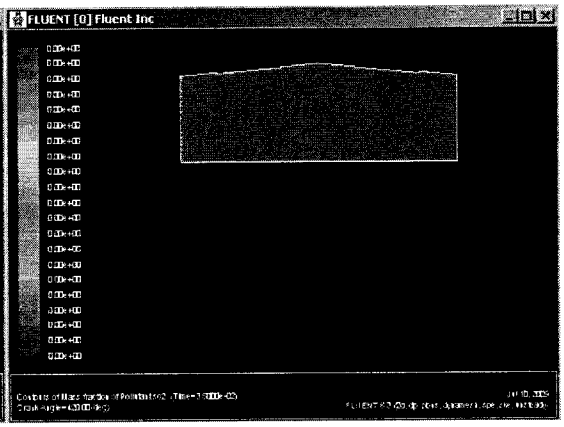


Mass fraction of SO2

Figure 4-13 - Piston is at 130° after TDC

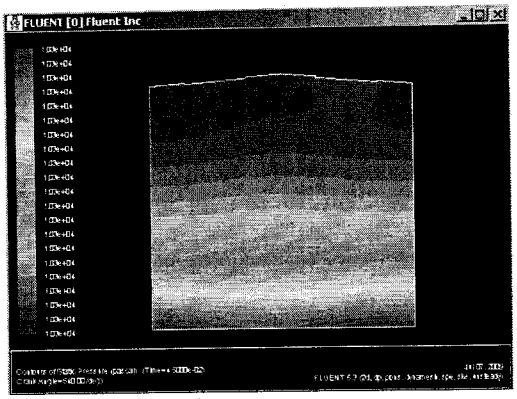


Static pressure

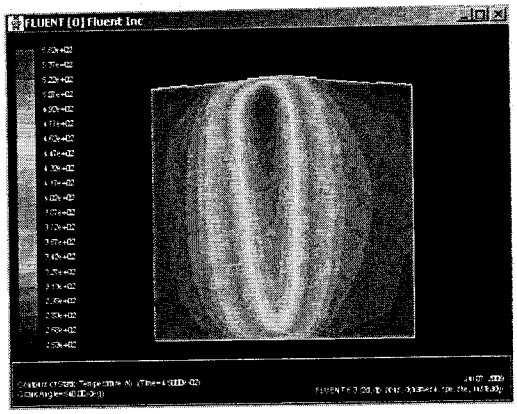


Temperature

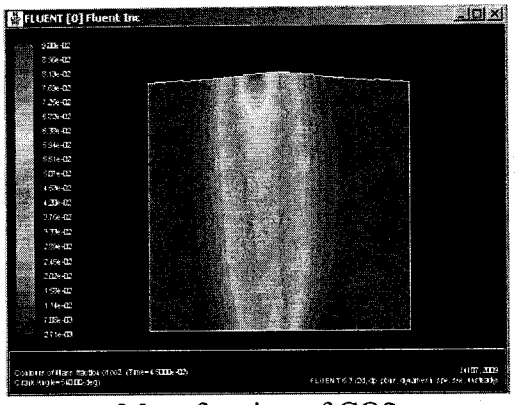


Mass fraction of CO2

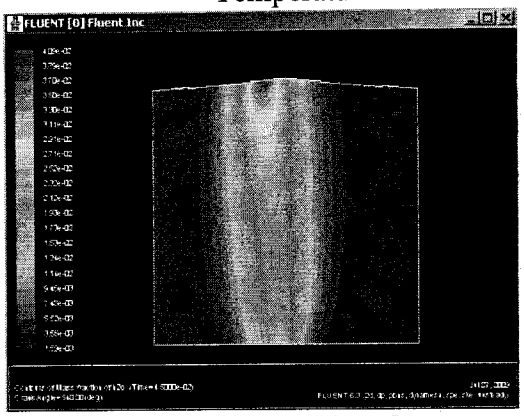


Mass fraction of H2O

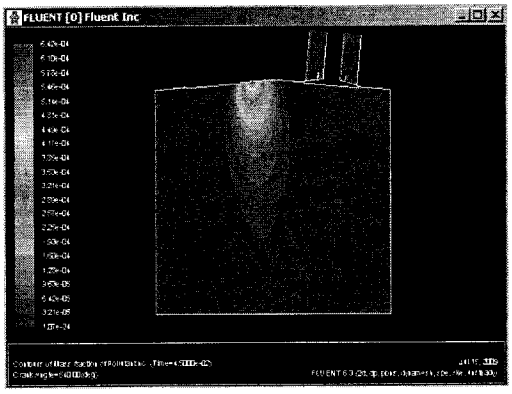


Mass fraction of NO

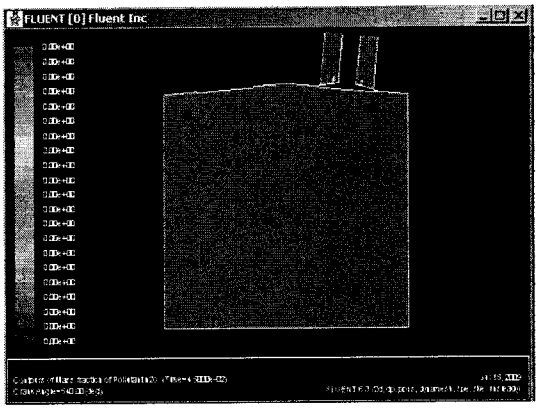


Mass fraction of N2O

Figure 4-14 - Piston is at BDC and completion of power expansion

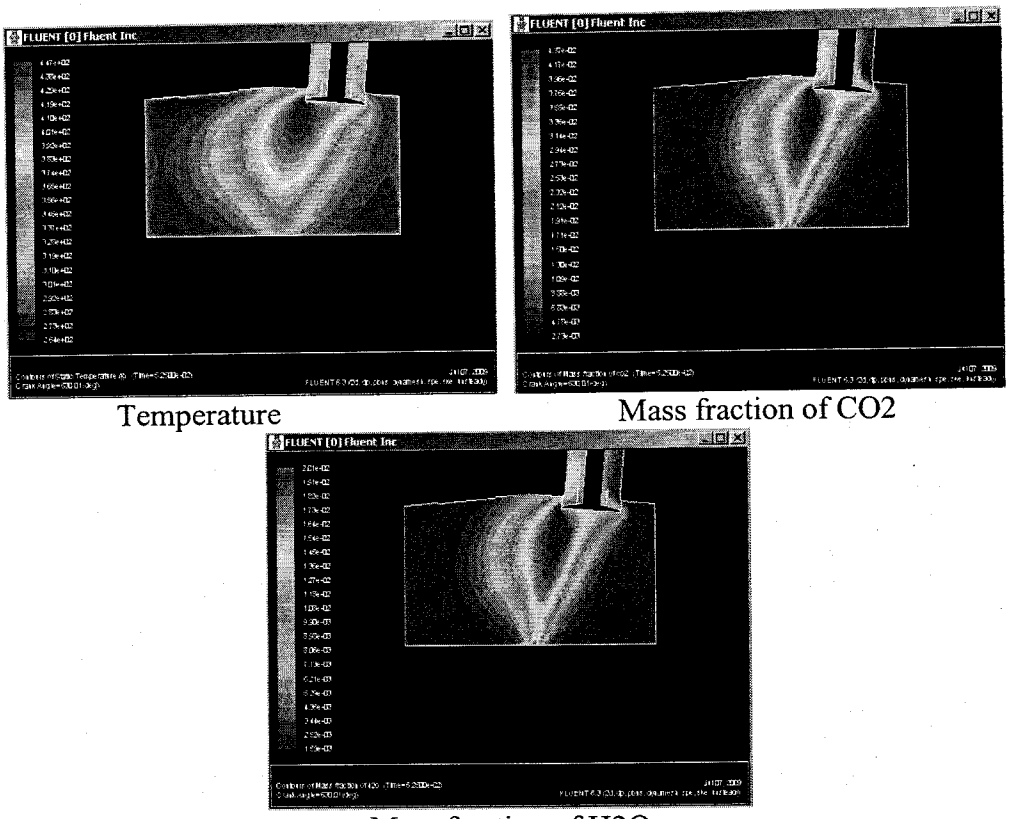


Temperature

Mass fraction of CO2

Mass fraction of H2O

Figure 4-15 - Piston at 90°after BDC during exhaust process

Work now in progress to estimate the average exhaust gas composition and comparison with experimental measurement data. The simulation model will be used to compare different fuel types under different operating conditions in terms of engine performance and emission composition.

Simulation Analysis of Engine Cooling system

An analysis of the engine cooling system is carried out to evaluate engine cooling load using model of the engine was created to examine the cooling properties. Data was collected from the manufacturer that contained properties for the engine such as coolant flow rates, heat rejection rates, fan speeds etc. These were used as input parameters for the simulation of the engine as well as a comparison for the outputs. The model was simulated with finite element commercial code Ansys CFX and FloWizard using Fluent solvers. All operating parameters and inlet conditions for the simulation is listed in Table 4-7.

Table 4-7 - Engine operating parameters and inlet conditions for simulation

| | |
|---|---|
| Coolant Flow Rate | 50 L/min (833.33 cm3/s) |
| Coolant Inlet Temperature | 100 °F (37.7 °C) |
| Ambient Air Temperature | 75 °F (23.89 °C) |
| Exhaust Gas Temperature | 1022 °F (550°C) |

| | |
|---|---|
| Cylinder Temperature | 650 °F (343.33 °C) |
| Engine speed | 3500 |

Initially a simple 3 cylinder engine model was developed. To simplify the simulation, a homogenous mean cylinder temperature of 650°F was assumed. While the major objective is to evaluate several different engine coolants including nanofluid, the simulation is first performed using water as coolant. Figure 4-16 showed a detail solid model of the three- combustion cylinder heads with integrated water cooling channel and the corresponding computational mesh for FEM flow and thermal analysis. The final refined mesh system includes about 615517 cells. The computational model include flow model based on Navier-stokes equations with $k-\varepsilon$ turbulence model for the cooling channel around engine cylinder and intake and exhaust port.

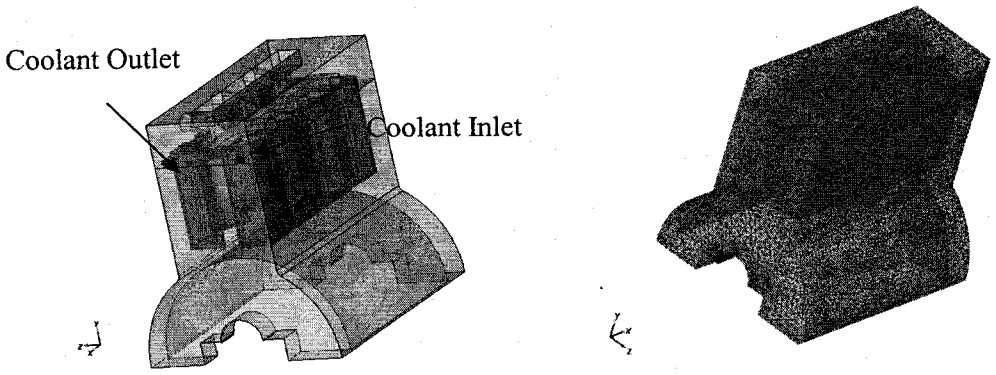


**(a)** Engine solid Model with Cylinders **(b):** Simplified engine model with mesh

Figure 4-16 - Engine model for cooling analysis

Figure 4-17 show coolant velocity magnitude and temperature variation from inlet to outlet port of the cooling channel. Flow passages caused considerable variation from inlet to out section and around different engine cylinders. It showed higher coolant temperature in regions in between the two cylinders where heat dissipation is predominantly by conduction through solid wall. This is more clearly demonstrated by contour plots for temperature in the engine blocks in Figure 4-18.

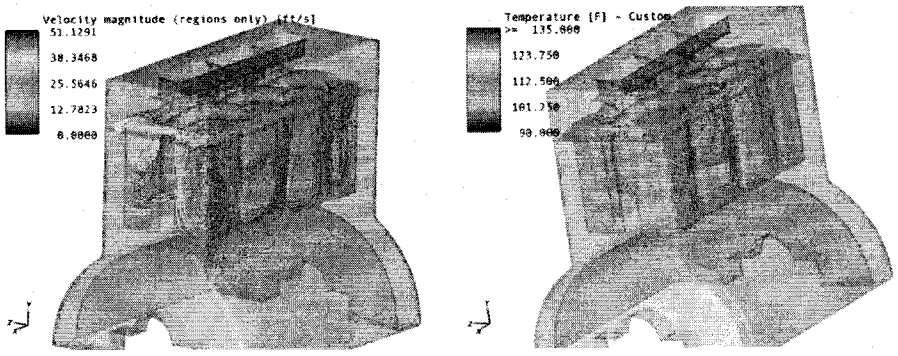


Coolant Velocity magnitude Temperature

Figure 4-17 - Coolant velocity and temperature along the cooling channel

While results show similar temperature variation around each cylinder, there is considerable variation at different sections around each cylinder. Temperature remains at a considerably higher level of 640 F in regions in between two cylinders. The cooling is very effective in cylinder wall regions close to cooling channel. Temperature plots at selected sections A-A and B-B are also presented in Figure 4-10 to demonstrate the variation of temperature across the engine wall. A temperature drop from 250 F is achieved from the cylinder wall to cooling channel.

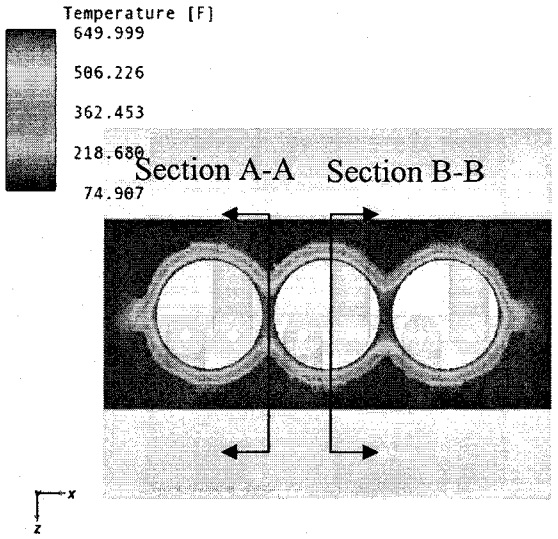


(a) Mid –section in x-z plane

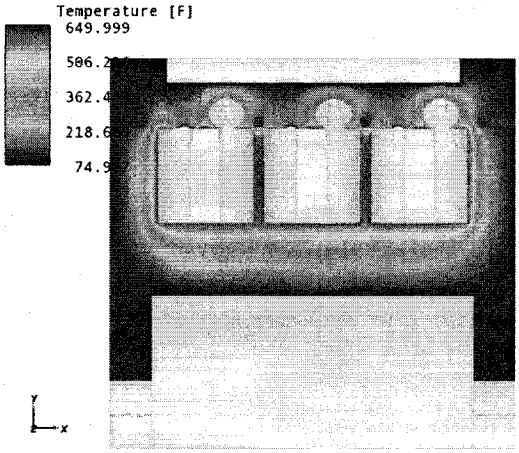


(b) Temperature Distribution across Cylinders in XY Plane,

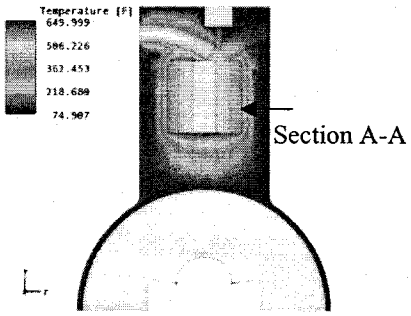


(c) at Cylinder walls, Section A-A

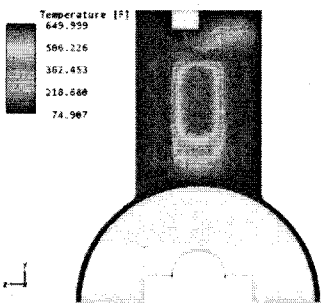


(d) between cylinders, section B-B

Figure 4-18 - Temperature distribution in engine wall

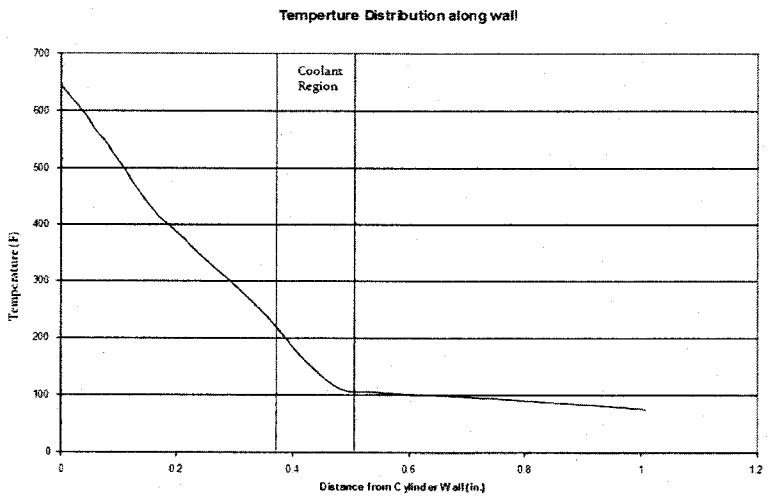


(a) Along section A-A at cylinder 2

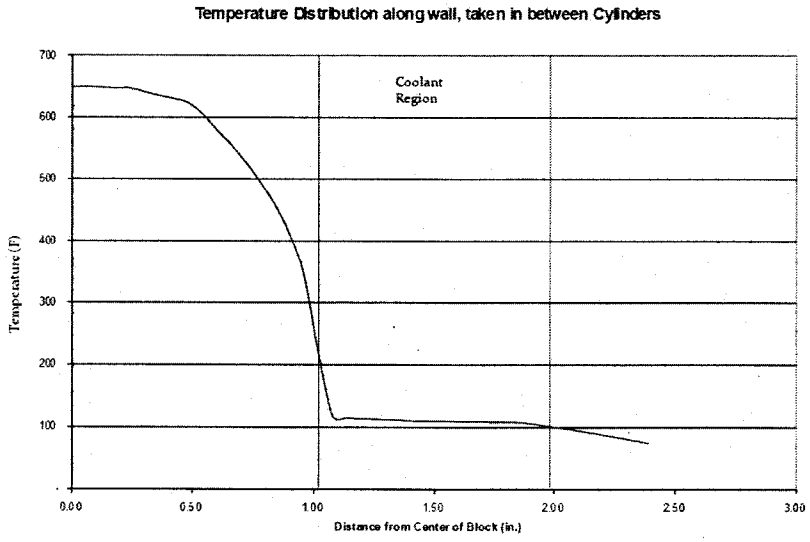


(b) Across engine wall along section B-B between cylinders 1 and 2

Figure 4-19 - Temperature distributions in engine wall with integrated cooling channel

With an exit temperature of 228°F the coolant experiences a 34 °F temperature increase between the inlet and the outlet. This is in comparison to 38 °F average temperature drop found in the experimental value. Work now in progress to integrate the cooling analysis model with the air-fuel mixing and combustion model. Further evaluation of engine heat loss and a comparison with the experimental data is also being performed.

Nano fluids as Engine Coolants

Thermal Conductivity (TC) and Nanofluid Flow & Heat-Transfer Apparatus (N-FHT Apparatus) for Exploring New Hybrid Polymer-Nanofluids with Enhanced Flow and Heat Transfer Characteristics

Use of exhaust heat to preheat air and the use of nanofluids to recover engine heat load more efficiently has potential to improve over-all thermal management and hence performance and efficiency of the diesel engine. Developing related experimental testing and computational analysis will identify several concepts that may be incorporated into innovative design and operation of diesel locomotives.

The potential use of nanofluids in thermal systems has been well documented throughout the scientific community. The addition of carbon, metal and metal oxide nanoparticles to standard base fluids has been shown to increase the thermal conductivity and heat transfer capabilities of these fluids. A myriad of studies have been performed during the past twenty years that exhibit the potential for a development of improved thermal fluids by utilizing colloidal suspensions of nanoparticles in standard base fluids. While these nanofluids can be used in a wide array of thermal applications, they can be further improved with the addition of polymers. Hypothetically, these polymer-enhanced nanofluids, dubbed POLY-nanofluids, will maintain or/and enhance the thermal properties observed in standard nanofluids while exhibiting enhanced suspension ability and reduced turbulent frictional drag, if the drag reducing polymer additives are also used. With these additional qualities, these POLY-nanofluids are suitable for use in a wider variety of industrial applications. These POLY-nanofluids have the potential to revolutionize the way thermal fluids are perceived, developed, produced, and used in the field of heat transfer. In the past, many analytical models have been developed in order to explain and predict the enhanced thermal properties of nanofluids. However, none of these previously developed models have been able to fully describe these observed enhancements. Therefore, in order to further explore the properties of POLY-nanofluids, the investigation must be approached experimentally.

In previous nanofluids research at NIU's ME Department, a novel concept of drag-reducing nanofluids and poly-nanofluids has been developed. Furthermore, an advanced transient Hot-Wire Thermal Conductivity (HWTC) apparatus was developed, and during the previous phase of this project a complementary steady-state, Parallel-Plates Thermal Conductivity (PPTC) apparatus was fabricated and calibrated, to provide concomitant measurements of nanofluid thermal conductivity, critical for planed flow and heat transfer investigation of nanofluids characteristics. The results of this study, using innovative nanofluids will provide necessary data for novel application of enhanced engine cooling and efficient regeneration of waste-heat for improved engine efficiency and reduced fuel consumption and environmental emission pollution.

One of the major objectives of this study is to explore the use of nanofluids as enhanced engine coolant for improved thermal management as well as for recovery of waste heat for improved engine performance and efficiency. While nanofluids have shown exceptional potential for heat transfer enhancements, there are several challenges to be resolved, like nanofluids' flow characteristics, colloidal stability, erosion and fouling, among others. Especially at elevated temperature, as would be present in an operating diesel engine, there is a tendency of the nanoparticles to overcome columbic repulsion that keeps them separated and to potentially form

large aggregates. To reduce this tendency it is necessary to add polymeric stabilizing agents to add both additional columbic repulsion and introduce steric stabilization. In addition, the inherent flow turbulence mixing will be beneficial to minimize agglomeration effects. Our research team has designed, fabricated and calibrated new research apparatus to measure thermo-mechanical properties, as well as the flow and heat transfer characteristics of nanofluids. In addition the influence of polymeric additives on flow and heat transfer properties has been initiated.

One of the objectives of a related prior and this project (faculty release time funded by this project) was to develop a steady-state, parallel plate apparatus in order to determine the thermal conductivity of POLY-nanofluids. We developed, fabricated and calibrated a steady-state thermal-conductivity apparatus (SSTC Apparatus) for nanofluids, which complements earlier developed transient, Hot-Wire Thermal Conductivity (HWTC) apparatus for nanofluids, and previously acquired cone-and-plate digital viscometer; analytic digital balance, and ultrasonic mixer for nanofluid preparation and characterization.

The apparatus consists of a heating element above the test fluid specimen and a chiller below the test fluid specimen. This creates a temperature gradient which is measured by thermocouples imbedded in the parallel plates. This temperature gradient is then used, along with the heating power, to calculate the thermal conductivity of the test fluid specimen. This scheme, along with a sufficiently small test fluid specimen thickness, retards convection in the test fluid specimen and creates a heat transfer mechanism consisting only of conduction. The apparatus is also well insulated, virtually restricting all heat conduction within the axial direction. The apparatus has been fully calibrated in order to insure accurate and precise measurement results. Finally, an automated data acquisition system has been developed using National Instruments' hardware and LabVIEW application software, which is used to obtain measurements and perform calculations.

This steady-state, parallel-plate steady-state thermal conductivity (SSTC) apparatus is used to explore the effects of polymer additives on the thermal conductivity of POLY-nanofluids. Comparative measurements have been made using the previously developed transient, hot-wire thermal conductivity apparatus, or HWTC, in order to explore the possible influence of different measurement techniques on the thermal conductivity results regarding complex POLY-nanofluids. In addition, the viscosity of POLY-nanofluids is explored in order to expand on the scope of nanofluids research. Thermal conductivity studies have been the focus of nanofluid research so far, but ultimately, their flow and heat transfer characteristics in real, practical applications will determine their usefulness as advanced heat-transfer fluids. Our new Flow & Heat-transfer apparatus for nanofluids (N-FHT) will contribute to these objectives, since many critical phenomena have not yet been investigated, and related underlying physical phenomena are not yet fully understood.

We completed design, fabrication and calibration of a Flow & Heat-Transfer apparatus for testing flow and heat transfer characteristic of nanofluids. The innovative apparatus design is presented on Figures 4-20 and 4-21, and the sensors and computerized data acquisition measurement system on Figure 4-22. The apparatus consists of a heated capillary test tube for measurement of flow friction factor and convective heat-transfer coefficient, i.e. Nusselt number, in wide range of the Reynolds numbers, including both laminar and turbulent flows. The

nanofluid flow is provided using nitrogen gas in the high-pressure reservoir, Figure 4-20, and thus avoided problems associated with pumping nanofluids. Heating of the fluid is achieved using low-voltage and high-current, direct electrical heating of the stainless steel test tube. Flow rate is measured by monitoring fluid level change in the specially designed open lower reservoir, using a high-resolution ultrasonic level sensor, see Figure 4-21. Pressure, fluid inlet and outlet temperature, and test tube wall temperature are measured to determine nanofluid flow and heat transfer characteristics. The apparatus is well instrumented and all measurements and data reductions are computerized using National Instruments data acquisition hardware and LabVIEW application software, as depicted on Figure 4-22. The computerized data acquisition hardware and software are optimized to minimize signal noise and enhance gathering and processing of useful data.

For this work, different nano size particles have been and will be tested with and without the addition of polymeric stabilizers, and with and without drag-reducing polymer additives. The current plan is to use poly (AMPS), 2-acrylamido-2-methyl-propane-1-sulphonic acid, as a stabilizing agent. This material is chosen because it can impart steric stabilization, as can any polymer attached to the surface, it will be attracted to the surface due to its anionic charge, and it has a large anionic charge to provide additional columbic stabilization (one de-protonated acid per monomer). Particles treated in this way will be tested in the experimental apparatus.

Friction factors and convective heat-transfer coefficients with polymer nanofluids are being experimentally tested over a wide range of operating conditions

- 2 base fluids: distilled water and ethylene glycol
- 3 nanoparticle types: CuO, Al2O3 and silica
- 2 nanoparticle concentrations: 1 wt%, and 3 wt%
- 2 drag-reducing polymer types: Polyacrylamide, Poly-Ethylene Oxide
- 2 particle surface-stabilizers: and Polyvinylpyrrolidone (PVP), poly (AMPS), 2-acrylamido-2-methyl-propane-1-sulphonic acid.
-

A wide specter of test samples with the following nanofluids and polymer additives are planed to be finished in Fall 2009 semester during the project extension.

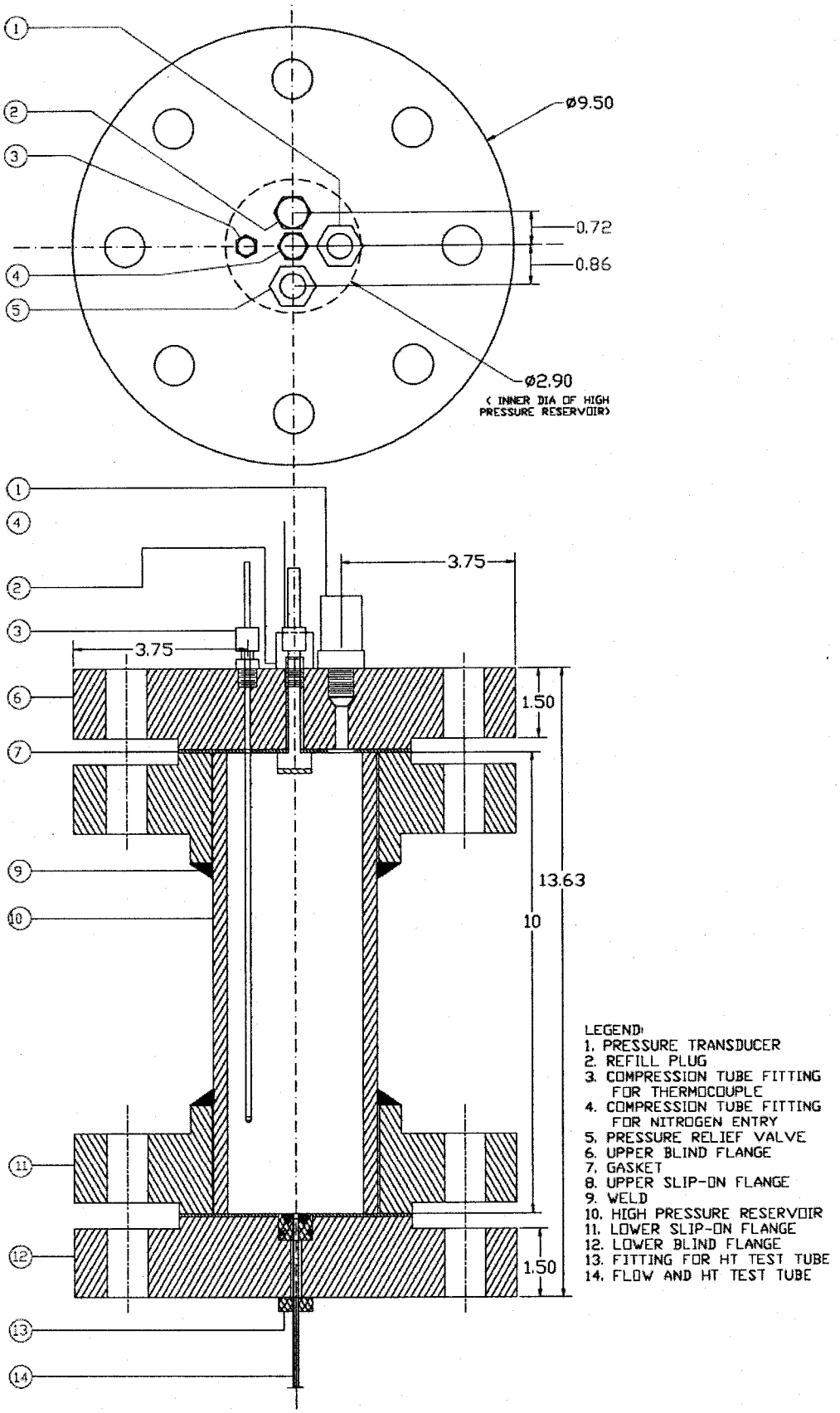


Figure 4-20 - Nanofluid Flow and Heat-Transfer Apparatus: Upper Assembly with High-Pressure Reservoir

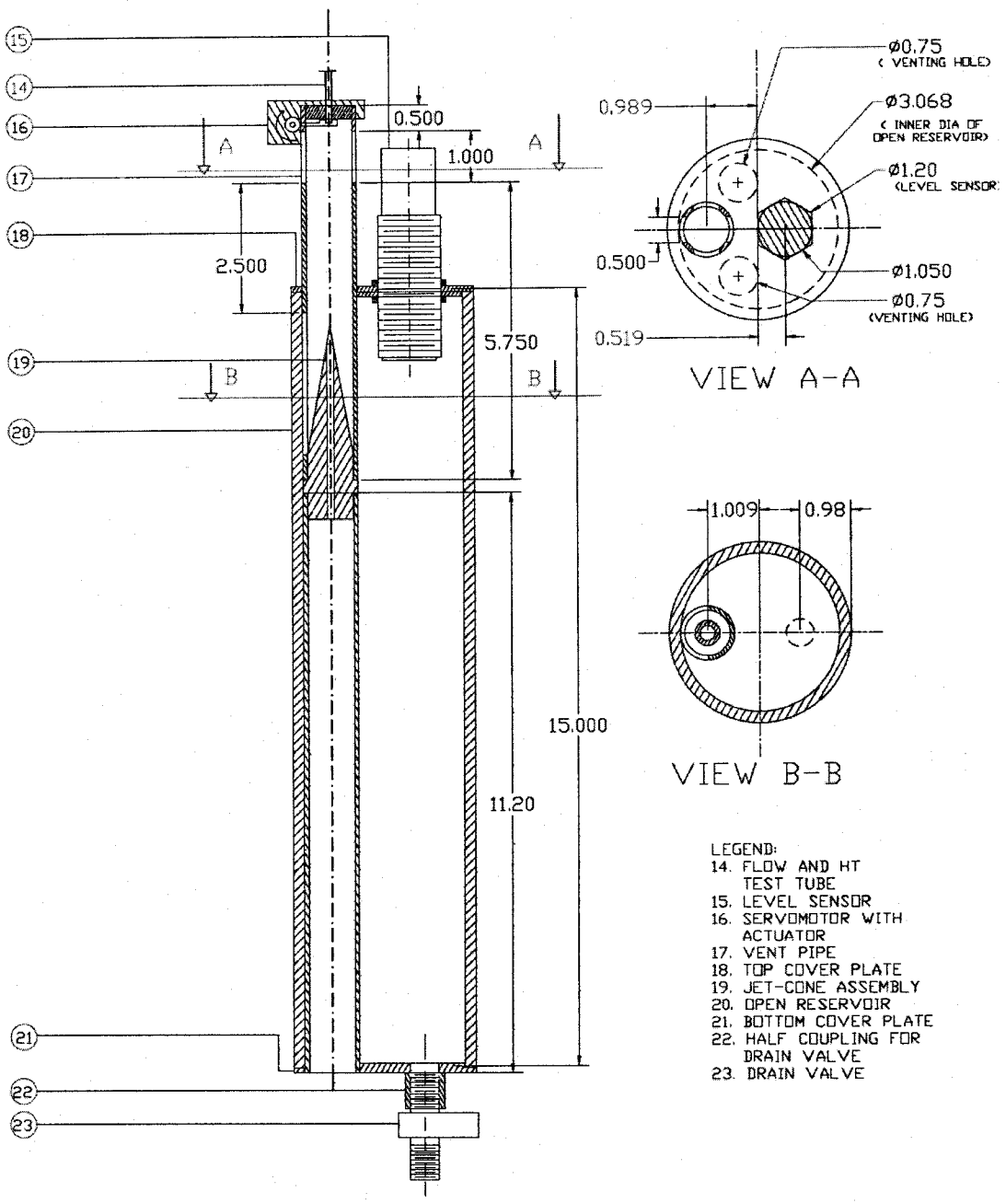


Figure 4-21 - Nanofluid Flow and Heat-Transfer Apparatus:
Lower Assembly with Open Reservoir

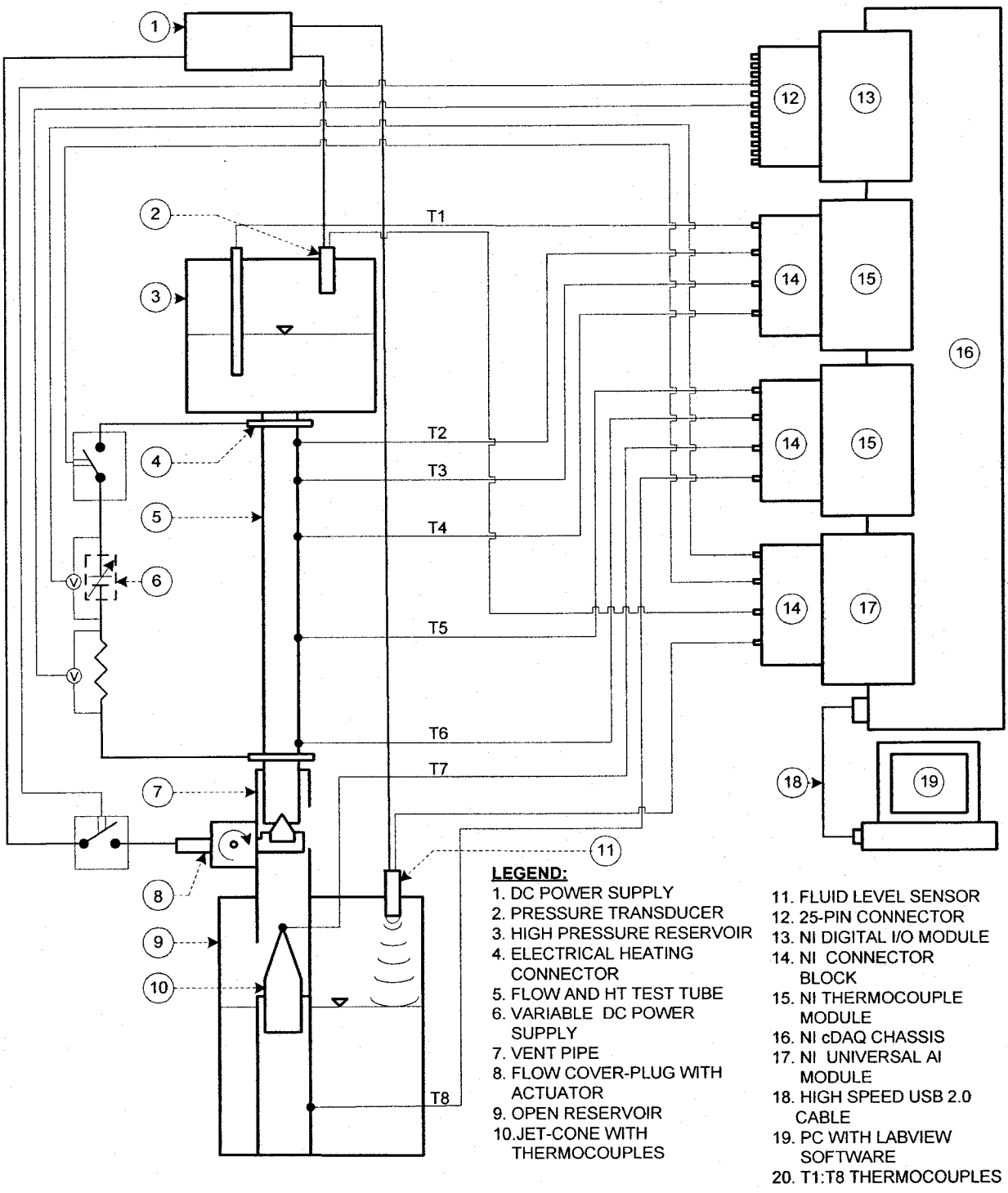


Figure 4-22 - Nanofluid Flow and Heat-Transfer Apparatus:
Sensors and Computerized Data-Acquisition Measurement System

**Task 5 - Use of Composite and Exotic Replacement Materials**

Currently, there are locomotive components which are poorly designed from an energy standpoint. The research team, with the assistance of Norfolk Southern Railroad, have identified the following parts or systems on the locomotive or attached cars that will be analyzed and redesigned, including,

- Eduction tubes – Exhaust ports on engine get clogged with the exhaust soot, and the team will look at low friction, high temperature coatings.
- Air brake hosing – Current hose is subject to wear and fatigue – Identify new material.
- Coupling knuckle – Train couplers put heavy fatigue loads on the coupling knuckle, which in turn fails at inopportune times. The research team is studying the failure of the component as well as solutions to the failure.
- Brake shoes – Current backing plate for the shoes allows for cracking as the material wears. New material and structure for the backing plates to be designed.

Analysis of railway composite brake shoe
A composite brake shoe is comprised of two parts, a steel back plate and a composite pad. Here failure is observed mainly in the composite pad, as composite is more rigid than steel, it tends to crack easily. So the composite part will be given more focus in the report.

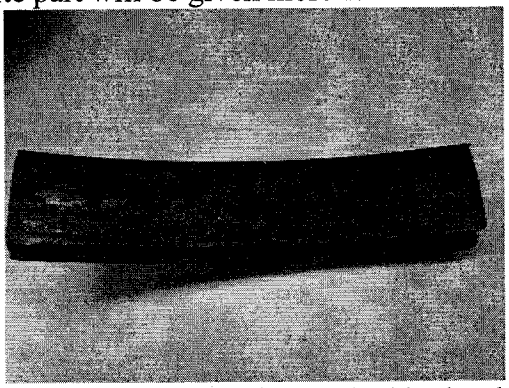

Figure 5-1 – Sample of a cracked brake shoe

Brake shoe fails mainly due to the high stress concentration and fatigue loading. In this report the analysis and evaluation for these problems has been discussed. The new brake shoe design developed to overcome the above state problem is also discussed.

For the analysis purpose total brake shoe force is assumed as the 60,000 Newton and acts at three places as shown below in the picture of the brake shoe with bracket. For the simplicity, the rotation of the wheel is neglected and the co-efficient of friction between wheel and brake shoe is assumed as 0.2.

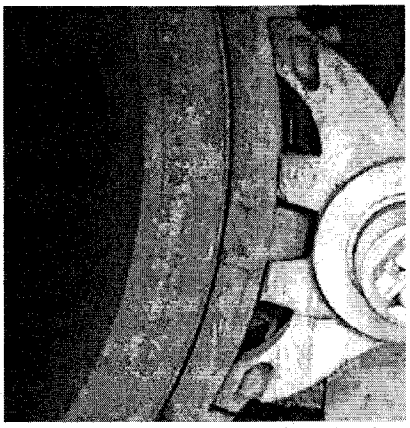

Figure 5-2 - Brake shoe with the bracket

Original design is taken from the brake shoe supplied by the Norfolk-southern company, the detail dimension drawing and material property is discussed in the following sections.

The material data table is shown in Table 5-1 for the composite material. The material properties for the steel backing plate is shown in Table 5-2.

Table 5-1 - Composite material Data

| **Structural** | |
|---|---|
| Young's Modulus | 9.9e+010 Pa |
| Poisson's Ratio | 0.22 |
| Density | 1900. kg/m³ |
| Thermal Expansion | 0. 1/°C |
| Tensile Yield Strength | 2.5e+008 Pa |
| Compressive Yield Strength | 2.5e+008 Pa |

To calculate the fatigue life S-N (stress-number of cycle) curve is required. This curve is also assumed from the available data of the similar products. This is a log-log curve and it is almost straight line, which shows the basic properties of the composite.

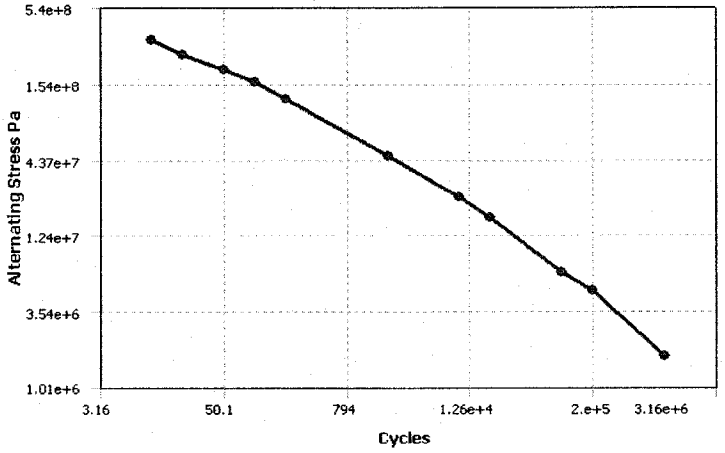


Figure 5-3 - S-N curve for Composite Material

Table 5-2 - Structural Steel material data

| **Structural** | |
|---|---|
| Young's Modulus | 2.e+011 Pa |
| Poisson's Ratio | 0.3 |
| Density | 7850. kg/m³ |
| Thermal Expansion | 1.2e-005 1/°C |
| Tensile Yield Strength | 2.5e+008 Pa |
| Compressive Yield Strength | 2.5e+008 Pa |
| Tensile Ultimate Strength | 4.6e+008 Pa |
| Compressive Ultimate Strength | 4.0e+008. Pa |
| **Thermal** | |
| Thermal Conductivity | 60.5 W/m·°C |
| Specific Heat | 434. J/kg·°C |

S-N curve for the structural steel is shown below; it is also a log-log curve for mean stress.

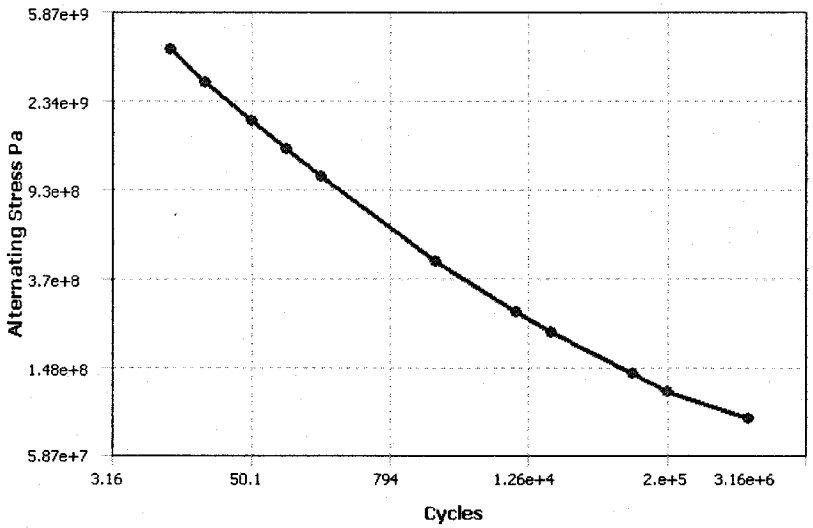


Figure 5-4 - S-N curve for Structural Steel

Static structural analysis has two cases; first case is the radius mismatch. In first case radius of the wheel is assumed 3 inches higher than the radius of the brake shoe which is 16.51 inch. In this case we will see the crack generation nearby the end of the brake shoe due to bending effect. Second case is the perfect matching radius, if radius is matching perfectly with the wheel radius, the crack may initiate near the center due to high stress concentration.

Case one occurs due to variety of the wheels is available and it is hard to find the perfect brake shoe for each wheel. In such case AAR suggests to grind the brake shoe according to the wheel's diameter, but it is not feasible because of the higher labor and machining cost. So they are using the one size brake shoes for the variety of the wheels and let the brake shoe grind by itself by the

friction material wear out and eventually case one converts into the case two of the perfect radius.

Now static structural analysis is performed under the 60,000 Newton [38] of load, which is applied at steel back plate side of brake shoe and the brake shoe is constrained for the displacement in just one direction. Wheel is assumed fixed and all constraints are shown below. Here the certain part of the wheel is used; remaining part is removed to reduce the load on the FEA solver.

In radius mismatch cases, the wheel is 3 inch higher than the brake shoe. Radius of the brake shoe is 16.51 inch and outer radius of the wheel is 19.51. Constraint image is show below, red faces shows the applied force (60000N), yellow shows the displacement control and blue surface is the fixed surface. So wheel is fixed and brake shoe is constrained to move in just one direction.

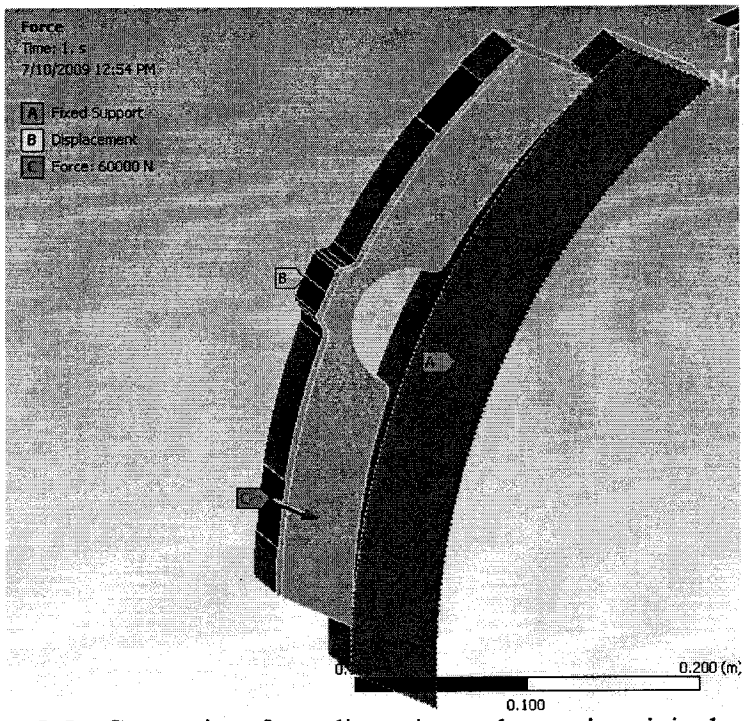


Figure 5-5 - Constraints for radius mismatch case in original model

The von-misses stress distribution after the application of the load is shown in figures 5-5 and 5-6. Maximum von-misses stress (145 MPa) is observed in the composite part of the shoe near the end of the brake shoe due to bending effect; this region is shown under the red circle (figure 5-7).

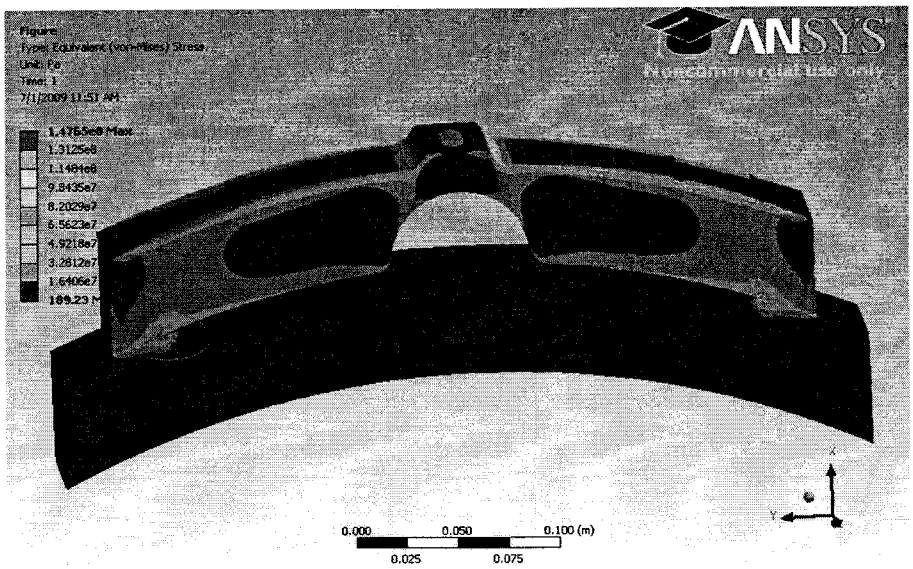


Figure 5-6 - Von-misses stress in the brake shoe in radius mismatch case in original model

Zoomed image of the area under the red circle is shown below for better view of the stress distribution. Maximum stress is almost half of the yield stress, which shows the part will not fail instantly but it will fail due to the fatigue stress.

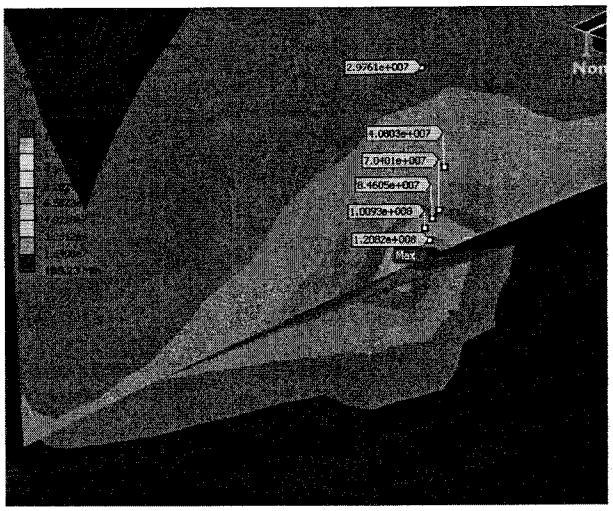


Figure 5-7 - Zoomed image of the maximum stress area for radius mismatch case

Iso-capped image of the von-misses stress provides the stress distribution at different layers, which is useful tool to determine the stress propagation. In the following image the red circled area shows the von-misses stress propagating in the same direction of the crack, which proves that the crack near by the end of brake shoe is due to the radius mismatch condition.

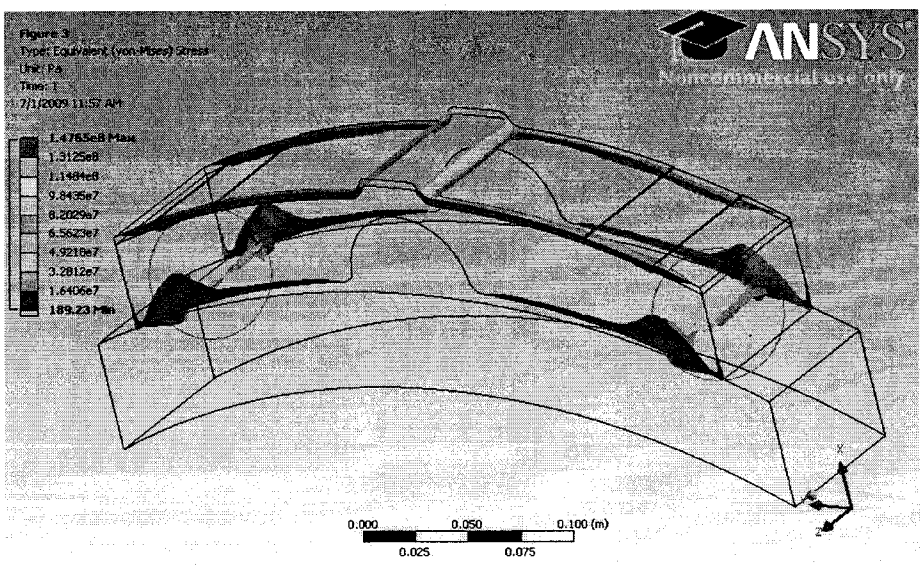


Figure 5-8 - Iso-capped image of the von-misses stress for radius mismatch case

In the case where there is a perfect radius matching between the wheel and the brake, where both have an external and internal radius of 16.51 inches, the following image shows the applied constraints in the model.

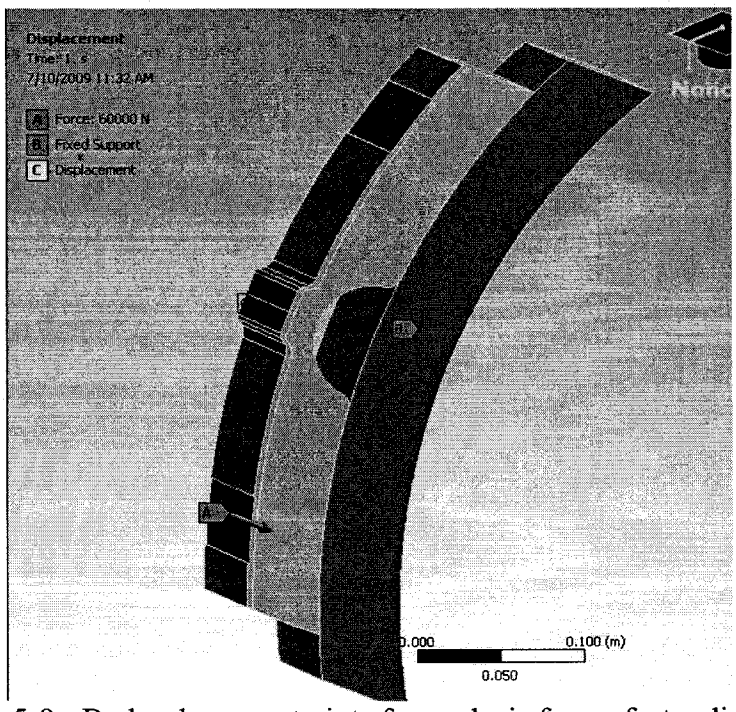


Figure 5-9 - Brake shoe constraints for analysis for perfect radius case

Here red face shows the load application, while the yellow face shows the displacement control for the brake shoe and blue faces shows the fixed surfaces for the wheel.

In the case of the perfect matching radius the maximum stress occurs near by the center of the brake shoe, which is shown by a red circle in the following image of the von-misses stress. In practice, all the radius-mismatch cases will be eventually converted in to the perfect matching condition because of the brake shoe material wear, and after that they will also shows the same characteristic as of the perfect radius matching case.

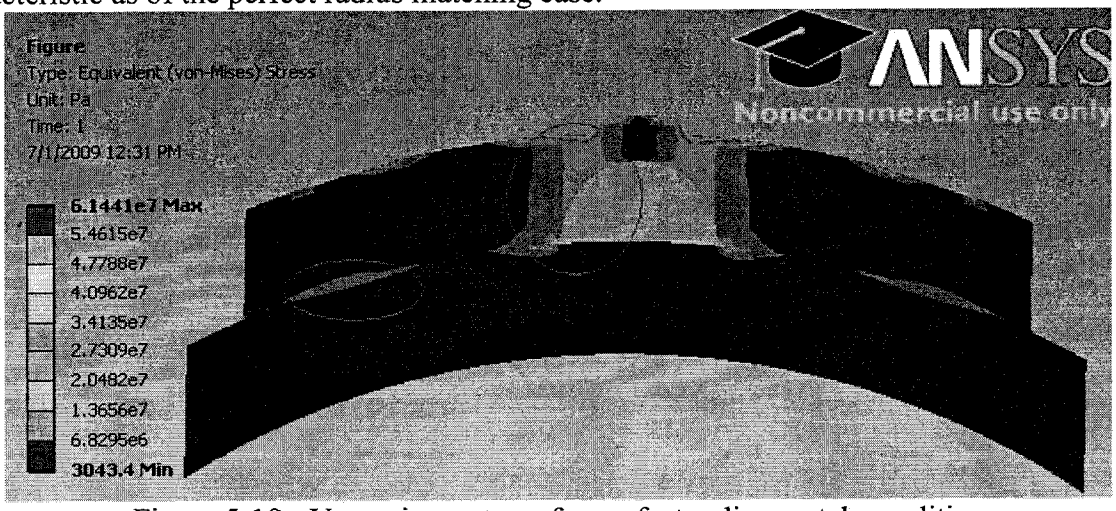


Figure 5-10 - Von-misses stress for perfect radius match condition

If we maximize the red circled area we can get the proper view of the stress distribution in the composite part of the brake shoe. Figures 5-11 and 5-12 show the zoomed view of the respectively left and right red circle.

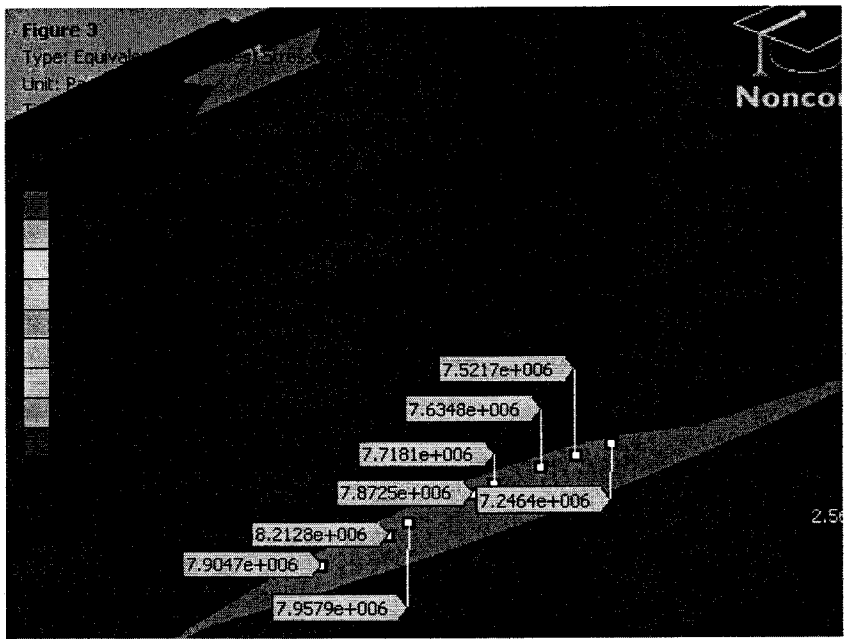


Figure 5-11 - Zoomed image of the left circled area

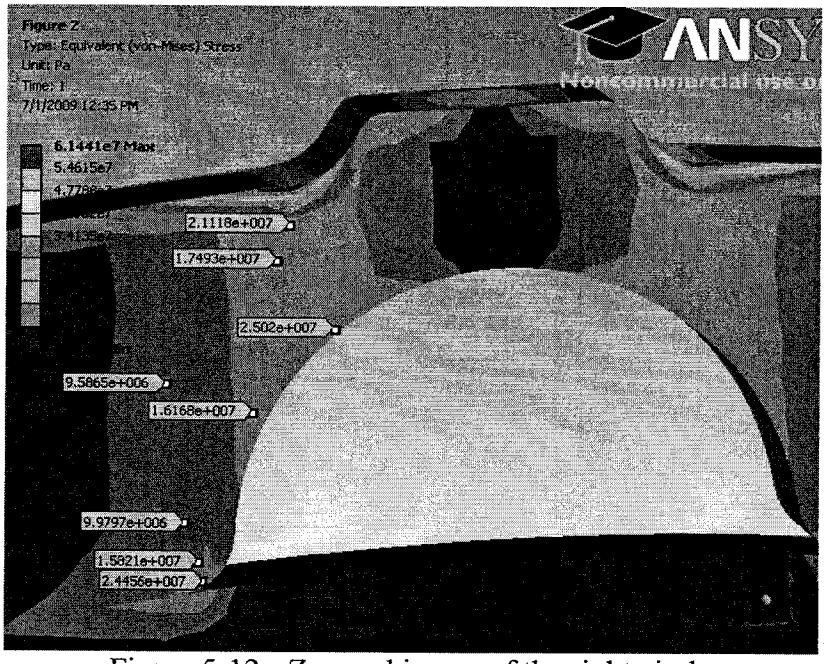


Figure 5-12 - Zoomed image of the right circle

From these images, the maximum stress in the composite part of the brake shoe is 25.02MPa, which is tenth part of the yield stress. But here the stress concentration in the composite part is shown by the green part and if we take the iso-capped image for the stress at different layers, we can see the stress concentration is in the same direction of the crack path.

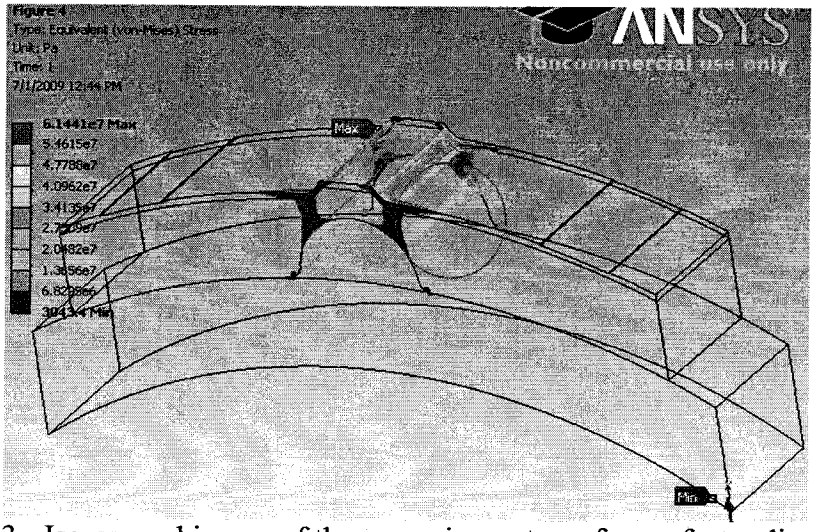


Figure 5-13 - Iso-capped image of the von-misses stress for perfect radius condition

Fatigue analysis:

In the case of the radius mismatch cases, the following image shows the fatigue life of the radius-mismatch condition model, minimum number of life of the model is estimated by the ANSYS fatigue tool is 121 cycles, after that, the first crack will propagate into the system. Life of the system is low because this is the case of radius mismatch and bending occurs nearby the end,

which is not good for the system, however, in practice the brake shoe will wear out eventually and will be converted into the case of the perfect match radius.

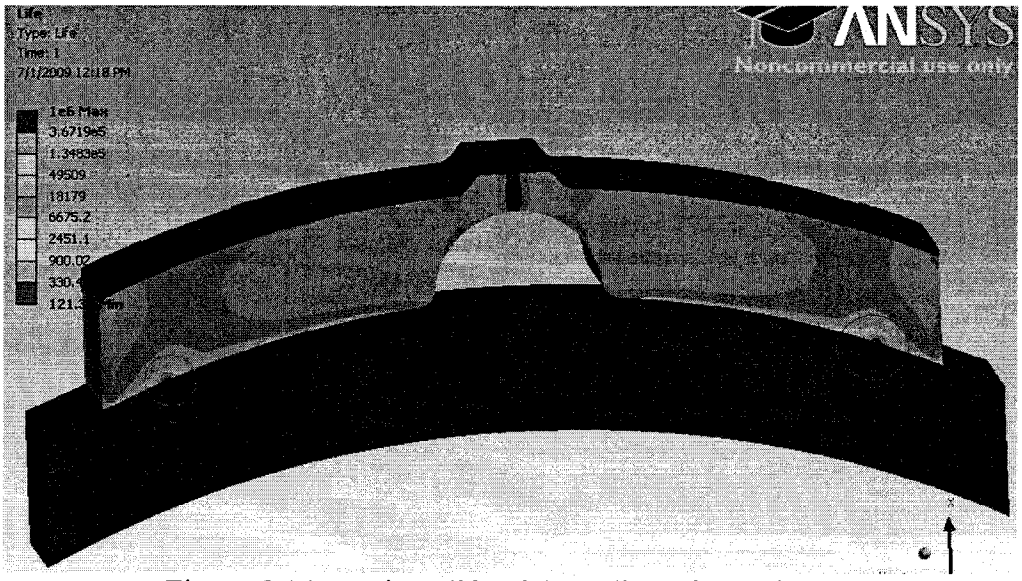


Figure 5-14 - Fatigue life of the radius mismatch case

In perfect radius cases, the radius of the brake shoe and wheel is exactly same (16.51 inches), and thus, from figure 5-13, the fatigue life is shown in the following image, and estimated at a minimum number of 6465 cycles before failure.

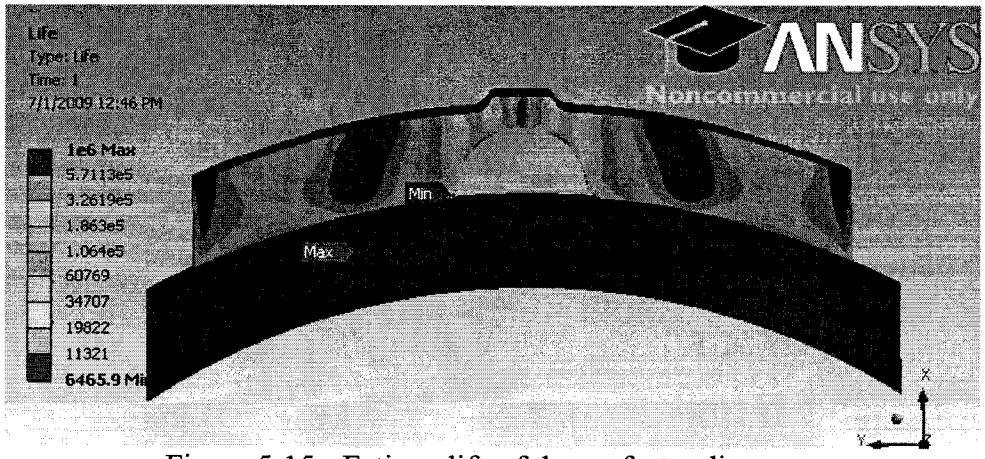


Figure 5-15 - Fatigue life of the perfect radius case

Identified problems and possible redesign:
Cracking near the end of brake shoes are generated due to the bending effect due to the radius mismatch. According to Figure 5-13 the crack at the center portion of the brake shoe is due to the excessive stress concentration at the center in ideal condition. Fatigue images shows that the first crack will initiate the system in case of radius mismatch after 121 cycles and after 6465 cycles in ideal condition case, which is very low for the brake shoe.

To reduce the problem of crack generation we need to redesign our brake shoe, and requirement of the new design is to lower the maximum von-Mises stress as well as to reduce the stress concentration by stress redistribution. In this operation brake shoe has one limitation as; composite brake shoe is not good conductor of heat. So to dissipate heat one semi-circular slot is required. In new design, instead of one semi-circular slot if we keep two semi-circular slots of smaller diameter, would give us the same heat dissipation with better distribution of the stress. To determine the best dimensions of the slots, group has created many different models with different dimensions and performed structural and fatigue analysis. Finally one of them proves superior to others and dimensions and analysis results are discussed in the following section.

A potential new design

We have developed a new design which will increase the estimated life of the brake shoe. In the new design all the major dimensions and materials are the same, however, there is a change in the shape. Original and new design has one major difference of the curved hole, in new design two semi circular holes are used instead of one of original to get the stress more distributed.

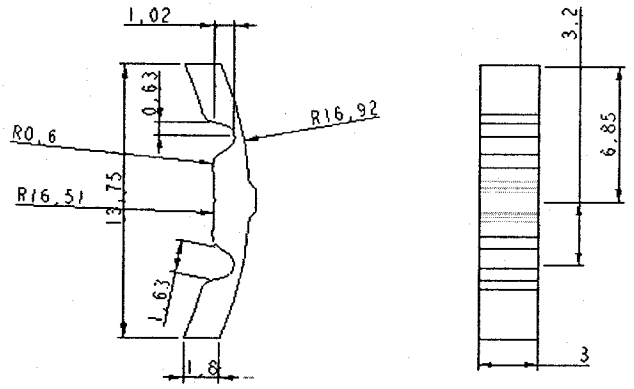


Figure 5-16 - Detail drawing of the new designed brake shoe.

In the radius mismatch case, the radius of the wheel is 3 inches higher than the brake shoe which is exactly similar case of the following. Here we have shown the constraints on the model. Red faces shows the force application, blue faces shows the fixed constraint and yellow faces shows the displacement constraints.

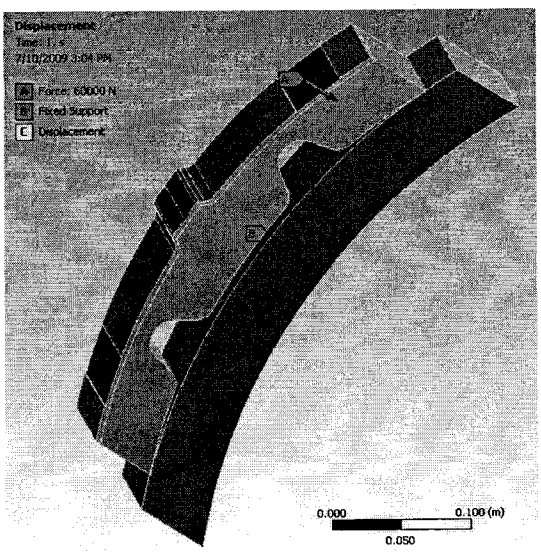


Figure 5-17 - Constraint on the radius mismatch model (new design model)

As discussed in the previous model the maximum stress is nearby the end due to bending, but it is higher than the previous case. But the maximum stress here is in the steel back plate which is not our area of interest, so the maximum stress in the composite part is shown by the red circle.

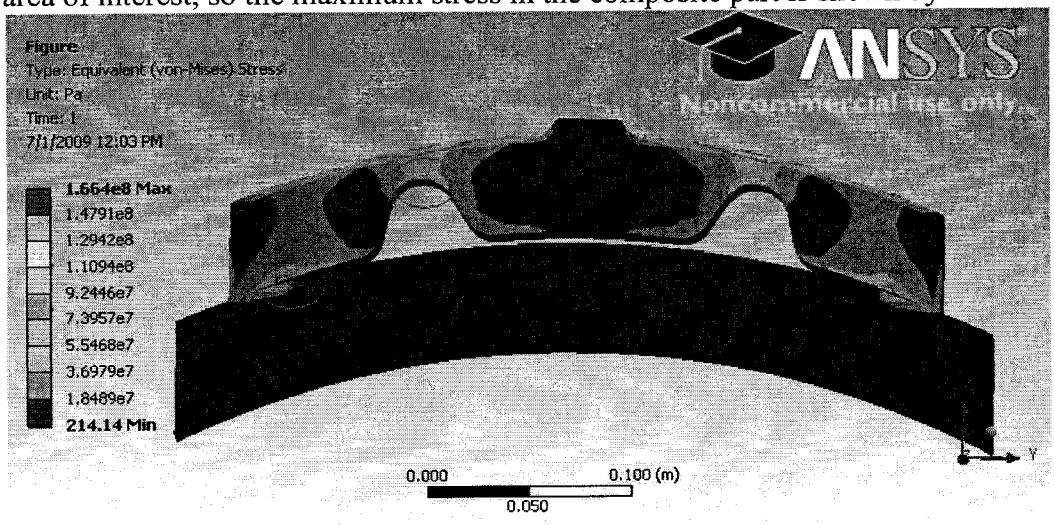


Figure 5-18 - Von-misses stress in the radius mismatch case (new design model)

Zoomed image of the red circled area is shown below, which gives the better view of the stress distribution. From these images, the maximum stress in the compoiste part is 129MPa which is considerably lower than the previous case, and this stress is also properly distributed stress.

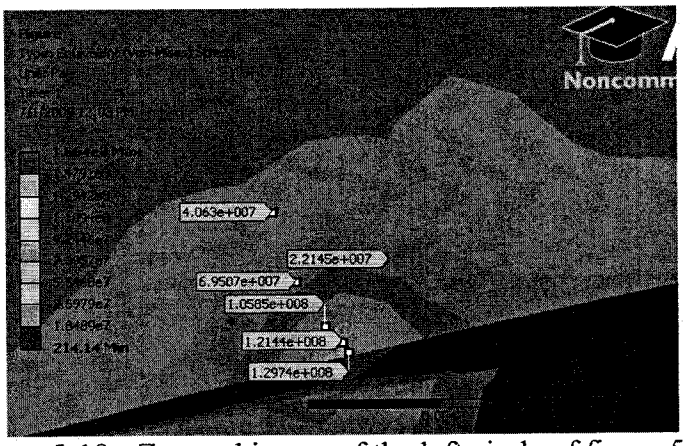

Figure 5-19 - Zoomed image of the left circle of figure 5-18

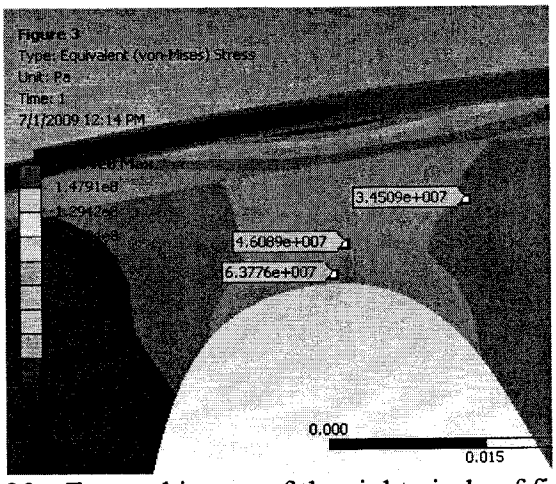

Figure 5-20 - Zoomed image of the right circle of figure 5-19

In the perfect radius condition, wheel and brake shoe has the same external and internal radius respectively. Now if we apply the same boundary condition to the model and analyze by the FEA software we can get the following results.

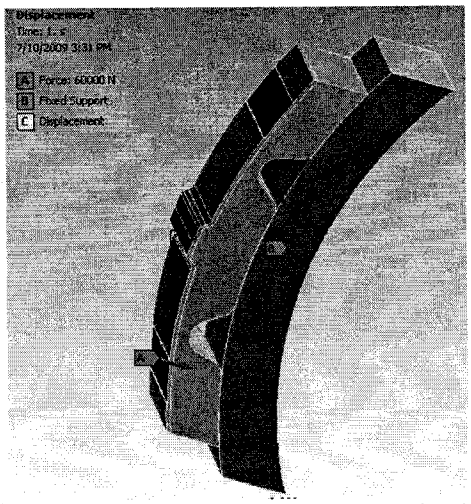

Figure 5-21 - Constraints for the perfect radius case in the new design model

In the constraint image the red face shows the force applied while yellow and blue faces shows the displacement control and fixed support respectively. The following image shows the von-misses stress distribution in the case of perfect radius match in new design model, the maximum stress in the composite part is shown under the red circled area.

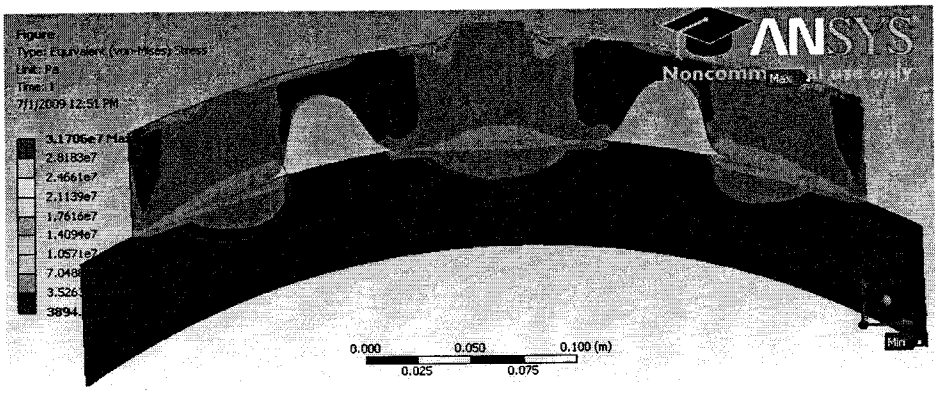


Figure 5-22 - Von-misses stress distribution in new-designed model

Images 5-22 and 5-23 shows the detail view of the left and right red circle of the above shown image. From the following figures, the maximum von-misses stress is 19.22 MPa which is also lower than the previous case.

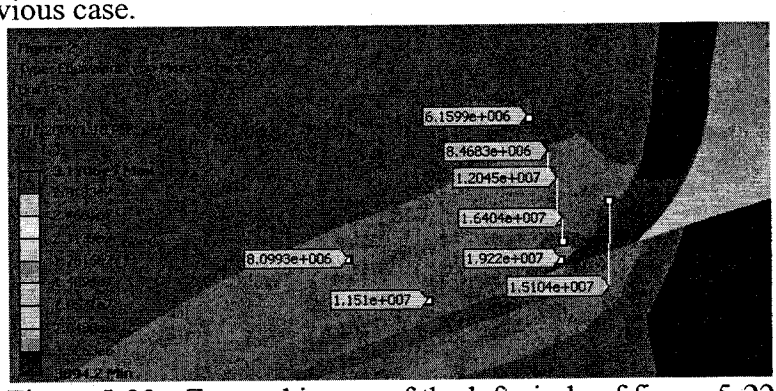


Figure 5-23 - Zoomed image of the left circle of figure 5-22

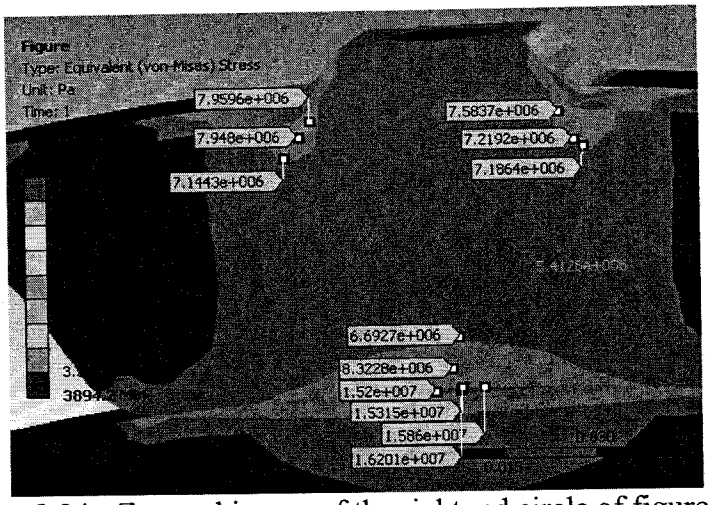

Figure 5-24 - Zoomed image of the right red circle of figure 5-22

Fatigue analysis for the new-designed model is shown below, for both radius mismatch and perfectly match radius case. In fatigue, the number of the cycles is 145 here which is better than the previous case. So this new design is more efficient than the previous design even in the radius mismatch case. In the perfect radius case, the new design model is more efficient. In such case the number of cycles is 13703 which is almost double from the previous case.

Results

In this section the original model and new designed model is discussed for the both radius mismatch and perfectly match radius case. In radius mismatch case the crack will propagate nearby the end of the brake shoe due to the high bending stress, as shown and discuss in the above sections. New model has the better design and has the lower maximum stress in the composite part, which is 129MPa compare to 147MPa almost 12.24% reduction from original model. While new designed model shows the improvement of 16.51% in the fatigue life, in the case of the radius mismatch, which is 145 cycles of minimum life in new designed model compare to 121 cycles in the original design model.

In the case of the perfectly match radius, the stress is concentrated nearby the center part, which is causing the crack generation nearby the center. In practice the radius mismatch case eventually converts into the perfectly match radius condition due to material wear out. Here in the case of the perfectly match radius, the original model has the maximum von-misses stress of 25.02MPa, while the new design model has sthe maximum von-misses stress of 19.22MPa, which shows 23.18% reduction in maximum von-misses stress. Even this stress is more distributed so it affects the fatigue life drastically. Fatigue life of the original design is 6465 cycles, while new design model has the fatigue life of the 13703 cycles which is improvement of 111.98%. From these result the new designed model proves more efficeint in the both cases of the radius mismatch and perfectly match radius.

Cost analysis of the railway composite brake shoe

The aim of this project is to provide cost analysis for the manufacturing process involved in producing the railway composite brake shoes. The current price for purchasing one composite brake shoe is approximately $10.52. The focus is to reduce the cost and increase the life of the

brake shoes using the new design. This analysis will detail the costs necessary to produce on new brake shoe in the same batch sizes as the original model. Based on a detailed analysis, the cost to manufacture the new shoe is approximately equivalent to the current shoe.

Train Coupler Analysis

The research team is also tasked with the analysis of the train coupler mechanism which securely attaches two adjacent cars. Currently, the railroads are experiencing failure at elevated rates of the coupler knuckle which is shown in Figures 5-25 and 5-26 (as a computer model).

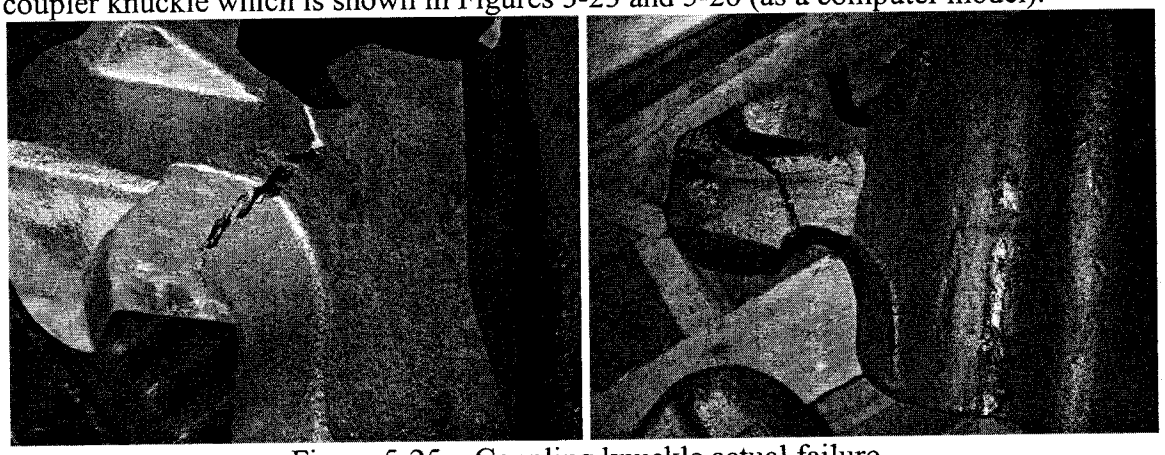

Figure 5-25 – Coupling knuckle actual failure

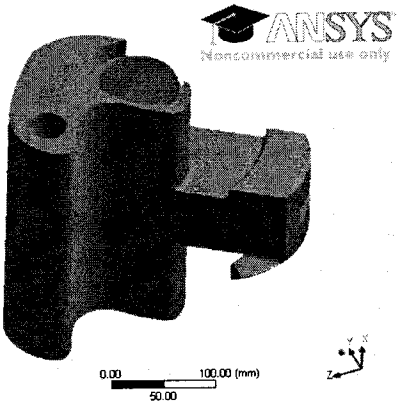


Figure 5-26 – Computer model of coupling knuckle

The design team modeled the current knuckle using the analysis ANSYS under an applied static load. It was found through analysis that the material used in the creation of this component is cast iron, and Figure 5-27 shows the finite element mesh that was used in the knuckle modeling, and Figure 5-28 details the force loadings for the knuckle.

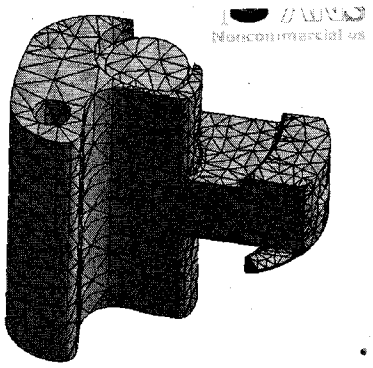

Figure 5-27 – FEA Meshing of coupling knuckle

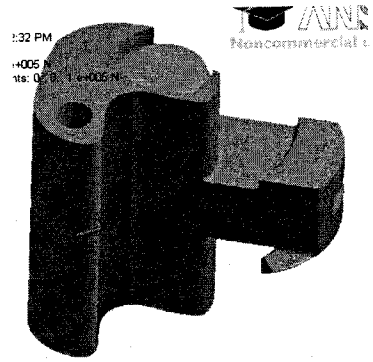

Figure 5-28 – Force application in the coupling knuckle

Based upon the initial results found through this analysis, the maximum stress in knuckle is occurring in the section shown below. However, in discussion with the NS shop staff, it was determined that the knuckle fractures across the flat connection area, shown in red below.

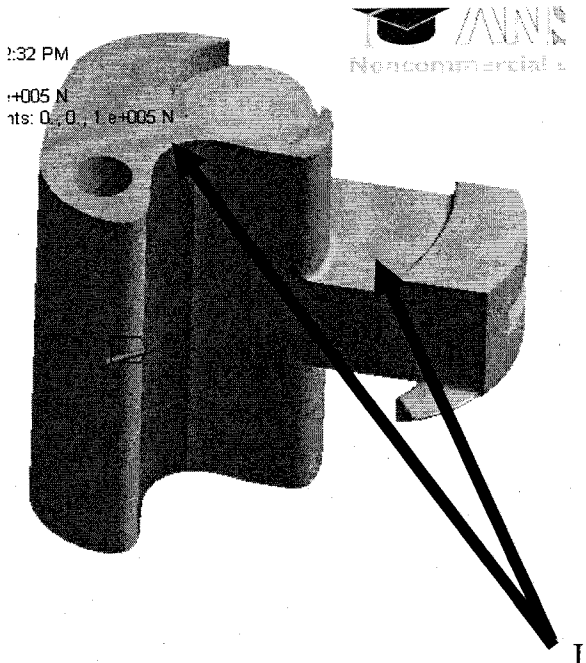


Figure 5-29

Conclusion

Based upon the results which were obtained through the finite-element analysis, the high stress levels were identified in the areas in which typical cracking occurred. As such, the team now has the tools to predict where cracking will occur. It has been determined that the typical source of this cracking was due to stress concentrations in the material and forming process. In addition, the removal of material from the internal cavities of the knuckle could contribute to the failure issues. To remedy this failure, the team is looked at two approaches.

- Laser Cladding
- Laser surface remelting

The laser cladding process will added about 1/8 inch of material to the areas which have been shown, through FEA analysis, to have high stress concentrations. This process will remove stresses and not add much weight to the structure.

The laser surface remelting is a process in which a NdYAG laser is used to remelt portions of the surface where high stresses occur. Through experimentation, it was learned that through the original casting process, large, deep voids exist in the cast iron material. These voids weaken the structure by adding stress concentrations. The issue exists that the voids can occur anywhere, however, the stresses are greatest at the outer surfaces. Thus, the researchers are using the remelt process to smooth out the exterior surfaces and remove voids and areas in which stress concentration factors can and do occur.

At this point, two knuckles have been through the laser cladding process and they have been sent to NS for strength testing. The results of the testing indicate that the laser cladding process did a little in the area of strength of the part. However in order to utilize this change, much more progress need to be shown. In order to obtain much better results in terms of strength and weight reduction, the knuckle is in need of complete redesign. However, at this point in time, introducing a more expensive knuckle to the industry is not going to work, and this industry will not make drastic changes.

Pneumatic air-brake hosing

Triple Crown trailer cars are experiencing pressure losses in brake lines resulting in unintentional application of the brakes. The rate of brake pipe reduction is defined as a pressure drop per unit of time of the brake pipe pressure used to cause a brake application. Two rates are used to cause brake application.

1. A pressure drop of 20 psi in more than 1.4 second is referred to as a service rate of reduction and causes a service brake application.
2. A pressure drop of 20 psi in less than 1.2 seconds is referred to as an emergency application and causes an emergency brake application.

Currently there are situations that trigger a false emergency brake application known as an undesired emergency (UDE) brake application. Therefore, there purpose of this project is to analyze the WABCO brake control valve used in the braking system to determine the cause of

the unintentional emergency brake applications. During operation vibrations experienced by the valve might contribute to these unwanted pressure drops. Additionally pressure fluctuations may occur due to the increases and decreases in the brake pipe volume with the possible addition of a rippling effect of the 320" hose that ties one trailer. The experiments conducted, measured vibrations and pressure. Vibration experiments involved two three-axis accelerometers measuring g-forces mounted directly on top of separate valves each held in place by either a fabricated or casted steel bracket. Several pressure sensors were also placed at the front, middle, and end of another train with the goal of recording what kind of pressure fluctuations Norfolk freight trains are undergoing. From the data received by the accelerometers, it was shown that the valve on the casted steel bracket was excited at a maximum frequency of approximately 35 Hz. The valve on the fabricated steel bracket was excited at maximum frequency of approximately 50 Hz. A conclusion was reached that these frequencies may approach natural frequencies of the two types of brackets. The data gathered from the pressure sensors revealed that with an increase in distance from the train locomotive, there was an increase in time it took for the pressure in the supply line to reach 88 psig which is the approximate amount required to release the brakes. While analyzing data, it was learned from a WABCO engineer that removing cars from the train had eliminated the pressure losses. When comparing information received from outside sources and the pressured data that was gathered, it was concluded that head loss from an unknown source rather than vibrations on the valve appeared to be a more likely cause of the UDE's.

Introduction

The Wabco ABDX brake valve is the part of choice on Norfolk Southern's train cars. The air brake valve is designed for the brakes to be fully engaged when no pressure is present. This "fail-safe" design is a necessary feature for a vehicle with such an extreme amount of potential for disaster if all brakes were lost. Norfolk Southern has experienced problems with the emergency brakes engaging during travel. This experiment analyzes the operating vibration experienced by the brake valve and the air line pressure throughout the length of the train. Conclusions will be drawn from the data collected to attempt to determine if ABDX valve failure is being caused by the vibrations it experiences during travel or by supply line pressure fluctuations.

Table 5-3 - Identification of various braking components

| **Part Number** | **Part List** |
|---|---|
| 2 | Hose and Coupling |
| 3 | Draft Gear |
| 4 | Brake Shoe |
| 5 | Truck-Mounted brake Assembly |
| 9 | Retaining Valve |
| 10 | End-of-Train Assembly |
| 11 | Two-Compartment Reservoir |
| 12 | Universal Handbrake |
| 13 | Brake Pipe End Cock |
| 14 | Empty and load Valve |
| 15 | Dirt Collector And Cut-out Valve |
| 16 | ***ABDX Freight Brake Control Valve*** |

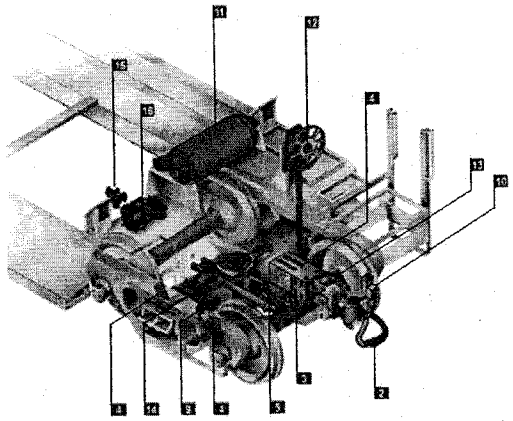

Figure 5-30 - Main braking components as they appear on the bogie assembly

The overall braking system is displayed in Figure 1 with main components identified in Table I. It is important to note the location of the ABDX valve (part number 16) as it sits on a mounting bracket attached to the bogie assembly. Prior to malfunctions in the braking system, the ABDX valve was originally positioned inside the actual train car itself. This information will be taken into account when data is recorded and analyzed.

Theory

Freight train braking systems are designed so that the brakes are released by air pressure, and applied when the pressure is reduced. The pressure that controls the braking operation originates from a main compressor located in the locomotive. The compressed air produced travels back to the train cars where the ABDX brake valve on each car will charge the auxiliary reservoir which stores the necessary pressure to release the brakes when needed.

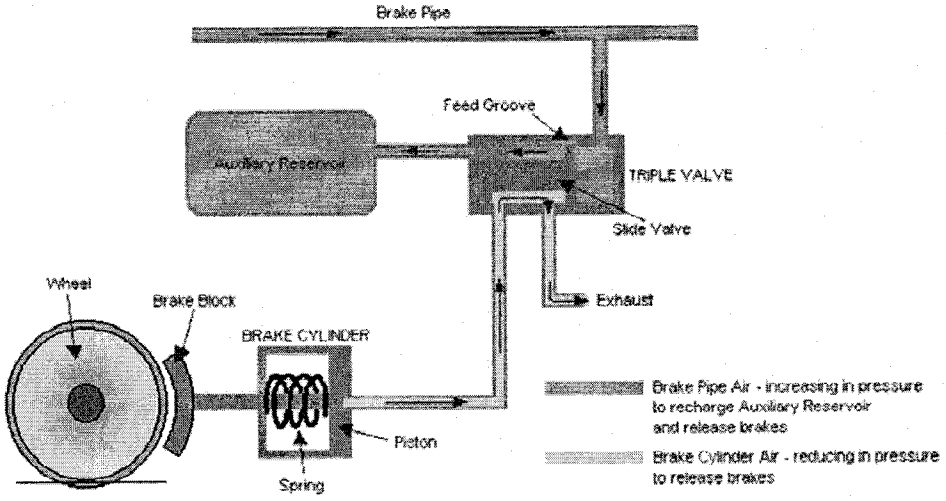


Figure 5-31 - Illustration of brake system operation during release position

Figure 2 illustrates how the control valve operations during the release position of the brake block from the wheel. After the pressures in the supply line and auxiliary reservoir reach a specified level the piston inside the brake valve moves to release the pressure inside the brake

cylinder. A spring is used inside the brake valve to assist in exhausting the air and releasing the brakes. The WABCO ABDX brake valve has been designed with long duration train use in mind. The seals, pistons, and mounting hardware all have been chosen to handle constant low amplitude vibration. Until recently, the valves were mounted inside of each train car where they were isolated from most vibration during travel. The current train car bogie design has been changed so that now the valve is mounted on a steel bracket that itself is secured to the bogie assembly. The fittings and layout of the air supply line have also been modified in order to accommodate the new mounting location. With these things in mind it was chosen to collect data related to what kind of vibrations the brake valve experienced during a normal trip. It was also determined that data needed to be collected relating to how the supply line pressure from the locomotive changed throughout the length of the train. If the vibrations occur during travel that are close to the natural frequencies of the new mounting brackets a resonance effect may occur causing the amplitude of the vibration to be amplified. Also, if the supply line pressure doesn't rise quickly enough to fully release the brakes in the rear of the train valve damage may occur as well.

Experimental Procedure - Vibration Data Acquisition

Vibration analysis of the ABDX Freight Brake Control Valve and triple valve mounting bracket was preformed so that the experimental vibration characteristics experienced during train transit could be calculated. A Triple Crown Services hub located in Ft. Wayne, Indiana was chosen as the experimental set up site based on the train availability. Two separate trials were completed. Trial one was completed with wheels clean of damage, trial two tested worn wheels. A train car was fitted with two different triple valve mounting bracket designs. An older fabricated valve bracket and a newer cast valve bracket were chosen to gain an understanding of how the bracket design effects the vibration characteristics experienced. Specific physical bracket characteristic are discussed further in the ANSYS Simulation Procedure. Accelerometers sensors were chosen to experimentally test the vibrations experienced because of their sensitivity, method of digital signals, and noninvasive qualities. The test included two SENSR GP1 Programmable Accelerometers, which are 3-axis MEMS accelerometers. The SENSR G1 consists of 6061-T6 Aluminum housing material, and is powered by 2xAA alkaline batteries for a 40 day operation life. The GP1 has a sample rate of 100HZ per axis, and stores all data on a 1 megabyte internal memory system. All SENSR GP1 Accelerometers are programmable through USB connection which is directly linked to a PC computer. Acceleration calibration was completed in lab at Northern Illinois University prior to shipment to the test site.

The GP1 Accelerometer was set to record data in two main methods. Method one is as a Data Recorder which continuously records data at all times. Data is recorded at a frequency of 100 Hz, storing maximum, minimum, and average G-Force experienced. This data will give a general trend of the experienced accelerations in three separate axes. The second recoding method is as an Event Recorder, which is designed to show a more detailed view of the experienced G-Forces. The Event Recorder is activated when a G-Force goes above 5 g's. Once the Event Recorder is activated, a pre-trigger of one second and three seconds after the event is recorded. Once the accelerometers are calibrated and sealed for testing the sensors will be directly mounted to steel casted plates with machine screws. The plates provide a rigid and reliable platform that is easily installed and removed from the ABDX Brake Valve bogie system.

A very important aspect of the accelerometer procedure is to introduce an orientation nomenclature that assigns orthogonal axes values which correlate the accelerometer axis to the orientation of the train.

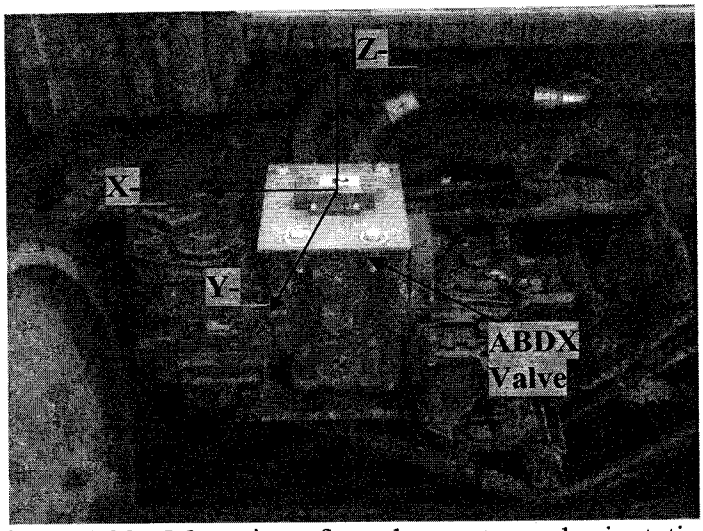

Figure 5-32 - Mounting of accelerometer and orientation of axis

Figure 3 shows the accelerometer and mounting plate bolted directly atop the ABDX Control valve using machine bolts and lock nuts. The bolts and nut linking system was chosen for ease of installation and removal as well as the linkage systems ability to resist loosening during testing. The orientation of the axes is overlaid onto the figure. The lateral axis or X corresponds to the axis perpendicular to the plane of the train tracks. The longitudinal or Y axis corresponds to the parallel plane of the train tracks and the direction of travel that the train and valve make. Last is the vertical or Z axis which corresponds to the plane perpendicular to the ground or train track surface.

Trial one of the vibrations experienced by the ABDX valve consisted of train trip from Ft. Wayne, Indiana to Chicago, Illinois were the accelerometers where then removed and shipped back to the lab for analysis. The test began on October 15, 2009 at 1:15am as the train left Ft. Wayne and the tested ended the same day as the train arrived in Chicago at 11:30am. The total train travel time was 10 hours and 15 minutes but the actual test time was about 4 hours which was the amount of time that the train was in motion. Accelerometer 1 for this test was mounted on bogie #3678 on a cast style bracket, while accelerometer 2 was mounted on bogie #4338 on a welded style bracket. Trial two consisted of a train trip from Chicago, Illinois to Harrisburg, Pennsylvania and again the accelerometers were removed and shipped back to the lab for analysis. For this test Accelerometer 1 mounted on bogie #6404 on a cast style bracket, while accelerometer 2 was mounted on bogie #3433 which is a welded style bracket.

ANSYS Simulation

Modal analysis of the triple valve mounting brackets was performed so the natural frequency of the different designs could be estimated. There are two different bracket designs currently in use

on the trains being examined. The older version is a fabricated bracket comprised of five separate parts that are spot welded during assembly. The newer design is a cast design that is molded to increase structural integrity and life. Both the fabricated and cast brackets are made from A572 Grade 50 steel which has a density of 0.284 lbm/in$^3$ and Young's Modulus of 2.9 x $10^7$ psi that make it a good choice given the application and material cost.

Prior to performing finite element analysis of the brackets, they were modeled using PTC ProEngineer Wildfire 4.0. ProEngineer allows for creation of detailed 3D models that can be exported directly into ANSYS v11.0 for modal analysis. Detailed engineering drawings were provided by Wabash International so that the models created were exact representations of the brackets being used.

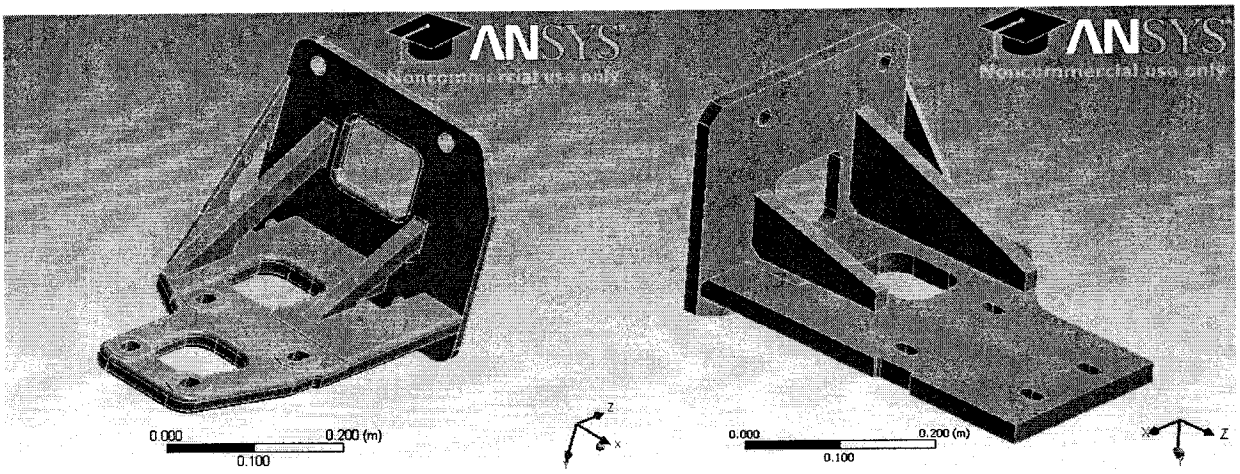


Figure 5-33 - 3D model of the casted and fabricated steel brackets on which the ABDX valve is mounted

After the modeling of each bracket was completed, the assemblies were exported to ANSYS Workbench for analysis. Figure 4 displays the casted bracket to the left and the fabricated bracket to the right as they appeared in the ANSYS Workbench. In order for the software to produce accurate results, various constraints must be defined. Structural steel was chosen for the material assignment as its properties are similar to those of the A572 that is used in production. ANSYS also allows the user to define the types of connections used during component assembly. This was used to demonstrate the difference between the welded surfaces on the fabricated brackets and the cast model. Furthermore the constraining locations of each part are defined so that simulations can be performed as if the bracket was actually installed on the train bogie. This was done by defining fixed supports at each of the four mounting holes where the bracket is bolted to the bogie. The rear surface of the mounting plate was also defined as a frictionless contact to further simulate the actual mounting conditions it experiences.

After the constraints had been defined modal analysis could be performed. The first 6 modes of each bracket were calculated along with alternating stresses and strain-life characteristics. The final post-simulation report also provided geometric properties such as approximate volume and mass which were compared to actual known values for each bracket. The agreement between these numbers provided some level of confirmation that the models used were indeed accurate representations of their real-world counterparts.

Air Supply Line Pressure Data Acquisition

The testing of the brake line pressure utilized three Omega Transient Pressure Data Loggers, Model number OM-CP-PRTRANS-1-300-G-SS. The Omega Transient Pressure Data Loggers utilizes a semiconductor strain gauge pressure sensor capable of a 100Hz sampling activated by high and low pressure thresholds. With a reliability of 2% FNR and a repeatability of ±0.5% combined with a 3.6 V lithium battery pack capable of 3 days of continuous data acquisition; the Omega Transient Pressure Data Loggers are suitable for the required extended data collection. The programmable threshold limits will allow for real time data acquisition of the brake pressure outside the limits, but when pressure is within the limits no data will be stored preserving memory capacity.

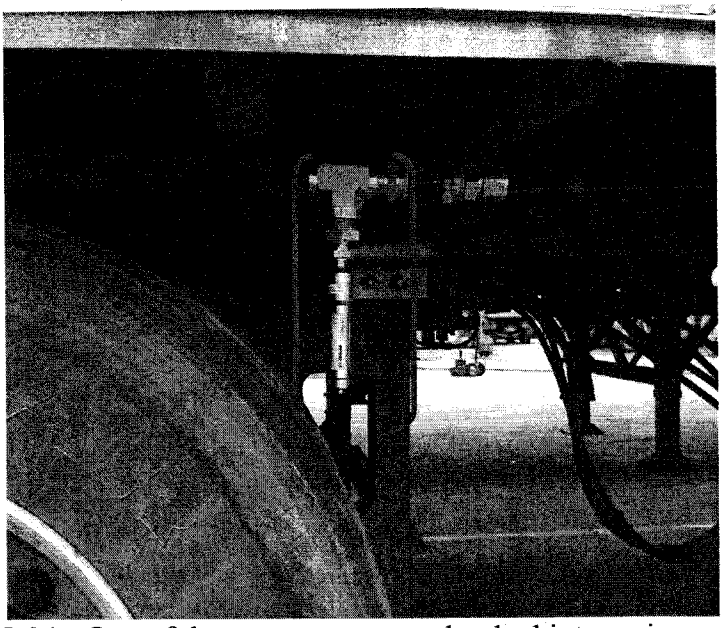

Figure 5-34 - One of the pressure sensors hooked into main supply line

The test will use three identical pressure transducers placed at various locations in the brake lines. This will help display brake pressure gradient from the train locomotive to the final 148$^{th}$ train car. The first sensor was located at the second car of the train, followed by one on the 75$^{th}$ train car, and finally a sensor at the 148$^{th}$ train car. Figure 5 shows how the pressure sensors are linked into the brake line using a series of pipe fittings. The sensors were installed by a professional who is experienced with train brake systems to insure that the sensors and fitting connections will not leak.

The Omega pressure sensors were programmed in lab at Northern Illinois University using a PC computer. Train cars 2 and 75 were calibrated to collect any pressure data from 0 to 87.8 PSIG. This window of pressure was chosen to gain an understanding of the increase and decrease of pressure within that range, any value outside does not affect the brakes effectiveness. The train car 148 was fitted with a pressure sensor with a window of 0 to 86.4 PSIG. The third sensor was set lower than that of the sensors located in the front of the train because it was thought that the back of the train due to pressure gradients reaches a lower max PSIG.

Data and Results - Vibration Data Results

In this section the raw vibration data is analyzed using an algorithm which finds the peak amplitudes in the signal, then using a Fast Fourier Transform (FFT) finds the dominate frequency components in the signal. The peak amplitude of the signal is an indicator which shows the axis that experiences the highest acceleration. The raw signal from the three orthogonal axes is analyzed individually for each four second event recoded. The algorithm for each event is to input the raw signal into MatLab R2008b software. The data results are input into an Excel spread sheet in order to more easily view and compare the results. The analysis is designed to be compared with the vibration test performed on 12/10/2008 which tested two air-brake control valves in the Triple Crown system.

The first step in the analysis was to look at the general trend of the data by view the Data recording portion of the both the clean and worn bogies. The cast bracket on the clean bogie #3678 experienced the greatest peak amplitude spikes on the (Y) axis with values as high as 7.68 and as negative as -10.83 g's. The (X) axis most closely trended with the (Y) axis while the (Z) axis experienced similar wave shapes but at lower amplitude. The (Y) axis experienced forces in a range of ±1 to 5 g's, the (X) axis in a range of ±1 to 4 and the (Z) axis experienced a range of ±0.5 to 4 g's. The welded bracket on bogie #4338 experienced very similar results to the cast bracket in the (Y) and (X) axis's. The (Y) axis experienced forces in a range of ±1 to 5.5 g's, the (X) axis in a range of ±1 to 4. The difference in the direct comparison is that the (Z) axis experienced forces from ±1 to 5.5 with peaks as spikes as high as 7 g's. Form this data it can be concluded that with a clean set of wheels, the ABDX control valves experience greater overall vibration with the cast bracket.

The general trend analysis of the Data recording mode of the worn bogie wheels proved to show much higher values of vibration. First the cast bracket on the worn bogie #6404 experienced vibrations which were higher in magnitude. The (Y) axis experienced forces in a range of ±0 to 6.0 g's, the (X) axis in a range of ±1 to 5.0 with high peaks as high as 7.5 g's. The (Z) axis experienced forces from ±0 to 5.5 g's. The results of this data highlight the increase in vibration caused by the damage in the wheels. The accelerometer experienced the higher vibration amplitudes levels than both the clean bogies. The welded bracket on worn bogie #3433 also experienced peak amplitude forces greater than the clean bogies. The data from bogie #3433 saw the vibration that was not consistent with the rest of the tests. In this data set the (X) axis experienced the greatest peak amplitudes consistently within a range of ±0 to 6.5 g's. The (Y) axis experienced g's in a range of ±0 to 5.0 g's, while the (Z) axis experienced a range of ±0 to 5.5 g's with spikes as great as ±7.5 g's. All of the spikes seen in the data are thought to be random events that though still effect the system are not consistent enough to be considered part of normal operating conditions.

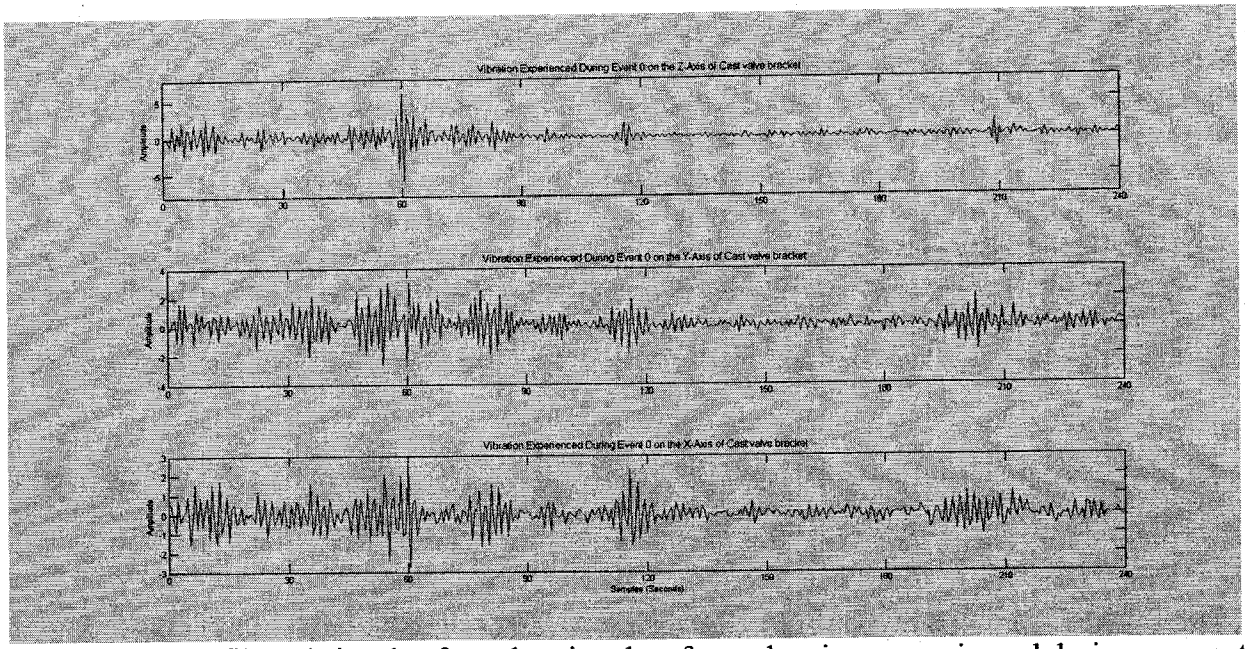

Figure 5-35 - Unfiltered signals of acceleration data for each axis as experienced during an event for the casted bracket.

The second portion of the test is to look at the events of the raw vibration data collected from the clean and worn wheels. The first indicator of the data is to look at the amount of events recorded by each accelerometer. The events were recorded if a 5 g force was experienced for durations of 0.01 seconds. In the test with the clean wheels bogie #3678 with the cast bracket recorded 12 events while bogie #4338 with the welded bracket recorded 20 events. According to this data the vibration transferred to the ABDX control valve is less on the cast than the welded bracket. In the test with worn wheel bogies, #6404 with the cast bracket recorded 443 events while bogie #4338 with the welded bracket recorded 246 events. The worn wheel test indicates that the style of bracket does not affect the amount of vibration transmitted to the ABDX control valve as much as the condition of the wheels.

The raw vibration signal is analyzed to gain an understanding of type of vibration that each axis experiences. The signal is graphed using Matlab R2008Bb software, to see if the accelerometer experiences low frequent vibration or large sudden jumps occur and then dissipate. Figure 6 is an example of an event recorded during testing. Figure 6 shows vibration experienced by the x, y, and z axis of the accelerometer during a typical event. From these plots peak amplitude can be recorded and compared to the other peak axial amplitudes of the same event. By comparing the axial peak amplitudes the axis that experiences the greatest acceleration during normal train operations can be identified.

By graphing the three orthogonal axes against each other as figure 6, the type of vibration can be directly compared. It can be seen that the vertical axis typically experiences a single vertical jump that dampens to near zero. The longitudinal (X) and the lateral (Y) axes show more excitation which is maintained for longer periods of time. This result is causes most likely by sharing the same two-dimensional plane and experiencing similar excitation forces. For both types of brackets it was found that the (Y) axis running parallel with the tracks experienced the

greatest forces. The (Y) axis having the greatest experienced force is believed to be due the train cars being loaded to different weights. When the cars are loaded to different weights they will have different momentums, as a result the cars length will experience compression and tension forces. The next step in analyzing the data is to find the frequency components that characterize the signals the most.

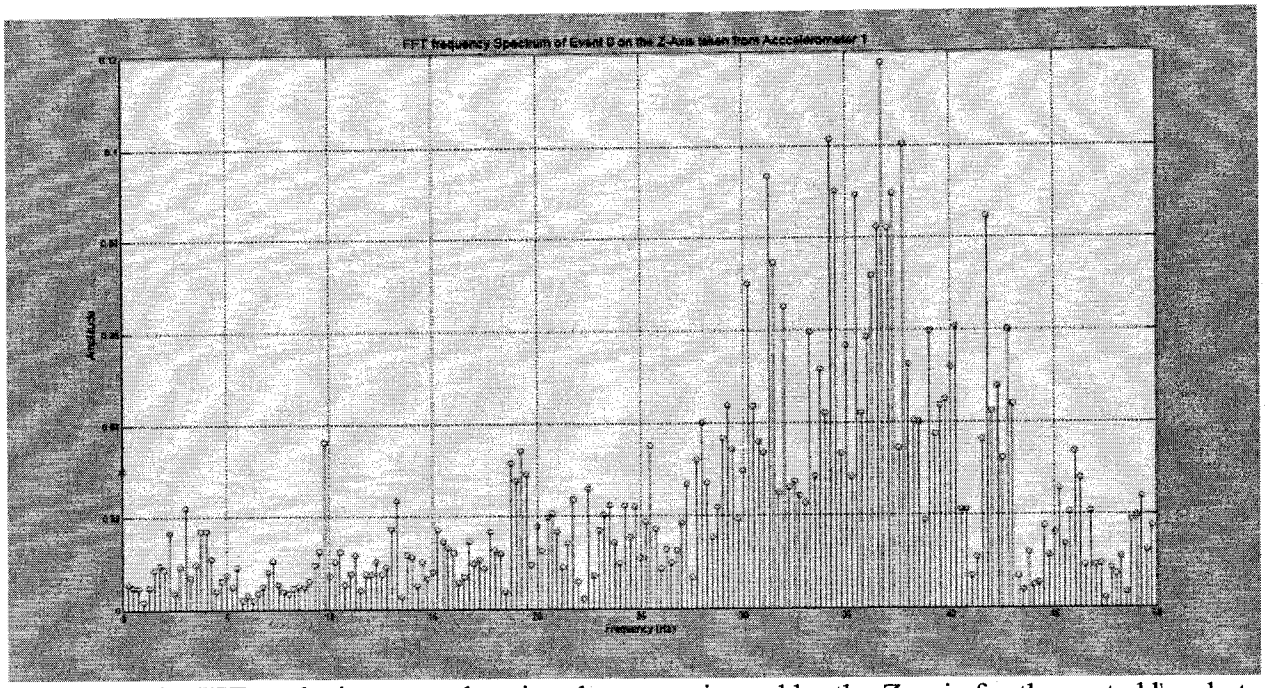

Figure 5-36 - FFT analysis on acceleration data experienced by the Z-axis for the casted bracket.

The frequency components that characterize the raw vibration signals can be found by implementing the FFT algorithm. The frequency spectrum shown in figure 5-7 is a typical example of the spectrums experienced in all three orthogonal axes. The frequencies that contribute to the raw signal the most in Figure 7 are in the range of 28 to 41 Hertz, with peak amplitude at 37.8 Hertz. This process of viewing the range and finding the peak amplitude frequency is recorded in an Excel spread sheet for comparison.

Table 5-4 - Average values as computed from events recorded by the accelerometers.

| Bracket type | Number of Events | Average Max X-Axis Amplitude (g) | Average Frequency (Hz) | Average Max Y-Axis Amplitude (g) | Average Frequency (Hz) | Average Max Z-Axis Amplitude (g) | Average Frequency (Hz) |
|---|---|---|---|---|---|---|---|
| Cast | 12 | 3.9 | 40.8 | 4.3 | 36.6 | 3.1 | 35.6 |
| Fabricated | 20 | 3.5 | 48.6 | 4.4 | 48.5 | 4.0 | 47.1 |

The final step in analyzing the vibration data is to compare that final results of the FFT and signal processing in a spread sheet form. Table II includes the computed average frequencies for each axis for both bracket types, as well as the number of events. Several interesting results can be seen from table II. The valve on the fabricated bracket experienced almost twice the events as did the valve on the cast bracket. The average frequencies experienced by the valve on the fabricated bracket were higher as well. The following figures (5-8 and 5-9) show the accelerometer results which were obtained from the placement on the trucks. The blue curve represents (X) (lateral) direction, green curve represents the (Y) (longitudinal) direction and pink represents the (Z) (vertical) direction. The vertical direction includes 1 g of gravity resulting in the pink signal appearing to have a higher peak amplitude.

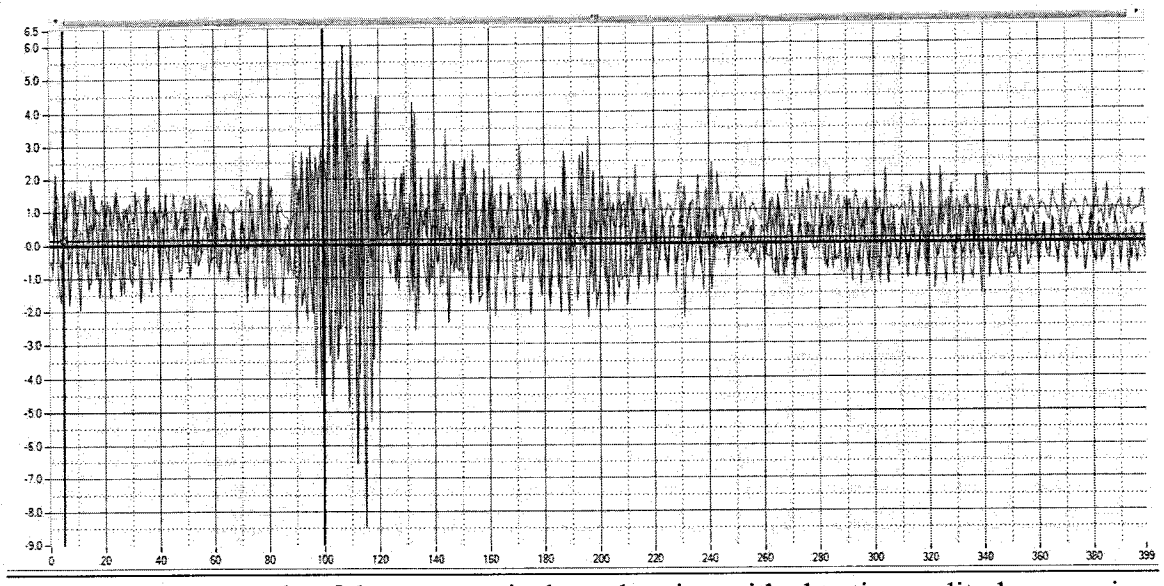

Figure 5-37 - An example of the most typical acceleration with chaotic amplitudes experienced during clean and most worn wheel events.

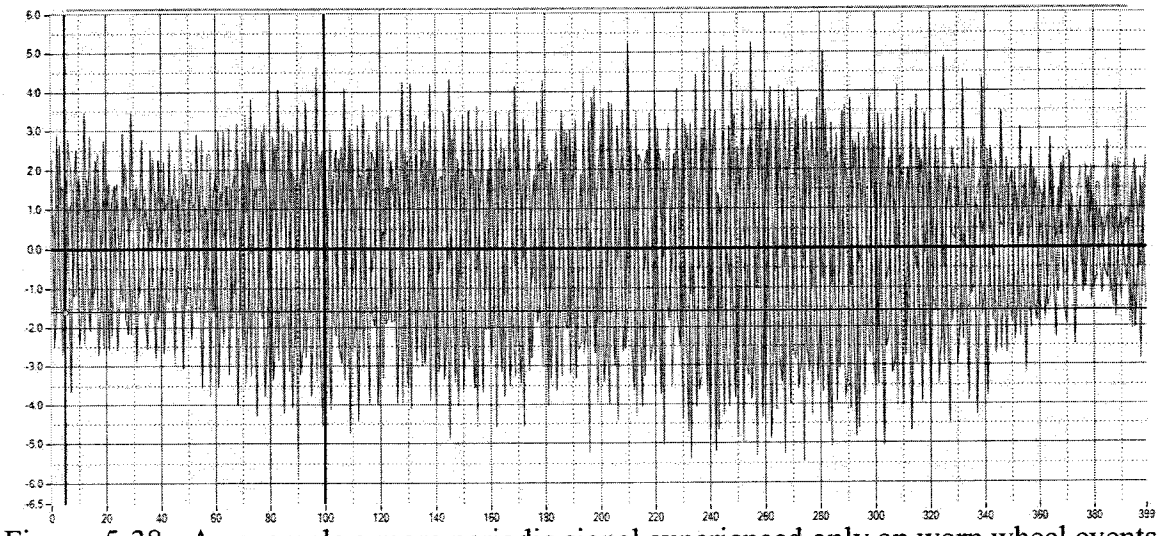

Figure 5-38 - An example a more periodic signal experienced only on worn wheel events.

Table 5-5 - Total events for casted bracket with maximum and minimum frequencies for each axis displayed

| **Event #** | **Data=10/15/2009** | | **Max Gs and frequencies Experienced during testing** | | | | | |
|---|---|---|---|---|---|---|---|---|
| - | Time of Event | Duration (sec) | X | Freq @max | Y | Freq @max | Z | Freq @max |
| 0 | 13.17.08 | 4.0 | 6.0 | 41.8 | 3.1 | 37.8 | 2.9 | 36.8 |
| 1 | 13.37.35 | 4.0 | 3.4 | 39.8 | 4.4 | 36.8 | 3.7 | 36.8 |
| 2 | 13.45.19 | 4.0 | 2.2 | 39.8 | 5.4 | 39.5 | 1.2 | 34.3 |
| 3 | 13.45.35 | 4.0 | 6.3 | 40.3 | 3.7 | 39.0 | 4.6 | 33.0 |
| 4 | 13.48.12 | 4.0 | 3.9 | 37.3 | 4.7 | 34.3 | 3.3 | 34.3 |
| 5 | 14.19.57 | 4.0 | 3.7 | 37.3 | 3.9 | 37.0 | 4.0 | 37.0 |
| 6 | 14.22.37 | 4.0 | 2.4 | 42.0 | 4.6 | 36.0 | 3.7 | 36.5 |
| 7 | 14.30.29 | 4.0 | 3.3 | 42.8 | 4.7 | 28.0 | 2.7 | 31.0 |
| 8 | 14.51.00 | 4.0 | 3.5 | 40.0 | 4.9 | 37.5 | 3.2 | 37.5 |
| 9 | 15.30.44 | 4.0 | 4.4 | 38.0 | 4.1 | 38.5 | 2.1 | 37.0 |
| 10 | 15.41.38 | 4.0 | 3.9 | 49.3 | 4.6 | 37.0 | 3.3 | 37.0 |
| 11 | 16.23.39 | 4.0 | 3.7 | 41.0 | 3.3 | 37.8 | 2.8 | 35.8 |

Table 5-6 - Total events for fabricated bracket with maximum and minimum frequencies for each axis displayed.

| **Event #** | **Data=10/15/2009** | | **Max Gs and frequencies Experienced during testing** | | | | | |
|---|---|---|---|---|---|---|---|---|
| - | Time of Event | Duration (sec) | X | Freq @max | Y | Freq @max | Z | Freq @max |
| 0 | 06.39.03 | 4.0 | 3.4 | 49.0 | 4.1 | 49.0 | 2.7 | 49.0 |
| 1 | 13.12.52 | 4.0 | 3.2 | 48.8 | 4.6 | 48.8 | 3.3 | 46.0 |
| 2 | 13.17.03 | 4.0 | 3.5 | 48.5 | 4.7 | 48.5 | 4.7 | 48.5 |
| 3 | 13.51.07 | 4.0 | 3.6 | 49.5 | 4.2 | 49.3 | 4.1 | 48.8 |
| 4 | 13.52.07 | 4.0 | 3.3 | 49.5 | 5.4 | 49.0 | 5.2 | 46.5 |
| 5 | 13.52.50 | 4.0 | 3.0 | 47.5 | 4.9 | 47.5 | 3.1 | 47.5 |
| 6 | 14.17.19 | 4.0 | 3.8 | 46.8 | 4.8 | 46.8 | 2.9 | 46.8 |
| 7 | 14.19.14 | 4.0 | 2.9 | 48.8 | 4.0 | 48.8 | 3.8 | 48.5 |
| 8 | 14.21.31 | 4.0 | 3.4 | 48.3 | 4.5 | 49.5 | 3.1 | 49.3 |
| 9 | 14.22.31 | 4.0 | 3.6 | 47.5 | 4.2 | 47.5 | 6.1 | 47.5 |
| 10 | 14.23.03 | 4.0 | 3.6 | 49.3 | 4.1 | 49.3 | 4.3 | 49.0 |
| 11 | 14.28.12 | 4.0 | 3.0 | 48.5 | 4.1 | 44.0 | 3.3 | 38.5 |
| 12 | 14.32.25 | 4.0 | 3.2 | 48.8 | 4.1 | 48.8 | 3.4 | 48.8 |
| 13 | 14.32.32 | 4.0 | 2.6 | 49.5 | 4.1 | 49.5 | 2.7 | 49.5 |
| 14 | 14.50.52 | 4.0 | 2.6 | 49.5 | 4.4 | 49.5 | 6.3 | 49.8 |
| 15 | 14.58.38 | 4.0 | 3.6 | 49.5 | 4.9 | 49.5 | 4.2 | 49.5 |
| 16 | 15.00.28 | 4.0 | 3.6 | 49.5 | 3.4 | 48.0 | 3.7 | 48.0 |
| 17 | 15.23.56 | 4.0 | 4.1 | 48.0 | 3.7 | 48.0 | 4.5 | 47.5 |
| 18 | 15.41.30 | 4.0 | 4.8 | 47.8 | 4.2 | 49.3 | 3.3 | 47.8 |
| 19 | 15.41.41 | 4.0 | 4.9 | 49.0 | 5.0 | 49.0 | 4.4 | 49.5 |

The analysis of the data from the worn was much similar to the data that is recorded in the clean test. The frequencies that contribute to the raw signal in the cast bracket the most were often in the range of 22 to 48 Hertz, with peak amplitude at 42.2 Hertz. This data shows that the data from the worn wheel displayed a wider energy distribution but still was close to the clean bracket. The frequencies that contribute to the raw signal in the welded bracket the most were most often in the range of 20 to 49 Hertz, with peak amplitude at 48.3 Hertz. During the test as well the amplitudes of the accelerations were chaotic during all types of wheels and brackets.

ANSYS Modal Analysis

Modal analysis of the cast and fabricated brackets provided the first five modes that correspond to the natural frequencies of the bracket design. The results of the modal analysis appear in Table I. The natural frequencies of the two brackets are very similar which indicates that the change in bracket design more than likely has not caused any changes in the vibration transmitted to the valve itself.

Table 5-7 - The theoretical natural frequencies for both the fabricated and cast brackets appear on the left side of the table.

| Natural Frequencies (Hz) | | | Aliasing Frequencies (Hz) | |
|---|---|---|---|---|
| Mode | Bracket Type | | | |
| | Fabricated | Cast | Fabricated | Cast |
| 1 | 223.33 | 229.26 | 23.5 | 29.5 |
| 2 | 633.69 | 635.25 | 33.5 | 35.5 |
| 3 | 837.87 | 880.64 | 38 | 19.5 |
| 4 | 976.79 | 985.8 | 23 | 14 |
| 5 | 1523.2 | 1376.8 | 23 | 23 |

After comparing the data between the brackets quantitatively it was determined that the sampling rate of the accelerometers used was too low to accurately detect any vibrations near the natural frequency. To gain insight into how the natural frequencies would appear if sampled by our accelerometers, the aliasing frequencies were calculated. The calculations were performed using the relation:

$$f_a = k_a f_n \qquad [5\text{-}1]$$

where $f_a$ is the aliasing frequency, $f_n$ is the Nyquist frequency or half of the sampling frequency of 100 Hz, and $k_a$ is the aliasing constant that is obtained from the folding diagram.

After performing the conversion, it turns out that vibrations occurring near some of the natural frequencies of the mounting brackets would appear in the 14 to 35Hz range if sampled at 100Hz as they were during our testing. When comparing the frequencies obtained through Fourier transformation to the aliasing frequencies it turns out that there is a possibility that resonance may occur during some of the vibrations experienced during travel.

Pressure Sensor Data

The brake system pressure analysis focuses on the system charge rates, rates of brake reduction, and how the system responds during prolonged stable transited. It is found that the brake line pressure before the system begins to charge is zero. The rate of the brake system to charge is found by looking at the time is the pressure increases from zero PSIG until constant PSIG reading recorded. The rate value is the total PSIG change divided by the time in seconds. The data recorded from the sensors shows that as the pressure in the lines first begin to increase the rate is linear, but as the brake lines begin to reach their maximum value the rates become more cubic in nature.

In order to gain an understanding of the typical behavior of the brake system as a whole three charges were analyzed which best represent the total train charge. It was found that the 2nd car which is closest to main air compressor in the system experienced an average charge rate of 9.23 PSIG/Second which is that fastest rate recorded. The average charge rates of the 75th and 148th train cars were 5.31 and 4.80 PSIG/Second. Comparing the average charge rates of the three cars it can be seen that the cars near the front of the train reach their maximum pressure at a faster rate. It can also be seen that the cars near the front of the train respond at a faster rate, while the cars near the 75th and 148th trend more closely to each other. The figure 5-8 shows the average charge rate against the car position in the train. The figure highlights the steep slope of the line between the 2nd and 75th car and how the slope trend more horizontal between the 75th and 148th car.

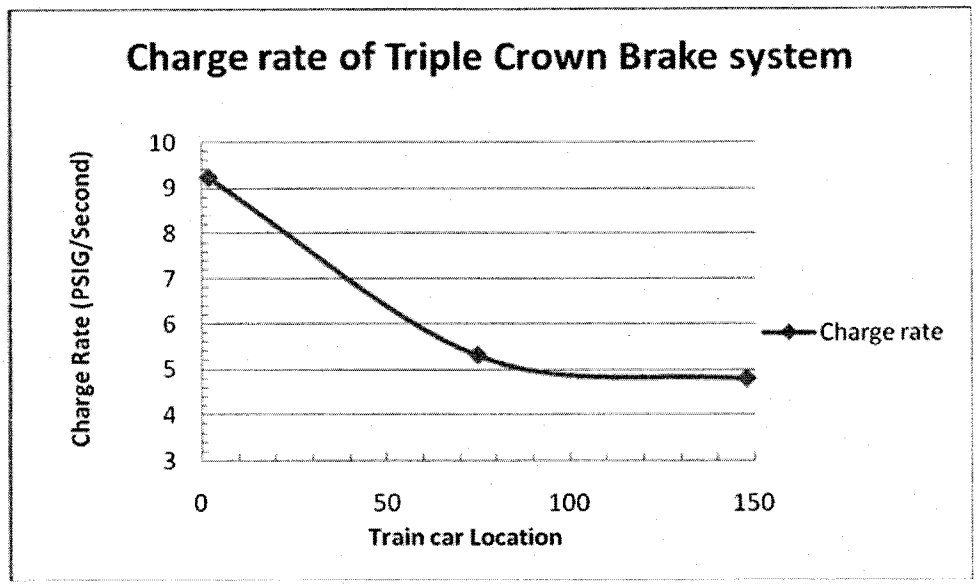


Figure 5-39 - Average charge rate of a Triple Crown brake line pressure vs.train car location. (markers represent 2nd, 75th, and 148th car position from front of the train)

A main focus of the pressure portion of the test is looking at the rate of brake pipe reduction. The brake pipe reduction is the pressure drop per unit of time in seconds that cause brake application. Data recorded from the 2nd car on the Triple Crown train is a good example of ideal brake pipe reductions. The data show pressure sensor #1, as it experiences a system charges and two types of brake pipe reductions. The data pressure values in the pressure figures change from left to right starting first with a complete system charge. The data reaches the 88 PSIG range at 11:03:49 PM and remains above that range until a brake pipe reduction is made at about 11:31:34 PM. It can be seen in the data that the rate of reduction is faster than the pressure transducer sampling rate resulting in at gap of 20.1 PSIG, only recording a drop from 67.9 PSIG to 0 PSIG in 6 seconds. It is believed that this initial unrecorded 20.1 PSIG pressure drop in less than 1.2 seconds is an example of an emergency brake pipe rate of reduction causing an emergency brake application. The pressure rate drop then slows from 67.9 PSIG to 0 PSIG resulting in a reduction rate of 11.32 PSIG/Seconds which is an example of a service rate of reduction of 20 psi drop in more than 1.4 seconds.

As discussed above a service rate of reduction is a pressure drop of 20 PSI in more than 1.4 seconds resulting in a service brake application. Two ideal examples of a service brake application can be seen in Figure 5-9, were it can be seen that the system charges from O to 87.2 PSIG in car 2. A service brake reduction of 20 PSI is made at 11:42:31 PM and again at 11:43:52 PM, in both reductions the 20 PSI drop is completed in about 29 seconds. The reason that the pressure data collected from the 2nd car responds in a desired fashion is believed to be due to the close proximity to the front of the train. The fast charge rate, and desired rates of brake pipe reductions experienced in car 2 are thought to be an example of an ideal operating Triple Crown Air Brake System.

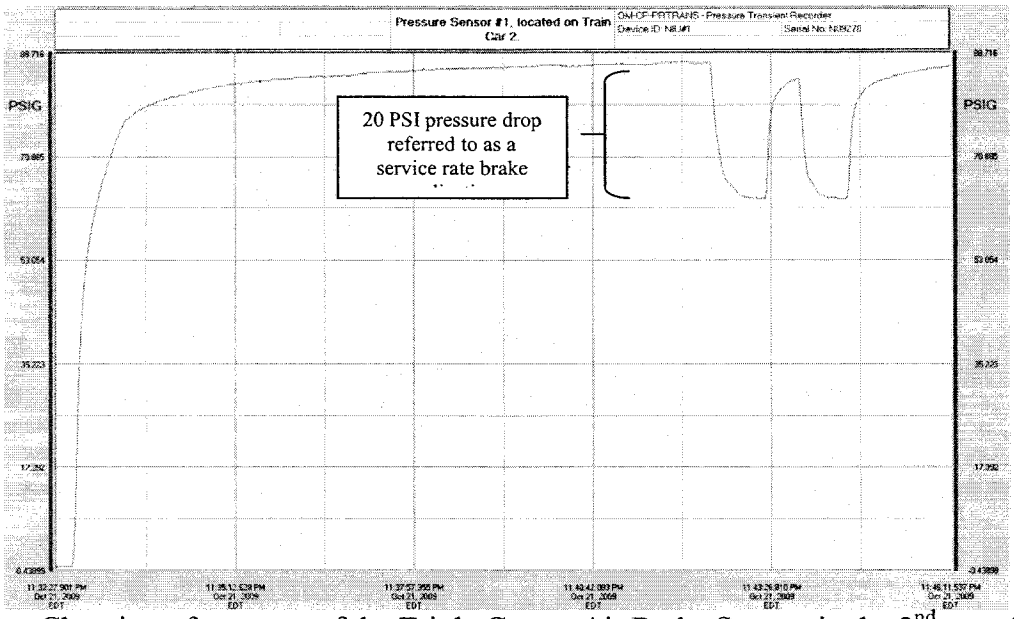


Figure 5-40 - Charging of pressure of the Triple Crown Air Brake System in the 2nd car of the train which releases the brakes of the car.

The Triple Crown Brake system is controlled by the front of the train, meaning that events of pressure drops in one car directly affect the pressure in the car behind it. Using this concept,

combined with the concept of the events in the 2nd car being an ideal braking operation, the times of pressure increases and decreases in the 2nd car can be directly compared to the times of pressure increases and decreases in the other car of the train. By directly comparing the 2nd car to the 75th car and the 75th car to the 148th car undesired losses and a pressure time line can be identified. During the data analysis three charge and brake reduction cycles were chosen which best represents the Triple Crown Brake System.

The first step in look at the data results is to look at the time of when the 2nd car begins to charge and then compare it with the pressure charge start times of the other cars. By comparing the start times of the charge processes an understanding of how long the middle and rear sections of the train lag behind the 2nd car. The data from the three charge cycles shows an average 16.3 seconds longer for the 75th car and 33.6 seconds longer for the 148th car to begin charging than the 2nd car. This means that the rear train cars begin charging on average of 33.6 seconds after the front cars begin charging. At this point it is important to note that the front of the train also has a faster charge rate then the rear of the train. Because the nature of the Triple Crown system the front of the train will reach brake release before the back of the train.

A similar lag in response is experienced when a service rate brake pipe reduction is introduced into the system. When the service brake reduction of 20 PSIG is experienced in the 2nd car the 75th car does not experience the drop till 13 seconds later and the 148th car does not experience the drop till 35 seconds later. Unlike the lag in the charging of the brakes that resulted in a full release of the brake, the lag in the pressure drop results in an ineffective brake application. The data supports that a 20 PSIG drop in the 2nd car translates only to a 3 PSIG drop in the 75th car and a less than 1 PSIG drop in the 148th car. During this type of service brake application the front portion of the train only experiences the 20 PSIG drop required to cause a brake application. This type of brake applications show an example of only 1/3 of the brakes being utilized, resulting in an increased strain on the front Triple Crown brake system components. Successful brake applications seen during the test in which all three cars experienced a 20 PSIG drop required to engage the brakes occurred when the front of the train decreased pressure long enough for the back of the train to reach a 20 PSIG drop.

During the analysis of the test undesired pressure drops were identified by comparing all drops in later cars with drops in the 2nd car. If a drop occurred in the back middle or back of the train and a pressure drop was not seen by the 2nd car it means that the drop was caused by some undesired event. During the test undesired drops that were seen by the middle of the train we seen by the back of the train as expected. All undesired drops seen during the test were not greater than a 10 PSIG loss and as a result was not are not assumed to have resulted in a brake application. The longest recorded undesired Pressure loss resulted in a drop of 10 PSIG for a time period of 156 seconds and occurred during the charging process. This unexplained pressure loss is characterized as a leak which has a rate that slowed as time elapsed until the system resumes charging.

In important aspect of the pressure sensor analysis is to gain an understanding of how the system pressure reacts one fully charged and under prolonged transit. During the Test sensors #2 never reached the cut up pressure of 88 PSIG allowing for a detailed view of the system pressure sustained over several hours of train transit. The data in figure 10 supports that if the system

allowed to fully charge the pressure in the system is very near to constant. The pressure in figure 10 shows that the 75th car charged to 86.8 PSIG, and over a several hour period the maintained that pressure value only varies to within 1 PSIG in ether the positive or negative direction. Even after an ideal service brake application and charge, sensor 2 reaches 86.8 PSIG and again is very stable under normal transit operation. Based on the data it can be concluded that the times when the system is most venerable to undesired pressure drops is when the system is charge, but is very stable once the system is allowed to reach a fully charged state.

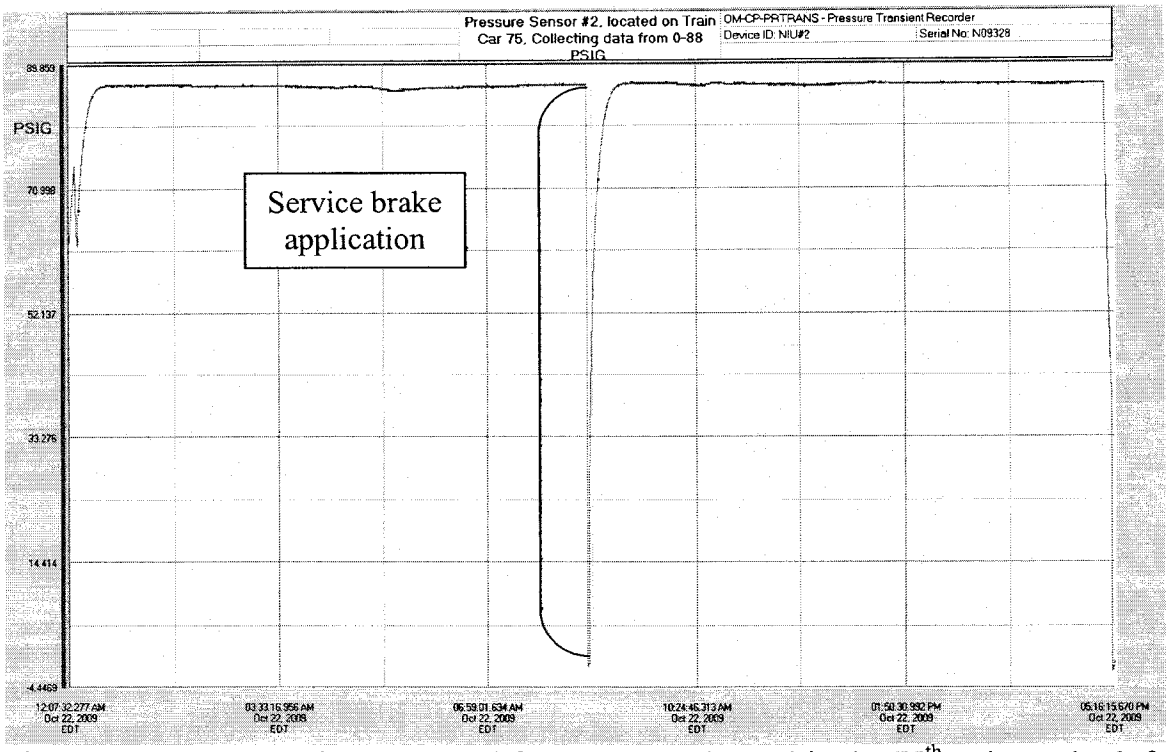


Figure 5-41 - Pressure data recovered from sensor 2 located in the 75th train car back from the front of the train.

Conclusion

After analyzing data gathered from each sensor in the experiment, several conclusions can be made regarding the issue of pressure loss. The vibration data from Tables II, IV, and V is mostly arbitrary as aliasing errors were encountered which prevented any observations to be made regarding the valves experiencing resonance. It was seen from table II that the frequencies experienced by the fabricated bracket were higher on average than those of the casted bracket. However, a general observation can be made that the average values for both brackets are relatively close and thus the bracket type can likely be ruled out as a variable causing valve failure. The average accelerations experienced by both valves with respect to the different axes in table two are similar as well. We do not see the brackets causing a bias in the accelerations felt by the valves in any one direction.

The pressure data revealed several features that were determined to be notable with respect to brake failure. It was seen that the pressure in the supply line for car two quickly reached the

requirement for brake release (approximately 87.5 PSIG), and the system also responded in a timely manner to engineer input for application of the brakes. From the following figures, it is shown that the pressure increase in the supply line for car 75 takes considerably longer than car two, and it does not even reach the maximum charge before possible brake applications are experienced. The braking system is shown to have also responded slower to brake application. Figures 11 thru 13 displays similar results, showing both the delay in the charge rate and reductions rates of the Triple Crown Brake System.

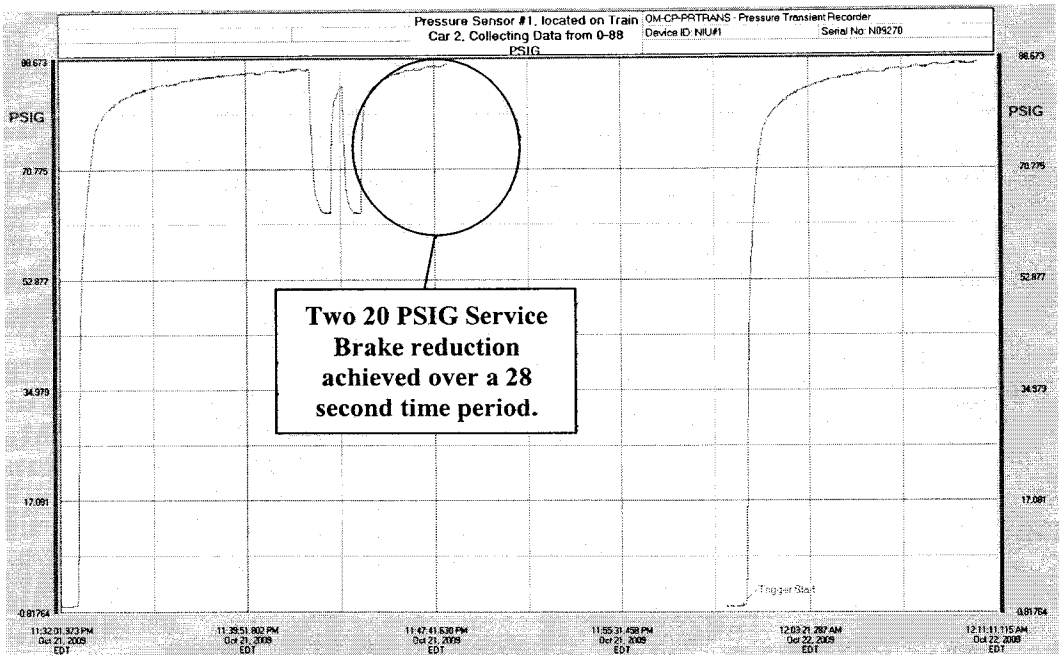


Figure 5-42 - Data recovered from the first two charge cycles of the Triple Crown Brake System located on the 2nd train car.

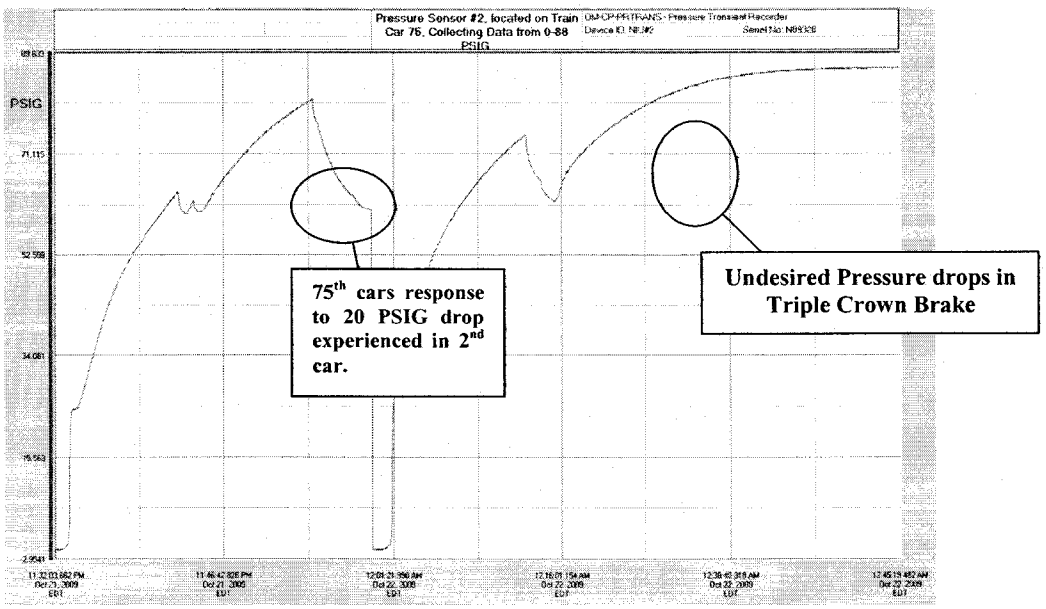

Figure 5-43 - Data recovered from the first two charge cycles of the Triple Crown Brake System located on the 75th train car.

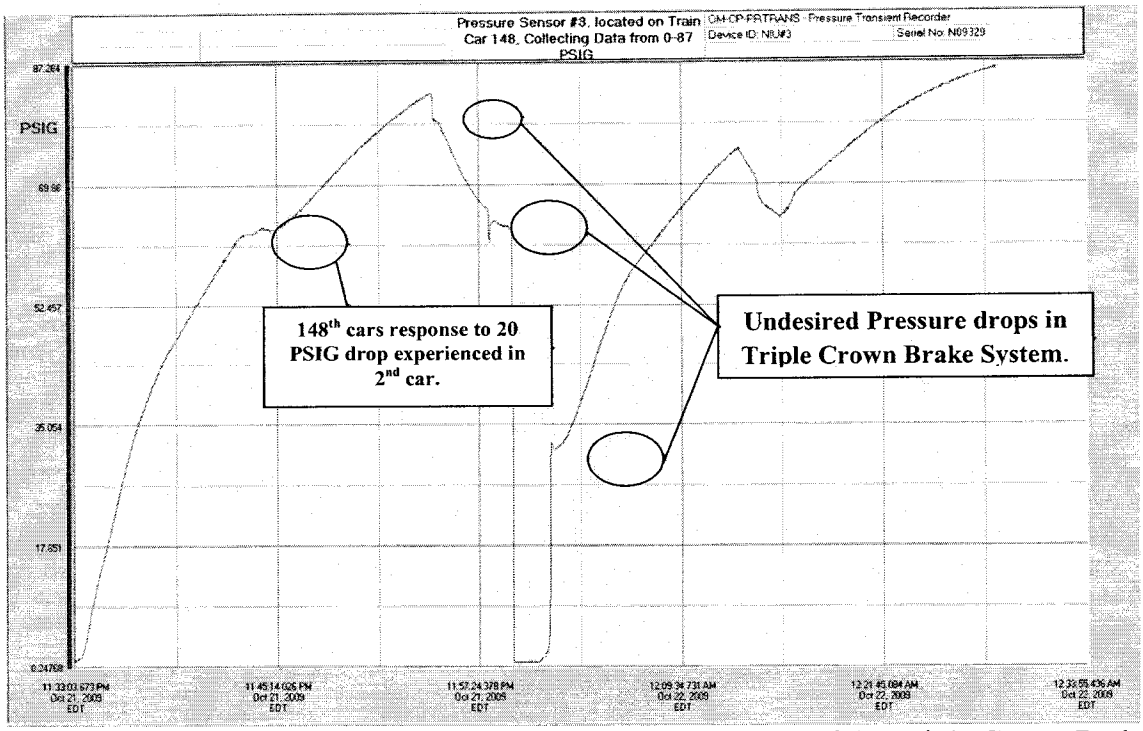


Figure 5-44 - Data recovered from the first two charge cycles of the Triple Crown Brake System located on the 148th train car.

Taking into consideration both areas of data collection, it can be seen that pressure loss is originating at a location before car 75 closer to the front end of the train. This pressure loss is most likely due to the overall length of the train. It is possible that vibration does play a factor in the undesired pressure drops during the charging process but it is difficult to label it the main cause. On the other hand the data supports that once the system is fully charged the system becomes very stable and pressure loss throughout the system is negligible. Since errors from vibration data collection were encountered, there cannot be a direct comparison between accelerations causing valve failure and pressure loss.

Recommendations

Conclusion of the experiment revealed several areas for improvement and some future considerations. The modal analysis revealed that the natural frequencies of the brackets were far above the 100 Hz sampling rate of the accelerometers. For any conclusions to be drawn regarding resonance of the valve, further testing is required using accelerometers that sample at least twice the frequency of the vibration of interest, in this case approximately 2000 Hz.

The data from the experiment shows that allowing for full charge of the total train is vital to the performance of the Triple Crown brake system. Also it has been seen that a 20 PSIG drop at the front of the train does not translate to a 20 PSIG at the back of the train. So it is recommended

that a larger drop at the front of the train is required to achieve the required drop at the back of the train.

Any further experiments conducted with the pressure sensors should place them at further distances to the locomotive. For example, the two sensors in the middle and rear of the train should be moved to cars 100 and 148 respectively or more sensors should be used. Data gathered should then be compared to what was recorded in this experiment. This will allow the origin of pressure loss to be narrowed down since the problem appears to be further to the front of the train. Also the sensors used sampled every second, it may be advantageous to sample every 30 seconds or even faster. A faster sampling rate would reduce the areas in the current data were the pressure drop was faster than the sampling rate.

Eductor tube redesign

The inductor tubes are used to vent the unused oil and fuel, which collects above the engine valves, into the intake, and thus, burned in the cylinder. At the start of the project, this was identified as a source of issue in the older model locomotives. In many cases, this 2 inch diameter tube was getting clogged, and thus could not remove the needed components. This project was to examine the current state of inductor tube and the cost to manufacture. The second phase was the redesign of the tube using cost effective materials and coatings, thus, saving the railroads some cost in replacement. This project was undertaken through continuing services provided by Atlas Manufacturing, through a sub contract. Initial design and analysis work was carried out by the NIU Engineering and Technology design team. The current tube is extruded with a gray paint coating. The initial analysis was to look at using a rolled tube with a welded seam. The design team examined the thermal deflection under varying orientations of the seam. The following figure details the physical appearance of the inductor tube.

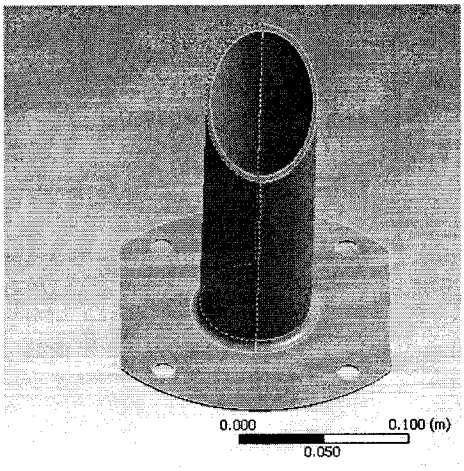


The next step was to model (mesh) the tube and apply the appropriate thermal boundary conditions and temperatures, thus, obtaining the resulting temperature stress distribution. It was determined that the seam location had no real effect on the thermal distortion.

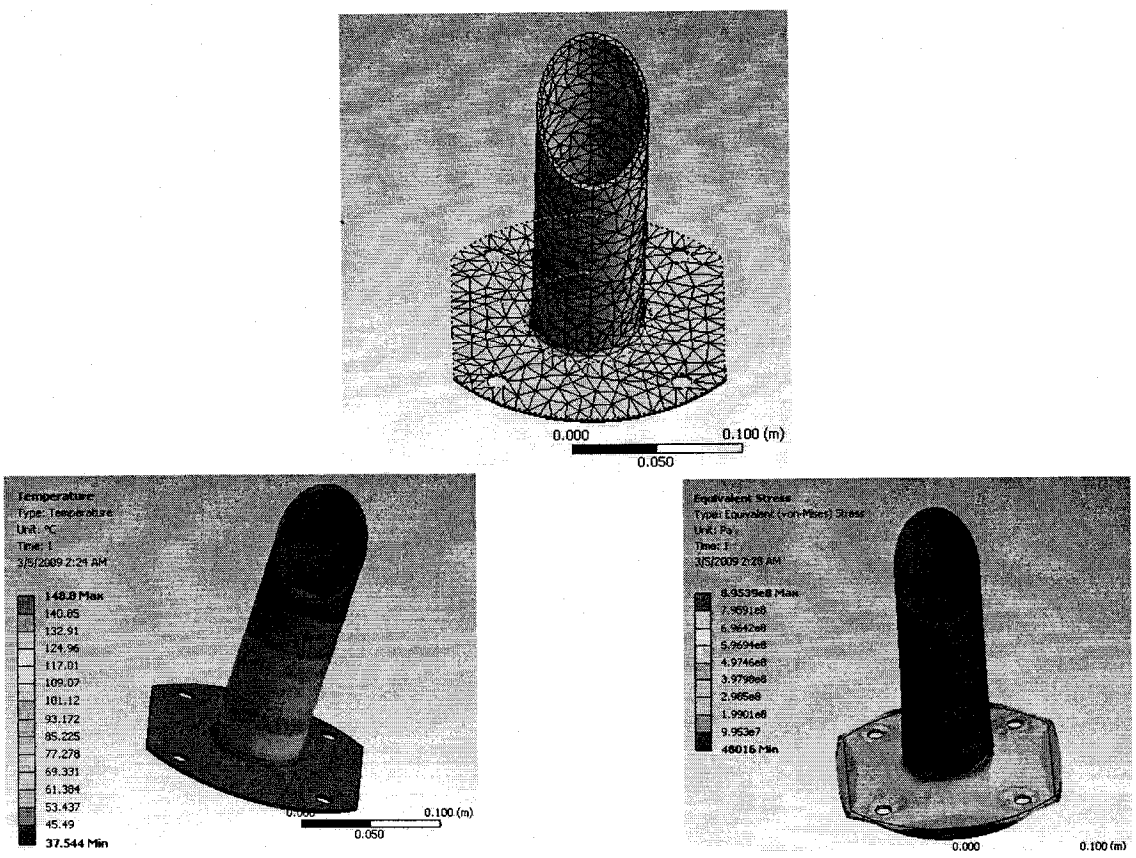


To obtain working models of the eductor tube which can actually be tested in real time in a real locomotive, Northern Illinois worked with Atlas Manufacturing, a regional manufacturer specializing in development of steel components and plating. As part of the task, Atlas was given the current specifications of the educator tubes and asked to develop new prototypes which reduce he purchase costs and provide added usability in the locomotive. As such, Atlas developed several new prototypes which utilize several different joining techniques, internal geometries, and coatings. In addition, Atlas studied the coasts associated with each aspect of the design.

Table 5-8 – Feature costs in development of new eductor tube

**BASIC INDUCTOR TUBE DESIGN AND COSTING ANALYSIS FOR NIU**

| QTY: | 100 | 250 | 500 | 1000 | |
|---|---|---|---|---|---|
| **BASIC ELEMENTS:** | | | | | |
| CUT TO 8.50" LONG 2.5" OD x 13 GA WALL STEEL TUBE | $2.80 | $2.65 | $2.55 | $2.35 | |
| BASE - MATERIAL - .120" CRS - 2.2# @ $0.45 / lb | $0.99 | $0.99 | $0.99 | $0.99 | |
| MITER TUBE (Done at same time as cut to length) | $0.30 | $0.30 | $0.30 | $0.30 | |
| LASER CUT BASE | $4.00 | $3.00 | $2.75 | $2.50 | |
| WELD TUBE TO BASE - ON TOP ONLY - NO GRIND | $3.00 | $3.00 | $2.75 | $1.30 | ** the $1.30 price is for robotic welding- need to build fixture and test weld 1st, but preliminary analysis indicates that robot weld is feasible |
| SUB TOTAL: | $11.09 | $9.94 | $9.34 | $7.44 | |
| **TOTAL WITH ATLAS MARKUP @ 25%** | **$13.86** | **$12.43** | **$11.68** | **$9.30** | |
| **OPTIONAL ELEMENTS** | | | | | |
| TUMBLE DEBURR | $0.63 | $0.38 | $0.31 | $0.25 | |
| DOUBLE WELD - add weld at bottom and grind smooth | $5.00 EA | $5.00 EA | $4.25 EA | $3.75 EA | ** the $3.75 price is for robotic welding- need to build fixture and test weld 1st, but preliminary analysis indicates that robot weld is feasible |
| MACHINED FLOW GROOVES --- IN PRODUCTION MACHINED GROOVES ARE NOT COST EFFECTIVE- WOULD REQUIRE HARD TOOLING - EST $6000 TOOLING COST - PRICES SHOWN FOR THIS FEATURE ARE BEST GUESS ESTIMATES AND WOULD REQUIRE HARD TOOLING | $5.00 | $4.25 EA | $3.50 EA | $3.00 EA | |
| ELECTRO POLISH LEVEL A (good) | $4.80 | $4.50 | $4.20 | $4.15 | |
| ELECTRO POLISH LEVEL B (better) | $10 | $9.65 | $9.35 | $9.35 | |
| Zinc and Clear Chromate | $1.88 | 1.25 | 1.25 | 1.25 | |
| Electroless nickel Plate | $5.63 | $3.75 | $3.75 | $3.75 | |
| Clear Teflon -Dip application | $1.15 | $0.75 | $0.75 | $0.75 | |
| Black Teflon Spray Application | $15.60 | $15.60 | $15.60 | $15.60 | |
| Black Teflon Spray Application - ID only wi overspray on outside | $6.55 | $6.55 | $6.55 | $6.55 | |

Table 5-4 shows the costs for each iteration of the new eductor tubes that have been supplied by Atlas Manufacturing. Currently, Norfolk Southern Railroad pays about $25 for each eductor tube which is purchased. One of the reasons that this part was chosen at the start of the project is due to the need to increase engine efficiency and reliability. At that point, it was learned that the current tube were getting clogged with soot and sludge from the engine. Thus, to provide better efficiency and reliability, the research tem decided to work with Atlas in the redesign of the tubes. The two guidelines that were used are that the initial dimensions and features had to be maintained, and the material had to operate at elevated (500-800 $^{o}$F). To keep costs low, it was decided to use low grade steel with plating that could withstand the elevated temperatures. To ensure survival at high temperatures, ASTM standard B 633 – 07 (Standard Specification for Electrodeposited Coatings of Zinc on Iron and Steel) was used in the process. From Table 5-4, one can see the combination of processes and coatings that were available to the research team.

Table 5-9 – total cost for completed new eductor tubes

**EDUCTOR TUBE DESIGN AND COSTING ANALYSIS FOR NIU**

| PROTOTYPE IDENTIFIER | BASIC TUBE DESIGN (includes single weld on top) | TUMBLE DEBURR | DOUBLE WELD & GRIND BOTTOM | MACHINED FLOW GROVES | ELECTRO POLISH LEVEL A | ELECTRO POLISH LEVEL B | ZINC AND CLEAR CHROMATE | ELECTROLESS NICKEL | TEFLON COAT CLEAR DIP APPLY | TEFLON COAT BLACK SPRAY APPLICATION | TEFLON COAT BLACK SPRAY APPLICATION TO OP TUBE ONLY W/ OVERSPRAY | TOTAL UNIT COST 100 PCS | TOTAL UNIT COST 250 PCS | TOTAL UNIT COST 500* PCS | TOTAL UNIT COST 1000 PCS |
|---|---|---|---|---|---|---|---|---|---|---|---|---|---|---|---|
| A | xx | | xx | | xx | | xx | | | | | $25.54 | $23.18 | $21.38 | $18.45 |
| B | xx | | | | | xx | | xx | | | | $29.49 | $25.83 | $24.78 | $22.40 |
| C | xx | xx | | | | | xx | | | | | $16.37 | $14.06 | $13.24 | $10.80 |
| D | xx | | xx | | | | xx | | | | | $20.74 | $18.68 | $17.18 | $14.30 |
| E | xx | | | | | | xx | | | | | $15.74 | $13.68 | $12.93 | $10.55 |
| F | xx | xx | | | | | | xx | | | | $20.12 | $16.56 | $15.74 | $13.30 |
| G | xx | | | | | | | xx | | | | $19.49 | $16.18 | $15.43 | $13.05 |
| H | xx | | xx | | | | | xx | | | | $24.49 | $21.18 | $19.68 | $16.80 |
| I | xx | | | | | | | xx | xx | | | $20.64 | $16.93 | $16.18 | $13.80 |
| J | xx | | xx | | | | | xx | xx | | | $25.64 | $21.93 | $20.43 | $17.55 |
| K | xx | | | | xx | | | | | | | $18.66 | $16.96 | $15.88 | $13.45 |
| L | xx | | | | | xx | | | | | | $23.86 | $22.08 | $21.03 | $18.65 |
| M | xx | xx | | | | | | | | | | $14.49 | $12.81 | $11.99 | $9.55 |
| N | xx | xx | | | | | | xx | | xx | | $35.72 | $32.16 | $31.34 | $28.90 |
| O | xx | xx | | xx | | | | xx | | xx | | $40.72 | $36.41 | $34.84 | $31.90 |
| P | xx | xx | | xx | | | xx | | | | | $21.37 | $18.31 | $16.74 | $13.80 |
| Q | xx | xx | | xx | | | | xx | | | | $25.12 | $20.81 | $19.24 | $16.30 |
| R | xx | | | | | | | | | | | $13.86 | $12.43 | $11.68 | $9.30 |

Based upon table 5-4, the research team selected new design "E" for testing. The current parts have been sent to Norfolk Southern Railroad's Roanoke (Virginia) repair facility. NS technicians will install three newly designed tubes into locomotives. These locomotives will be tracked over the next four months.

Based on data provided by the manufacturing experts at Atlas Manufacturing, the new, coated tubes will save almost 30% in cost (more at high volume), while reducing the need for engine maintenance and increasing the overall fuel efficiency of the locomotive.

The group redesigned the two major parts based on the Q2 results by performing extensive static and fatigue analyses for various shapes and material choices as well as manufacturing processes. The redesigned components show improvements of 23.18% (static analysis), 111.98% (fatigue analysis), and 2.06% (manufacturing cost) with almost doubled life in ideal case compare to original components. Some of the testing aspects are complete, however, there are some that are remaining, and they will be carried out during the project extension time-frame.

**Task 6 - Tribology Applications**

The objective of the task is to examine the current lubricants used in the railroad industry and come up with improved alternatives. These alternatives should yield lower friction force in railroad operation, and thus less energy needed by the locomotive engines. Other important factor is that new lubricants need to reduce wear, thus increasing life of rail/wheel.

Key areas for investigation are decided with consultation with NS and rail/road industry vendors. After selecting current lubricants, are analyzed its tribological properties for friction and wear. New lubricants are developed by adding polymer additives with nano-particles. The lubricant performance is evaluated by modeling wheel/rail contact.

Selection of Lubricants
Two commonly lubricants for wheel axle bearings and locomotive engine lubrication are Arapen RB 320, Lithium (Mobilith SHC 100). Lithium is synthetic grease for high performance. Special Curve Grease 213 (Exxon Mobil) is used on curve track to minimize friction and wear on wheel flange and rail.

Arapen is high performance long-life grease developed for the roller bearings of railroad car journals where no provision is provided for in-service re-lubrication. It is formulated with a mineral base fluid and a mixed lithium/calcium soap thickener. ARAPEN RB 320 grease has the high oxidation stability required to maintain good lubrication throughout extended periods of service or storage. It is highly resistant to chemical deterioration that might otherwise produce acids or deposits that are detrimental to long bearing life. ARAPEN RB 320 grease has exceptional ability to withstand shear, i.e. retain consistency after prolonged working, as in the churning action of an anti-friction bearing. This grease has been shown to have little effect on seal materials. Largely because of its special calcium-lithium-soap base, ARAPEN RB 320 grease has a high resistance to structural change in the presence of water. It is also inhibited to give protection against rusting. ARAPEN RB 320 gas an application temperature range of -20 degrees Centigrade to +120 degrees Centigrade.

Lithium-based grease, often referred to simply as "lithium grease", is a lubricant grease to which lithium compounds are added, giving it higher performance and temperature tolerance. Some formulations also include PTFE and/or other substances, such as molybdenum compounds. Lithium grease adheres well to metal, is non-corrosive, and may be used under heavy loads. It has a drip temperature of 190° to 220°C (350° to 400°F) and it resists moisture, so it is commonly used as lubricant in household products, such as electric garage doors. Lithium grease is formed by the same kind of reaction that forms other greases. Lithium hydroxide or lithium carbonate is reacted with fatty acids, particularly 12-hydroxy satiric acid, to form salts that disperse into and viscosity oils to form stable gels.

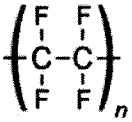

POLYTETRAFLUOROETHYLENE (PTFE) (TEFLON STRUCTURE)

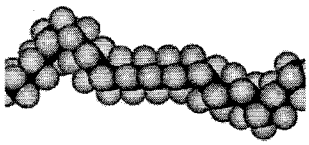

3D VIEW OF POLYTETRAFLUOROETHYLENE (PTFE) (TEFLON STRUCTURE)

Curve grease has been specifically designed to reduce friction between the wheel flange and the rail, especially when curves are encountered. The reduction in friction leads directly to savings in motive energy. It is extremely environmentally friendly because it is bio-degradable and non-toxic. Great care is taken in the manufacturing of the curve grease to ensure total environmental protection and effective rail curve lubrication. Testing in severe mountain service has demonstrated excellent extreme pressure properties. The unique lubrication film in the grease is capable of carrying heavy loads. This reduces track and wheel wear. Testing using a tribometer demonstrated friction reduction equaling that of premium mineral based rail curve grease. The grease has a dropping point of 112 degrees centigrade (230 degrees Fahrenheit) ensuring consistent performance even at extremely high ambient temperatures. At the other extreme curve grease demonstrates remarkable pump ability at temperatures as low as -30 degrees centigrade (-22 degrees Fahrenheit). The calcium soap thickener used in this grease provides excellent EP properties as well as remarkable water wash resistance. This is very beneficial in extending the lubricating film life of the grease. The curve grease has been designed to be highly compatible with all of the traditional and synthetic greases currently in use.

An environmental and safety review was conducted for a chemical used in grease. Apapen RB 320 is petroleum-based grease manufactured by Exxon-Mobil. The Material Safety Data Sheet (MSDS) dated September 3, 2008, supplied by Exxon was reviewed. Per, Exxon, this chemical is not considered hazardous according to regulatory guidelines. This evaluation is consistent with generic chemical family of greases. However, each potential hazard was reviewed in detail. The flash point is 430 F, will not ignite unless heated to high temperatures. Based on the vapor pressure (0.1 mm of mercury), the grease would burn but not explode under typical "fire" conditions.

Selection of Nano-particles

The use of certain solid lubricating materials is well known. Graphite as well as metal disulfides (primarily $MoS_2$ and $WS_2$) have been used for many years as industrial lubricants. Traditionally the structure of these materials has been in the 2H (hexagonal) crystal structure. More recently inorganic fullerene (IF) structures of these materials have been developed and tested for tribological purposes with results generally shown to be superior to the 2H structure perhaps due to the lack of edges at the crystallite boundaries.

In selecting materials for testing for rail lubrication application a couple of important points should be considered. The method of application to the track surface is such that any particles present in the lubricant will be loaded to very high stresses repeatedly. The load on the rail car wheels is expected to be as high as 2 GPa. This has been shown to cause a conversion from the IF structure to the 2H structure under non-hydrostatic loads. The load in a rail lubrication application will certainly be non-hydrostatic. Thus the potential advantages of the IF structure are unlikely to be realized. Also, the amount of lubricants that are used in rail applications is

very large. For widespread adoption any additive to the lubricants must be either inexpensive or active at very low concentration. Readily available nano-particle sized solid lubricants that can be used to modify the properties of rail greases include $MoS_2$ and $WS_2$ of the 2H variety in a range of particle sizes and graphite, also in a range of particle size. The thickness of the boundary layer for the application at hand is unknown but it has been estimated to be as thin as a few microns. For this reason, particle sizes substantially smaller than one micron should be tested.

The principle challenge in improving the wear rate of the steel wheels using these additives is the correlation that tends to exist between reducing friction coefficient and reducing wear. In general these additives have all been shown to decrease both friction and wear rate, but reduction in friction below a coefficient of about 0.3 is undesirable for top of rail application as it tends to cause slippage leading to wandering of cars, difficulty in acceleration and in braking. However, friction and wear are not always directly correlated. The intent of testing particles of varying particle dosage, size, and chemistry is to determine if an operating range can be found that improves wear rates without substantially reducing coefficient of friction.

Evaluation and Development of New Lubricants

The lubricants need to perform for typical wheel/rail loads and stress conditions. A Hertzian model is used to compute the contact stress condition, as shown in Figure 6-1.

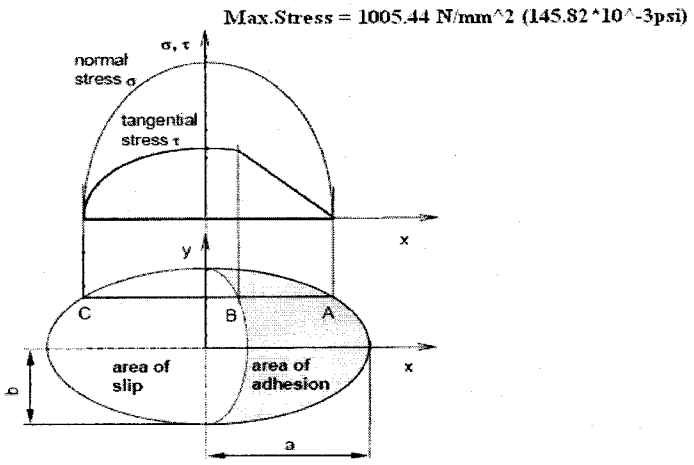


Figure 6-1- Slip, adhesion, maximum normal and shear stress.

For wheel/rail profile the contact stresses, contact ellipse major and minor axis are computed, using data shown in Table 6-1.

Table 6-1 – Values used in calculations for a range of load values (Q)

| **Q** (10^3*Newton) | **a** (mm) | **b** (mm) | **Po** (Newton/mm^2) | **τmax** (metric) (Newton/mm^2) | **Po** (psi*10^-3) | **τmax** (English) (psi*10^-3) |
|---|---|---|---|---|---|---|
| **0** | **0** | **0** | **0** | **0** | **0** | **0** |
| **5** | **3.94** | **0.39** | **466.09** | **144.48** | **67.60** | **20.95** |
| **10** | **4.96** | **0.49** | **589.36** | **182.70** | **85.47** | **26.49** |
| **15** | **5.68** | **0.56** | **675.48** | **209.39** | **97.97** | **30.36** |
| **20** | **6.25** | **0.62** | **739.30** | **229.18** | **107.22** | **33.23** |
| **25** | **6.73** | **0.67** | **794.16** | **246.18** | **115.18** | **35.70** |
| **30** | **7.15** | **0.71** | **846.48** | **262.40** | **122.77** | **38.05** |
| **35** | **7.53** | **0.75** | **887.71** | **275.19** | **128.75** | **39.91** |
| **40** | **7.87** | **0.78** | **933.36** | **289.34** | **135.37** | **41.96** |
| **45** | **8.19** | **0.81** | **971.64** | **301.20** | **140.92** | **43.68** |
| **50** | **8.48** | **0.84** | **1005.44** | **311.68** | **145.82** | **45.20** |

In order to test the friction and wear values, the NIU research team is working with Falex, Inc. of Sugar Grove, Illinois. Falex is a world leader in tribology testing and developing tribology test equipment and standards. Falex has designed and built a tester to evaluate lubricants for friction and wear under high Hertzian contact stresses during sliding. The tester consists of four steel balls, one ball (top) ball rotating on three fixed balls (bottom), shown in Figure 6-2. The ASTM standard D-2266 test method is followed explicitly to evaluate lubricants. The test method covers the determination of the wear preventive characteristics of greases in sliding steel-on-steel application, where the friction torque (coefficient of friction) is monitored throughout the test. At the end of the test the test balls are cleaned ultrasonically using isopropyl alcohol. The wear X, Y values are measured at magnification under microscope and a test load of 40 kilograms is used to generate maximum Hertzian stress of the order of 400k psi, thus appropriately simulating wheel/rail stresses.

To determine the proper nano-lube percentage, the base lube is first tested at varying force ranges. Nano-particles are then mixed into base lube by weight basis, lube plus varying % of nano-particles, in order to gauge the benefits of the nano-lube addition.

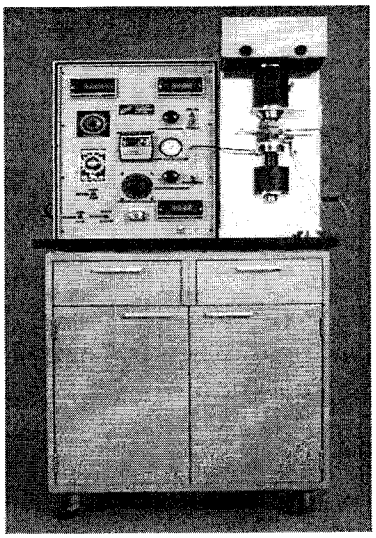

Figure 6-2 – Falex 4-Ball High Hertzian Contact Stress Tester

Test Results

Figure 6-3 shows the typical wear scar on the top rotating ball after the test. A corresponding circular wear (Figure 6-4) is observed on the bottom balls during the test. Figure 6-5 through Figure 6-37 show the friction force in grams (force) versus time for each individual test run. At the bottom of each graph are the wear scare dimensions. The nano-materials used in development of lubricants are

- Molybdenum Disulphide (MD) 50nm, 1.5 micron
- Tungsten Disulphide (TD) 55nm, 0.9 micron
- Graphite 400nm

All of the nano-materials were tested at concentrations of 2% and 4% by weight, as noted on the figures. In addition, all of the figures show the base lubricant performance followed by the varying percentages of the modifying nano-lubricant

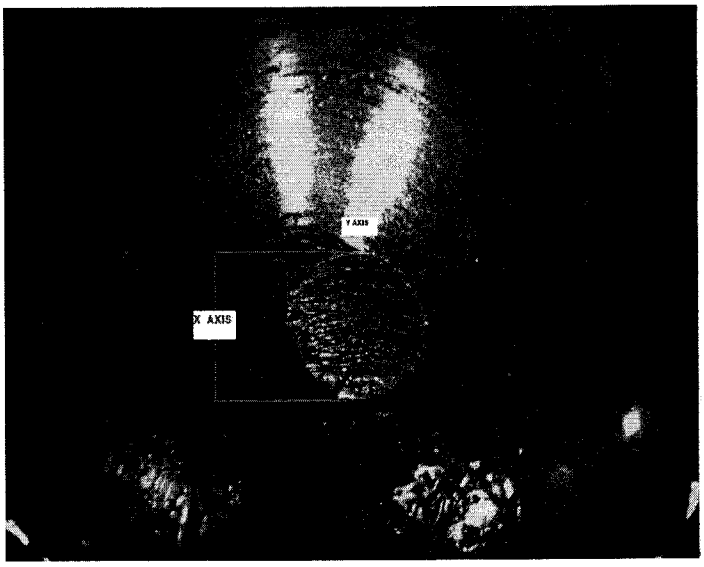

Figure 6-3 – Post test wear scar on the top rotating ball

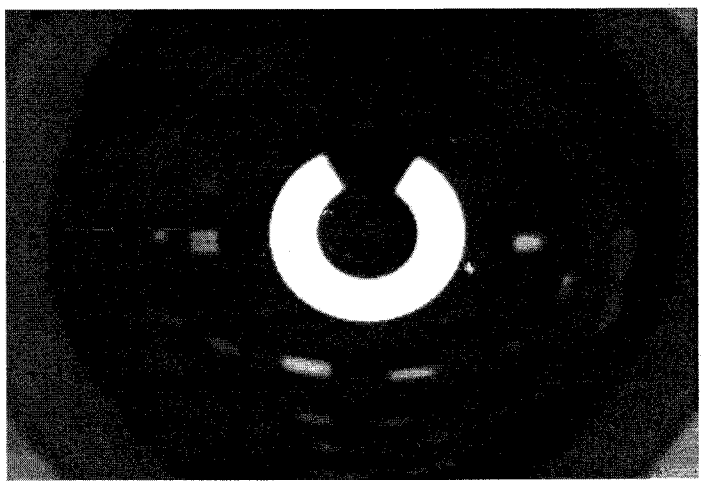

Figure 6-4 – Post test wear scar on the bottom rotating ball

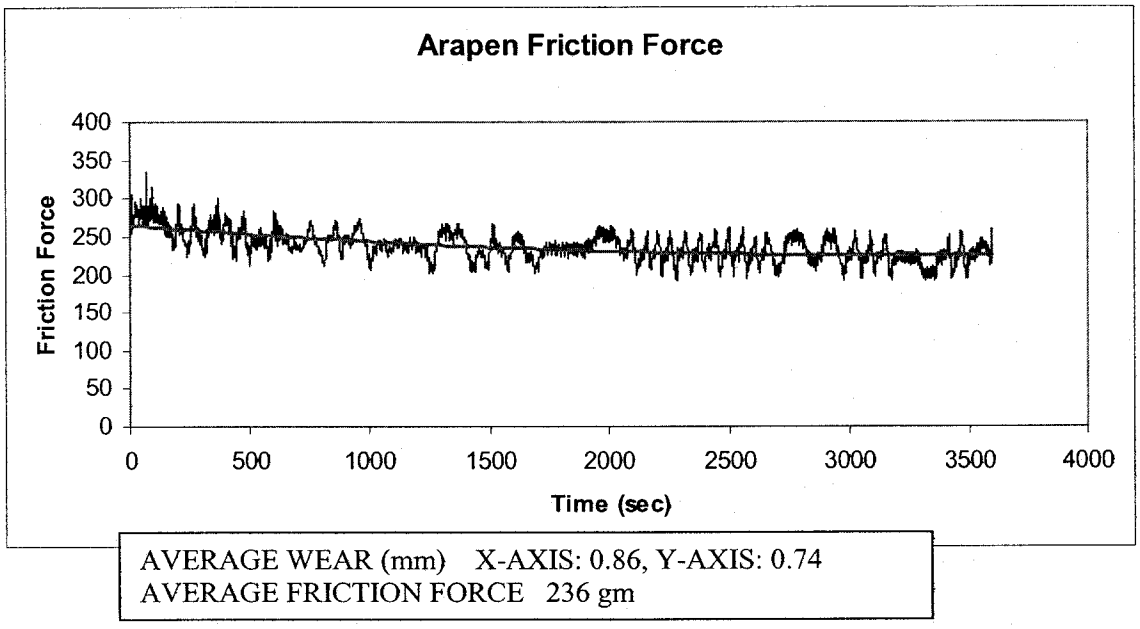


AVERAGE WEAR (mm) X-AXIS: 0.86, Y-AXIS: 0.74
AVERAGE FRICTION FORCE 236 gm

Figure 6-5 – Arapen Lube-Friction Vs Time

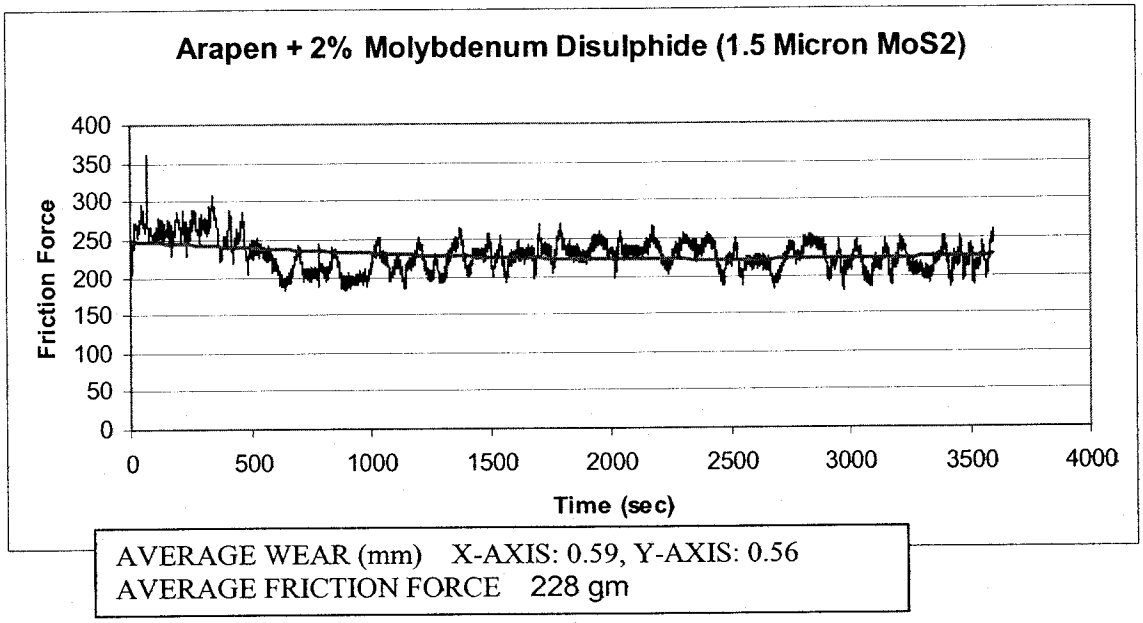


AVERAGE WEAR (mm) X-AXIS: 0.59, Y-AXIS: 0.56
AVERAGE FRICTION FORCE 228 gm

Figure 6-6 – Arapen Lube Plus 2% MoS2(1.5 micron)- Friction Vs Time

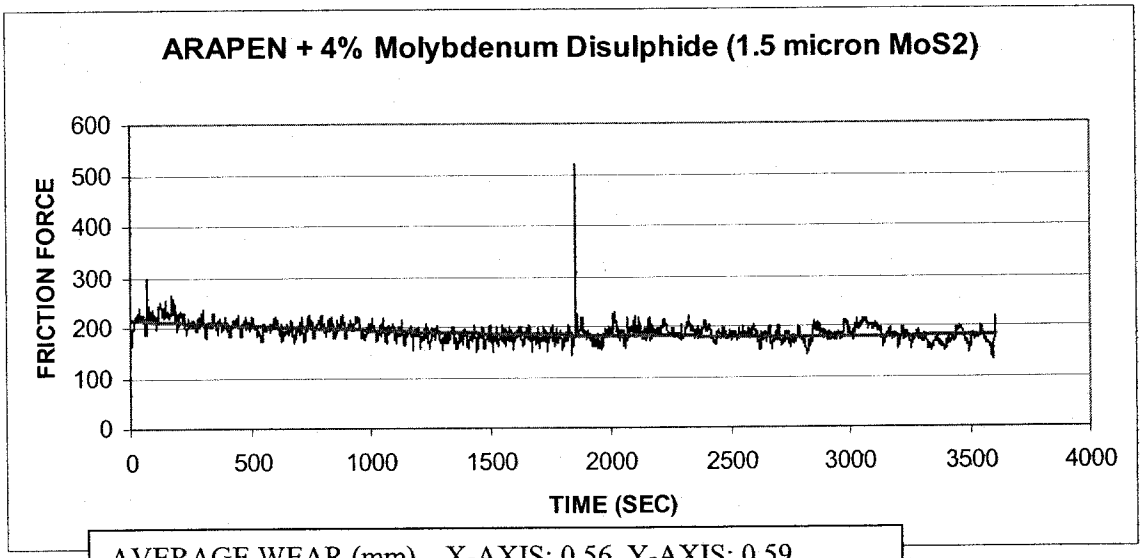


AVERAGE WEAR (mm) X-AXIS: 0.56, Y-AXIS: 0.59
AVERAGE FRICTION FORCE 188 gm

Figure 6.7 – Arapen Lube Plus 4% MoS2(1.5 micron)-Friction Vs Time

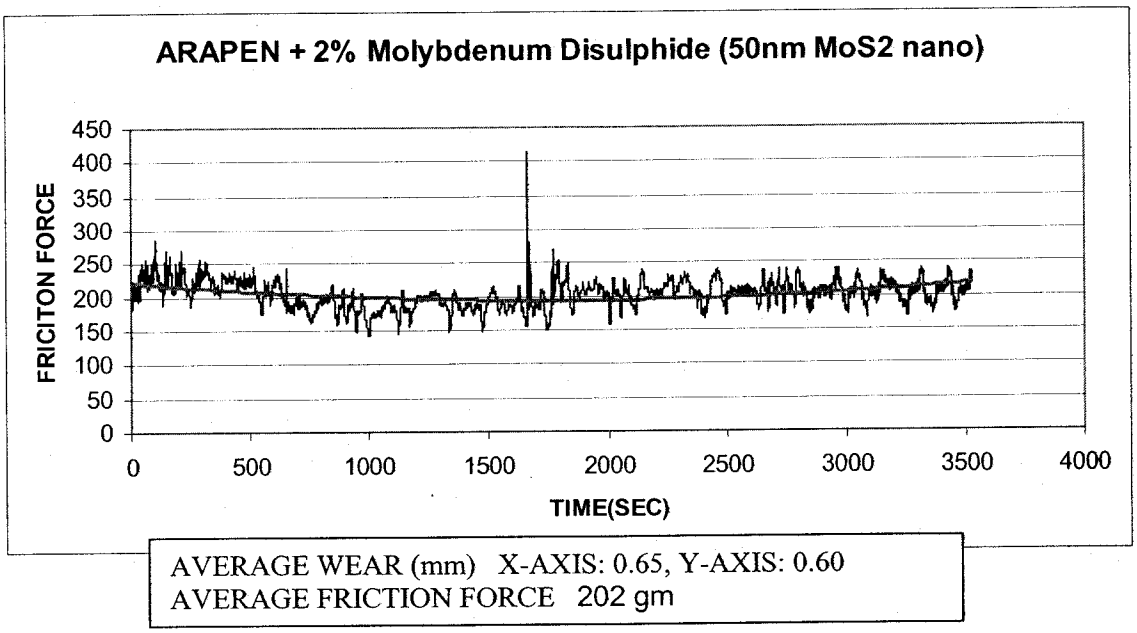


Figure 6-8 – Arapen Lube Plus 2% MoS2(50 nm)-Friction Vs Time

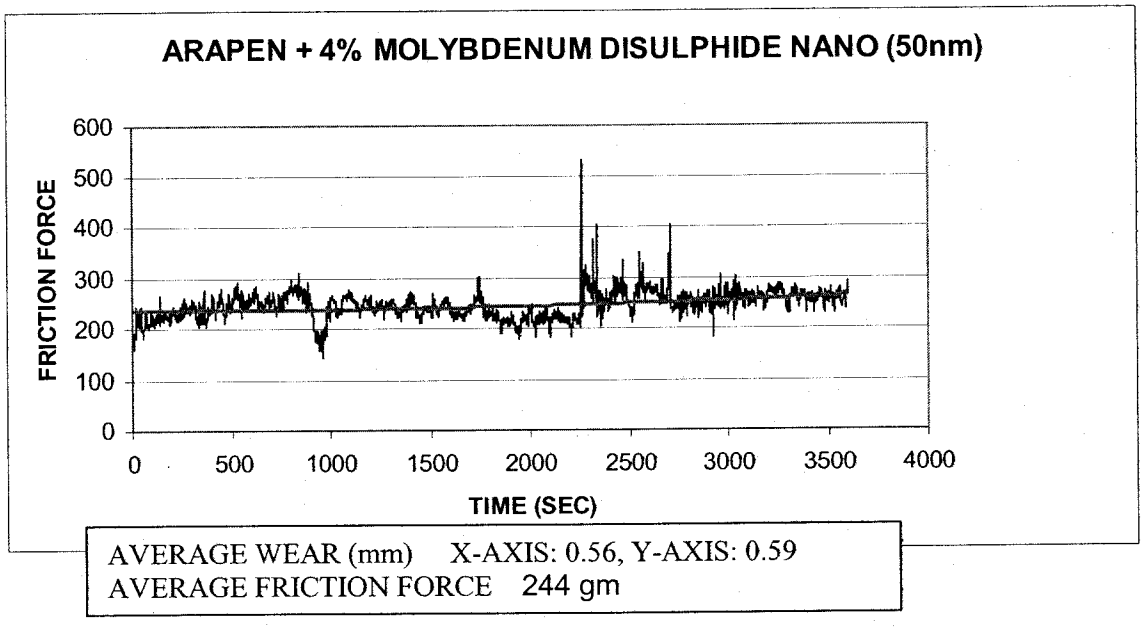


Figure 6-9 – Arapen Lube Plus 4% MoS2(50 nm)-Friction Vs Time

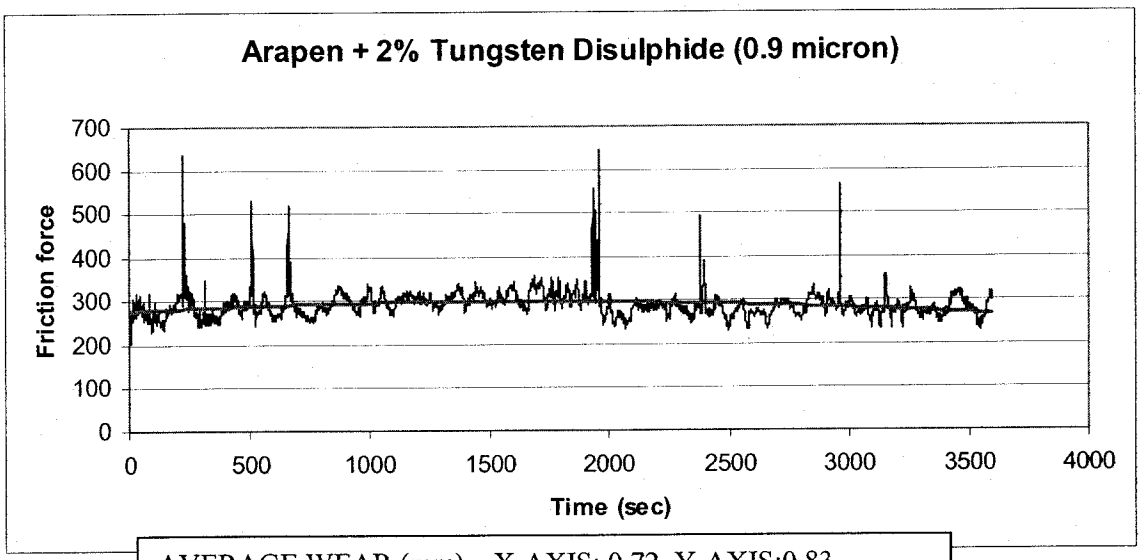


AVERAGE WEAR (mm) X-AXIS: 0.72, Y-AXIS:0.83
AVERAGE FRICTION FORCE 288 gm

Figure 6-10 – Arapen Lube Plus 2% WS2 (0.9 micron)-Friction Vs Time

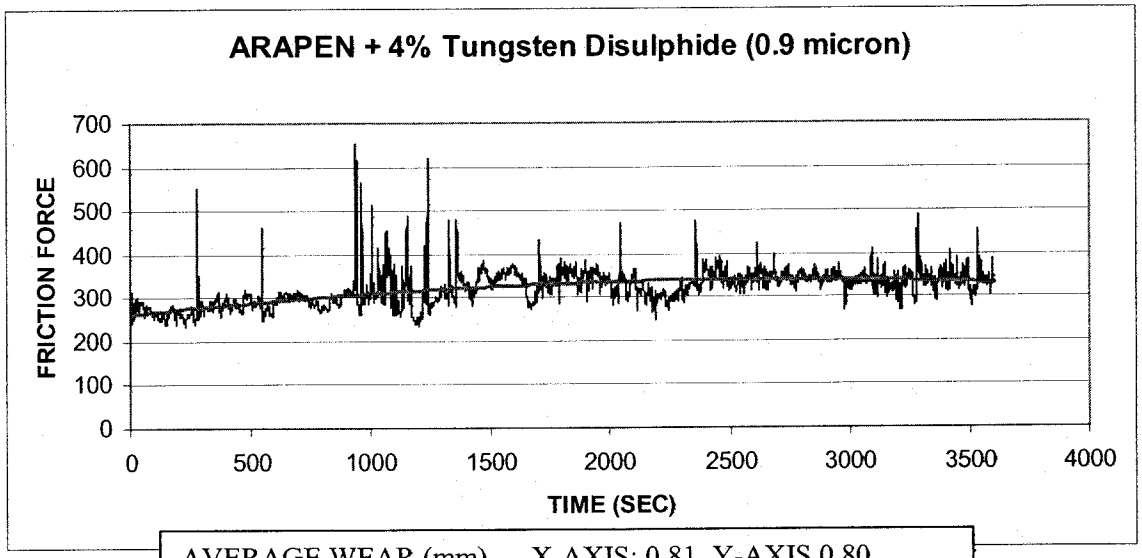


AVERAGE WEAR (mm) X-AXIS: 0.81, Y-AXIS 0.80
AVERAGE FRICTION FORCE 319 gm

Figure 6-11 – Arapen Lube Plus 4% WS2 (0.9 micron)-Friction Vs Time

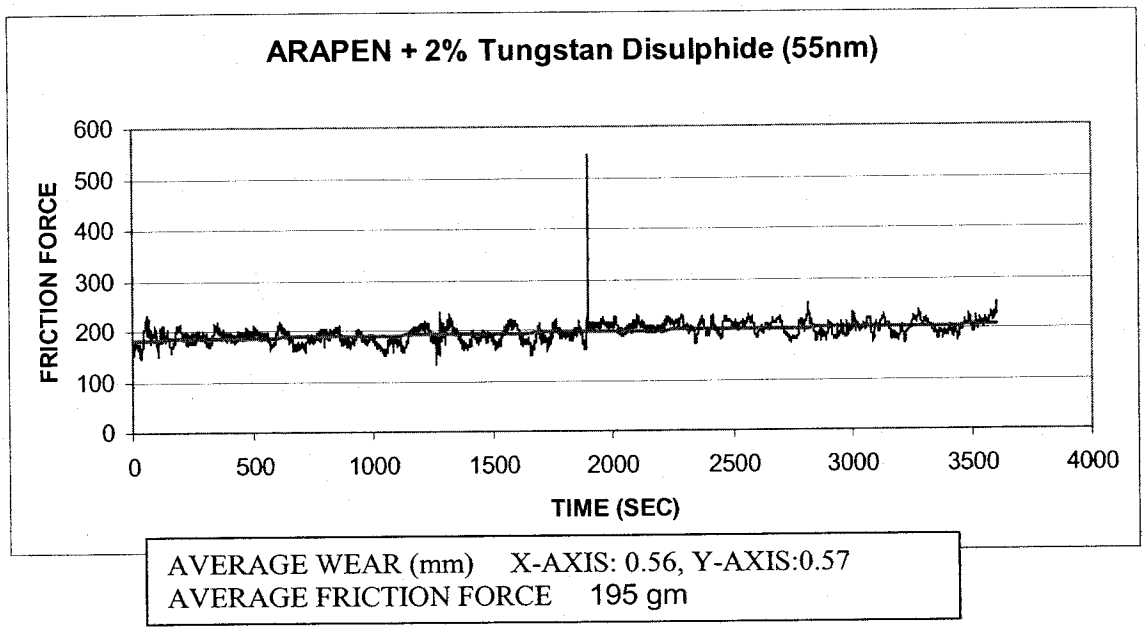


Figure 6-12 – Arapen Lube Plus 2% WS2 (55nm)-Friction Vs Time

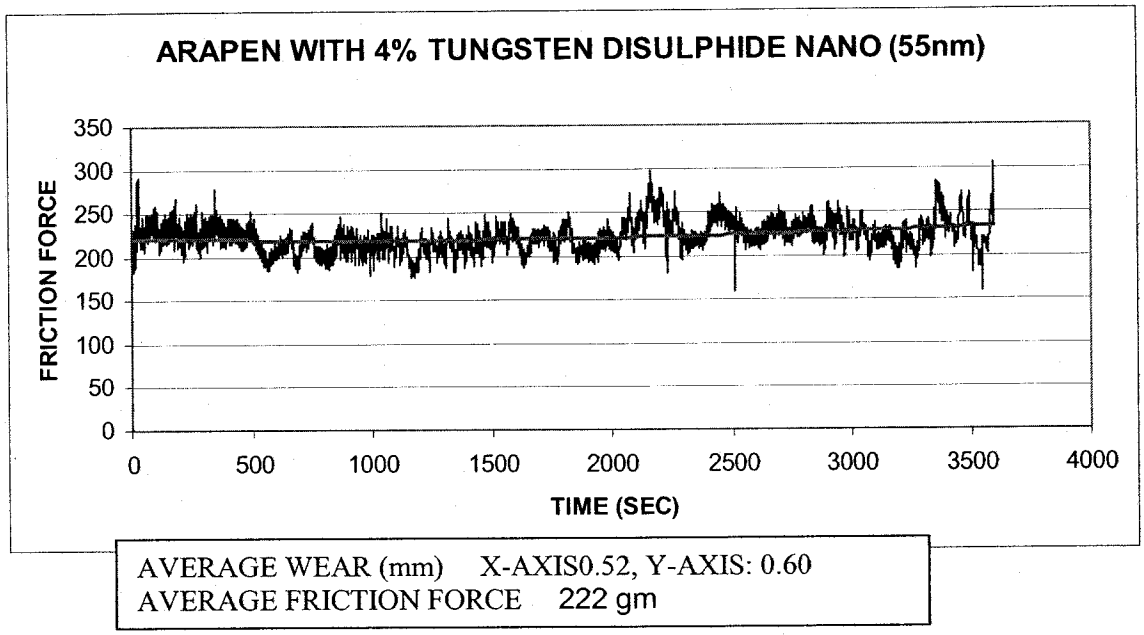


Figure 6-13 – Arapen Lube Plus 4% WS2 (55nm)-Friction Vs Time

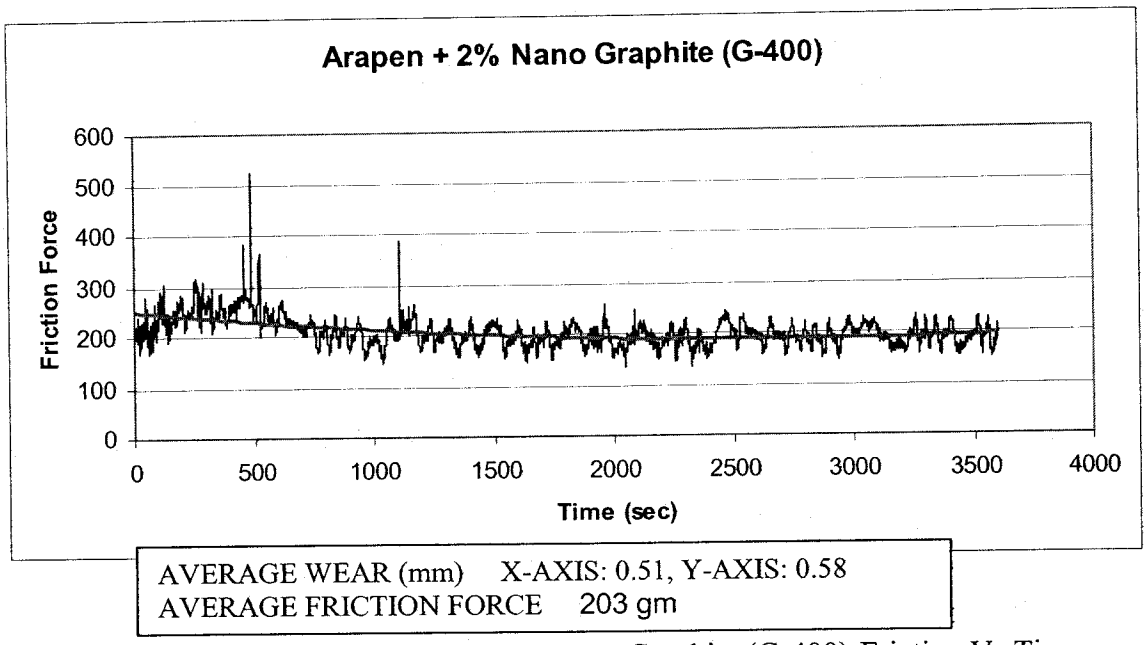


Figure 6-14 – Arapen Lube Plus 2% Nano Graphite (G-400)-Friction Vs Time

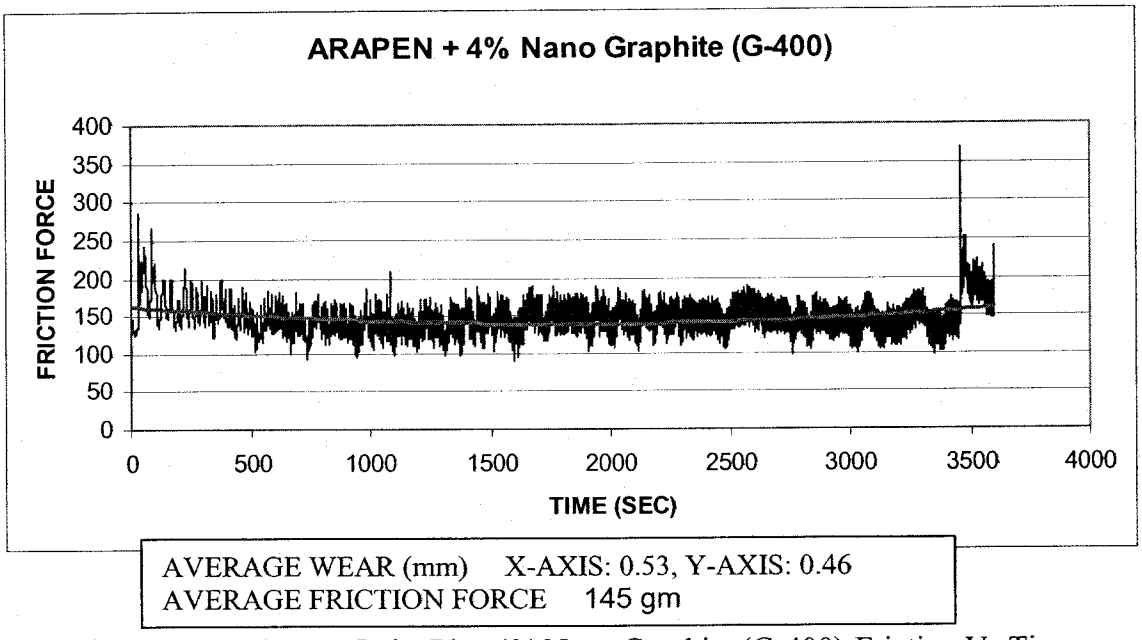


Figure 6-15 – Arapen Lube Plus 4% Nano Graphite (G-400)-Friction Vs Time

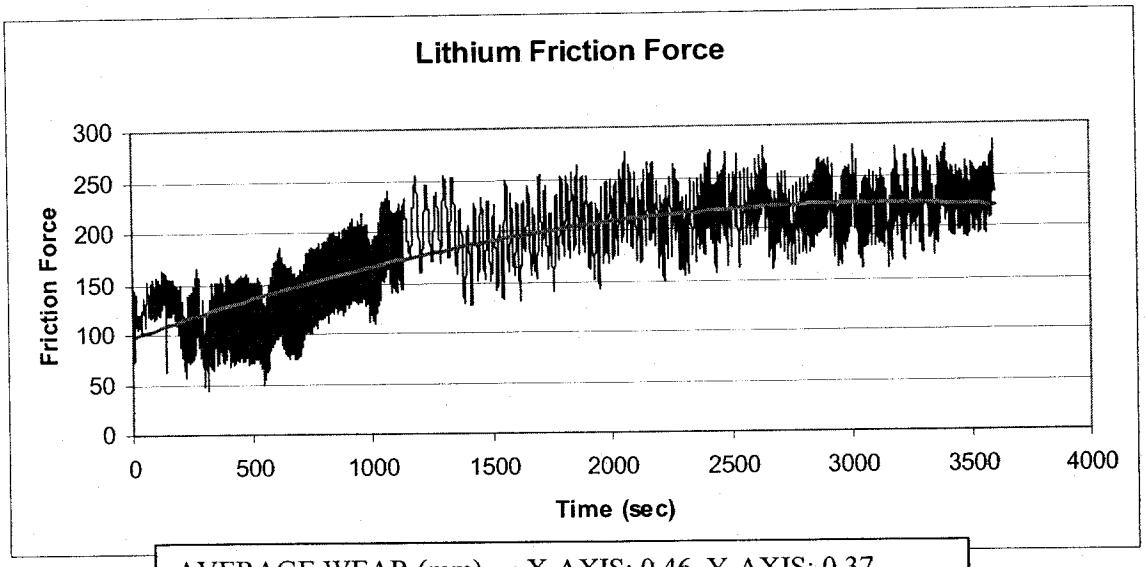


AVERAGE WEAR (mm) X-AXIS: 0.46, Y-AXIS: 0.37
AVERAGE FRICTION FORCE 187 gm

Figure 6-16 – Lithium Lube-Friction Vs Time

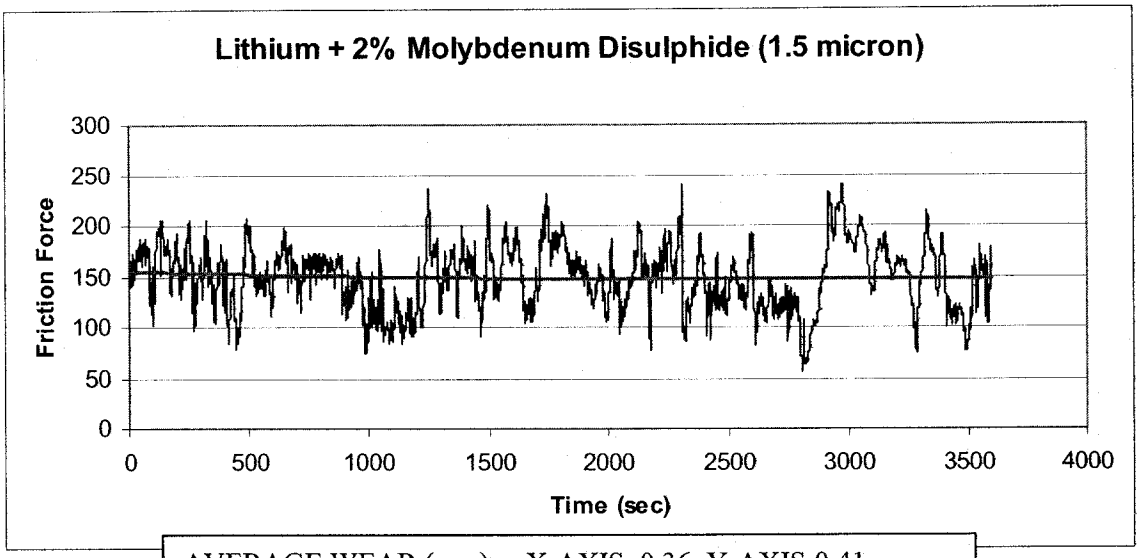


AVERAGE WEAR (mm) X-AXIS: 0.36, Y-AXIS:0.41
AVERAGE FRICTION FORCE 148 gm

Figure 6-17 – Lithium Lube Plus 2% MoS2 (1.5 micron)-Friction Vs Time

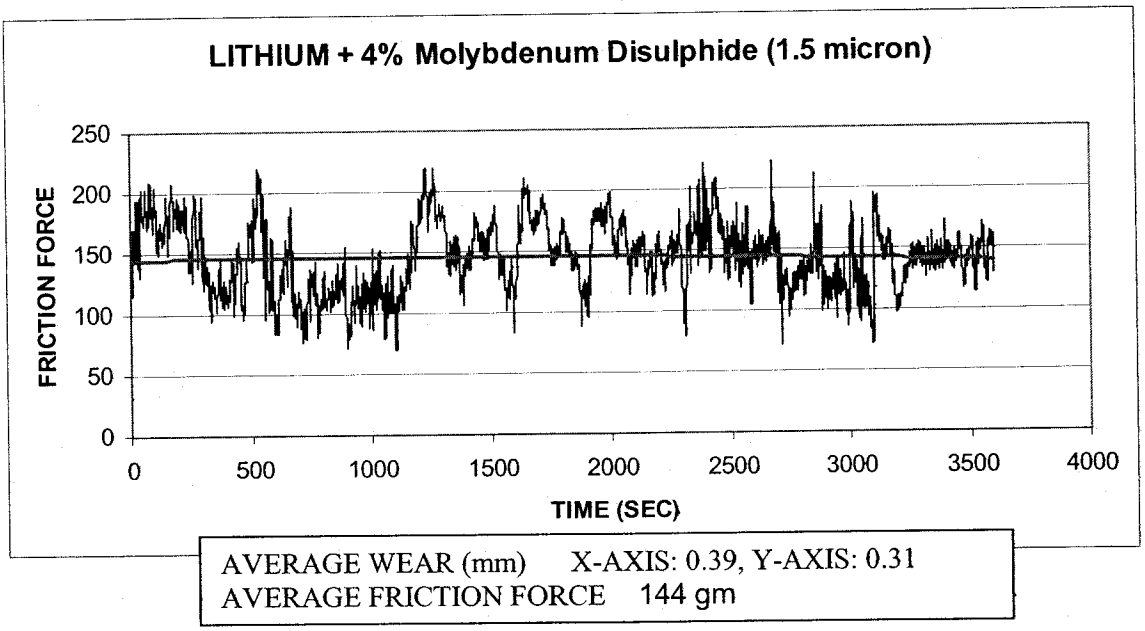


AVERAGE WEAR (mm) X-AXIS: 0.39, Y-AXIS: 0.31
AVERAGE FRICTION FORCE 144 gm

Figure 6-18 – Lithium Lube Plus 4% MoS2 (1.5 micron)-Friction Vs Time

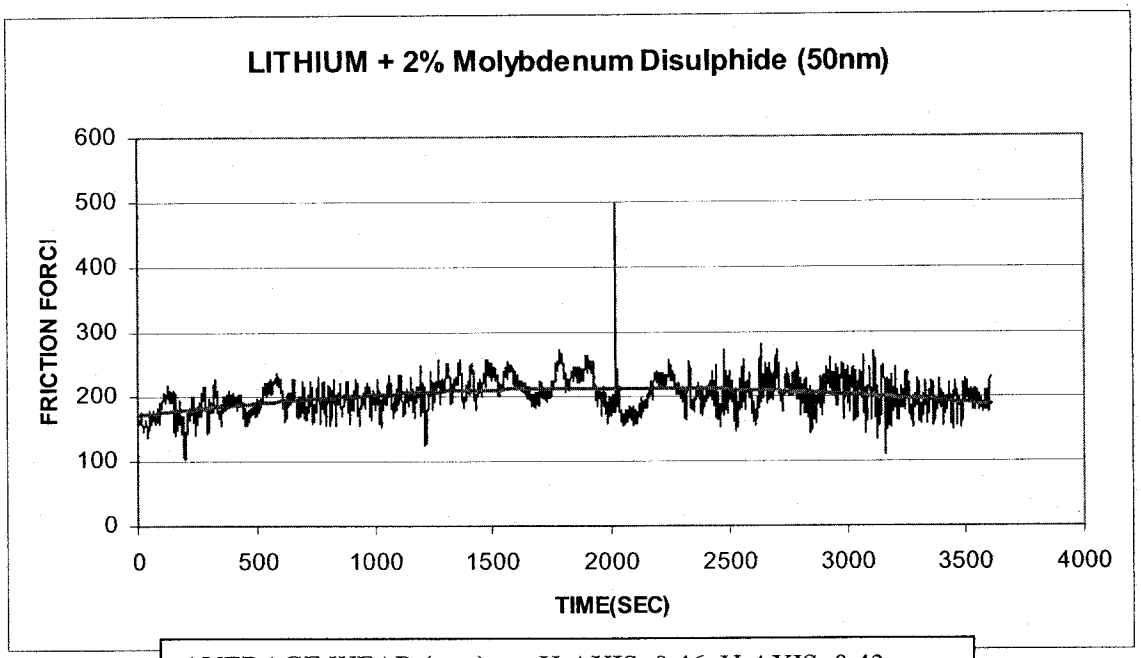


AVERAGE WEAR (mm) X-AXIS: 0.46, Y-AXIS: 0.43
AVERAGE FRICTION FORCE 201 gm

Figure 6-19 – Lithium Lube Plus 2% MoS2 (50 nm)-Friction Vs Time

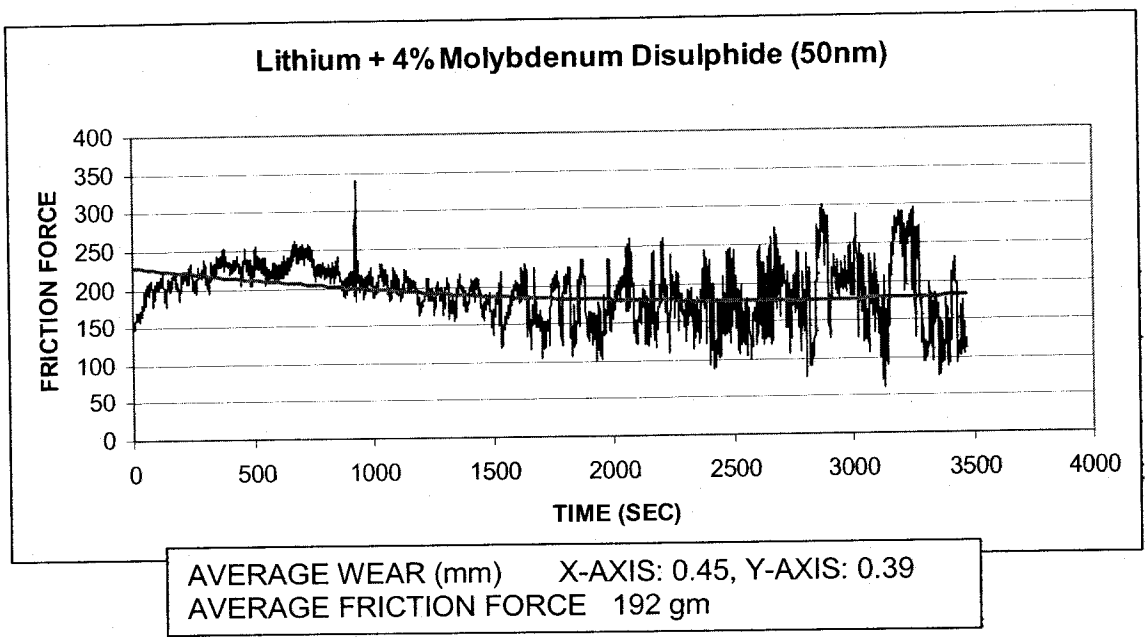


Figure 6-20 – Lithium Lube Plus 4% MoS2 (50 nm)-Friction Vs Time

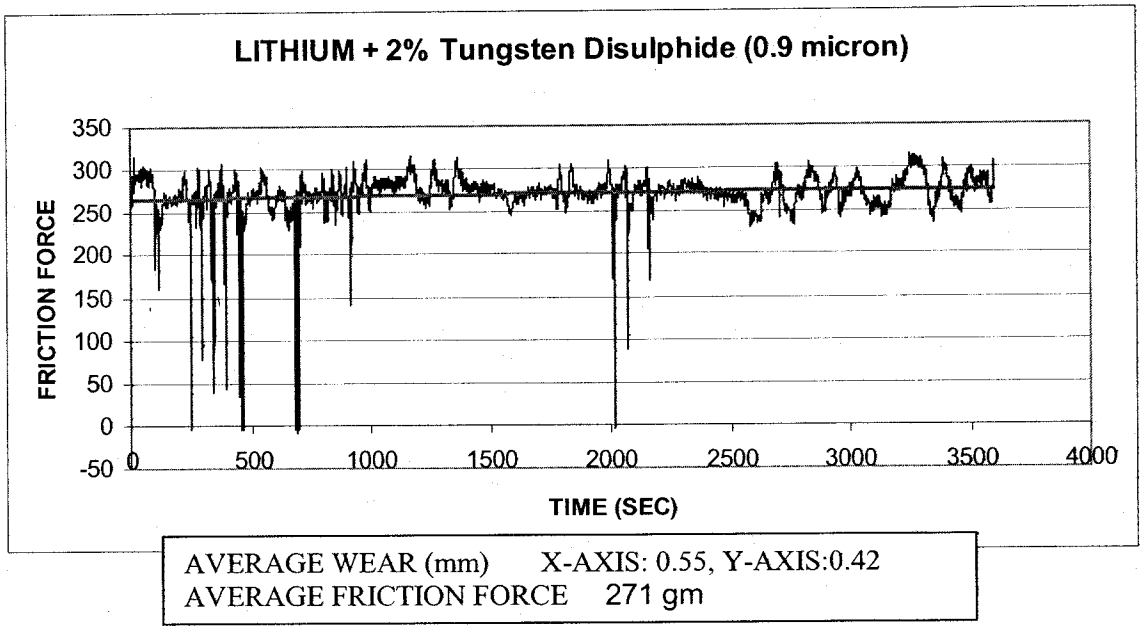


Figure 6-21 – Lithium Lube Plus 2% WS2 (0.9 micron)-Friction Vs Time

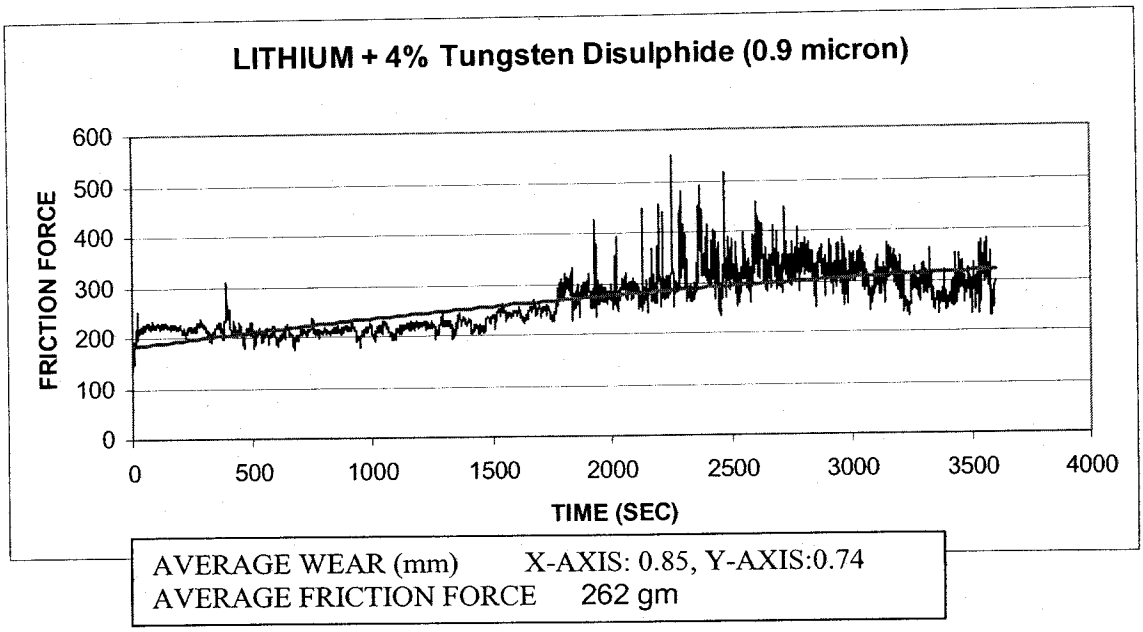


Figure 6-22 – Lithium Lube Plus 4% WS2 (0.9 micron)-Friction Vs Time

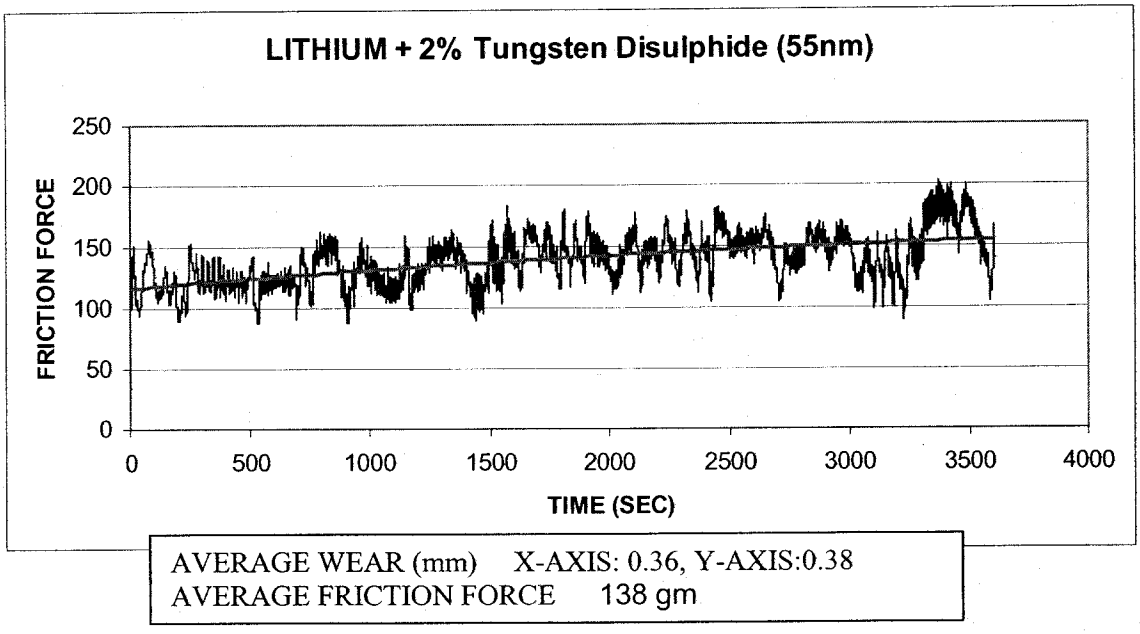


Figure 6-23 – Lithium Lube Plus 2% WS2 (55 nm)-Friction Vs Time

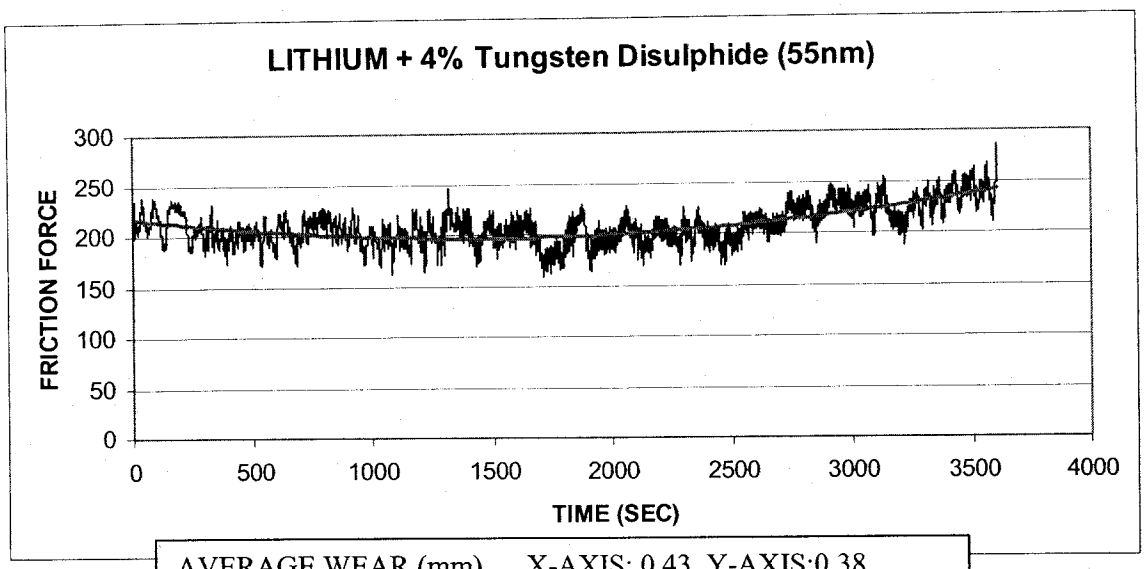


AVERAGE WEAR (mm) X-AXIS: 0.43, Y-AXIS:0.38
AVERAGE FRICTION FORCE 208 gm

Figure 6-24 – Lithium Lube Plus 4% WS2 (55 nm)-Friction Vs Time

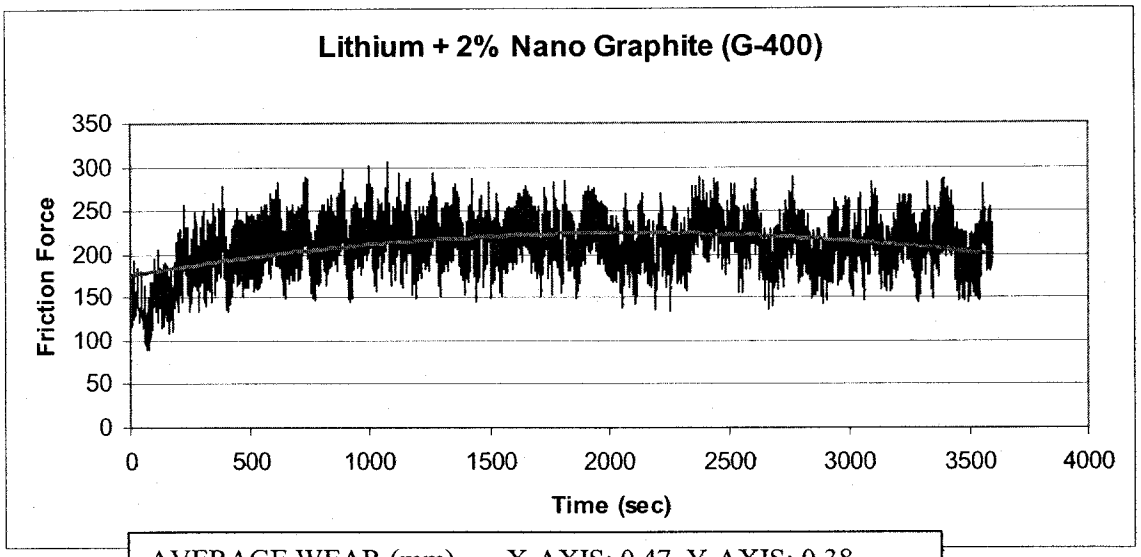


AVERAGE WEAR (mm) X-AXIS: 0.47, Y-AXIS: 0.38
AVERAGE FRICTION FORCE 211 gm

Figure 6-25 – Lithium Lube Plus 2% Nano Graphite (G-400)-Friction Vs Time

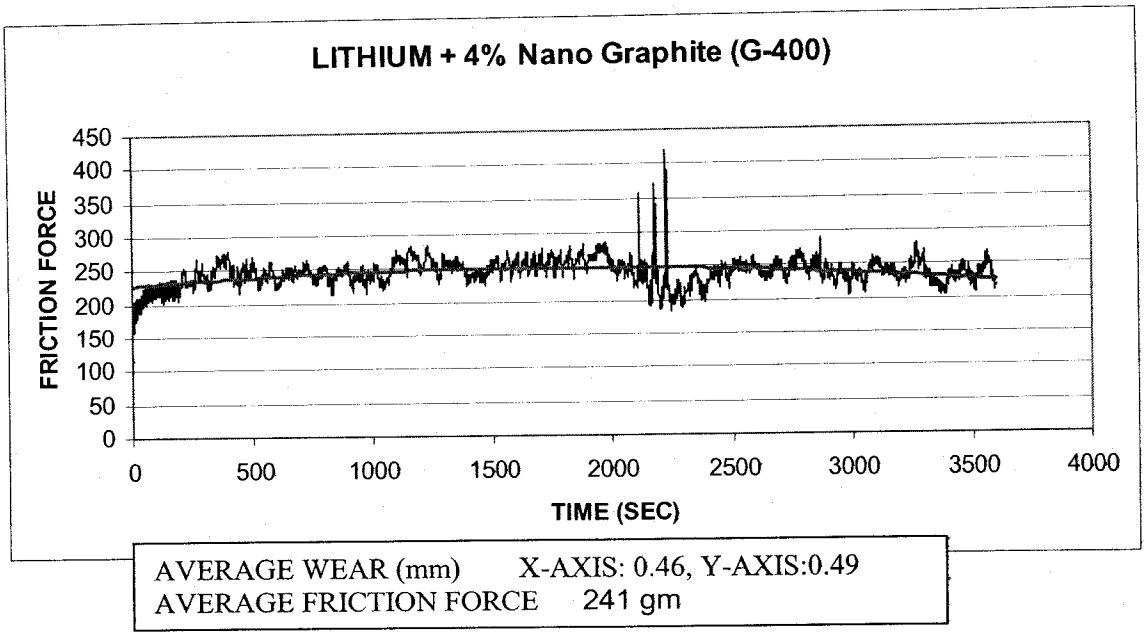


AVERAGE WEAR (mm) X-AXIS: 0.46, Y-AXIS:0.49
AVERAGE FRICTION FORCE 241 gm

Figure 6-26 – Lithium Lube Plus 4% Nano Graphite (G-400)-Friction Vs Time

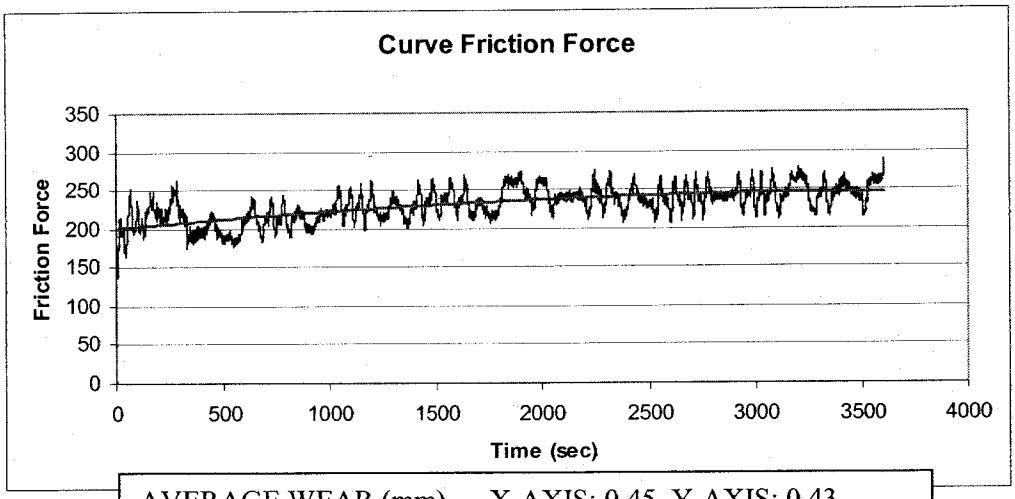


AVERAGE WEAR (mm) X-AXIS: 0.45, Y-AXIS: 0.43
AVERAGE FRICTION FORCE 230 gm

Figure 6-27 – Curve Lube-Friction Vs Time

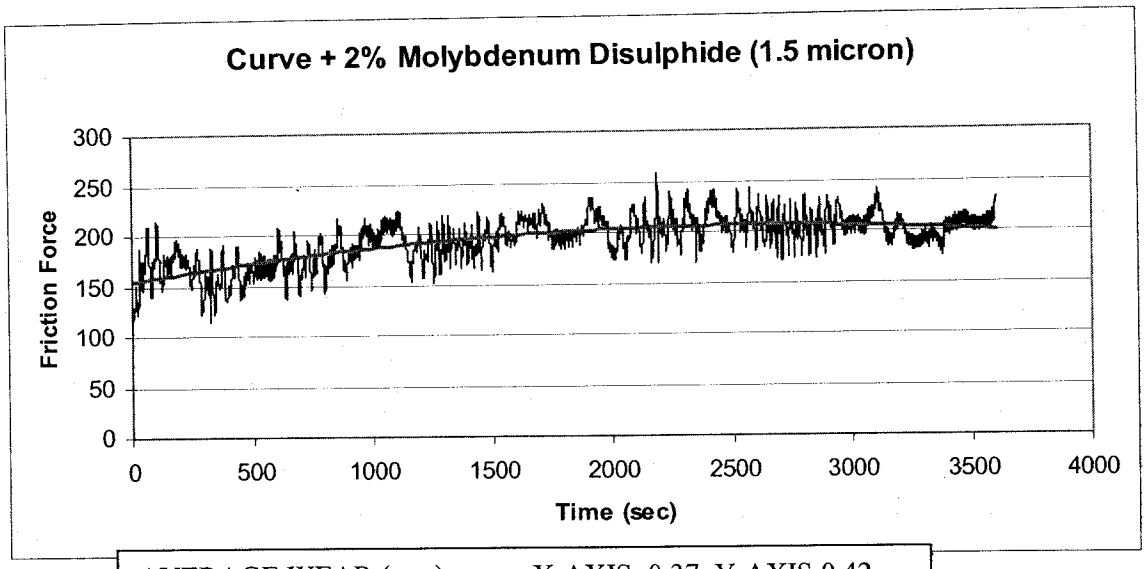


AVERAGE WEAR (mm) X-AXIS: 0.37, Y-AXIS:0.42
AVERAGE FRICTION FORCE 193 gm

Figure 6-28 – Curve Lube Plus 2% MoS2 (1.5 microns)-Friction Vs Time

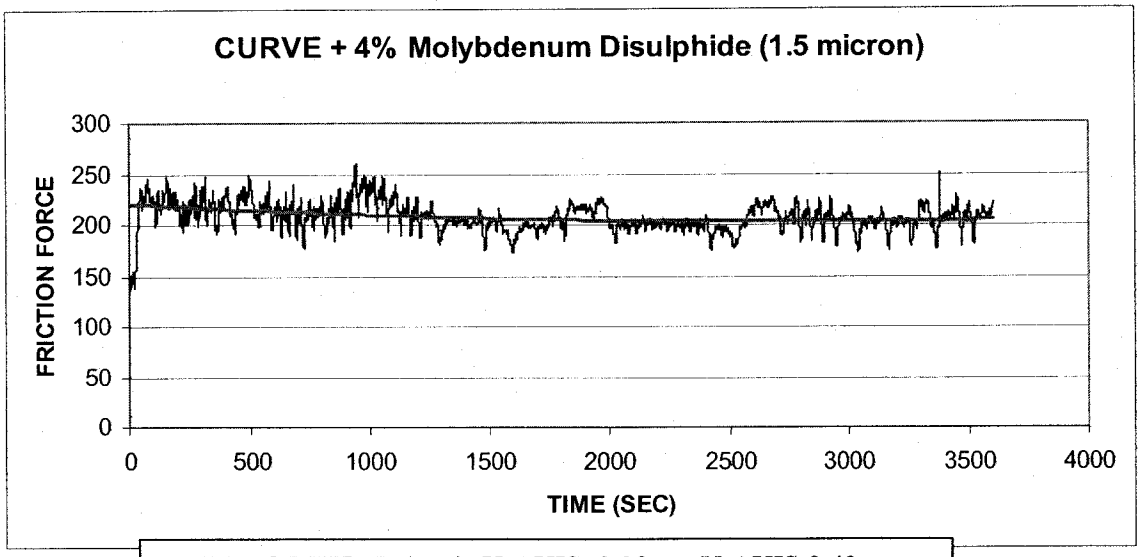


AVERAGE WEAR (mm): X-AXIS: 0.38 Y-AXIS:0.43
AVERAGE FRICTION FORCE 207 gm

Figure 6-29 – Curve Lube Plus 4% MoS2 (1.5 microns)-Friction Vs Time

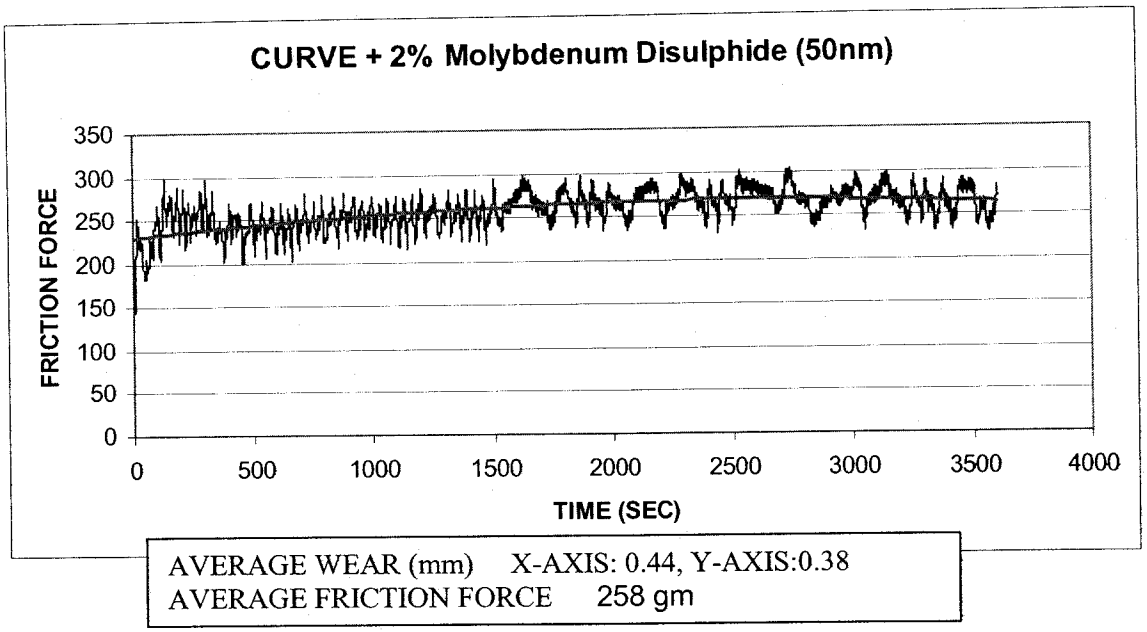


Figure 6-30 – Curve Lube Plus 2% MoS2 (50 nm)-Friction Vs Time

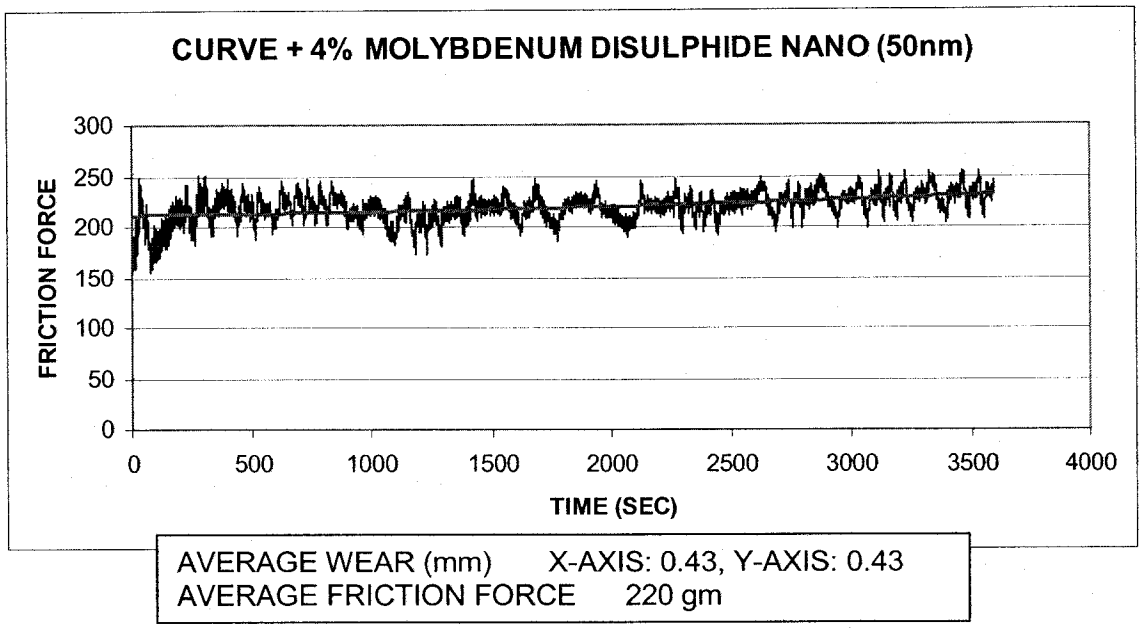


Figure 6-31 – Curve Lube Plus 4% MoS2 (50 nm)-Friction Vs Time

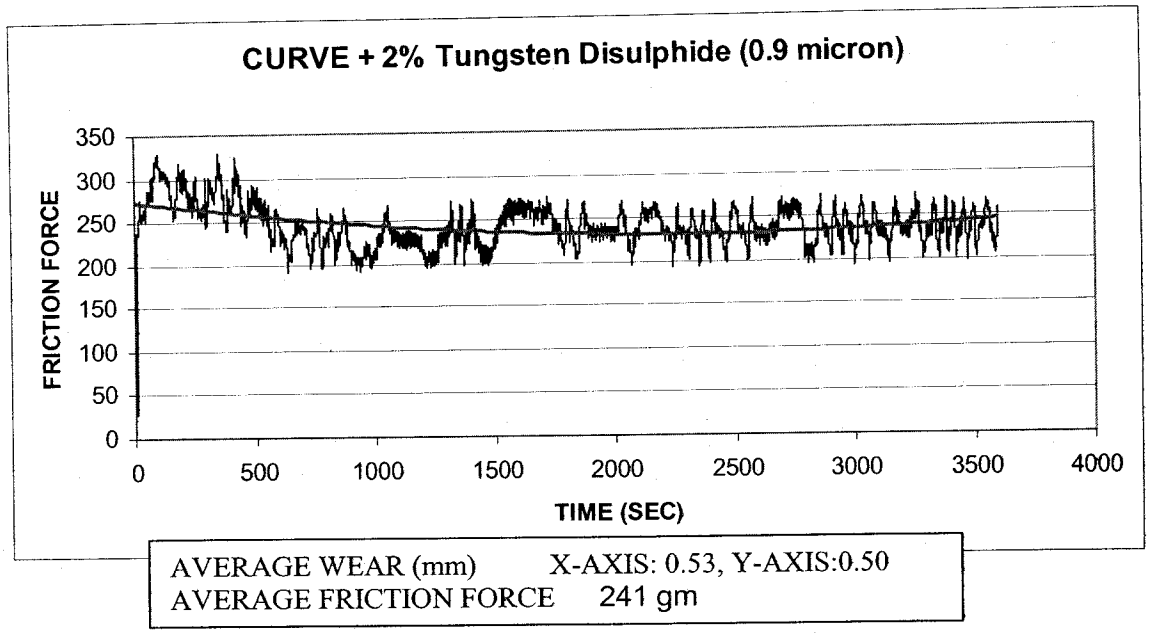


AVERAGE WEAR (mm) X-AXIS: 0.53, Y-AXIS:0.50
AVERAGE FRICTION FORCE 241 gm

Figure 6-32 – Curve Lube Plus 2% WS2 (0.9 micron)-Friction Vs Time

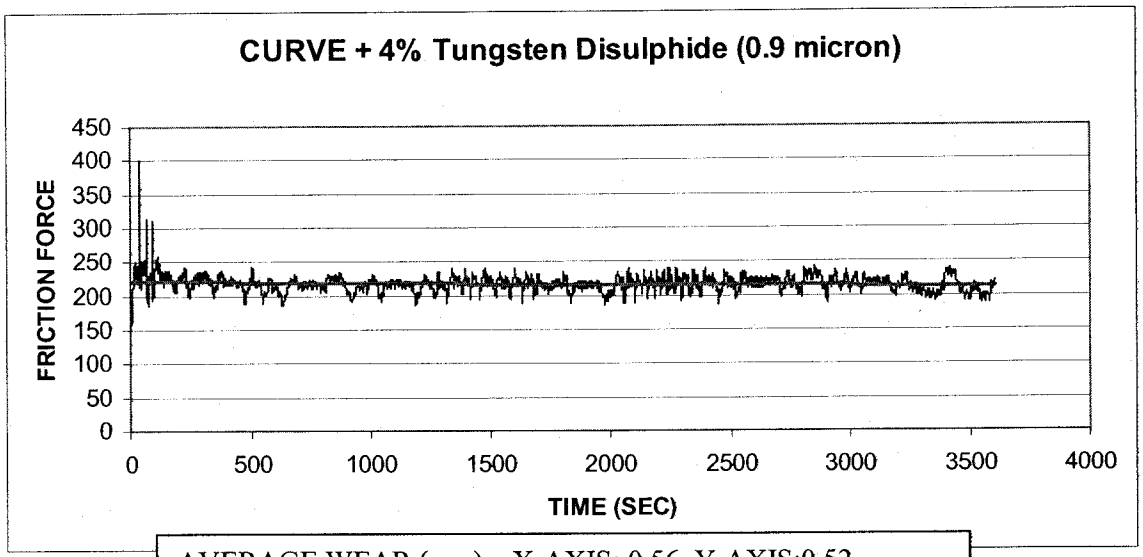


AVERAGE WEAR (mm) X-AXIS: 0.56, Y-AXIS:0.52
AVERAGE FRICTION FORCE 216 gm

Figure 6-33 – Curve Lube Plus 4% WS2 (0.9 micron)-Friction Vs Time

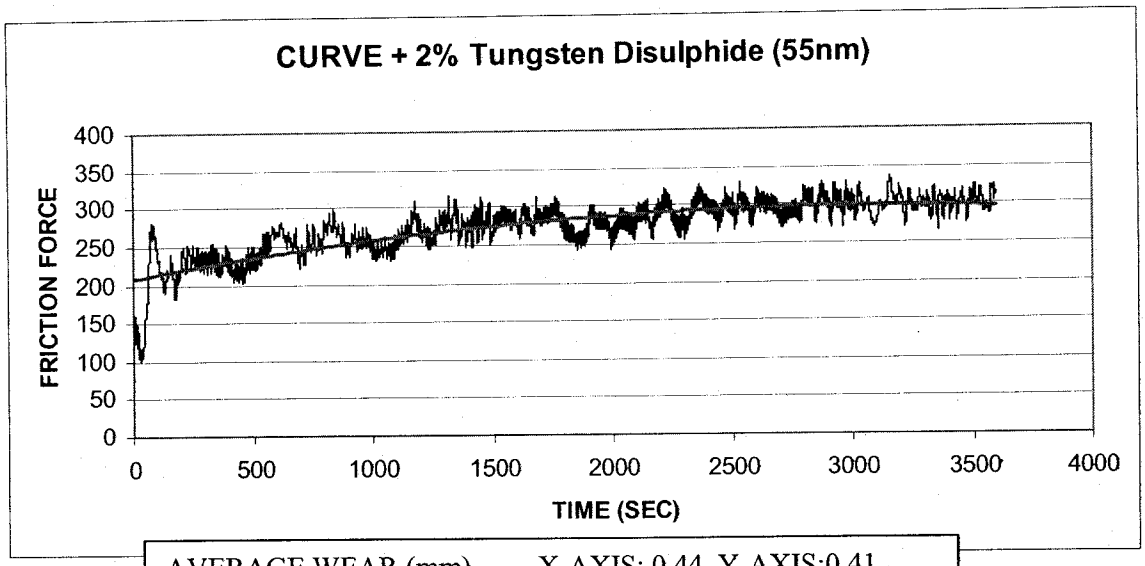


AVERAGE WEAR (mm) X-AXIS: 0.44, Y-AXIS:0.41
AVERAGE FRICTION FORCE 272 gm

Figure 6-34 – Curve Lube Plus 2% WS2 (55 nm)-Friction Vs Time

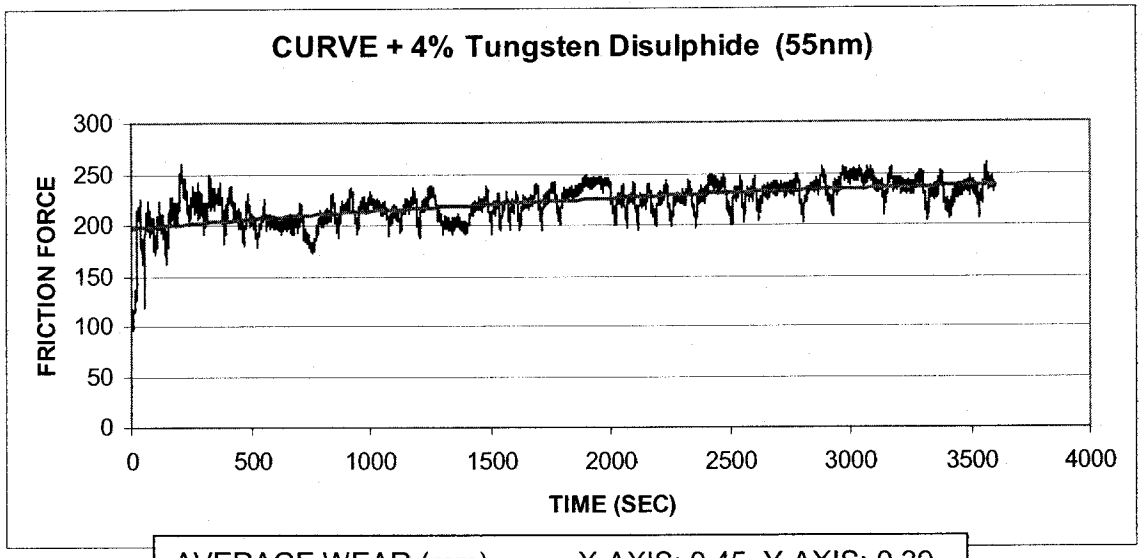


AVERAGE WEAR (mm) X-AXIS: 0.45, Y-AXIS: 0.39
AVERAGE FRICTION FORCE 221 gm

Figure 6-35 – Curve Lube Plus 4% WS2 (55 nm)-Friction Vs Time

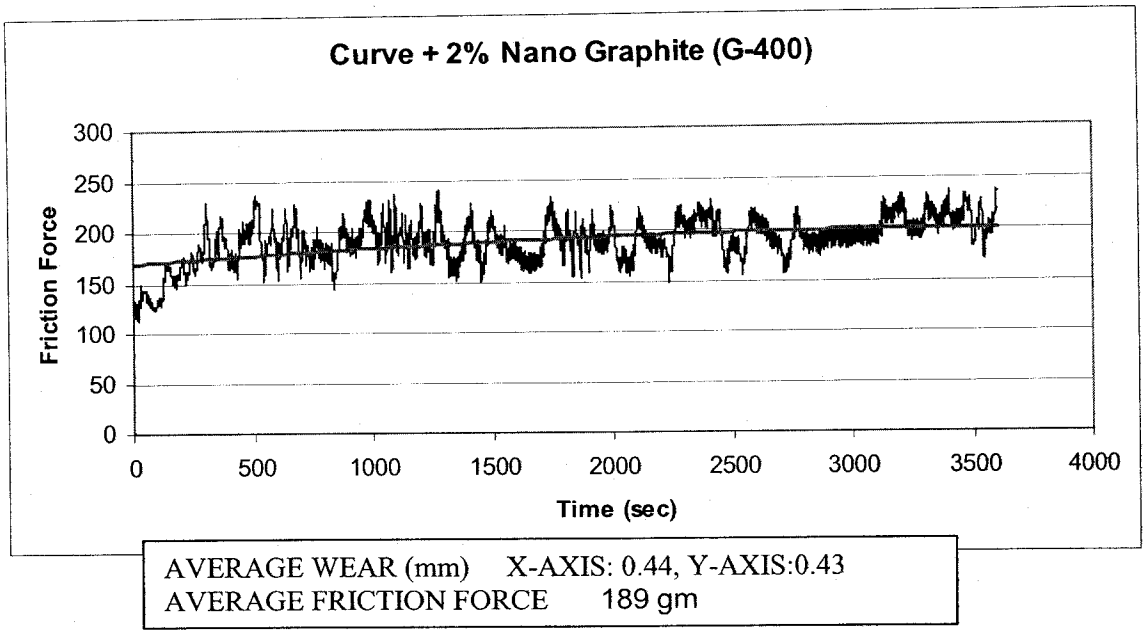


AVERAGE WEAR (mm) X-AXIS: 0.44, Y-AXIS:0.43
AVERAGE FRICTION FORCE 189 gm

Figure 6-36 – Curve Lube Plus 2% Nano Graphite (G-400)-Friction Vs Time

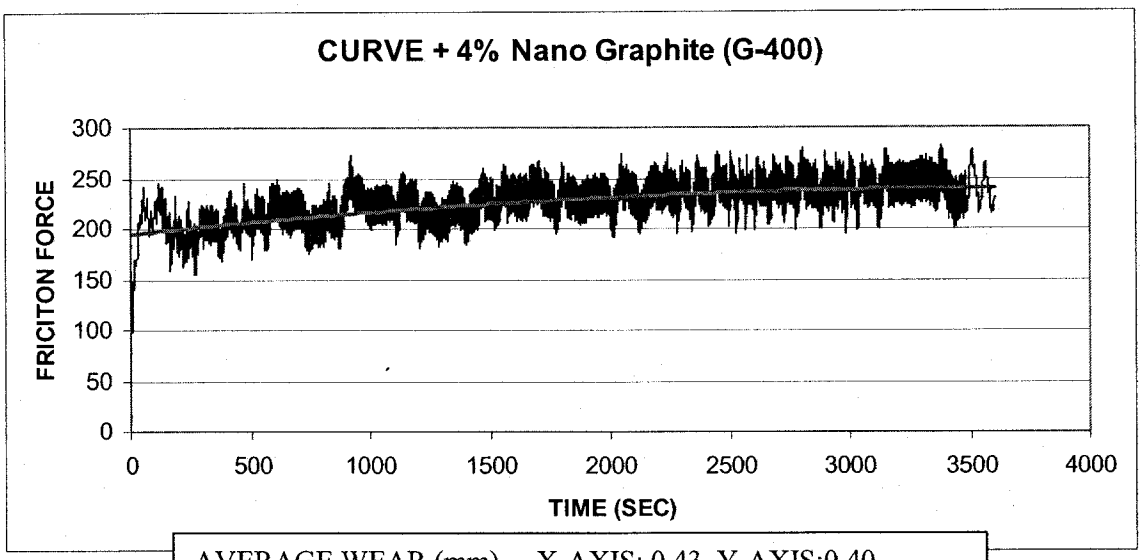


AVERAGE WEAR (mm) X-AXIS: 0.43, Y-AXIS:0.40
AVERAGE FRICTION FORCE 224 gm

Figure 6-37 – Curve Lube Plus 4% Nano Graphite (G-400)-Friction Vs Time

For better understanding of effects of nano-material on the performance of lubricants summary data charts (Figure 6.38- Figure 6.42) are derived from the above data. Wear scar and friction force of the modified lube (Nano-Lube) are compared against the base lube.

ARAPEN

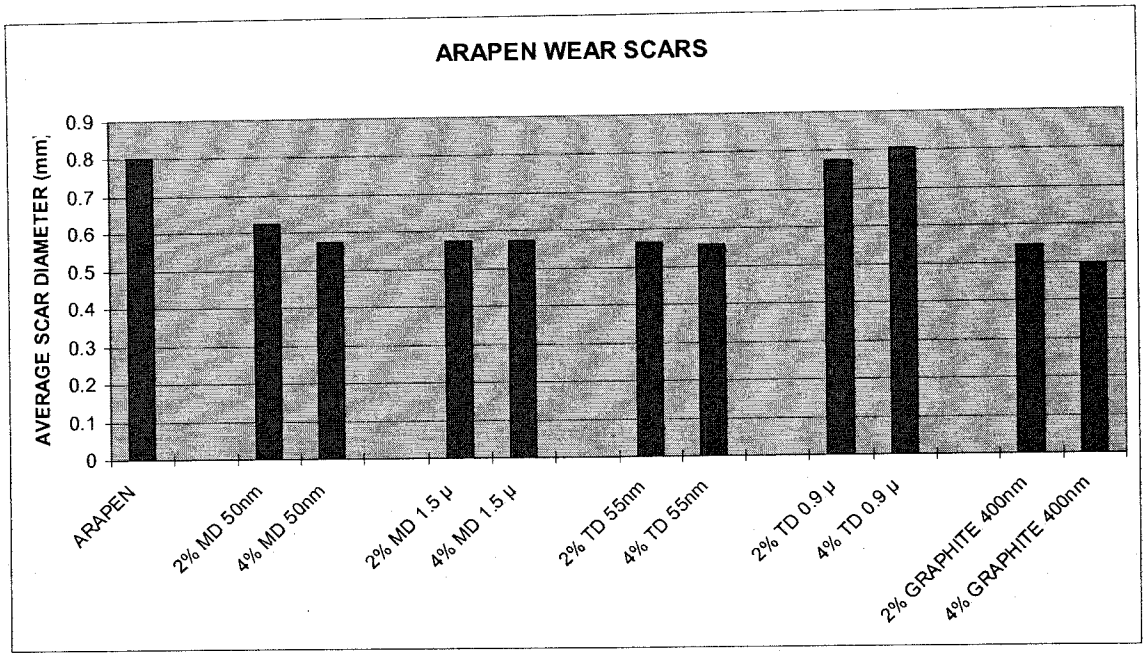


Figure 6-38 – Arapen Lube Wear Scar Vs Modified Arapen (Nano-Lube)

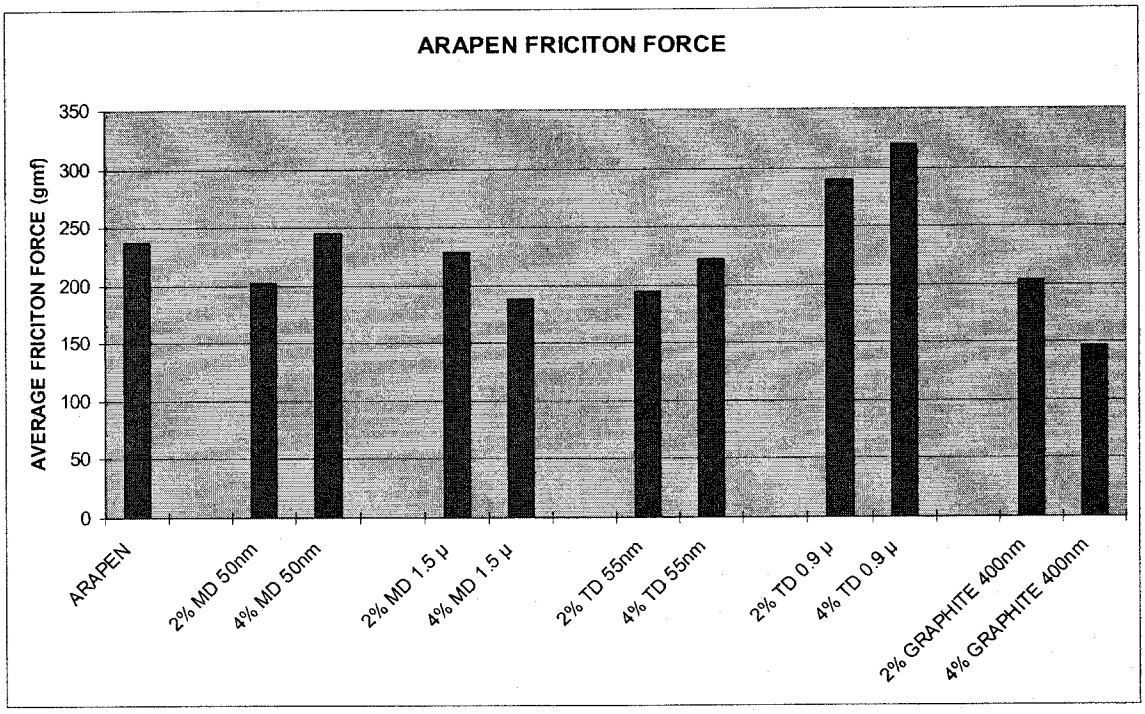


Figure 6-39 – Arapen Lube Friction Vs Modified Arapen (Nano-Lube)

## LITHIUM GREASE

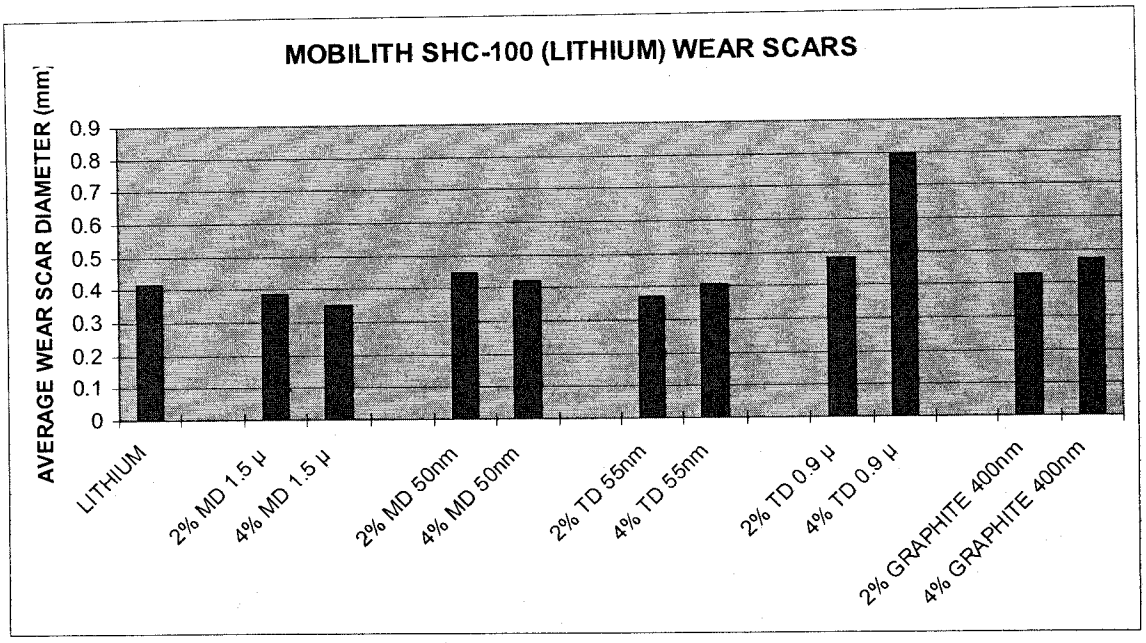


Figure 6-40 – Lithium Lube Wear Scar Vs Modified Lithium (Nano-Lube)

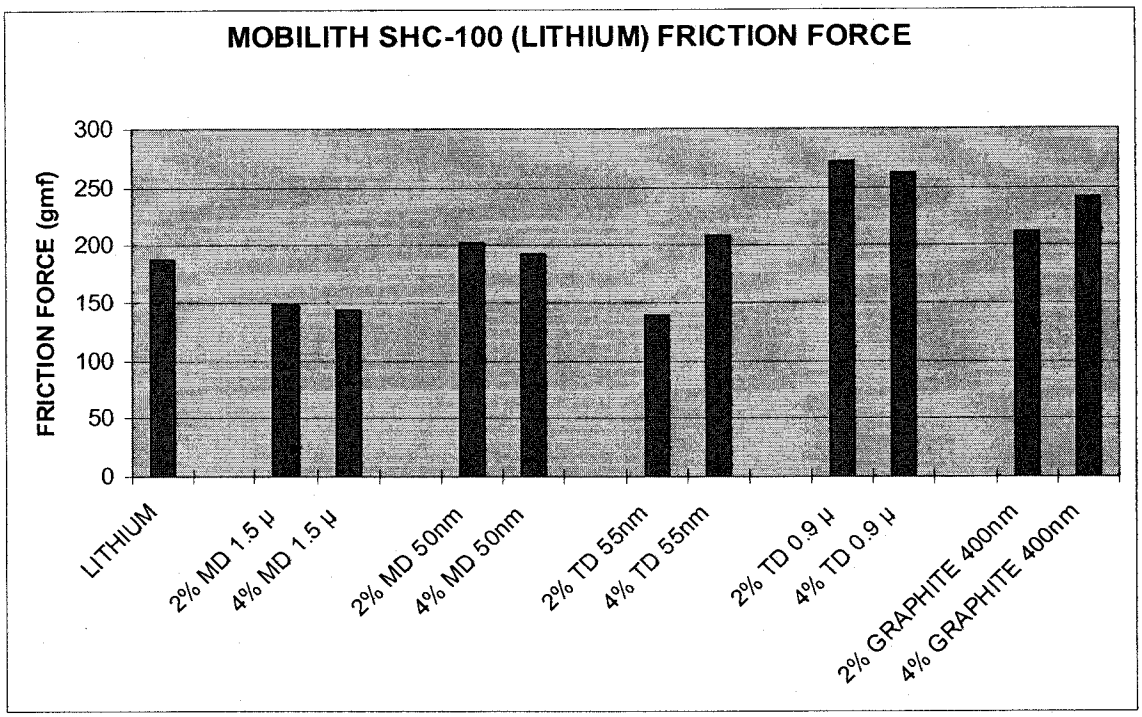


Figure 6-40 – Lithium Lube Friction Vs Modified Lithium (Nano-Lube)

## CURVE GREASE

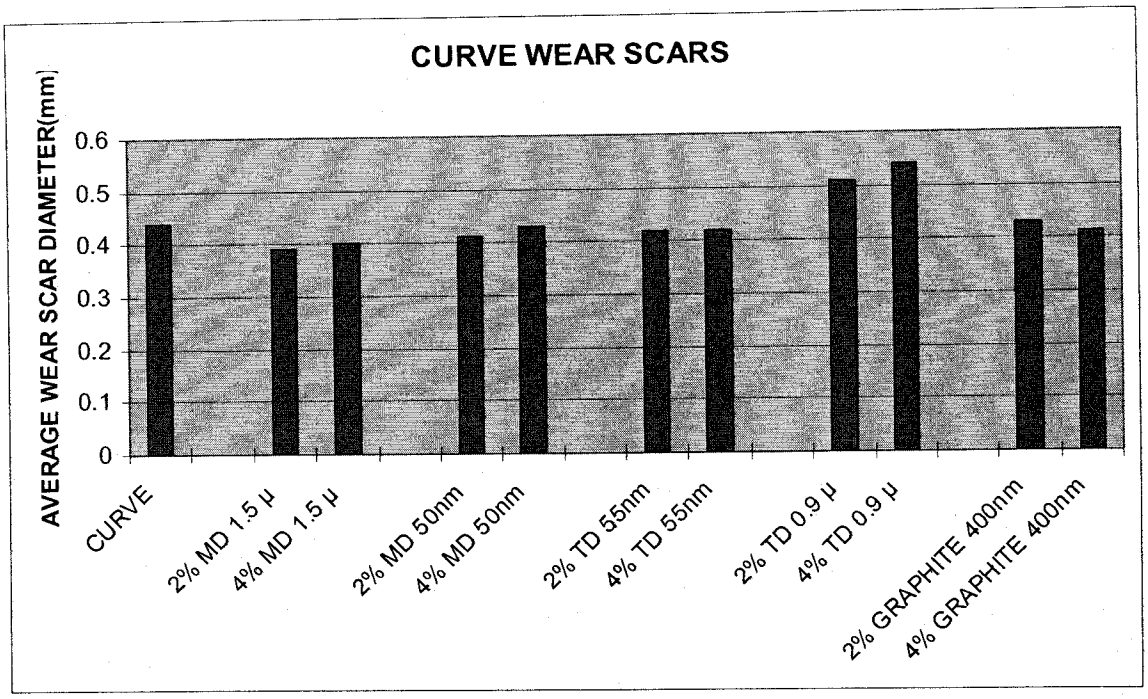


Figure 6-41 – Curve Lube Wear Scar Vs Modified Curve Lube (Nano-Lube)

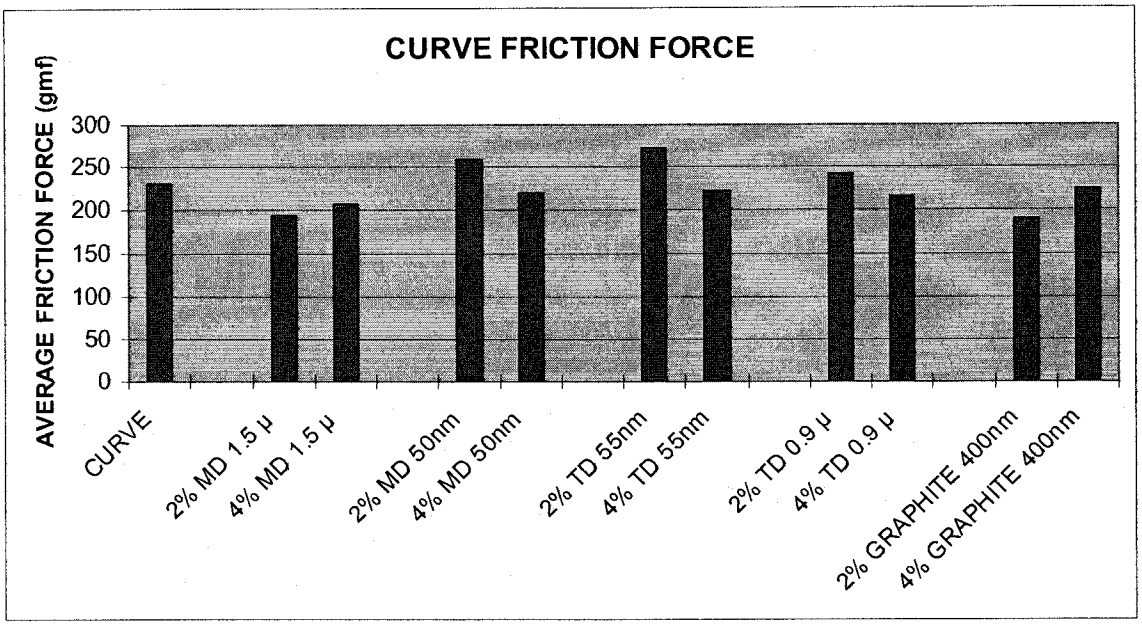


Figure 6-42 – Curve Lube Friction Vs Modified Curve Lube (Nano-Lube)

The results show that the base lubricants improved performance with some combination and amount of nano-material for both friction and wear. Arapen grease with 4% Graphite 400nm has less friction and wear. Whereas, Tungsten Disulphide has a negative effect on the grease. Lithium (synthetic) has better performance as base lubricant compared to Arapen. Even Lithium has shown superior performance with 4% Molybdenum Disulphide (MD)-1.5 microns. For this

lube 2% Tungsten Disulphide-55nm showed comparable performance. Curve grease 2% Molybdenum Disulphide (MD)-1.5 microns has the best performance.

Every so often there is sudden increase in loads at wheel/rail interface due to rail track condition. That means for very short time the contact stresses between at wheel/rail interface go to several times to that of normal operating stress. The final optimum combination of base lube and nano-particles in above experimental study are based normal operating loads. The load in 4 ball wear test corresponding to normal rail-road operation is 40 Kg. The lubes also had to with stand without major damage (like wheel-rail seizure) for sudden high loads (very short duration). EP (Extreme Pressure) 4 ball test simulates high load condition. The loads are increased starting with normal load in short time, about one minute till the 4 balls seize.

The following figures, 6-43 through 6-45, show the EP loads for Arapen, Lithium, and Curve grease for all combinations of nano-particles. Based on friction and wear Arapen with 4% graphite 400 nm was selected for normal operating condition (40 Kg). For this combination the EP load is 160 Kg, not the highest EP load but is 4 times higher than normal load. For the Lithium the optimum combination for normal load is also highest EP load 400 Kg. Whereas, curve grease EP load is 200 Kg, not the highest EP load combination. The optimum base lube and nano-particles combination based on normal load condition is not changed since EP loads are 4 times or greater than normal load.

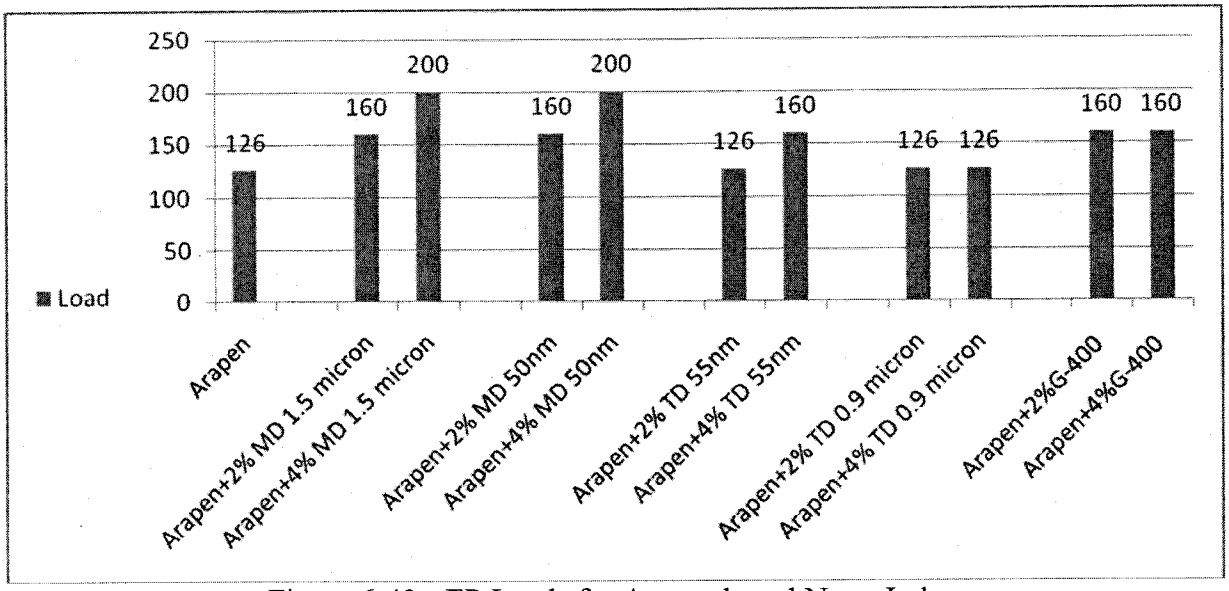


Figure 6-43 - EP Loads for Arapen based Nano-Lubes

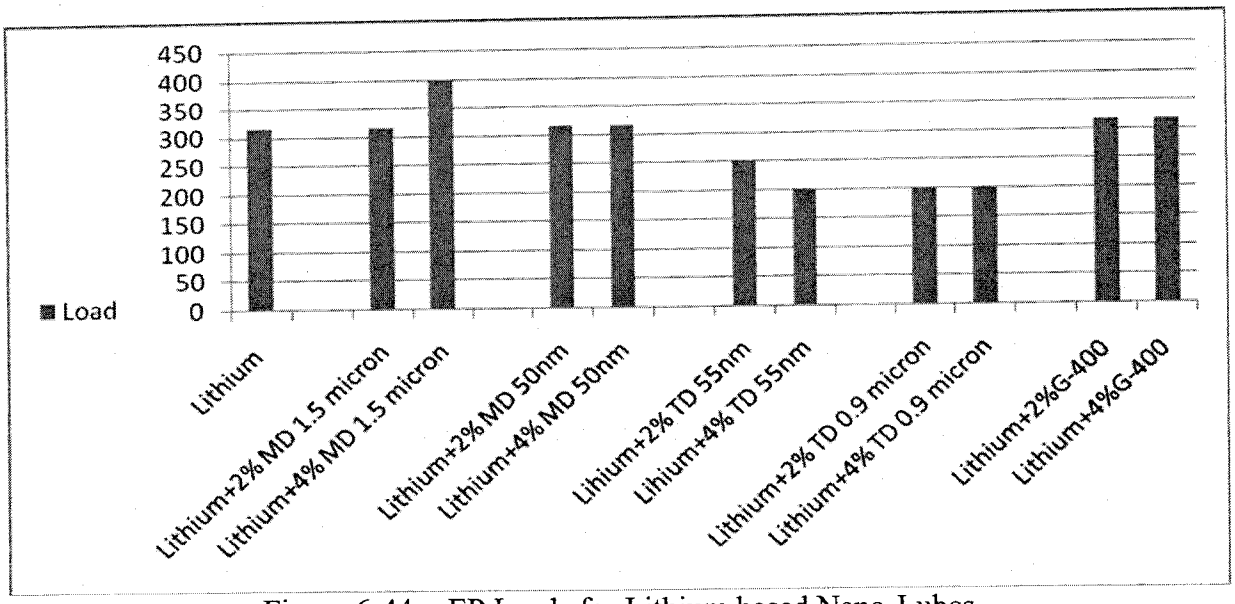


Figure 6-44 - EP Loads for Lithium based Nano-Lubes

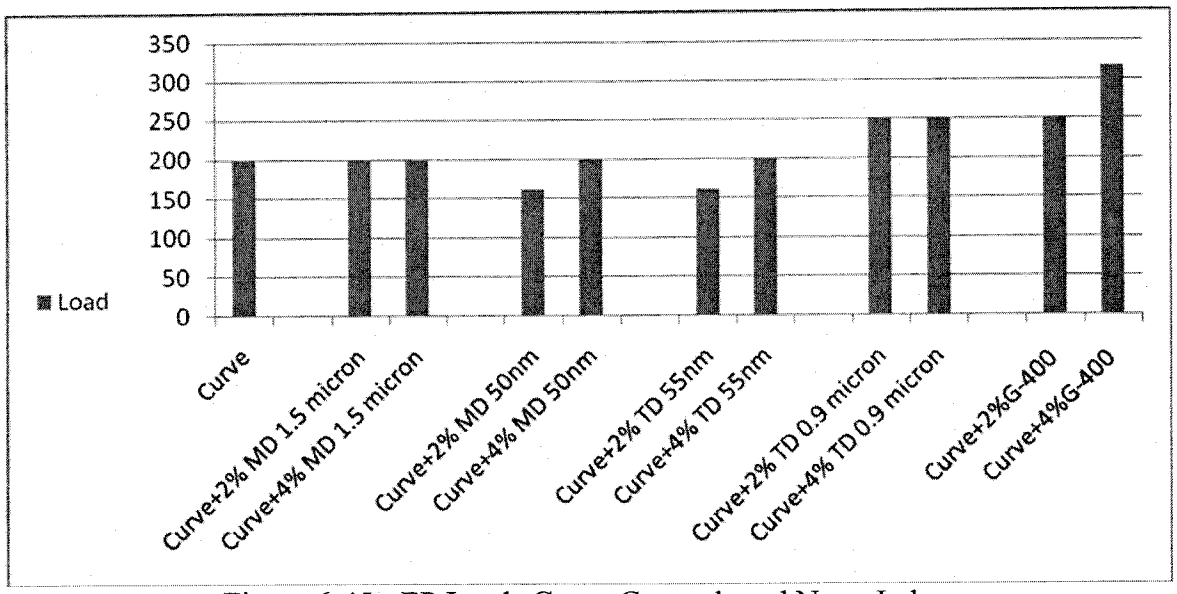


Figure 6-45 - EP Loads Curve Grease based Nano-Lubes

**References**

[1] "Guidance for Biodiesel Producers and Biodiesel Blenders/Users," U. S. Environmental Protection Agency, Transportation and Regional Programs Division, Office of Transportation and Air Quality, Report EPA420-B-07-019, November 2007.

[2] "Short Term Energy Outlook," Energy Information Administration, September 9, 2009.

[3] "Clean Cities Alternative Fuel Price Report," United States Department of Energy, Energy Efficiency and Renewable Energy, September 2005, June 2006, July and October 2007, January, April, July 2008, October 2008, January 2009, April 2009 and July 2009.

[4] Coyle, William, "The Future of Biofuels –A Global Perspective," Economic Research Service, USDA, May 2007.

[5] "US Projected to Lead World Biodiesel Market," Biodiesel Magazine, December 2008.

[6] Fritz, S. G., "Evaluation of Biodiesel Fuel in an EMD GP38-2 Locomotive," National Renewable Energy Laboratory, Southwest Research Institute, Report NREL/SR-510-33436, Golden, Colorado, May 2004.

[7] McKenna, D., et al., "Evaluation of Emissions and Performance of Diesel Locomotives with B20 Biodiesel Blends: Static Test Results," RTDF2008-74030, ASME Rail Transportation Division Fall Technical Conference, Chicago, IL, September 24-25, 2008.

[8] *Gavrich, D., Bob Grady, Don Chernich, Mark Burnitzki, Roelof Riemersma, Wayne Sobieralski, Harlan Quan, and Don Holve, "SFBR Biodiesel Test Study:* Emissions Evaluation of a 1944 Alco S2 Switch Locomotive Operated on Biodiesel and California, Ultra Low Sulfur Diesel," California Environmental Protection Agency Air Resources Board, September 24, 2008.

[9] Lelio, Jim, "Terminal & Pipeline Infrastructure Development for Biodiesel Applications," National Biodiesel Conference, Session 12, February 2009.

[10] "Biodiesel Handling and Use Guide," National Renewable Energy Laboratory, NREL/TP-540-43672, 4th edition, September 2008.

[11] Browning, John, "A Distributor's Perspective on Biodiesel," National Biodiesel Conference, Session 19, February 2009.

[12] "Clean Cities, Fact Sheet: Biodiesel Blends," National Renewable Energy Laboratory, DOE/GO-102008-2542, April 2008.

[13] Holden, Bruce, "Case Study; The Switch to Biodiesel at Camp Pendleton Marine Corps Base," Air & Waste Management Association's Magazine for Environmental Managers, May, 2006, pp. 18-20.

[14] "Brazilian Miner Vale to make Switch to Biodiesel," Progressive Railroading Daily News, June 26, 2009.

[15] Parvate-Patil, G., Manuel Vasquez, and Malcolm Payne, "Effects of Different Biodiesel Blends on Heat Release and it's Related Parameters," ASME Internal Combustion Engine Division, Fall Technical Conference, Sacramento, California, November 5-8, 2006, pp. 225-231.

[16] "Clean Cities, Fact Sheet: Biodiesel Blends," National Renewable Energy Laboratory, DOE/GO-102005-2029, April 2005.

[17] Conley, S. P. and Bernie Tao, "Biodiesel Quality: Is All Biodiesel Created Equal?" Purdue University Extension, Purdue Agriculture, ID-338, December 2006.

[18] Morcos, Michelle, "Biodiesel and Engine Oil," Session 34, National Biodiesel Conference, Session 19, February 2009.

[19] A. Gebregergis, P. Pillay, D. Bhattacharyya and R. Rengaswemy, "Solid oxide fuel cell modeling," IEEE Transaction on Industrial Electronics, Vol. 56, pp. 139-148, Jan 2009

[20] A. Gebregergis, P. Pillay, "The development of solid oxide fuel cell (SOFC) emulator," 2007 IEEE Power Electronics Specialists Conference, pp. 1232-1238, June 2007

[21] Massimo Ceraolo, "New Dynamical Models of Lead-Acid Batteries", *IEEE transactions on Power Systems*, Vol. 15, Issue 4, Nov, 2000. Page(s):1184-1190.

[22] G. Barbee, "Duty Cycle", Norfolk Southern Report, 2008

[23] G. Barbee, "Pusher Duty Cycle / Battery Applications", Norfolk Southern Report, April 2009

[24] Biodiesel Handling and Use Guide, National Renewable Energy Laboratory, Sept 2008, NREL/TP-540-43672

[25] Organic Fuel, MSDS B100, Biodiesel, June 30, 2006

[26] Peterson, Charles and Moller, Gregory. "Biodegradability, BOD4, COD and Toxicity of Biodiesel Fuels", University of Idaho Biodiesel Education Program.

[27] Crabtree, George W., Dresselhaus, Mildred S. and Buchanan, Michelle V., The Hydrogen Economy, Physics Today, December, 2004

[28] Health Effects of Carbon Dioxide Gas, http://www.ccohs.ca/oshanswers/chemicals/chem_profiles/carbon_dioxide/health_cd.htm

[29] BOC Gases, Material Safety Data Sheet for Carbon Monoxide, http://www.vngas.com/pdf/g112.pdf revised June 7, 1996

[30] US Department of Labor, Occupational Safety and Health Administration, Carbon Monoxide, http://www.osha.gov/SLTC/healthguidelines/carbonmonoxide/

[31] Linde Gas, Material Safety Data Sheet for Carbon Monoxide, http://www.orcbs.msu.edu/msds/linde_msds/pdf/017.pdf, January 1995

[32] Center for Disease Control (CDC) and the National Institute for Occupational Safety and Health (NIOSH), Documentation for Immediately Dangerous to Life or Health Concentrations (IDLH): NIOSH Chemical Listing and Documentation of Revised IDLH Values (as of 3/1/95), NTIS Publication No. PB-94-195047:

[33] BOC Gases, Material Safety Data Sheet for Hydrogen, http://www.vngas.com/pdf/g4.pdf, Revised June, 1996

[34] Chemical properties of hydrogen, Lenntech Water treatment & Air Purification Holding B.V.Rotterdamseweg, The Netherlands, http://www.lenntech.com/Periodic-chart-elements/H-en.htm

[35] Hydrogen Embrittlement Mechanisms in Metals, Material Science and Technology, Sandia National Laboratories, http://www.sandia.gov/mission/ste/stories/2007/hydrogen_embrittlement.pdf

[36] New material in automotive tribology; Y.Enomoto, T.Yamamoto; Tokyo University of engineering and technology; 1998.

[37] Basic properties of reference cross-ply carbon fiber composite; J.Corum, L.Battiste, K.Liu, M.Ruggles; Oak ridge national laboratory; February, 2000.

[38] Train accident reconstruction and FELA & railroad litigation; By J. R. Loumiet, W.G. Jungbauer; Lawyers and judge publishing company inc; fourth edition.

[39] http://www.freepatentsonline.com/4466513.html

[40] Chryssolouris, G. 2006. Manufacturing Systems Theory and Practice. New York: Springer

[41] Rinjiro Nakamura, D.Eng., Keizaburo Fukuoka. 1960. Tentative Manufacture of Molded Composition Brake Shoes.

[42] http://www.google.com/search?hl=en&defl=en&q=define:stoving&ei=etHZSeXKHZvAM4uV8e0O&sa=X&oi=glossary_definition&ct=title&cts=1239011736595

[43] http://en.wikipedia.org/wiki/Curing_(chemistry)

[44] Leland Blank, Anthony Tarquin., 2005. Engineering Economy

[45] http://www.nscorp.com/nscorphtml/ar08/2008_10K.pdf

[46] http://www.eia.doe.gov/cneaf/electricity/epm/tablees1a.html